

DISCLAIMER:

This document does not meet the
current format guidelines of
the Graduate School at
The University of Texas at Austin.

It has been published for
informational use only.

Copyright
by
William Guy Hardin
2017

**The Dissertation Committee for William Guy Hardin Certifies that this is the
approved version of the following dissertation:**

**Tuning the Electrocatalytic Activity of Perovskites and Related Oxides
and the Elucidation of New Catalyst Design Criteria**

Committee:

Keith P. Johnston, Supervisor

Keith J. Stevenson, Co-Supervisor

Charles B. Mullins

Graeme A. Henkelman

**Tuning the Electrocatalytic Activity of Perovskites and Related Oxides
and the Elucidation of New Catalyst Design Criteria**

by

William Guy Hardin, B.S. M.S.E.

Dissertation

Presented to the Faculty of the Graduate School of

The University of Texas at Austin

in Partial Fulfillment

of the Requirements

for the Degree of

Doctor of Philosophy

The University of Texas at Austin

May 2017

Dedication

To Sasha, my rock.

Acknowledgements

I would like to thank my advisors Dr. Keith Stevenson and Dr. Keith Johnston. When I first visited Texas, I never dreamed of pursuing electrochemistry and catalysis. When I saw the vision and energy (no pun intended) from you both, I knew right then and there where I would go. I can't possibly list everything I've learned from you both, but know that I'm forever grateful for your experience, guidance and lessons. Keith, you always trusted my intuition and supported me in whatever way you could, thank you.

I would also like to thank the two former graduate students that I've worked with, my mentor Dr. Daniel Slanac and Dr. Tyler Mefford. Dan, not only were you an outstanding example of a meticulous scientist and engineer, you were a great friend and lab mate. I thought we were going insane that summer you graduated, but it turned out that we both just really love bad metal. Never forget the (David) Arkenstone. Tyler, thank you for constantly pushing me to think about problems from a different angles and doing it with a smile and a joke, like when we *correctly* estimated how many humans had lived and died on Earth. From our scientific conversations and collaborations grew the work presented in Chapter 4, and I'm incredibly proud of everything we've worked on together, my perovskite brother.

Thanks to Robin Forslund and Caleb Alexander, my lab-mates, for all the support and suggestions through the past few years. Both of your antics and intellect have elevated my work. I would also like to thank Bijal Patel, the undergraduate who helped with a lot of the earlier work in my dissertation.

Finally I want to thank all of the great collaborators I've had the pleasure of working with over the course of my dissertation, including Dr. Sheng Dai at ORNL, Prof.

Alexie Kolpak at MIT, and Dr. Artem Abakumov at Skoltech. You were all incredibly helpful, and your insights have been crucial to our research, thank you.

Tuning the Electrocatalytic Activity of Perovskites and Related Oxides and the Elucidation of New Catalyst Design Criteria

William Guy Hardin, Ph.D.

The University of Texas at Austin, 2017

Supervisor: Keith P. Johnston

Co-Supervisor: Keith J. Stevenson

Increasing global energy demand requires greater efficiency in water electrolyzers for low cost hydrogen generation and rechargeable metal-air batteries to enable pragmatic development of these key technologies. Given that the efficiencies of these technologies are limited primarily by the sluggish kinetics of the oxygen evolution reaction (OER) and/or oxygen reduction reaction (ORR), I have made extensive efforts to reduce the overpotential for the OER and ORR in alkaline media by designing advanced non-precious metal electrocatalysts. Alkaline conditions were chosen owing to the more facile kinetics of the ORR, as compared to acid, and because alkaline electrolytes enable the use of catalysts containing non-precious metals. Perovskites, represented by $ABO_{3\pm\delta}$, in which A is a rare-earth or alkaline earth element and B is a transition metal, were selected because of their demonstrated ability to promote the OER and the ORR, owing to their high ionic and electronic conductivities, good structural stability, and synthetic versatility. This made perovskites an ideal crystal structure for the development of rational catalyst design criteria.

To this goal, I designed a series of lanthanum-based perovskite electrocatalysts $LaBO_3$, B = Ni, $Ni_{0.75}Fe_{0.25}$, Co, Mn) that are highly active for both the OER and ORR in

an aqueous alkaline electrolyte. LaCoO_3 supported on nitrogen-doped carbon is shown to be ~ 3 times more active for the OER than high surface-area IrO_2 , and was demonstrated to be highly bifunctional by having a lower total overpotential between the OER and ORR ($\Delta E = 1.00$ V) than Pt ($\Delta E = 1.16$) and Ru ($\Delta E = 1.01$). I discovered a new catalyst design principle using a series of Ruddlesden-Popper (RP) $\text{La}_{0.5}\text{Sr}_{1.5}\text{Ni}_{1-x}\text{Fe}_x\text{O}_{4+\delta}$ oxides that promote Ni-O-Fe charge transfer interactions which significantly enhance OER catalysis. Using selective substitution of Sr and Fe to control the extent of hybridization between $e_g(\text{Ni})$, $p(\text{O})$ and $e_g(\text{Fe})$ bands, I have demonstrated exceptional OER activity of 10 mA cm^{-2} at a 360 mV overpotential and mass activity of $1930 \text{ mA mg}^{-1}_{\text{ox}}$ at 1.63 V, over an order of magnitude more than the leading precious-metal oxide electrocatalyst IrO_2 . In the course of this work, I also helped discover reversible charge storage via anion-based intercalation in $\text{LaMnO}_{3\pm\delta}$ electrodes, and a new OER mechanism whereby redox-active lattice oxygen directly participates in the formation of O_2 .

Table of Contents

List of Tables	xiv
List of Figures	xv
Chapter 1: Introduction	1
1.1 Mechanisms and Kinetics of The OER and ORR.....	2
1.2 Alkaline Oxygen Electrochemistry	3
1.3 Oxygen Electrocatalysis on Perovskites and Ruddlesden-Popper Electrodes	4
1.4 Objectives	7
1.5 Dissertation Outline	9
1.6 References	14
Chapter 2: Highly Active, Non-precious Metal Perovskite Electrocatalysts for Bifunctional Metal Air Battery Electrodes	20
2.1 Introduction.....	20
2.2 Results and Discussion	23
2.3 Conclusions.....	32
2.4 Experimental Methods.....	33
2.4.1 Chemicals	33
2.4.2 Synthesis of the nanostructured LaNiO ₃ catalyst (nsLaNiO ₃).	33
2.4.3 Materials Characterization.	34
2.4.4 Electrochemical Characterization.	34
2.5 Additional Information	35
2.6 References.....	35
Chapter 3: Tuning the Electrocatalytic Activity of Perovskites Through Active Site Variation and Support Interactions	40
3.1 Introduction.....	40
3.2 Experimental	45
3.2.1 Catalyst Synthesis	46
3.2.2 Physical Characterization.....	47

3.2.3 Electrochemical Characterization	48
3.3 Results and Discussion	49
3.4 Conclusions.....	62
3.5 Additional Information	63
3.6 References.....	63
Chapter 4: Exceptional Electrocatalytic Oxygen Evolution Via Tunable Charge Transfer Interactions in $\text{La}_{0.5}\text{Sr}_{1.5}\text{Ni}_{1-x}\text{Fe}_x\text{O}_{4+\delta}$ Ruddlesden-Popper Oxides.	67
4.1 Introduction.....	67
4.2 Results and Discussion	70
4.2.1 Material Characterization.....	70
4.2.2 Electrochemistry	72
4.2.3 Chemical States and Electronic Structure.....	76
4.3 Conclusions.....	82
4.4 Methods.....	83
4.5 Additional Information	90
4.6 References.....	90
Chapter 5: Highly Active Perovskite and Ruddlesden-Popper Composite Electrocatalysts for Water Oxidation.....	97
5.1 Introduction.....	97
5.2 Results and Discussion	100
5.3 Electrochemical Characterization and Discussion.....	103
5.4 Conclusions.....	109
5.5 Additional Information	109
5.6 References.....	110
Chapter 6: Anion charge storage through oxygen intercalation in LaMnO_3 perovskite pseudocapacitor electrodes	116
6.1 Introduction.....	116
6.2 Nanoscale Perovskites	121
6.3 Electrochemical Characterization	122
6.4 Oxygen Intercalation.....	124

6.5 Practical Applications of LaMnO_3 Pseudocapacitors	131
6.6 Conclusions.....	132
6.7 Methods.....	132
6.8 Additional Information	135
6.9 References.....	135
Chapter 7: Conclusions	138
7.1 Conclusions.....	138
7.1.1 Highly Active, Non-precious Metal Perovskite Electrocatalysts for Bifunctional Metal Air Battery Electrodes	138
7.1.2 Tuning the Electrocatalytic Activity of Perovskites Through Active Site Variation and Support Interactions	138
7.1.3 Exceptional Electrocatalytic Oxygen Evolution Via Tunable Charge Transfer Interactions in $\text{La}_{0.5}\text{Sr}_{1.5}\text{Ni}_{1-x}\text{Fe}_x\text{O}_{4+\delta}$ Ruddlesden-Popper Oxides	139
7.1.4 Highly Active Perovskite and Ruddlesden-Popper Composite Electrocatalysts for Water Oxidation.....	140
7.1.5 Anion charge storage through oxygen intercalation in LaMnO_3 perovskite pseudocapacitor electrodes.....	141
7.2 Recommendations.....	141
7.3 References.....	143
Appendix A: Atomic Ensemble and Electronic Effects in Ag-Rich AgPd Nanoalloy Catalysts for Oxygen Reduction in Alkaline Media	145
A.1 Introduction.....	145
A.2 Experimental	148
A.2.1 Catalyst Synthesis	149
A.2.1.1 Particle Synthesis	149
A.2.1.2 Adsorption of particles onto carbon support.....	149
A.2.2 Electron Microscopy	150
A.2.2.1 Transmission Electron Microscopy (TEM)	150
A.2.2.2 Scanning Transmission Electron Microscopy (STEM).....	150
A.2.3 X-ray Diffraction (XRD)	151
A.2.4 X-ray Photoelectron Spectroscopy (XPS).....	151

A.2.4 Thermogravimetric Analysis (TGA).....	152
A.2.4 Electrochemical Characterization	152
A.3 Results and Discussion.....	154
A.4 Conclusions.....	168
A.5 Additional Information	169
A.6 References.....	169
A.7 Supporting Information.....	172
Appendix B: Highly Active, Non-precious Metal Perovskite Electrocatalysts for Bifunctional Metal Air Battery Electrodes	179
B.1 Experimental	179
B.2 Catalyst Synthesis	179
B.2.1 Particle Synthesis	179
B.2.2 Particle Harvesting and Crystallization.....	180
B.3 Dynamic light scattering (DLS).	180
B.4 X-ray Diffraction (XRD).....	181
B.5 Electron Microscopy	181
B.6 Surface Area Analysis.....	181
B.7 X-ray Photoelectron Spectroscopy (XPS).....	182
B.8 Electrochemical Characterization	182
B.8.1 Quantification of Oxygen Reduction Activities.....	183
B.8.2 Quantification of Oxygen Evolution Activities	183
B.9 Bifunctionality Comparison	184
B.10 References	192
Appendix C: Tuning the Electrocatalytic Activity of Perovskites Through Active Site Variation and Support Interactions	193
C.1 Notes on $\text{LaNi}_{0.75}\text{Fe}_{0.25}\text{O}_3$ and the Dual-Site Mechanism	193
C.2 References	202
Appendix D: Exceptional Electrocatalytic Oxygen Evolution Via Tunable Charge Transfer Interactions in $\text{La}_{0.5}\text{Sr}_{1.5}\text{Ni}_{1-x}\text{Fe}_x\text{O}_{4+\delta}$ Ruddlesden-Popper Oxides.....	203
D.1 Note on Oxygen hyperstoichiometry and oxidation states	203

D.2 Note on Band structure and cross-gap hybridization	204
D.3 Note on Band structure and OER mechanism(s)	205
D.4 Note on DFT methods, magnetic ordering and oxygen content	206
D.5 References	230
Appendix E: Highly Active Perovskite and Ruddlesden-Popper Composite	
Electrocatalysts for Water Oxidation	236
E.1 Extended Experimental Information	236
E.1.1 Catalyst Synthesis	236
E.1.2 Electrochemical Characterization	239
E.2 Alternative Oil Phase Tests	243
E.3 References	246
Appendix F: Anion charge storage through oxygen intercalation in LaMnO_3	
perovskite pseudocapacitor electrodes	249
F.1 Experimental	249
F.1.1 XPS of Electrochemically Cycled $\text{LaMnO}_{3.09}$ and r- $\text{LaMnO}_{2.91}$	
Electrodes	250
F.2 References	265
Bibliography	266

List of Tables

Table 2.1: Assessment of catalyst bifunctionality for nsLaNiO ₃ /NC and other benchmarks.	32
Table 3.1: Perovskite Catalyst Bifunctionality	62
Table 4.1: Oxygen hyperstoichiometry (δ) in La _{0.5} Sr _{1.5} Ni _{1-x} Fe _x O _{4+δ} , average B-site oxidation states determined by iodometry, the results of Mössbauer spectroscopy and the calculated average Ni oxidation state	78
Table A.1. Summary of catalyst loading, morphology and composition.	156
Table A.2. Summary of ORR Activity for AgPd alloy compositions and pure component benchmarks at -0.05 V vs NHE.....	161
Table A.3.1. XPS shifts for the various alloy ratios.	178
Table C.1: DLS size, Crystallite size, BET surface area, XRD phase identification.	201
Table D.1: The results of Rietveld refinement for La _{0.5} Sr _{1.5} Ni _{1-x} Fe _x O _{4+δ}	227
Table D.2: Comparison of LSNF30 with other promising OER catalysts and accompanying notes.....	228
Table D.3: Summary of the physical, chemical and electrochemical properties of the LSNF series.....	229
Table E.1: Results of decane oil phase tests	243
Table E.2: Results of cyclohexane oil phase tests	245

List of Figures

Figure 1.1: Schematic of the overpotentials required for the OER and ORR due to the poor kinetics.....	3
Figure 1.2: Ideal crystal structure of Perovskite and Ruddlesden-Popper oxides ...	5
Figure 2.1: Physical Characterization of LaNiO_3	22
Figure 2.2: LaNiO_3 OER activity trends.....	27
Figure 2.3: ORR activity trends in O_2 saturated 0.1 M KOH at 1600 RPM.....	30
Figure 3.1: Generalized synthetic route to form phase pure nanostructured perovskites	50
Figure 3.2: Electrochemical OER testing of perovskites.....	52
Figure 3.3: Oxygen evolution cycle utilizing lattice oxygen	54
Figure 3.4: Electrochem ORR characterization of perovskites	56
Figure 3.5: Oxygen reduction waves observed by cyclic voltammetry at 5 mV/s in deoxygenated 0.1 M KOH after injection of 5 mM H_2O_2	59
Figure 3.6: Stability Comparison with Carbon	61
Figure 4.1: Crystallographic characterization of the $\text{La}_{0.5}\text{Sr}_{1.5}\text{Ni}_{1-x}\text{Fe}_x\text{O}_{4\pm\delta}$ series	71
Figure 4.2: Oxygen evolution results and catalytic activities for the LSNF series taken in O_2 saturated 0.1 M KOH at 10 mV s^{-1} and 1600 rpm.....	73
Figure 4.3: Cyclic voltammetry (CV) of LSNF catalysts in O_2 saturated 0.1 M KOH unless otherwise specified.....	75
Figure 4.4: Schematic evolution of the electronic structure of semiconducting $\text{La}_2\text{NiO}_{4+\delta}$ as Sr and Fe are substituted into it.	77
Figure 4.5: Density functional theory modeling of atomic and electronic structures of bulk LSNF in ferromagnetic configuration.....	79

Figure 5.1: X-ray diffraction patterns of SNF, LSNF and LNO electrocatalysts	102
Figure 5.2: Electrochemical characterization of the SNF, LSNF and LNO compsites and comparison to recently reported non-precious metal oxide catalysts.	104
Figure 5.3: Selected catalyst mass activities at 1.63 V vs RHE-iR	106
Figure 5.1: Schematic of the expected band diagram of $\text{LaNiO}_{3\pm\delta}$ as first Sr and then Fe are substituted into it.....	107
Figure 6.1: Nanocrystal morphology of $\text{LaMnO}_{3.09}$	120
Figure 6.2: Electrochemical characterization of $\text{LaMnO}_{3\pm\delta}$	122
Figure 6.3: Effect of Electrolyte Concentration on Redox Reactions $\text{LaMnO}_{3\pm\delta}$	124
Figure 6.4: Electrolyte Studies of $\text{LaMnO}_{3.09}$	126
Figure 6.5: Mechanism of oxygen intercalation into $\text{LaMnO}_{3\pm\delta}$	129
Figure 6.6: Symmetric Cell Cyclic Voltammetry of r- $\text{LaMnO}_{2.91}$	131
Figure A.1. Ag_9Pd nanoparticles supported on Vulcan XC72 carbon after calcination at 350°C in N_2	155
Figure A.2. XPS spectra for the (A) Pd3d and (B) Ag3d regions for all Pd:Ag alloy ratios as well as the pure metals.....	157
Figure A.3. Oxygen reduction activity comparison between Ag-rich alloys and pure components.	160
Figure A.4. Cyclic voltammograms showing the characteristic redox peaks for the alloy and pure metal catalysts supported on Vulcan XC72 carbon.	163
Figure A.5: Low mag TEM micrographs	172
Figure A.6: TEM for pure Ag nanoparticles.....	173
Figure A.7: X-ray diffraction for all Pd:Ag ratios.	174

Figure A.9: Polarization curves for all alloy ratios studied as well as pure Ag and commercial Pd.	175
Figure A.10: Cyclic voltammograms for all Ag:Pd ratios in Ar purged 0.1 KOH.	176
Figure A.11: CO stripping voltammograms of Vulcan XC72 carbon supported (A) Pd, (B) Ag ₉ Pd, and (C) Ag.	177
Figure B.1: SEM micrographs of particles calcined at 700°C in air.	184
Figure B.2: BET adsorption curves for unsupported nsLaNiO ₃ and LaNiO ₃ , used to calculate respective surface areas of 11 m ² /g and 6 m ² /g.	186
Figure B.3: BET adsorption curve and pore size distribution (PSD) for NC	187
Figure B.4: OER polarization curves for both iR corrected and uncorrected nsLaNiO ₃ /NC in O ₂ saturated 0.1 M KOH at 1600 rpm and 10 mV/s.	188
Figure B.5: Tafel plot of the iR corrected average OER polarization curve	189
Figure B.6: The proposed alkaline oxygen evolution cycle on LaNiO ₃	190
Figure B.7: High resolution XPS spectra of the N 1s core region	191
Figure C.1: High resolution XPS spectra.	196
Figure C.2: Representative oxygen evolution rotating disk electrode polarization curves	197
Figure C.3: Representative oxygen reduction rotating disk electrode polarization curves	198
Figure C.4: Polarization curves taken in O ₂ saturated 0.1 M KOH.	199
Figure C.5: Oxygen Probe Results.	200
Figure D.1: Electron diffraction (ED) patterns	209
Figure D.2: Unit cell volume as a function of x in the La _{0.5} Sr _{1.5} Ni _{1-x} Fe _x O _{4+δ} solid solutions	210

Figure D.3: Typical experimental, calculated and difference curves after the Rietveld refinement	211
Figure D.4: The crystal structure of the $n=1$ Ruddlesden-Popper $\text{La}_{0.5}\text{Sr}_{1.5}\text{Ni}_{1-x}\text{Fe}_x\text{O}_{4+\delta}$ series.	212
Figure D.5: HAADF-STEM images of $\text{La}_{0.5}\text{Sr}_{1.5}\text{Ni}_{1-x}\text{Fe}_x\text{O}_{4+\delta}$	213
Figure D.6: Nitrogen sorption isotherms for BET surface area analysis of the $\text{La}_{0.5}\text{Sr}_{1.5}\text{Ni}_{1-x}\text{Fe}_x\text{O}_{4+\delta}$ series	214
Figure D.7: Representative OER polarization curves	215
Figure D.8: OER tafel plots of LSNF30 and other leading metal oxide catalysts	216
Figure D.9: Galvanostatic stability test of LSNF30	217
Figure D.10: Intercalation CVs	218
Figure D.11: Fitted intercalation CVs for $\text{La}_{0.5}\text{Sr}_{1.5}\text{Ni}_{1-x}\text{Fe}_x\text{O}_4$	219
Figure D.12: Electrochemical diffusion rate data for the Sr-nickelate system	220
Figure D.13: Room temperature Mössbauer spectroscopy	221
Figure D.14: XPS deconvolution of the Ni 3p spectra for $\text{La}_{0.5}\text{Sr}_{1.5}\text{Ni}_{1-x}\text{Fe}_x\text{O}_{4+\delta}$	222
Figure D.15: DFT modeling of atomic and electronic structures of bulk LSNF	223
Figure D.16: Reversible hydrogen electrode (RHE) calibration	224
Figure D.17: Comparison of ferromagnetic, anti-ferromagnetic and non-magnetic structures from DFT modeling	225
Figure E.1: X-ray diffraction pattern of SNF made by the polymerizable complex synthetic method	241
Figure E.2: Representative polarization curves for LNO, LSNF and SNF	242
Figure F.1: Dynamic light scattering measurements of initial mixed metal hydroxides	252
Figure F.2: Electrolyte studies of $\text{LaMnO}_{3+\delta}$	253

Figure F.3: Capacitive responses of LaNiO ₃ and peroxide CV	255
Figure F.4: Cycling <i>ex-situ</i> Mn 2p _{1/2} XPS Studies of LaMnO _{3±δ}	256
Figure F.5: Particle thickness analysis for diffusion rate calculation	257
Figure F.6: Diffusion rate calculations on unsupported LaMnO _{3±δ}	258
Figure F.7: Cycling <i>ex-situ</i> XRD Studies of LaMnO _{3±δ}	259
Figure F.8: Effect of weight loading on the capacitive contributions of LaMnO _{3.09}	261
Figure F.9: b-value analysis of LaMnO _{3±δ}	263
Figure F.10: Capacitive contributions of N-OMC Support	264

Chapter 1: Introduction

The generation and reduction of oxygen are crucial chemical reactions in large-scale hydrogen production via water electrolysis, and are the principal reactions at air electrodes in rechargeable metal-air batteries.[1-3] These reactions are known as the oxygen evolution reaction (OER) and the oxygen reduction reaction (ORR). In the electrolysis of water, two electrodes are immersed in water and placed in electrical contact with a power source and each other. One electrode is driven to a positive potential creating an anode that oxidizes water to form oxygen (the OER) while the other electrode balances the reaction by being at a reductive potential creating a cathode that reduces protons to form hydrogen. To generate hydrogen, a voltage must be applied across the electrodes and electric current must flow from anode to cathode. Likewise, aqueous metal-air batteries are comprised of an anode and cathode in physical contact with an electrolyte, and in electrical contact with a device to be powered. The anode is typically a non-precious metal, such as zinc, that when placed in electrical contact with a precious metal cathode in the presence of air, establishes a galvanic potential difference. The galvanic potential difference between the electrodes drives the oxidation of the anode and the reduction of oxygen at the cathode (the ORR). If the anode oxidation product can be reduced by reversing the polarity of the metal-air battery injecting current into the anode, that system is called a reversible metal-air battery. Bifunctionality, where one electrode is capable of catalyzing both the OER as well as the ORR, is also a highly desirable property for such a system. Metal-air batteries produce electricity while discharging, and consume it while charging. Whether generating electricity or consuming it, both usage scenarios rely on the electrochemical evolution and reduction of oxygen, complex four electron reactions that are kinetically sluggish. The poor kinetics of the OER and ORR

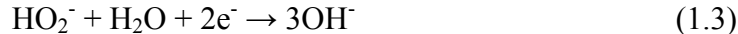
means that hydrogen generation is energy intensive, and metal-air batteries produce less energy than they are theoretically capable of.

1.1 MECHANISMS AND KINETICS OF THE OER AND ORR

The OER and ORR are multistep four electron reactions that proceed via different intermediates and mechanistic routes which are highly dependent on the catalyst and electrolyte.[1-4] The ORR in alkaline media proceeds via one of two ways: by a direct four-electron reduction, according to Equation 1.1,



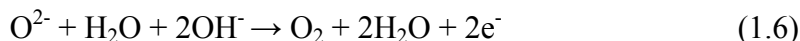
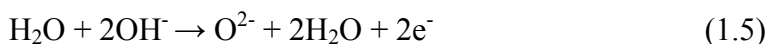
or proceeding in a stepwise fashion in a 2-by-2 electron pathway, according to Equations 1.2 and 1.3,



in which the reduction of the hydroperoxide intermediate (Equation 1.3) is often identified as a rate determining step in the ORR, although the large chemisorption energy required for the initial activation of oxygen on certain electrode materials has also been identified as rate determining. [5-7] The OER in alkaline media can be represented by a direct four electron reaction, as written in Equation 1.4,



or via a sequential, 2-by-2 electron pathway, according to Equations 1.5 and 1.6,



in which the formation of the hydroperoxide intermediate (HOO^-) during Equation 1.6 is one of the proposed rate determining steps.[8, 9] These rate limiting steps for both the

ORR and OER require additional activation energy to overcome, in excess of the thermodynamic potentials at which they should theoretically begin, commonly referred to as the overpotential. The overpotential required to facilitate the ORR and OER is partly responsible for the decreased efficiency of metal-air batteries or the high energy input required for water hydrolysis due to the large overpotentials required, shown in Figure 1.1.

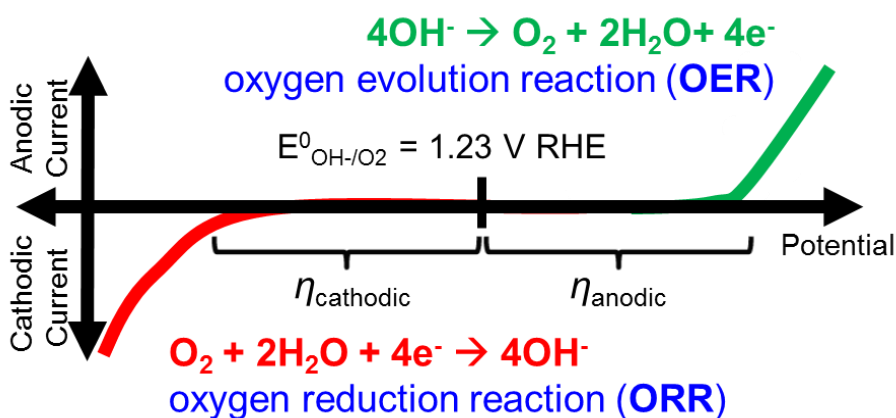


Figure 1.1: Schematic of the overpotentials required for the OER and ORR due to the poor kinetics.

1.2 ALKALINE OXYGEN ELECTROCHEMISTRY

A persistent challenge in the development of active ORR catalysts is the reduction in overpotential required to facilitate the full four electron reduction of oxygen and oxidation of hydroxide. Equations 1.1 and 1.4 are balanced for an alkaline electrolyte, but the ORR and OER can likewise proceed in acid environments, where much research has been conducted on precious metal catalysts such as Pt, Pd, and IrO_2 . [10, 11] The use of precious metal electrodes is in part due to their stability in acidic electrolyte (pH \sim 0 to

1), and because they were experimentally found to be more active than other less precious metals and oxides. The cost of these electrodes materials is a large barrier to the commercialization of technologies relying on the OER and ORR, and likewise makes the resulting products (i.e. electrical current, H_2) less commercially viable.[12] Conversely, in alkaline electrolyte metal and metal oxide catalysts that would otherwise be too unstable in acidic media become practical. Several oxides such as Co_3O_4 , Mn_yO_x , $NiCo_2O_4$, and $LaNiO_3$ have been shown to be nearly as active for the OER or ORR in alkaline media as some precious metals in acidic electrolyte.[3, 4, 13-18] In addition to enabling the use of highly active metal oxides, alkaline ORR kinetics are also faster in part due to the more facile formation and stability of the hydroperoxide intermediate in alkaline electrolyte and decreased anion adsorption strength.[19-21]

1.3 OXYGEN ELECTROCATALYSIS ON PEROVSKITES AND RUDDLESDEN-POPPER ELECTRODES

Recently, ABO_3 -type oxides known as perovskites, where A is commonly a rare-earth or alkali element and B is commonly a transition metal, have attracted much attention due to their reported high specific catalytic activity ($\mu A/cm^2_{ox}$) towards the OER and ORR in alkaline conditions,[18, 22, 23] and their ability to store charge as an electrochemical pseudocapacitor by oxygen intercalation.[24] However, perovskites typically have low surface areas ($< 4 m^2/g$) and/or inactive secondary phases that result in low current densities of practical interest (mass activity, mA/mg_{ox}).

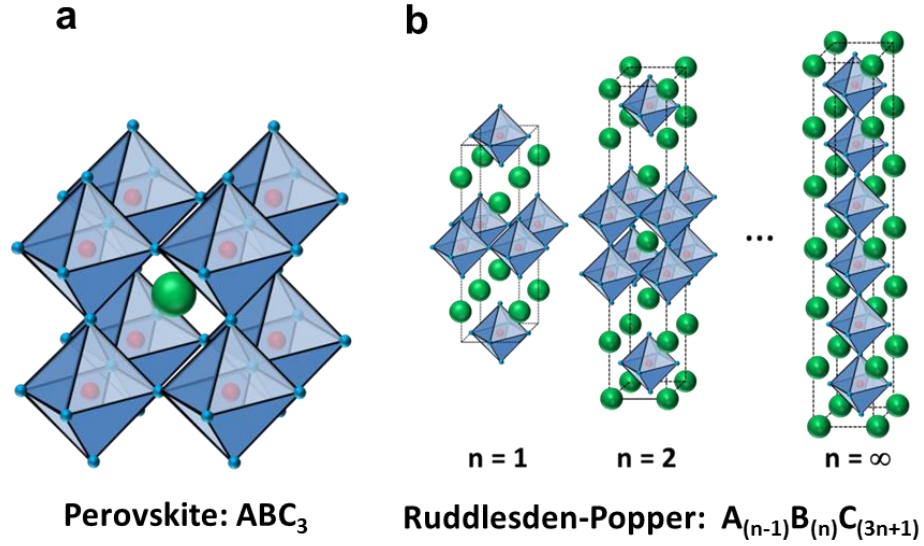


Figure 1.2: Ideal crystal structure of Perovskite and Ruddlesden-Popper oxides

(a) Ideal cubic perovskite (ABO_3) in which a lanthanide, rare or alkali earth ion (A, green) is the largest ion, and is coordinated by transition metal cations (B, red), that are in octahedral coordination with oxygen anions (C, blue). b) The Ruddlesden-Popper (RP) crystal structure wherein n perovskite layers with a thickness of n (BO_6) octahedra are separated by rocksalt (AO)(OA) double layers.

The perovskite structure encompasses a wide array of materials with differing physical, chemical, optical, and electronic properties. The perovskite crystal structure can be either cubic, rhombohedral or orthorhombic depending on the ionic radii and charge of the A and B site cations and are only stable at neutral to basic pH. The cubic perovskite structure is presented in Figure 1.2a. They are a robust family of materials, exhibiting oxygen non-stoichiometry and capable of a wide degree of atomic replacements and substitutions, including aliovalent doping. If no more than one substitution is considered per A and B site, the formula for a perovskite can be written generally as $A_{1-x}A'_x B_{1-y}B'_y O_{3-\delta}$, such that charge neutrality is maintained (with x and $y \leq 1$, and $\delta \pm 0.5$). Regardless of specific crystallographic structure, the B site is coordinated by six oxygen

anions, forming a BO_6 octahedral unit. Within the octahedral unit, the valence d -band orbitals interact with the oxygen $2p$ orbitals, causing a discretization of d -electron energy levels. These discretized energy levels change the strength and nature of chemisorption of reactants and intermediates.[25, 26] Furthermore, the endothermic or exothermic nature of these interactions are governed by the B site element and oxidation state, which are intrinsically tied to the perovskite structure, including the A element and oxidation state.[27-29] It is this complex and tunable (via atomic replacements) energetic landscape that makes the perovskite family a compelling system to study for catalysis. The Ruddlesden-Popper (RP) crystal structure is represented as $\text{A}_{n+1}\text{B}_n\text{O}_{3n+1}$ or equivalently $(\text{AO})(\text{ABO}_{3\pm\delta})_n$, wherein perovskite layers with a thickness of n (BO_6) octahedra are separated by rocksalt $(\text{AO})(\text{OA})$ double layers (Figure 1.2b). This RP phase can accommodate all the elemental substitutions available to perovskites as well as additional compositions that are not stable in the perovskite structure.²⁰ While Ruddlesden-Popper materials have been explored as solid oxide fuel cell cathodes owing to their chemical flexibility and labile lattice oxygen, they have not been fully examined for room temperature water oxidation.^{21, 22, 23, 24, 25, 26, 27}

OER and ORR studies with perovskites were first reported during the 1970s, and their activity was described in terms of surface and bulk electronic properties. The active sites are believed to be the transition metal (B site) atoms, and much attention recently has been focused on the e_g orbital filling of the transition metal B site as the activity descriptor.[4, 18]. Alternatively, it has been suggested that the total number of valence electrons is the critical parameter (activity descriptor) for both the OER and ORR. DFT calculations suggest that the adsorption strengths of intermediates monotonically increase as the number of outer B site valence electrons increases across row 4 in the periodic table (with the exception of Sc).[25] Similar trends were found when

dissociation chemisorption and transition state energies were computed by DFT for diatomic oxygen on LaBO_3 perovskites.[26] While these computational trends assist in theoretically understanding why some perovskites are more active than others, none of them account for the support interactions that exist between the catalyst and carbon support.

To enable perovskites to achieve current densities of practical interest, they must be synthesized such that the formation of catalytically inactive secondary phases is minimized and that they possess a moderate to high surface area.[18, 23] A high temperature calcination step is required to crystallize perovskites and frequently results in significant coalescence and sintering which produces low surface area particles ranging from 200 nm to 1 μm or greater.[32-34] Solid state syntheses wherein simple oxides are ground together and fired at $\geq 1100^\circ\text{C}$ also result in multi-micron sized particles. A common technique to increase perovskite surface area is the ball milling of bulk materials to obtain particles $>200\text{ nm}$ to several micrometers in diameter.[29, 35] An alternative strategy is to synthesize amorphous perovskite nanoparticles with bottom up approaches by sol-gel methods,[32, 34, 35] reactions in reverse micelles,[36-38] coprecipitation hydrolysis processes,[39-41] and hydrothermal routes followed by calcination at high temperature.

1.4 OBJECTIVES

The principal objectives of this dissertation are to synthesize perovskite and Ruddlesden-Popper (RP) electrocatalysts that display high mass and specific activities ($\text{mA mg}^{-1}_{\text{ox}}$ and $\text{mA cm}^{-2}_{\text{ox}}$, respectively) through precise synthetic control of their chemical, structural and electronic configurations. Furthermore, insights into the

mechanisms governing the OER and ORR on these materials will be gained, and new catalyst design criteria will be proposed to aid in the future development of non-precious metal OER and ORR electrocatalysts. Initial work will focus on synthesizing a phase-pure nanostructured LaNiO_3 using a reverse-phase coprecipitation method to form nanoparticulate precursors having adequate atomic intermixing. Examination of surface states and the role of lattice hydroxylation on the OER mechanism will be proposed, and LaNiO_3 demonstrated to be an efficient bifunctional OER-ORR electrocatalyst.

The coprecipitation synthesis previously developed for LaNiO_3 is then extended to other perovskite compositions, and a series of LaMO_3 ($M = \text{Ni, Co, Mn}$) perovskites were synthesized and the validity of a commonly ascribed OER activity descriptor, e_g filling is tested. Building upon previous work where we observed that the carbon support structure and composition had a significant impact on the perovskite catalytic activity, the impact of high surface area graphitic and N-doped carbons on the OER and ORR are tested. Previously, N-doped carbons were known to improve the OER due to their ability to disproportionate an ORR intermediate, HOO^\cdot , as seen in equation 1.3. To test this theory, chemical peroxide disproportionation functionality was also introduced in the LaNiO_3 electrochemistry through 25% Fe substitution for Ni. If the N-doped carbon's role in enhancing perovskite ORR activity is indeed peroxide disproportionation, then the catalytic activity of $\text{LaNi}_{0.75}\text{Fe}_{0.25}\text{O}_3$ is not expected to be improved as much, or at all, by the use of N-doped carbon.

Finally, the Ruddlesden-Popper crystal is used to achieve electronic configurations not realizable in perovskite and other metal oxides by the precise synthesis of a series of $\text{La}_{0.5}\text{Sr}_{1.5}\text{Ni}_{1-x}\text{Fe}_x\text{O}_{4+\delta}$ (LSNF, $x = 0$ to 1) electrocatalysts. The role of Fe substitution on the oxidation state distribution, electronic configuration, oxygen content and ultimately the catalytic activity of the oxides will be examined. It is expected that the

additional Fe 3*d* orbitals will hybridize with the Ni 3*d* near the Fermi level which will result in increased catalytic activity as seen for other mixed Ni-Fe systems. A modified Pechini synthesis is used to synthesize phase-pure LSNF materials, to overcome the difficulty in hydrolyzing Sr^{2+} . It is expected that a low to moderate amount of Fe substitution will increase the catalytic activity as compared to $x = 0$ based on previous studies of $\text{LaNi}_{1-x}\text{Fe}_x\text{O}_3$ OER electrocatalysts and Ni-Fe oxyhydroxides films.

1.5 DISSERTATION OUTLINE

Chapter 2 focuses on the synthesis and catalytic activity of LaNiO_3 in context of other leading metal oxide OER catalysts such as IrO_2 and RuO_2 . A general scheme for synthesis of phase pure, catalytically active LaNiO_3 that displays exceptionally high OER mass activities and a strong OER/ORR bifunctional character when supported on nitrogen doped carbon (NC) is presented. A key advance was to prepare uniform 25 nm nanoparticle dispersions in aqueous solution via rapid simultaneous hydrolysis of both La^{3+} and Ni^{2+} nitrates by reverse phase arrested growth precipitation, which when calcined, form nearly phase pure LaNiO_3 nanocrystalline catalysts. Scanning electron microscopy (SEM), X-ray diffraction (XRD), dynamic light scattering (DLS) and X-ray photoelectron spectroscopy (XPS) indicated that calcination of 25 nm amorphous mixed metal hydroxide particles yielded 20-50 nm phase pure aggregates of relatively distinct primary nanoparticles that exhibit significant surface hydroxylation and possess a surface area of $\sim 11 \text{ m}^2/\text{g}$. Coalescence was mitigated by the large interparticle spacing in highly open, low fractal dimension nanoparticulate powders produced by rapid freeze drying enabled by thin film freezing followed by lyophilization. LaNiO_3 prepared by this method. The high activity of the nanostructured LaNiO_3 was rationalized by the

participation of lattice oxygen during the OER, and a new OER mechanism was proposed which unified the known chemical intermediates of the OER with a chemical wherein the HOO^- intermediate forms from the reaction between a lattice oxygen and chemisorbed intermediate. This work was done in collaboration with Daniel Slanac (co-first author on the published paper) who contributed in the design of the synthesis, conducting the experiments, interpretation of the data and writing of the manuscript. An earlier draft of this manuscript appeared in the PhD dissertation of Slanac. A major advance in the version in Chapter 2 that was published in the Journal of Physical Chemistry Letters is the proposed OER mechanism utilizing lattice oxygen, and supporting XPS analysis of the O 1s region.

In Chapter 3, the reverse phase hydrolysis synthetic scheme used in Chapter 2 is extended to a series of LaMO_3 ($\text{M} = \text{Ni}, \text{Co}, \text{Mn}, \text{Ni}_{0.75}\text{Fe}_{0.25}$) perovskite electrocatalysts that are highly active for both the oxygen evolution reaction (OER) and oxygen reduction reaction (ORR) in an aqueous alkaline electrolyte. Lanthanum-based perovskites containing different transition metal active sites (LaBO_3 , $\text{B} = \text{Ni}, \text{Ni}_{0.75}\text{Fe}_{0.25}, \text{Co}, \text{Mn}$) are synthesized by a general colloidal method, yielding phase pure catalysts of homogenous morphology and surface area ($8 - 14 \text{ m}^2/\text{g}$). Each perovskites' ability to catalyze the OER and ORR is examined using thin film rotating disk electrochemistry (RDE). LaCoO_3 supported on nitrogen-doped carbon is shown to be ~ 3 times more active for the OER than high surface-area IrO_2 . Furthermore, LaCoO_3 is demonstrated to be highly bifunctional by having a lower total overpotential between the OER and ORR ($\Delta E = 1.00 \text{ V}$) than Pt ($\Delta E = 1.16$) and Ru ($\Delta E = 1.01$). The OER and ORR pathways are perturbed by the introduction of peroxide disproportionation functionality via support-interactions and selective doping of the catalyst. $\text{LaNi}_{0.75}\text{Fe}_{0.25}\text{O}_3$'s ability to disproportionate peroxide is theorized to be responsible for the $\sim 50\%$ improvement over LaNiO_3 in catalytic

activity towards the ORR, despite similar electronic structure. These results allow us to examine the pathways for OER and ORR in context of support-interactions, transition metal redox processes and catalytic bifunctionality. Daniel Slanac and Bijal Patel aided in the synthesis of materials, and Tyler Mefford (co-first author in the published manuscript) collected some data, contributed intellectually to the analysis and assisted in editing the manuscript.

Chapter 4 utilizes a modified Pechini method which enables our precise synthetic approach to explore the influence of Sr and Fe substitution on Ni-based electrocatalysts by exploiting the crystalline Ruddlesden-Popper phase to study the influence of atomic and electronic configurations that are unrealizable in other electrocatalyst systems. We report the discovery of a new catalyst design principle using a series of Ruddlesden-Popper (RP) $\text{La}_{0.5}\text{Sr}_{1.5}\text{Ni}_{1-x}\text{Fe}_x\text{O}_{4\pm\delta}$ oxides that promote Ni-O-Fe charge transfer interactions which significantly enhance OER catalysis. Using selective substitution of Sr and Fe to control the extent of hybridization between $e_g(\text{Ni})$, $p(\text{O})$ and $e_g(\text{Fe})$ bands, we demonstrate exceptional OER activity of 10 mA cm^{-2} at a 360 mV overpotential and mass activity of $1930 \text{ mA mg}^{-1}_{\text{ox}}$ at 1.63 V. In particular, we show that Sr substitution promotes high catalytic activity by further oxidizing Ni via charge compensation, enhancing Ni-O covalency and electronic conductivity. Chemical substitution of Fe for Ni introduces and tunes the overlap between the Ni and Fe $3d$ bands and the O $2p$ band. Density functional theory (DFT) modeling confirms that cross-gap hybridization across Fe-O-Ni bridges enhances charge transfer interactions and the bandwidth near the Fermi level available for electrode-adsorbate electron transfer. We propose the concept of cross-gap hybridization of transition metal $3d$ states and O $2p$ orbitals as an effective new catalyst design criteria for improving OER activity. This precise synthesis of RP compositions enables the elucidation of crucial structural-chemical-electronic relationships that have not been

possible with Ni-M oxyhydroxides and other reported metal oxide catalysts for OER. Yet by analogy, cross gap hybridization of $3d$ states with $O2p$ possibly explains the reported high OER activity for Fe-doped Ni- and Co-based oxide systems. This project was a collaboration between UT, MIT, ORNL and Skolkovo Institute of Technology, and my collaborator Robin Forslund (listed as co-first author on the published manuscript) helped design, perform and analyze experimental data, as well edit the manuscript. MIT contributed the DFT modeling and analysis, while Skolkovo provided physical characterization, Mössbauer spectroscopy, helped plan the experiments and develop the intellectual framework for interpretation of the data.

Chapter 5 revisits the aqueous synthesis of perovskite and RP electrocatalysts by using a reverse-phase water-in-oil microemulsion to synthesize a nickel-based perovskite $La_{0.4}Sr_{0.6}Ni_{0.8}Fe_{0.2}O_{3\pm\delta}$ (LSNF) and a La-free Ruddlesden-Popper (RP) oxide $Sr_4Ni_{2.4}Fe_{0.6}O_{10\pm\delta}$ (SNF) electrocatalysts which are compared to $LaNiO_3$ made by similar means. The high activities for these two catalysts were discovered at the start of the work in Chapter 4, which also examined Ni-Fe based catalysts. Elemental substitution of 60% Sr for La in $LaNiO_3$ was performed to increase Ni-O bond covalency in the perovskite phase and promote higher catalytic activities by utilizing the more energetically favorable lattice oxygen mediated OER mechanism. Efficient atomic intermixing in the precursors improved the Sr solubility beyond the ~20% previously demonstrated. Complete Sr substitution for La and targeting of the $n=3$ RP phase was performed to maximize Ni-O bond covalency and triple the amount of perovskite units as compared to the $n=1$ phase. Fe was substituted for 20% Ni in LSNF and SNF to introduce triple band overlap of Fe and Ni $3d$ orbitals with O $2p$, which was previously demonstrated to significantly enhance the OER activity for other RP catalysts. Upon complete substitution of Sr for La, the highest mass activity of $1541\text{ mA mg}^{-1}_{ox}$ at a 361 mV overpotential, with a low Tafel

slope of 55 mV dec^{-1} , was approximately an order of magnitude higher compared to LaNiO_3 and IrO_2 as seen for other recent RP catalysts with Ni-O-Fe cross-gap hybridization. An undergraduate student Hrishikesh Iyer assisted with catalyst synthesis, and Karalee Jarvis and Andrei Duncan assisted with electron microscopy.

Chapter 6. The redox-active lattice oxygen of some perovskites was explored as a mechanism to store energy pseudocapacitively in $\text{LaMnO}_{3\pm\delta}$ electrodes via OH^- anion intercalation. Remarkable pseudocapacitance for a nanostructured lanthanum based perovskite, LaMnO_3 , was achieved by varying the ionic composition of the electrolyte and we present evidence for a new anion based charge storage mechanism based on oxygen intercalation. The significance of oxygen vacancies as charge storage sites for oxygen intercalation in these perovskite type oxides is demonstrated through a low temperature topotactic reduction of LaMnO_3 . The high anion storage through the crystal lattice leads to 92% utilization of the electroactive perovskite and a remarkable pseudocapacitance up to $611.9 \text{ F g}^{-1}_{\text{ox}}$. This is the first example of anion-based intercalation pseudocapacitance as well as the first time oxygen intercalation has been exploited for fast energy storage. Whereas previous pseudocapacitor and rechargeable battery charge storage studies have focused on cation intercalation, the anion based mechanism presented here offers a new field of research in energy storage materials. This project was a collaborative effort with Tyler Mefford and Will Hardin (co-first author) performing experimental work and data analysis, while Sheng Dai contributed the carbon support. Hardin provided the method of LaMnO_3 synthesis, performed, analyzed, and interpreted the XPS, provided intellectual contribution to the analysis of the data and intercalation mechanism, and assisted in editing the manuscript. This chapter also appeared in the PhD dissertation of Tyler Mefford.

Appendix A was the first study I contributed to in course of obtaining my PhD, wherein we demonstrate that simultaneous reduction of Ag and Pd precursors provides uniform, Ag-rich AgPd alloy nanoparticles (~ 5 nm) with high activities for the oxygen reduction reaction (ORR) in alkaline media. The particles are crystalline and uniformly alloyed, as shown by X-ray diffraction and probe corrected scanning transmission electron microscopy. The mass activities for the ORR were 3.0 and 3.8 times higher for Ag₉Pd (333 mA/mg_{metal}) and Ag₄Pd (646 mA/mg_{metal}), respectively, than expected from a linear combination of mass activities of Ag (42 mA/mg_{Ag}) and Pd (799 mA/mg_{Pd}) particles, and up to 5x higher on Pd mass basis, as determined by rotating disk voltammetry. Alloy specific activities are up to ~ 3 x beyond a linear combination of activities. For silver-rich alloys (Ag _{≥ 4} Pd), the particle surface is shown to contain Pd primarily dispersed as single atoms surrounded by Ag from cyclic voltammetry and CO stripping measurements for Ag₉Pd. This morphology is favorable for the high activity through a combination of modified electronic structure, as shown by XPS, and ensemble effects, which facilitate the steps of oxygen bond breaking and desorption for the ORR. This concept of tuning the hetero-atomic interactions on the surface of small nanoparticles with low concentrations of precious metals for high synergy in catalytic activity may be expected to be applicable to a wide variety of nanoalloys. Daniel Slanac was the lead author of this study, while I contributed to the experimental design, collection, analysis and interpretation of all data, and writing of the manuscript.

1.6 REFERENCES

1. Bidault, F., et al., *Review of gas diffusion cathodes for alkaline fuel cells*. Journal of Power Sources, 2009. 187(1): p. 39-48.

2. Cheng, F.Y. and J. Chen, *Metal-air batteries: from oxygen reduction electrochemistry to cathode catalysts*. Chemical Society Reviews, 2012. 41(6): p. 2172-2192.
3. Neburchilov, V., et al., *A review on air cathodes for zinc-air fuel cells*. Journal of Power Sources, 2010. 195(5): p. 1271-1291.
4. Bockris, J.O. and T. Otagawa, *MECHANISM OF OXYGEN EVOLUTION ON PEROVSKITES*. Journal of Physical Chemistry, 1983. 87(15): p. 2960-2971.
5. Markovic, N., H. Gasteiger, and P.N. Ross, *Kinetics of oxygen reduction on Pt(hkl) electrodes: Implications for the crystallite size effect with supported Pt electrocatalysts*. Journal of the Electrochemical Society, 1997. 144(5): p. 1591-1597.
6. Nørskov, J.K., et al., *Origin of the overpotential for oxygen reduction at a fuel-cell cathode*. The Journal of Physical Chemistry B, 2004. 108(46): p. 17886-17892.
7. Spendelov, J.S. and A. Wieckowski, *Electrocatalysis of oxygen reduction and small alcohol oxidation in alkaline media*. Physical Chemistry Chemical Physics, 2007. 9(21): p. 2654-2675.
8. Dau, H., et al., *The Mechanism of Water Oxidation: From Electrolysis via Homogeneous to Biological Catalysis*. Chemcatchem, 2010. 2(7): p. 724-761.
9. Man, I.C., et al., *Universality in Oxygen Evolution Electrocatalysis on Oxide Surfaces*. Chemcatchem, 2011. 3(7): p. 1159-1165.
10. Gasteiger, H.A., et al., *Activity benchmarks and requirements for Pt, Pt-alloy, and non-Pt oxygen reduction catalysts for PEMFCs*. Applied Catalysis B: Environmental, 2005. 56(1): p. 9-35.
11. Lee, Y., et al., *Synthesis and Activities of Rutile IrO₂ and RuO₂ Nanoparticles for Oxygen Evolution in Acid and Alkaline Solutions*. Journal of Physical Chemistry Letters, 2012. 3(3): p. 399-404.
12. Wagner, F.T., et al., *Catalyst development needs and pathways for automotive PEM fuel cells*. ECS Transactions, 2006. 3(1): p. 19-29.
13. Hamdani, M., R. Singh, and P. Chartier, *Co₃O₄ and Co-based spinel oxides bifunctional oxygen electrodes*. Int. J. Electrochem. Sci, 2010. 5: p. 556-577.
14. Hardin, W.G., et al., *Tuning the Electrocatalytic Activity of Perovskites through Active Site Variation and Support Interactions*. Chemistry of Materials, 2014. 26(11): p. 3368-3376.
15. Koza, J.A., et al., *Deposition of β -Co (OH)₂ films by electrochemical reduction of tris (ethylenediamine) cobalt (III) in alkaline solution*. Chemistry of Materials, 2013. 25(9): p. 1922-1926.

16. Pletcher, D. and X. Li, *Prospects for alkaline zero gap water electrolyzers for hydrogen production*. International Journal of Hydrogen Energy, 2011. 36(23): p. 15089-15104.
17. Slanac, D.A., et al., *Bifunctional Catalysts for Alkaline Oxygen Reduction Reaction via Promotion of Ligand and Ensemble Effects at Ag/MnOx Nanodomains*. Journal of Physical Chemistry C, 2012. 116(20): p. 11032-11039.
18. Suntivich, J., et al., *A Perovskite Oxide Optimized for Oxygen Evolution Catalysis from Molecular Orbital Principles*. Science, 2011. 334(6061): p. 1383-1385.
19. Blizanac, B., P. Ross, and N. Markovic, *Oxygen Reduction on Silver Low-Index Single-Crystal Surfaces in Alkaline Solution: Rotating Ring Disk Ag(hkl) Studies*. The Journal of Physical Chemistry B, 2006. 110(10): p. 4735-4741.
20. Sepa, D., M. Vojnovic, and A. Damjanovic, *Reaction intermediates as a controlling factor in the kinetics and mechanism of oxygen reduction at platinum electrodes*. Electrochimica Acta, 1981. 26(6): p. 781-793.
21. Wiggins-Camacho, J.D. and K.J. Stevenson, *Mechanistic Discussion of the Oxygen Reduction Reaction at Nitrogen-Doped Carbon Nanotubes*. Journal of Physical Chemistry C, 2011. 115(40): p. 20002-20010.
22. Hardin, W.G., et al., *Highly Active, Nonprecious Metal Perovskite Electrocatalysts for Bifunctional Metal Air Battery Electrodes*. The Journal of Physical Chemistry Letters, 2013. 4(8): p. 1254-1259.
23. Suntivich, J., et al., *Design principles for oxygen-reduction activity on perovskite oxide catalysts for fuel cells and metal-air batteries*. Nature Chemistry, 2011. 3(7): p. 546-550.
24. Mefford, J.T., et al., *Anion charge storage through oxygen intercalation in LaMnO₃ perovskite pseudocapacitor electrodes*. Nat Mater, 2014. 13(7): p. 726-732.
25. Calle-Vallejo, F., et al., *Number of outer electrons as descriptor for adsorption processes on transition metals and their oxides*. Chemical Science, 2013. 4(3): p. 1245-1249.
26. Vojvodic, A., et al., *On the behavior of Brønsted-Evans-Polanyi relations for transition metal oxides*. The Journal of chemical physics, 2011. 134: p. 244509.
27. Bhalla, A.S., R.Y. Guo, and R. Roy, *The perovskite structure - a review of its role in ceramic science and technology*. Materials Research Innovations, 2000. 4(1): p. 3-26.
28. Calle-Vallejo, F., et al., *Trends in stability of perovskite oxides*. Angewandte Chemie, 2010. 122(42): p. 7865-7867.

29. Twu, J. and P.K. Gallagher, *Preparation of Bulk and Supported Perovskites*, in *Properties and Applications of Perovskite-Type Oxides*, J.L.G.F. L.G. Tejuca, Editor 1993, Marcel Dekker, Inc.: New York.
30. Slanac, D.A., et al., *Atomic resolution structural insights into PdPt nanoparticle–carbon interactions for the design of highly active and stable electrocatalysts*. *Electrochimica Acta*, 2012. 64: p. 35-45.
31. Stoneham, A., *Systematics of metal-insulator interfacial energies: A new rule for wetting and strong catalyst-support interactions*. *Applications of Surface Science*, 1983. 14(3): p. 249-259.
32. Chen, Z., et al., *Highly Active and Durable Core-Corona Structured Bifunctional Catalyst for Rechargeable Metal-Air Battery Application*. *Nano Letters*, 2012. 12(4): p. 1946-1952.
33. Overhoff, K.A., et al., *Novel ultra-rapid freezing particle engineering process for enhancement of dissolution rates of poorly water-soluble drugs*. *European Journal of Pharmaceutics and Biopharmaceutics*, 2007. 65(1): p. 57-67.
34. Zhuang, S.X., et al., *Preparation of homogeneous nanoporous $\text{La}_{0.6}\text{Ca}_{0.4}\text{CoO}_3$ for bi-functional catalysis in an alkaline electrolyte*. *Electrochemistry Communications*, 2011. 13(4): p. 321-324.
35. Sunarso, J., et al., *Oxygen Reduction Reaction Activity of La-Based Perovskite Oxides in Alkaline Medium: A Thin-Film Rotating Ring-Disk Electrode Study*. *Journal of Physical Chemistry C*, 2012. 116(9): p. 5827-5834.
36. Haider, M.A., et al., *Reverse micelle synthesis of perovskite oxide nanoparticles*. *Solid State Ionics*, 2011. 196(1): p. 65-72.
37. Yuasa, M., et al., *Bi-Functional Oxygen Electrodes Using $\text{LaMnO}_3/\text{LaNiO}_3$ for Rechargeable Metal-Air Batteries*. *Journal of the Electrochemical Society*, 2011. 158(5): p. A605-A610.
38. Yuasa, M., et al., *Exploration of reverse micelle synthesis of carbon-supported LaMnO_3* . *Journal of the Electrochemical Society*, 2004. 151(9): p. A1477-A1482.
39. Imaizumi, S., et al., *Preparation of carbon-supported perovskite-type oxides $\text{LaMn}_{1-y}\text{Fe}_y\text{O}_{3+\delta}$ based on reverse homogeneous precipitation method*. *Journal of the Electrochemical Society*, 2004. 151(10): p. A1559-A1564.
40. Suntivich, J., et al., *Electrocatalytic Measurement Methodology of Oxide Catalysts Using a Thin-Film Rotating Disk Electrode*. *Journal of the Electrochemical Society*, 2010. 157(8): p. B1263-B1268.
41. Yuasa, M., et al., *High-Performance Oxygen Reduction Catalyst Using Carbon-Supported La-Mn-Based Perovskite-Type Oxide*. *Electrochemical and Solid State Letters*, 2011. 14(5): p. A67-A69.

42. Ovenstone, J., K.C. Chan, and C.B. Ponton, *Hydrothermal processing and characterisation of doped lanthanum chromite for use in SOFCs*. Journal of Materials Science, 2002. 37(15): p. 3315-3322.
43. Shao, Z.P., W. Zhou, and Z.H. Zhu, *Advanced synthesis of materials for intermediate-temperature solid oxide fuel cells*. Progress in Materials Science, 2012. 57(4): p. 804-874.
44. Wang, X.Q., et al., *Ammonia-Treated Ordered Mesoporous Carbons as Catalytic Materials for Oxygen Reduction Reaction*. Chemistry of Materials, 2010. 22(7): p. 2178-2180.
45. Falcon, H., R. Carbonio, and J. Fierro, *Correlation of oxidation states in $\text{LaFe}_{1-x}\text{Ni}_x\text{O}_{3+\delta}$ oxides with catalytic activity for H_2O_2 decomposition*. Journal of Catalysis, 2001. 203(2): p. 264-272.
46. Bielański, A., *Oxygen in catalysis*. Vol. 43. 1991: CRC Press.
47. Schaak, R.E. and T.E. Mallouk, *Prying apart Ruddlesden-Popper phases: exfoliation into sheets and nanotubes for assembly of perovskite thin films*. Chemistry of Materials, 2000. 12(11): p. 3427-3434.
48. Cao, L. and M. Kruk, *Short synthesis of ordered silicas with very large mesopores*. RSC Advances, 2014. 4(1): p. 331-339.
49. Yi, N., et al., *Nanocrystalline LaCoO_3 perovskite particles confined in SBA-15 silica as a new efficient catalyst for hydrocarbon oxidation*. Journal of Catalysis, 2005. 230(1): p. 249-253.
50. Poux, T., et al., *Dual role of carbon in the catalytic layers of perovskite/carbon composites for the electrocatalytic oxygen reduction reaction*. Catalysis Today, 2012. 189(1): p. 83-92.
51. Huang, K. and J.B. Goodenough, *Oxygen permeation through cobalt-containing perovskites: surface oxygen exchange vs. lattice oxygen diffusion*. Journal of The Electrochemical Society, 2001. 148(5): p. E203-E214.
52. Karlsson, G., *PEROVSKITE CATALYSTS FOR AIR ELECTRODES*. Electrochimica Acta, 1985. 30(11): p. 1555-1561.
53. Maldonado, S., S. Morin, and K.J. Stevenson, *Structure, composition, and chemical reactivity of carbon nanotubes by selective nitrogen doping*. Carbon, 2006. 44(8): p. 1429-1437.
54. Antolini, E., *Carbon supports for low-temperature fuel cell catalysts*. Applied Catalysis B: Environmental, 2009. 88(1): p. 1-24.
55. Bontempi, E., et al., *Structural study of $\text{LaNi}_x\text{Fe}_{1-x}\text{O}_3$ prepared from precursor salts*. Journal of the European Ceramic Society, 2003. 23(12): p. 2135-2142.

56. Falcón, H., et al., *Crystal Structure Refinement and Stability of LaFe_xNi_{1-x}O₃ Solid Solutions*. Journal of Solid State Chemistry, 1997. 133(2): p. 379-385.
57. Koc, R. and H. Anderson, *Electrical conductivity and Seebeck coefficient of (La, Ca)(Cr, Co) O₃*. Journal of materials science, 1992. 27(20): p. 5477-5482.
58. Crumlin, E.J., et al., *Oxygen Electrocatalysis on Epitaxial La_{0.6}Sr_{0.4}CoO_{3-δ} Perovskite Thin Films for Solid Oxide Fuel Cells*. Journal of The Electrochemical Society, 2012. 159(7): p. F219-F225.
59. Alonso-Vante, N., *Platinum and Non-Platinum Nanomaterials for the Molecular Oxygen Reduction Reaction*. ChemPhysChem, 2010. 11(13): p. 2732-2744.
60. Liu, J.J., *Advanced electron microscopy of metal-support interactions in supported metal catalysts*. ChemCatChem, 2011. 3(6): p. 934-948.
61. Souza Filho, A., et al., *Raman spectroscopy for probing chemically/physically induced phenomena in carbon nanotubes*. Nanotechnology, 2003. 14(10): p. 1130.
62. Karlsson, G., *REDUCTION OF OXYGEN ON LANiO₃ IN ALKALINE-SOLUTION*. Journal of Power Sources, 1983. 10(4): p. 319-331.
63. Trasatti, S., *ELECTROCATALYSIS BY OXIDES - ATTEMPT AT A UNIFYING APPROACH*. Journal of Electroanalytical Chemistry, 1980. 111(1): p. 125-131.
64. Wang, N., et al., *A comparison study on methane dry reforming with carbon dioxide over LaNiO₃ perovskite catalysts supported on mesoporous SBA-15, MCM-41 and silica carrier*. Catalysis Today, 2013. 212(0): p. 98-107.
65. Cushing, B.L., V.L. Kolesnichenko, and C.J. O'Connor, *Recent advances in the liquid-phase syntheses of inorganic nanoparticles*. Chemical Reviews, 2004. 104(9): p. 3893-3946.
66. Galal, A., N.F. Atta, and S.M. Ali, *Investigation of the catalytic activity of LaBO₃ (B = Ni, Co, Fe or Mn) prepared by the microwave-assisted method for hydrogen evolution in acidic medium*. Electrochimica Acta, 2011. 56(16): p. 5722-5730.
67. Yuasa, M., et al., *Preparation of nano-LaNiO₃ support electrode for rechargeable metal-air batteries*. Electrochemistry Communications, 2012. 24(0): p. 50-52.
68. Pourbaix, M., *Atlas of Electrochemical Equilibria in Aqueous Solutions* 1974: NACE International.

Chapter 2: Highly Active, Non-precious Metal Perovskite Electrocatalysts for Bifunctional Metal Air Battery Electrodes¹

2.1 INTRODUCTION

Rechargeable metal-air batteries that utilize aqueous alkaline electrolytes may be designed with non-precious metals to offer high theoretical specific energy densities, for example, 1084 Wh/kg for Zn-air. For such systems, including alkaline electrolyzers and fuel cells, catalyst bifunctionality is a key requirement for rechargeable and/or reversible systems. However, applications have been limited by the sluggish kinetics of the oxygen evolution (OER) and oxygen reduction (ORR) reactions.¹⁻⁴ In alkaline conditions, current state of the art OER and ORR catalysts utilize expensive precious metals such as IrO₂ and Pt, respectively.^{5,6} Interestingly, precious metal-free perovskite oxides (ABO₃, where A is a rare-earth and B a transition metal) display bifunctional activity for both the OER and ORR. In each reaction, the activities display a volcano-type relationship with respect to the number of electrons in the e_g orbital of the B site atom.^{7,8} In particular, LaNiO₃ lies near the top of both ORR and OER volcano plots, and furthermore, has been shown to display metal-like conductivities. Consequently, OER specific activity, up to 370 $\mu\text{A}/\text{cm}^2$,^{9,10} of low surface area LaNiO₃ approaches the benchmark value for high surface area IrO₂ of 500 $\mu\text{A}/\text{cm}^2$.^{5,8} However, recently reported mass activities for LaNiO₃ are more than 10x lower than those of precious metal oxides, presumably due to the inability of current synthetic schemes to achieve both high perovskite phase purity and high surface area (<4 m²/g for LaNiO₃ vs >70 m²/g for IrO₂).^{5,7,8}

Perovskite catalysts are typically formed by ball milling of bulk materials to obtain particles >200 nm to several micrometers in diameter.^{11,12} An alternative strategy

¹Large parts of this chapter have been published as Hardin WG, Slanac DA, Wang X, Dai S, Johnston KP, Stevenson KJ. Highly Active, Nonprecious Metal Perovskite Electrocatalysts for Bifunctional Metal–Air Battery Electrodes. *J Phys Chem Lett* 2013, 4(8): 1254-1259.

is to synthesize amorphous perovskite nanoparticles with bottom up approaches by sol-gel methods,¹²⁻¹⁴ reactions in reverse micelles,¹⁵⁻¹⁷ coprecipitation hydrolysis processes,¹⁸⁻²⁰ and hydrothermal routes.^{21,22} Nanoparticles as small as ~10 nm may be synthesized by precipitation of metal hydroxides in the presence of capping ligands.^{14,20} However, due to disparities in hydrolysis rates for systems with two or more metals^{12,22} and undesired side reactions with carbon supports at high temperatures ($\geq 600^{\circ}\text{C}$),^{13,14,16} phase impurities have been observed and have led to low mass activities. Furthermore, calcination steps required to form crystalline perovskites result in significant coalescence and typically produce low surface area particles ranging from 200 nm to 1 μm or greater.^{13,14,21} Phase purity and high surface area are also important requirements for other applications of perovskites such as solid oxide fuel cell electrodes and membranes, chlor-alkali and water electrolysis electrodes, capacitors, sensors and nonvolatile memory.²²⁻²⁴ Thus key challenges remain to synthesize phase pure materials while minimizing agglomeration during calcination for the formation of catalysts with high electrocatalytic mass activities.

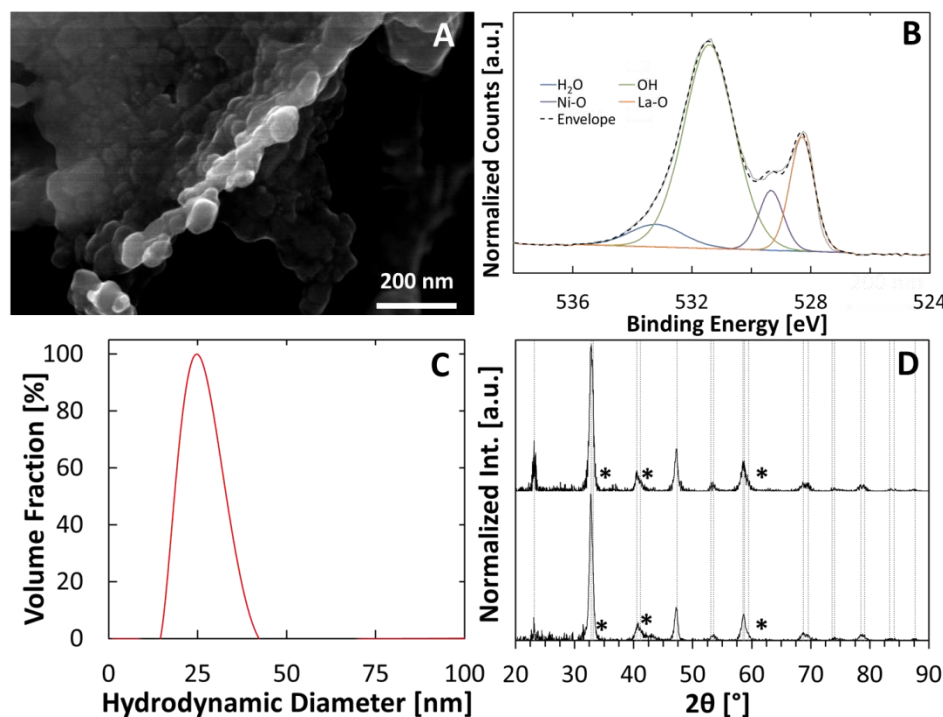


Figure 2.1: Physical Characterization of LaNiO_3

(A) Scanning electron microscopy image of calcined LaNiO_3 after freeze drying. (B) De-convoluted O 1s core level spectrum of freeze dried LaNiO_3 . (C) Dynamic light scattering size distribution curve for as-synthesized amorphous hydroxide precursor particles, indicating a hydrodynamic diameter of 25 ± 8 nm. (D) X-ray diffraction spectra of (top) oven dried and (bottom) freeze dried LaNiO_3 . NiO phase impurities marked with a star.

Herein, we present a general scheme for synthesis of phase pure, catalytically active LaNiO_3 that displays exceptionally high OER mass activities and a strong OER/ORR bifunctional character when supported on nitrogen doped carbon (NC). A key advance was to prepare uniform 25 nm nanoparticle dispersions in aqueous solution via rapid simultaneous hydrolysis of both La^{3+} and Ni^{2+} nitrates by reverse phase arrested growth precipitation, which when calcined, form nearly phase pure LaNiO_3 nanocrystalline catalysts. Scanning electron microscopy (SEM), X-ray diffraction (XRD),

dynamic light scattering (DLS) and X-ray photoelectron spectroscopy (XPS) indicated that calcination of 25 nm amorphous mixed metal hydroxide particles yielded 20-50 nm phase pure aggregates of relatively distinct primary nanoparticles that exhibit significant surface hydroxylation and possess a surface area of $\sim 11 \text{ m}^2/\text{g}$. Coalescence was mitigated by the large interparticle spacing in highly open, low fractal dimension nanoparticulate powders produced by rapid freeze drying enabled by thin film freezing followed by lyophilization. LaNiO_3 prepared by this method, which will be referred to as ‘freeze drying’, has been designated as ‘nano-structured’ LaNiO_3 (ns LaNiO_3) due to the morphology observed in Figure 2.1A.

2.2 RESULTS AND DISCUSSION

To obtain an aqueous dispersion of amorphous perovskite precursor nanoparticles, metal nitrates of La^{3+} and Ni^{2+} were hydrolyzed rapidly in the presence of a capping ligand, tetrapropylammonium bromide (TPAB) as described in detail in Appendix B. This approach created amorphous particles of La and Ni hydroxides with a hydrodynamic diameter of 25 nm (peak width ± 8 nm), as shown via DLS in Figure 2.1C. To promote complete and rapid hydrolysis of both La and Ni nitrates while maintaining a constant pH during the reaction,¹⁸ an excess volume of pH 14 tetramethylammonium hydroxide (TMAOH) was used. The capping ligand TPAB provided colloidal stabilization through a combination of electrostatic and steric repulsion.²⁵ Without TPAB, the particles agglomerated, even after sonication, presumably leading to lower phase purity and lower surface areas, as seen previously in a similar synthesis.²¹ Prior to calcination, the amorphous particle dispersions were either freeze dried by a combination of thin film freezing followed by lyophilization, or dried in an oven at 120°C for ~ 1 h. In the freeze drying process, droplets of the amorphous particle dispersion were spread onto the

surface of a rotating metal drum at -78°C and frozen into a thin film ($\sim 100\text{ }\mu\text{m}$ thick) at fast freezing rates ($\sim 100\text{ K/s}$).²⁶ The time scale for freezing (order of milliseconds) was sufficiently fast to prevent significant growth of the amorphous nanoparticles. After lyophilization, a fluffy powder was produced, with open flocs of the nanoparticles with a low fractal dimension, consistent with numerous related studies of organic substances.^{27,28} In contrast, oven drying of the aqueous dispersion led to gelation whereby, the capillary forces produced somewhat more dense aggregates. In essence, the frozen freeze dried material may be considered to be closer to the rapid diffusion limited aggregation regime, whereas the slowly dried material is closer to the reaction limited regime, where particles explore a greater number of configurations to lower the surface area, resulting in a larger aggregate density.²⁹

After particles formed via reverse phase precipitation were calcined in air at 700°C for 4 hours to form crystalline LaNiO_3 , the morphology of the oven dried precursor was aggregates of sintered primary nanoparticles, with modest coalescence and particle growth, as shown by the SEM images in Appendix B (B.1C,D). For the freeze dried dispersions, the amount of coalescence and growth was less prevalent, resulting in aggregates of $\sim 20\text{-}50\text{ nm}$ partially coalesced primary nanoparticles, as seen in Figures 2.1A and B.1A,B. It is possible that the large interparticle spacing in the highly open, low fractal dimension aggregates suppressed sintering despite the 700°C calcination temperature. Remarkably, the original 25 nm precursor ($33\text{ m}^2/\text{g}$ for individual spheres) particles grew only modestly during calcination. The nitrogen adsorption (BET) measured surface areas of the freeze dried and oven dried samples, after calcination, were $11\text{ m}^2/\text{g}$, and $6\text{ m}^2/\text{g}$, respectively (Figure B.1, Figure B.2). Both catalysts were comprised of an essentially phase pure crystalline rhombohedral LaNiO_3 phase, as shown in the XRD spectra in Figure 2.1D. The slight impure phase identified in both samples

was NiO, as the peaks were barely visible at 2θ s of 35° , 42.5° , and 62.5° . According to Scherrer analysis performed on the most intense reflection due to a single crystalline plane, {024} for LaNiO_3 , similar crystallite sizes of ~ 15 nm were calculated for the two drying approaches. Note that crystallite size is not indicative of particle size, surface area, or resulting catalytic activities.

The phase purity and relatively high surface area after calcination may be attributed to rapid and simultaneous reduction of both metal nitrates to form nanoparticle precursors leading to an appropriate level of intermixing of the metal hydroxides. Instantaneously, upon adding the nitrates into the pH 14 solution in this reverse phase precipitation reaction,^{18,25} a light green dispersion was visible. The burst nucleation followed by arrested growth led to 25 nm nanoparticles with apparently adequate intermixing of both metal hydroxides. Thus, this approach overcomes the dissimilar hydrolysis rate constants for La^{3+} and Ni^{2+} , which differ by up to almost one order of magnitude at a lower pH $< \sim 10$.²² This is in contrast to normal phase coprecipitation, whereby the pH immediately decreases upon drop-wise addition of base into a solution of dissolved metal salts which could lead to phase impurities, as has been seen previously for coprecipitation of other systems.^{22,30} It is likely that hydrolysis of the less reactive component lags nucleation and growth of the more reactive one. Thus, the burst nucleation and high pH in the reverse phase method enables rapid hydrolysis of both metal nitrates to form amorphous composite nanoparticles that upon calcination formed phase pure nanocrystal aggregates.

To probe the physical and chemical properties of the catalyst surface, the O 1s core level spectrum of unsupported nsLaNiO_3 was collected via high resolution XPS and deconvoluted in the same manner as reported by Mickevicius et al.³¹ The spectrum, shown in Figure 2.1B, contains four distinct species of oxygen corresponding to lattice

oxygen in lanthanum oxide (528.3 eV) and nickel oxide (529.3 eV), lanthanum and nickel hydroxides (531.4 eV) and adsorbed water (533.2 eV). Upon deconvolution, it was found that the catalyst surface was significantly hydroxylated (~65 rel. at.%). It has been previously shown that the least energetically favorable step of the OER is either chemisorbed OOH^- formation, or oxidation of surface OH^- .³²⁻³⁴ Furthermore, it has been proposed that the concentration of lattice hydroxide directly affects the rate at which surface peroxide forms during the OER.³⁵ Thus, the presence of lattice hydroxide is expected to have a positive effect on measured OER activity.

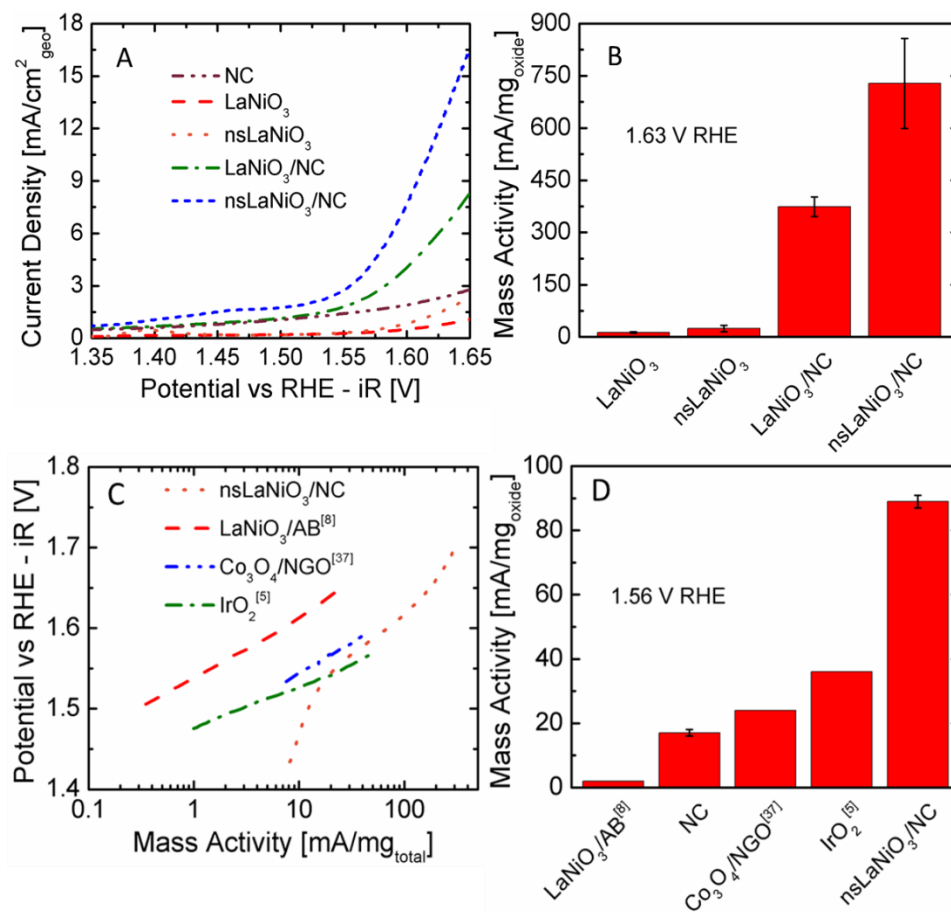


Figure 2.2: LaNiO₃ OER activity trends.

OER activity trends in (A,B) Ar saturated 0.1 M KOH at 900 rpm and 50 mV/s and (C,D) O₂ saturated 0.1 M KOH at 1600 rpm and 10 mV/s. (A) Linear sweep voltammogram and (B) selected oxide OER mass activities calculated at 1.63 V from data in (A). (C) Tafel plot comparing nsLaNiO₃ mass activity in O₂ saturated 0.1 M KOH to other leading OER catalysts, and (D) oxide (total in case of NC) OER mass activity in O₂ saturated 0.1 M KOH. Note that at potentials >1.53 V, nsLaNiO₃/NC has considerably higher OER activity than the pure nitrogen doped carbon.

To determine the effect of perovskite morphology and surface area on OER activity, polarization curves were measured in Ar saturated 0.1 M KOH at 900 rpm

(Figure 2.2A). At 1.63 V vs the reversible hydrogen electrode (RHE), or a 0.4 V overpotential, the total OER mass activity for unsupported nsLaNiO₃ was 24 mA/mg, nearly two times greater than for the lower surface area oven dried LaNiO₃ (13 mA/mg), seen in Figures 2.2A,B. For the unsupported perovskites, such low activities are expected given their lower conductivities relative to the high surface area (~1080 m²/g, Figure B.3), conductive nitrogen doped carbon support.³⁶ The carbon support provides a conductive network by which the catalyst is electrically wired to the electrode, while the bare catalyst is only in electrical contact with the electrode by point contacts. For nsLaNiO₃ supported on nitrogen doped carbon (nsLaNiO₃/NC), the mass activity was 728 mA/mg_{oxide}, again nearly two times higher than the value of 374 mA/mg_{oxide} obtained for the lower surface area LaNiO₃/NC catalyst.

In Figure 2.2C,D the OER total mass activities (representative polarization curve shown in Figure B.4) for nsLaNiO₃/NC are comparable to a leading benchmark catalyst, IrO₂.⁵ Furthermore, they are well above recently reported values for coprecipitated LaNiO₃ supported on acetylene black (AB),⁸ and Co₃O₄ supported on nitrogen doped reduced graphene oxide (Co₃O₄/NGO).³⁷ In these comparisons, the electrolyte was saturated with oxygen. At a chosen potential of 1.56 V, the nsLaNiO₃/NC activity was already markedly above that of the NC baseline, as is evident in Figure 2.2C. Remarkably, on an oxide mass basis, the activity for nsLaNiO₃/NC (89 mA/mg_{oxide}) reached 2.5x that of a leading benchmark catalyst, 6 nm IrO₂ (36 mA/mg_{oxide}). Since the surface area to mass ratio of IrO₂ is 71 m²/g, compared to 11 m²/g for nsLaNiO₃/NC, the apparent specific activity (based on surface area measurement via BET) was ~450 μA/cm²_{oxide}, compared to ~50 μA/cm²_{oxide} for IrO₂. The value for the former was corrected for the small NC current contribution. Relative to literature values reported for LaNiO₃ synthesized via normal phase coprecipitation (3.5 m²/g) and supported on AB the

activity of nsLaNiO₃/NC is ~45 times higher at 1.56 V. The oxide mass activity of nsLaNiO₃/NC is ~3.8 times that of a highly active 6 nm Co₃O₄ supported on nitrogen doped graphene oxide (24 mA/mg_{oxide}). Additionally, the mass activity is ~18 times higher than that reported in a recent study of the most OER active perovskite, Ba_{0.5}Sr_{0.5}Co_{0.8}Fe_{0.2}O₃ (0.2 m²/g),⁸ despite its high specific activity of ~2500 μA/cm²_{oxide}.⁸

The high mass activity for nsLaNiO₃/NC partially reflects the phase pure high surface area crystalline LaNiO₃ nanoparticle aggregates, enabled by the precursor synthetic approach. The large numbers of facets in the nanoparticle domains and the regions between them offers the possibility of more access to most active surfaces, such as the {100} planes in LaNiO₃.³⁵ The morphology of thin layers of nanocrystal aggregates on the carbon substrate is also beneficial, for example, as seen for MnO_x³⁸ and highly active oxyhydroxide thin films.³⁹

To further understand the mechanism responsible for the high electrocatalytic activity reported herein, it is necessary to reexamine the role of lattice hydroxides in the OER. Lattice oxygen in LaNiO₃ is weakly bound,^{40,41} and can be considered protonated such that it contributes a lattice hydroxide to the formation of OOH⁻ during the OER.^{31,35,42} Lattice oxygen directly participating in the OER has been observed for similar oxides such as Li-NiO, IrO₂ and RuO₂.⁴³⁻⁴⁵ Figure B.6 depicts this OER cycle, wherein the formation of OH, O²⁻, and OOH⁻ intermediates are reconciled with the utilization of lattice (hydr)oxide in the formation of surface adsorbed hydroperoxide. This cycle rationalizes the unusually high OER mass activities observed herein. The rate determining step of the OER on LaNiO₃ (Figure B.6, step 3) is governed by the concentration of lattice (hydr)oxide species that participate in the formation of the O-O bond in hydroperoxide, thus the high lattice (hydr)oxide concentration of nsLaNiO₃ increases the rate at which HOO⁻ forms and consequently the rate at which the OER

proceeds.³²⁻³⁵ Furthermore, as lattice (hydr)oxides are oxidized to form hydroperoxide, a positively charged vacancy is left behind. This lattice oxygen vacancy is rapidly replenished from the bulk electrolyte (Figure B.6, step L),⁴² resulting in the lack of hysteresis observed during OER testing (Figure B.4).

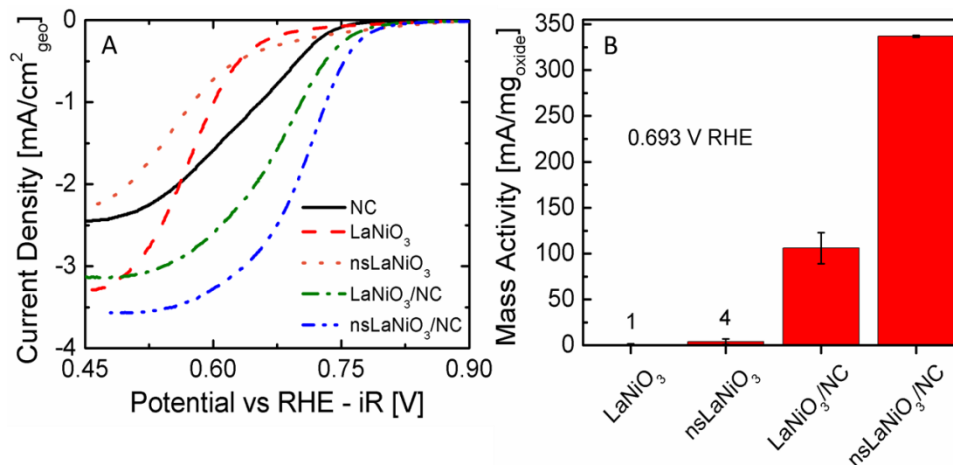


Figure 2.3: ORR activity trends in O₂ saturated 0.1 M KOH at 1600 RPM.

(A) Polarization curves for the ORR, including pure NC, and supported / unsupported LaNiO₃ / nsLaNiO₃. (B) Oxide mass activities taken at 0.693 V, showing high mass activity for the nsLaNiO₃/NC catalyst.

These nanocrystalline perovskites also displayed appreciable activity for the ORR. Polarization curves for ORR in oxygen saturated 0.1 M KOH at 1600 rpm and 5 mV/s are shown in Figure 2.3A, with activity measurements taken at 0.693 V. Low activities were observed for unsupported LaNiO₃ and nsLaNiO₃, 1 mA/mg and 4 mA/mg, respectively. As for the OER, this was likely due to the lower conductivity of the pure oxide. However, when LaNiO₃ and nsLaNiO₃ were supported on nitrogen doped carbon, the half wave potential shifted >100 mV positive and resulted in significantly higher activities of 32 mA/mg_{total} and 101 mA/mg_{total}, respectively. The activity increased more than an order of magnitude for the ORR, as was also seen for the OER. The activity of nsLaNiO₃/NC

reached 337 mA/mg_{oxide}, ~3 times higher than for the oven dried LaNiO₃/NC (Figure 2.3B) similar to the observed increase in BET surface area as summarized in Figure B.1. The nitrogen doped carbon further contributes to the activity, due most likely to the presence of pyridinic functional groups in the surface as shown by XPS in Figure B.7.^{46,47}

As a measure of the overall bifunctionality of the catalyst, we determined the difference in potential between the ORR at -3 mA/cm² and OER at 10 mA/cm² (ΔE), current densities of practical importance for electrochemical and photoelectrochemical applications.³⁸ ΔE is simply the sum of the overpotentials for the two reactions. Table 2.1 shows the excellent bifunctional character ($\Delta V = 1.02$ V) of the nsLaNiO₃/NC catalyst, which is exceeded by 100 mV only for the ORR active precious metal Ir ($\Delta E = 0.92$ V)³⁸ that also forms an OER-active oxide at anodic potentials.

Table 2.1: Assessment of catalyst bifunctionality for nsLaNiO₃/NC and other benchmarks.

catalyst	ORR Potential (V) vs RHE @ - 3 mA/cm ²	OER Potential (V) vs RHE @ 10 mA/cm ²	ΔE (V)
nsLaNiO ₃ /NC	0.64	1.66	1.02
20% Ir/C ³⁸	0.69	1.61	0.92
20% Pt/C ³⁸	0.86	2.02	1.16

Remarkably, the ΔE of 1.02 for the nsLaNiO₃/NC catalyst is significantly better than for Pt/C ($\Delta E = 1.16$ V),³⁸ a leading ORR catalyst but a poor OER catalyst. While it has been demonstrated that phase purity is important for achieving high bifunctional character, the specific interactions between the perovskite catalyst and nitrogen doped carbon are not well understood. Electronic and ensemble effects, like those recently observed for bimetallic and mixed metal-metal oxide catalyst,^{48,49} could be contributing to the high activities reported here. Additionally, the specific interactions between the perovskite catalyst and nitrogen doped carbon likely play a much smaller secondary role, such as H₂O₂ disproportionation and improved support hydrophilicity. Future work will explore the interplay between these various effects.

2.3 CONCLUSIONS

In conclusion, LaNiO₃ nanocrystalline aggregates on nitrogen doped carbon exhibit extremely high activity for the OER and strong OER/ORR bifunctional character, as a result of high phase purity, lattice hydroxylation and increased surface area. This bifunctional character is crucial to the development of inexpensive aqueous metal-air batteries, fuel cells and electrolyzers. This highly active morphology is produced by rapid, simultaneous hydrolysis of La³⁺ and Ni²⁺ nitrates during reverse phase arrested growth precipitation, followed by rapid drying. This synthetic concept to generate

precursors that are calcined to form phase pure nanocrystalline aggregates is general and thus a directly applicable route to prepare a wide variety of nonprecious metal, nanocrystalline perovskites as highly active catalysts.

2.4 EXPERIMENTAL METHODS

2.4.1 Chemicals.

All chemicals were used as received. Anhydrous ethanol and 5 wt % nafion solution in lower alcohols were purchased from Sigma-Aldrich. Nickel(II) nitrate hexahydrate (99%), lanthanum(III) nitrate hexa-hydrate (99.999%), tetrapropylammonium bromide (TPAB, 98%), tetramethylammonium hydroxide pentahydrate (TMAOH, 99%), 2-propanol and potassium hydroxide were obtained from Fisher Scientific, and ethanol (Absolute 200 proof) from Aaper alcohol. Millipore high purity water (18 M Ω) was used. Oxygen (research grade, 99.999% purity) and argon (research grade, 99.999% purity) were obtained from Praxair. Nitrogen doped carbon (NC) was prepared as reported elsewhere.⁵⁰

2.4.2 Synthesis of the nanostructured LaNiO₃ catalyst (nsLaNiO₃).

Mixed metal hydroxide particles were prepared by reverse hydrolysis of La and Ni nitrates in the presence of an equimolar amount of TPAB dissolved into 1 wt% TMAOH. In a typical synthesis, 50 mL of a mixed metal nitrates (~10 mM) solution was added drop-wise (~2 mL/min) to 200 mL of vigorously stirring TMAOH. The solution was left stirring for 30 min, and the resulting suspension was washed with DI water via centrifugation 3 times, followed by probe sonication. The resulting washed particle solution was frozen into a thin film and then lyophilized at -10°C and a fixed pressure of ~50 mTorr for 20 hours. The lyophilized powder was calcined at 700°C for 4 hours under

flowing dehumidified air. Following calcination, all particles were washed with EtOH and filtered to obtain the final nsLaNiO₃ catalyst. Synthesis of LaNiO₃ was identical to that of nsLaNiO₃, except that the washed hydroxide gel was spread over a glass dish and dried at 120°C under air for a minimum of 1 hour prior to calcination, rather than thin film freezing followed by lyophilization.

2.4.3 Materials Characterization.

The hydrodynamic diameter (D_H) of as-synthesized hydrolysis particles was measured via dynamic light scattering (DLS, Brookhaven ZetaPALS instrument) and fit with the CONTIN routine. Structural information of as-calcined oxides were obtained using wide-angle X-ray diffraction (Bruker Nokius AXS D8 Advance) emitting Cu K α radiation (1.54 Å) and the background removed with JADE software (Molecular Diffraction Inc.). Surface morphologies of the perovskite catalysts were observed using scanning electron microscopy (SEM, Hitachi S-5500), while surface areas were quantified using nitrogen sorption (Quantachrome Instruments NOVA 2000) at 77 K. Chemical states were probed by X-ray photoelectron spectroscopy (XPS, Kratos AXIS Ultra DLD) using a monochromatic Al X-ray source (Al α , 1.4866 keV).

2.4.4 Electrochemical Characterization.

Electrochemical testing was performed on either a CH Instruments CHI832a or a Metrohm Autolab PGSTAT302N potentiostat, both equipped with high speed rotators from Pine Instruments. All testing was done at room temperature in 0.1M KOH (measured pH \approx 12.6), and all data was iR corrected (50 Ω) after testing. Electrolyte resistance was found prior to testing by a combination of the current-interrupt and positive feedback methods. Each test was performed in a standard 3 electrode cell using a Hg/HgO (1M KOH) reference electrode, a Pt wire counter electrode, and a film of

catalyst ink on glassy carbon as the working electrode. All potentials are reported versus the regular hydrogen electrode (RHE), which were shifted +0.843 V vs. Hg/HgO (Hg/HgO (1 M KOH) + 0.1 V = NHE; NHE + 0.059 * pH = RHE). Catalyst inks were prepared by addition of 1 mL of NaOH neutralized 0.05 wt% Nafion solution¹⁹ to 1 mg of catalyst powder and bath sonicated for 30 min. 10 μ L of ink was placed onto a clean 5 mm (0.196 cm²) glassy carbon electrode and left to dry under a glass jar. The activity of the catalyst towards the oxygen reduction reaction was determined by rotating the electrode at 1600 rpm in O₂ saturated media and performing a linear potential sweep at 5 mV/s. Kinetic currents were calculated according to the Koutecky-Levich equation from the resulting polarization curves. All ORR mass activities reported herein are averages from cathodic scans taken of multiple electrodes. Oxygen evolution activities were quantified in either O₂ saturated or deoxygenated media by performing anodic potential sweeps at 10 mV/s and 50 mV/s, respectively. All electrochemical tests were performed on freshly prepared electrodes, except for deoxygenated OER tests. These tests were conducted on the same electrode following O₂ saturated ORR measurements. All OER mass activities reported herein are averages from anodic scans taken of multiple electrodes.

2.5 ADDITIONAL INFORMATION

Detailed experimental methods, electron microscopy images, summary of catalyst surface areas, nitrogen adsorption curves, OER polarization curve, and XPS spectra for the N 1s core region are provided in Appendix B

2.6 REFERENCES

- (1) Bidault, F.; Brett, D. J. L.; Middleton, P. H.; Brandon, N. P. Review of Gas Diffusion Cathodes for Alkaline Fuel Cells. *J. Power Sources* **2009**, *187*, 39-48.

- (2) Cheng, F. Y.; Chen, J. Metal-Air Batteries: From Oxygen Reduction Electrochemistry to Cathode Catalysts. *Chem. Soc. Rev.* **2012**, *41*, 2172-2192.
- (3) Neburchilov, V.; Wang, H.; Martin, J. J.; Qu, W. A Review on Air Cathodes for Zinc-Air Fuel Cells. *J. Power Sources* **2010**, *195*, 1271-1291.
- (4) Harting, K.; Kunz, U.; Turek, T. Zinc-Air Batteries: Prospects and Challenges for Future Improvement. *Z. Phys. Chem.* **2012**, *226*, 151-166.
- (5) Lee, Y.; Suntivich, J.; May, K. J.; Perry, E. E.; Shao-Horn, Y. Synthesis and Activities of Rutile IrO₂ and RuO₂ Nanoparticles for Oxygen Evolution in Acid and Alkaline Solutions. *J. Phys. Chem. Lett.* **2012**, *3*, 399-404.
- (6) Spendelow, J. S.; Wieckowski, A. Electrocatalysis of Oxygen Reduction and Small Alcohol Oxidation in Alkaline Media. *Phys. Chem. Chem. Phys.* **2007**, *9*, 2654-2675.
- (7) Suntivich, J.; Gasteiger, H. A.; Yabuuchi, N.; Nakanishi, H.; Goodenough, J. B.; Shao-Horn, Y. Design Principles for Oxygen-Reduction Activity on Perovskite Oxide Catalysts for Fuel Cells and Metal-Air Batteries. *Nat. Chem.* **2011**, *3*, 546-550.
- (8) Suntivich, J.; May, K. J.; Gasteiger, H. A.; Goodenough, J. B.; Shao-Horn, Y. A Perovskite Oxide Optimized for Oxygen Evolution Catalysis from Molecular Orbital Principles. *Science* **2011**, *334*, 1383-1385.
- (9) Karlsson, G. Reduction of Oxygen on LaNiO₃ in Alkaline-Solution. *J. Power Sources* **1983**, *10*, 319-331.
- (10) Trasatti, S. Electrocatalysis by Oxides - Attempt at a Unifying Approach. *J. Electroanal. Chem.* **1980**, *111*, 125-131.
- (11) J. Twu, P. K. G. In *Properties and Applications of Perovskite-Type Oxides*; L.G. Tejuca, J. L. G. F., Ed.; Marcel Dekker, Inc.: New York, 1993.
- (12) Sunarso, J.; Torriero, A. A. J.; Zhou, W.; Howlett, P. C.; Forsyth, M. Oxygen Reduction Reaction Activity of La-Based Perovskite Oxides in Alkaline Medium: A Thin-Film Rotating Ring-Disk Electrode Study. *J. Phys. Chem. C* **2012**, *116*, 5827-5834.
- (13) Chen, Z.; Yu, A. P.; Higgins, D.; Li, H.; Wang, H. J.; Chen, Z. W. Highly Active and Durable Core-Corona Structured Bifunctional Catalyst for Rechargeable Metal-Air Battery Application. *Nano Lett.* **2012**, *12*, 1946-1952.
- (14) Zhuang, S. X.; Huang, C. H.; Huang, K. L.; Hu, X.; Tu, F. Y.; Huang, H. X. Preparation of Homogeneous Nanoporous La_{0.6}Ca_{0.4}CoO₃ for Bi-Functional Catalysis in an Alkaline Electrolyte. *Electrochem. Commun.* **2011**, *13*, 321-324.

- (15) Haider, M. A.; Capizzi, A. J.; Murayama, M.; McIntosh, S. Reverse Micelle Synthesis of Perovskite Oxide Nanoparticles. *Solid State Ionics* **2011**, *196*, 65-72.
- (16) Yuasa, M.; Sakai, G.; Shimanoe, K.; Teraoka, Y.; Yamazoe, N. Exploration of Reverse Micelle Synthesis of Carbon-Supported LaMnO₃. *J. Electrochem. Soc.* **2004**, *151*, A1477-A1482.
- (17) Yuasa, M.; Shimanoe, K.; Teraoka, Y.; Yamazoe, N. High-Performance Oxygen Reduction Catalyst Using Carbon-Supported La-Mn-Based Perovskite-Type Oxide. *Electrochem. Solid St.* **2011**, *14*, A67-A69.
- (18) Imaizumi, S.; Shimanoe, K.; Teraoka, Y.; Miura, N.; Yamazoe, N. Preparation of Carbon-Supported Perovskite-Type Oxides LaMn_{1-y}Fe_yO_{3+Delta} Based on Reverse Homogeneous Precipitation Method. *J. Electrochem. Soc.* **2004**, *151*, A1559-A1564.
- (19) Suntivich, J.; Gasteiger, H. A.; Yabuuchi, N.; Shao-Horn, Y. Electrocatalytic Measurement Methodology of Oxide Catalysts Using a Thin-Film Rotating Disk Electrode. *J. Electrochem. Soc.* **2010**, *157*, B1263-B1268.
- (20) Yuasa, M.; Nishida, M.; Kida, T.; Yamazoe, N.; Shimanoe, K. Bi-Functional Oxygen Electrodes Using LaMnO₃/LaNiO₃ for Rechargeable Metal-Air Batteries. *J. Electrochem. Soc.* **2011**, *158*, A605-A610.
- (21) Ovenstone, J.; Chan, K. C.; Ponton, C. B. Hydrothermal Processing and Characterisation of Doped Lanthanum Chromite for Use in Sofcs. *J. Mater. Sci.* **2002**, *37*, 3315-3322.
- (22) Shao, Z. P.; Zhou, W.; Zhu, Z. H. Advanced Synthesis of Materials for Intermediate-Temperature Solid Oxide Fuel Cells. *Prog. Mater. Sci.* **2012**, *57*, 804-874.
- (23) Bhalla, A. S.; Guo, R. Y.; Roy, R. The Perovskite Structure - a Review of Its Role in Ceramic Science and Technology. *Mater. Res. Innovations* **2000**, *4*, 3-26.
- (24) Patzke, G. R.; Zhou, Y.; Kontic, R.; Conrad, F. Oxide Nanomaterials: Synthetic Developments, Mechanistic Studies, and Technological Innovations. *Angew. Chem.-Int. Edit.* **2011**, *50*, 826-859.
- (25) Teraoka, Y.; Nanri, S.; Moriguchi, I.; Kagawa, S.; Shimanoe, K.; Yamazoe, N. Synthesis of Manganite Perovskites by Reverse Homogeneous Precipitation Method in the Presence of Alkylammonium Cations. *Chem. Lett.* **2000**, 1202-1203.
- (26) Bennett, T.; Poulikakos, D. Splat-Quench Solidification: Estimating the Maximum Spreading of a Droplet Impacting a Solid Surface. *J. Mater. Sci.* **1993**, *28*, 963-970.

- (27) Engstrom, J. D.; Lai, E. S.; Ludher, B. S.; Chen, B.; Milner, T. E.; Williams, R. O.; Kitto, G. B.; Johnston, K. P. Formation of Stable Submicron Protein Particles by Thin Film Freezing. *Pharm. Res.* **2008**, *25*, 1334-1346.
- (28) Overhoff, K. A.; Engstrom, J. D.; Chen, B.; Scherzer, B. D.; Milner, T. E.; Johnston, K. P.; Williams, R. O. Novel Ultra-Rapid Freezing Particle Engineering Process for Enhancement of Dissolution Rates of Poorly Water-Soluble Drugs. *Eur. J. Pharm. Biopharm.* **2007**, *65*, 57-67.
- (29) Lin, M. Y.; Lindsay, H. M.; Weitz, D. A.; Ball, R. C.; Klein, R.; Meakin, P. Universality in Colloid Aggregation. *Nature* **1989**, *339*, 360-362.
- (30) Cushing, B. L.; Kolesnichenko, V. L.; O'Connor, C. J. Recent Advances in the Liquid-Phase Syntheses of Inorganic Nanoparticles. *Chem. Rev.* **2004**, *104*, 3893-3946.
- (31) Mickevicius, S.; Grebinskij, S.; Bondarenka, V.; Vengalis, B.; Sliuziene, K.; Orłowski, B. A.; Osinniy, V.; Drube, W. Investigation of Epitaxial LaNiO_{3-x} Thin Films by High-Energy XPS. *J. Alloys Compd.* **2006**, *423*, 107-111.
- (32) Dau, H.; Limberg, C.; Reier, T.; Risch, M.; Roggan, S.; Strasser, P. The Mechanism of Water Oxidation: From Electrolysis via Homogeneous to Biological Catalysis. *ChemCatChem* **2010**, *2*, 724-761.
- (33) Man, I. C.; Su, H. Y.; Calle-Vallejo, F.; Hansen, H. A.; Martinez, J. I.; Inoglu, N. G.; Kitchin, J.; Jaramillo, T. F.; Norskov, J. K.; Rossmeisl, J. Universality in Oxygen Evolution Electrocatalysis on Oxide Surfaces. *ChemCatChem* **2011**, *3*, 1159-1165.
- (34) Rossmeisl, J.; Qu, Z. W.; Zhu, H.; Kroes, G. J.; Norskov, J. K. Electrolysis of Water on Oxide Surfaces. *J. Electroanal. Chem.* **2007**, *607*, 83-89.
- (35) Bockris, J. O.; Otagawa, T. Mechanism of Oxygen Evolution on Perovskites. *J. Phys. Chem.* **1983**, *87*, 2960-2971.
- (36) Karlsson, G. Perovskite Catalysts for Air Electrodes. *Electrochim. Acta* **1985**, *30*, 1555-1561.
- (37) Liang, Y. Y.; Li, Y. G.; Wang, H. L.; Zhou, J. G.; Wang, J.; Regier, T.; Dai, H. J. Co_3O_4 Nanocrystals on Graphene as a Synergistic Catalyst for Oxygen Reduction Reaction. *Nat. Mater.* **2011**, *10*, 780-786.
- (38) Gorlin, Y.; Jaramillo, T. F. A Bifunctional Nonprecious Metal Catalyst for Oxygen Reduction and Water Oxidation. *J. Am. Chem. Soc.* **2010**, *132*, 13612-13614.
- (39) Trotochaud, L.; Ranney, J. K.; Williams, K. N.; Boettcher, S. W. Solution-Cast Metal Oxide Thin Film Electrocatalysts for Oxygen Evolution. *J. Am. Chem. Soc.* **2012**, *134*, 17253-17261.

- (40) Konysheva, E.; Irvine, J. T. S. Thermochemical and Structural Stability of A- and B-Site-Substituted Perovskites in Hydrogen-Containing Atmosphere. *Chem. Mater.* **2009**, *21*, 1514-1523.
- (41) Subbaraman, R.; Tripkovic, D.; Chang, K.-C.; Strmcnik, D.; Paulikas, A. P.; Hirunsit, P.; Chan, M.; Greeley, J.; Stamenkovic, V.; Markovic, N. M. Trends in Activity for the Water Electrolyser Reactions on 3d M(Ni,Co,Fe,Mn) Hydr(Oxy)Oxide Catalysts. *Nat. Mater.* **2012**, *11*, 550-557.
- (42) Boehm, H. P. Acidic and Basic Properties of Hydroxylated Metal Oxide Surfaces. *Discuss. Faraday Soc.* **1971**, *52*, 264-275.
- (43) Lee, C.; Riga, A.; Yeager, E. In *Mass Transport Phenomena in Ceramics*; Gordon, R. S., Cooper, A. R., Heuer, A. H., Eds.; Plenum Press: New York, 1975, p 489.
- (44) Fierro, S.; Nagel, T.; Baltruschat, H.; Comninellis, C. Investigation of the Oxygen Evolution Reaction on Ti/IrO₂ Electrodes Using Isotope Labelling and on-Line Mass Spectrometry. *Electrochem. Commun.* **2007**, *9*, 1969-1974.
- (45) Wohlfahrt-Mehrens, M.; Heitbaum, J. Oxygen Evolution on Ru and RuO₂ Electrodes Studied Using Isotope Labelling and on-Line Mass Spectrometry. *Journal of Electroanalytical Chemistry and Interfacial Electrochemistry* **1987**, *237*, 251-260.
- (46) Maldonado, S.; Stevenson, K. J. Influence of Nitrogen Doping on Oxygen Reduction Electrocatalysis at Carbon Nanofiber Electrodes. *J. Phys. Chem. B* **2005**, *109*, 4707-4716.
- (47) Wiggins-Camacho, J. D.; Stevenson, K. J. Mechanistic Discussion of the Oxygen Reduction Reaction at Nitrogen-Doped Carbon Nanotubes. *J. Phys. Chem. C* **2011**, *115*, 20002-20010.
- (48) Slanac, D. A.; Hardin, W. G.; Johnston, K. P.; Stevenson, K. J. Atomic Ensemble and Electronic Effects in Ag-Rich AgPd Nanoalloy Catalysts for Oxygen Reduction in Alkaline Media. *J. Am. Chem. Soc.* **2012**, *134*, 9812-9819.
- (49) Slanac, D. A.; Lie, A.; Paulson, J. A.; Stevenson, K. J.; Johnston, K. P. Bifunctional Catalysts for Alkaline Oxygen Reduction Reaction Via Promotion of Ligand and Ensemble Effects at Ag/MnO_x Nanodomains. *J. Phys. Chem. C* **2012**, *116*, 11032-11039.
- (50) Wang, X. Q.; Lee, J. S.; Zhu, Q.; Liu, J.; Wang, Y.; Dai, S. Ammonia-Treated Ordered Mesoporous Carbons as Catalytic Materials for Oxygen Reduction Reaction. *Chem. Mater.* **2010**, *22*, 2178-2180.

Chapter 3: Tuning the Electrocatalytic Activity of Perovskites Through Active Site Variation and Support Interactions²

3.1 INTRODUCTION

The oxidation and reduction of oxygen are crucial chemical reactions in large-scale hydrogen production via water electrolysis, the generation of chlorine gas in the chlor-alkali process, and for bifunctional air electrodes in rechargeable metal-air batteries such as Zn-air. The oxygen evolution reaction (OER) and oxygen reduction reaction (ORR) are multistep four electron reactions that proceed via different intermediates and mechanistic routes which are highly dependent on the catalyst and electrolyte.¹⁻⁷ Alkaline electrolytes have received much attention recently due to facile oxygen evolution and reduction kinetics with earth abundant nonprecious metal oxide catalysts, as alternatives to Pt, IrO₂ and RuO₂.^{7,8} Bifunctionality, whereby one electrode material is capable of catalyzing both the OER as well as the ORR, is also a desirable goal for regenerative or rechargeable systems.⁸⁻¹⁰

Recently, ABO₃-type oxides known as perovskites, where A is commonly a rare-earth or alkali element and B commonly a transition metal, have attracted much attention due to their reported high specific catalytic activity ($\mu\text{A}/\text{cm}^2$) towards the OER and ORR in alkaline conditions.¹¹⁻¹³ However, perovskites typically display low mass activities (mA/mg) due to low surface areas ($< 4 \text{ m}^2/\text{g}$) and/or uncontrolled phase impurities. In contrast, a nanostructured, phase pure LaNiO₃ with a moderate surface area of $11 \text{ m}^2/\text{g}$ and supported on nitrogen doped carbon (NC) was shown be nearly three times as active as 6 nm IrO₂ towards the OER, despite having nearly 7 times lower surface area.¹¹ Thus the development of higher surface area, phase pure perovskites displaying high mass

²Large parts of this chapter have been published as Hardin WG, Mefford JT, Slanac DA, Patel BB, Wang X, Dai S, *et al.* Tuning the Electrocatalytic Activity of Perovskites through Active Site Variation and Support Interactions. *Chem Mater* 2014, **26**(11): 3368-3376.

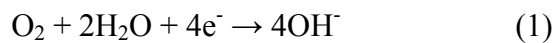
activities is crucial towards identifying replacements for precious metals and their oxides as catalysts.

The perovskite structure encompasses a wide array of materials with differing physical, chemical, optical, and electronic properties. In perovskites, the metal (or B-site) atom is in octahedral coordination with six oxygen ligands. This splits the degeneracy of the valence d -band into sigma bonding and anti-bonding (e_g) levels and pi bonding and anti-bonding (t_{2g}) levels. When the B-site atom lies on the surface {100} plane, the symmetry of the BO_6 octahedral unit is broken, and the energy levels are further discretized. It is this complex and tunable (via atomic replacements) energetic landscape that makes the perovskite family a compelling system to study for catalysis. Indeed, it has been observed that for some perovskites their specific activities exceed that of precious metals.

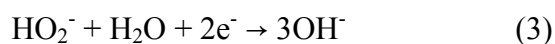
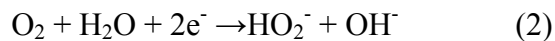
OER and ORR studies with perovskites were first reported during the 1970s, and their activity was described in terms of surface and bulk electronic properties. The active sites are believed to be the transition metal (B site) atoms, and much attention recently has been focused on the e_g orbital filling of the transition metal B-site as the activity descriptor.^{3,13} For the OER, an ideal of e_g just above ~ 1 has been proposed, as observed in materials such as $Ba_{0.5}Sr_{0.5}Co_{0.8}Fe_{0.2}O_3$ (BSCF). For the ORR, an ideal e_g just below 1 was proposed, with perovskites such as $LaNiO_3$, $LaMnO_3$ and $LaCoO_3$ identified as the most active.¹² For both reactions, it was hypothesized that too little e_g filling promotes overly-strong oxygen binding, whereby intermediates do not desorb sufficiently. Conversely, too great an e_g filling is speculated to inhibit oxygen activation and involve weak binding of intermediates. Alternatively, it has been suggested that the total number of valence electrons is the critical parameter (activity descriptor) for both the OER and ORR. DFT calculations suggest that that the adsorption strength of intermediates

monotonically increase as the number of outer B-site valence electrons increases across row 4 in the periodic table (with the exception of Sc).¹⁴ Following Sabatier's principle, the most active catalysts should facilitate the activation of O₂ and OH⁻, but it should not be so energetically favorable as to effectively passivate the surface. Similar trends were found when dissociation chemisorption and transition state energies were computed by DFT for diatomic oxygen on LaBO₃ perovskites.¹⁵ For the ORR in solid oxide fuel cells (O_{2(g)} + 4e⁻ → 2O²⁻), the oxygen p-band centers were computed for a range of perovskites and it was shown to linearly scale with experimentally observed ORR activity.¹⁶ Additionally, the oxygen p-band centers for LaBO₃ were found to be well correlated to the rate of surface oxygen exchange and oxygen vacancy formation, two often neglected parameters in the discussion of ambient temperature OER and ORR results on perovskites. The identification of a single physicochemical descriptor that captures all perovskites' catalytic affinity towards the OER and ORR is desirable, but clearly represents a great challenge due to the varying nature of different perovskite systems.

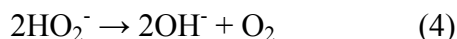
To facilitate a better understanding of the OER and ORR mechanisms on a series of LaBO₃ perovskites, we sought to introduce peroxide disproportionation functionality through the use of a nitrogen doped carbon support (or, in the case of LaNiO₃, by selective doping with Fe). Peroxide disproportionation was chosen because it is a crucial chemical intermediate in both the OER and ORR. For instance, ORR in alkaline media proceeds via one of two ways: by a direct four-electron reduction:



or proceeding in a stepwise fashion, in a 2-by-2 electron pathway:



in which the reduction of the hydroperoxide intermediate (Eqn. 3) is often identified as a rate limiting step in the ORR.^{1,7,17} Carbons lacking pyridinic nitrogen functionality are either limited to the first 2e⁻ reduction of O₂ (Eqn. 2) or a two successive two-electron processes (Eqns. 2 & 3),^{5,18} while carbons containing pyridinic nitrogen are able to chemically disproportionate the HO₂⁻ intermediate via:



Catalyst supports, such as nitrogen-doped carbon, can be paired with electrocatalysts that are able to catalyze the initial 2e⁻ reduction of O₂ (Eqn. 2), but are kinetically limited by Eqn. 3. When combined with a support or co-catalyst that disproportionates the hydroperoxide intermediate, a pseudo four electron ORR pathway is enabled that utilizes four electrons per oxygen molecule, but bypasses the kinetically slow rate limiting step, Eqn. 3.^{5,18} In contrast, the role of nitrogen doped carbon in the OER is not well understood, despite its frequent use.^{11,19} Support functionality has been practically observed to complement perovskite catalysts, as seen recently for the ORR and OER.^{11,20} Therefore, to maximize the catalytic ability of perovskite oxides, it is necessary to understand which catalysts benefit from the addition of functionality such as peroxide disproportionation.

The identification of rate limiting steps requires an understanding of the catalytic pathway through which each perovskite proceeds. While previous studies of perovskite electrocatalysts have focused on electronic and chemical descriptors to identify OER and ORR activity trends,^{3,13} the role of lattice oxygen and secondary chemical reactions (i.e. peroxide disproportionation) in the identification of activity trends for perovskites is relatively unexplored. The utilization of oxygen originating in the lattice of metal oxides is a common phenomenon in gas phase catalytic reactions.²¹ For the OER, isotope labeling studies have shown that anodically generated O₂ is partially from lattice oxygen

in IrO_2 , RuO_2 , and Li-NiO_2 and is proposed for LaNiO_3 .^{[11,22-26](#)} Lattice oxygen participating in the formation of O_2 is not expected for all catalysts, necessitating the case-by-case investigation of pathways. This complicates the determination of a single guiding parameter for OER catalyst. Furthermore, the role of catalyst support is multifaceted. Many perovskites are semiconducting at room temperature, or have metal-like conductivity that is still several orders of magnitude lower than metallic conductors such as Ag or Cu. To improve the effective conductivity of perovskites, they are often mixed with carbons.^{[11,27-30](#)}

To aid the investigation of different transition metals in lanthanum-based LaBO_3 perovskite electrocatalysts, we have developed a general synthetic approach to form phase pure perovskite materials with comparable surface areas and morphologies. We have previously utilized this method to synthesize phase pure LaNiO_3 and LaMnO_3 with similar dimensions and morphology.^{[11,31](#)} Importantly, the dissimilar rates of hydrolysis are minimized and adequate elemental intermixing is promoted by burst nucleation in a high pH environment which is essential for compositional and morphological control. This current study is now extended to a series of LaBO_3 perovskites ($\text{B} = \text{Ni}, \text{Ni}_{0.75}\text{Fe}_{0.25}, \text{Co}, \text{Mn}$), allowing for the systematic investigation of the OER and ORR through thin film rotating disk electrochemistry (RDE) methods. This approach enables the electrochemical interrogation of the perovskite catalysts, free from confounding factors such as phase impurities or surface morphology, and removes the need for the normalization of current with respect to electron microscope estimated surface areas, both of which are known sources of error in the measuring and analysis of electrocatalytic activity trends.^{[13,28](#)} Additionally, having a common baseline of phase purity, surface area and morphology allows for the probing of support interactions, including the role of functionalized or non-functionalized carbon and their contributions to the ORR or OER.

By carefully selecting the functional group, such that it selectively interacts with a chemical intermediate in the OER and ORR, it is then possible to see how each LaBO_3 catalyst responds to the perturbation of intermediates via the support functionalization. Additionally, new catalytic functionality may be imparted to the LaBO_3 electrocatalysts by selective doping of the transition metal site, B, such that similar perturbations in the OER and ORR occur, as by support functionalization. Such an approach enables an investigation of surface-specific mechanisms and rate determining steps.

Furthermore, we will show that these catalysts possess OER and ORR bifunctionality on par or better than precious metals and their oxides such as Pt, Ir, IrO_2 and Ag. We demonstrate that among a series of perovskite electrocatalysts having the same nominal e_g filling of ~ 1 , their respective OER and ORR rate determining steps differ, strongly suggesting that this is a poor activity descriptor for describing the OER and ORR activity of perovskites. Rather, the activity appears to trend with the formation and disproportionation of the hydroperoxide intermediate in both OER and ORR. .

3.2 EXPERIMENTAL

All chemicals were used as received. Anhydrous ethanol and 5 wt % Nafion solution in lower alcohols were purchased from Sigma-Aldrich. Lanthanum(III) nitrate hexahydrate (99.999%), nickel(II) nitrate hexahydrate (99%), iron(III) nitrate nonahydrate (99.99%), manganese(II) nitrate tetrahydrate (99.999%), cobalt(II) nitrate hexahydrate (98+%), strontium(II) nitrate (99+%), barium(II) nitrate (99+%), tetrapropylammonium bromide (TPAB, 98%), tetramethylammonium hydroxide pentahydrate (TMAH, 99%), 2-propanol and potassium hydroxide were obtained from Fisher Scientific, and ethanol (Absolute 200 proof) from Aaper alcohol. Millipore high purity water (18 M Ω) was used. Oxygen (research grade, 99.999% purity) and argon

(research grade, 99.999% purity) were obtained from Praxair. Mesoporous nitrogen doped carbon (NC) and activated microwave exfoliated graphene oxide (G) were prepared as reported elsewhere.^{32,33}

3.2.1 Catalyst Synthesis

Particle Synthesis. Amorphous particles composed of constituent hydroxides (La, Ni, Co etc) were prepared by slowly dripping (~2 mL/min) an aqueous metal nitrate solution into concentrated base containing dissolved TPAB (‘reverse phase’ coprecipitation), as reported previously.¹¹ Stoichiometrically correct amounts of metal and rare earth nitrates were dissolved under stirring in 50 mL of DI water, such that the total metal and rare earth concentration was 9.9 mM. Separately, an equimolar amount of TPAB relative to nitrates was dissolved into 200 mL of 1 wt% TMAH (pH ~14) under vigorous stirring. The nitrate solution was slowly dripped into the stirred base. The solution was left to stir until hydrolysis was complete, and was then collected by centrifugation and washed with DI water.

Particle Harvesting and Crystallization. The washed hydroxide gel was dispersed in DI water through probe sonication. This solution was then rapidly frozen using a thin film freezing (TFF) apparatus, as described elsewhere.³⁴ Briefly, the particle solution was slowly pipetted (~3 mL/min) onto a rotating drum, whereupon it rapidly froze and was scraped by the plate into the dish. Lyophilization was performed at -20°C at a fixed pressure of ~50 mTorr for 20 hours to remove all traces of water. All perovskite precursor powders were calcined at 700°C for 4 hours under flowing dehumidified. Following calcination, all particles were washed with ethanol and filtered to obtain the final perovskite catalyst. All catalysts, unless otherwise noted, were loaded to 30 wt% by

mass of perovskite on NC or G carbon by mixing with ball milling for 3 minutes using a Wig-L-Bug.

3.2.2 Physical Characterization

Dynamic light scattering (DLS). The hydrodynamic diameter (D_{Hs}) of as-synthesized hydrolysis particles was measured with a Brookhaven ZetaPALS instrument with the ZetaPlus option. Scattered light was collected with a 90° avalanche photodiode detector and all data were fit with the CONTIN routine. The diameter of as-synthesized metal hydroxide particles were measured at a concentration of ~1 mg/mL in DI water. All measurements were made over a period of 3 min and repeated in triplicate.

X-ray Diffraction (XRD). Catalyst structure was probed by X-ray diffraction using a Rigaku R-Axis Spider Diffractometer at 298 K in ambient conditions, utilizing Cu K α radiation (1.54 Å wavelength) operating at 40 kV and 40 mA. For all tests, bare perovskite powder was suspended within a 0.5 mm nylon loop rotating at 10° per second while the image plate detector was exposed for 10 minutes. Radial scattering data was integrated over 20 - 90° 2 θ , and analyzed using JADE software (Molecular Diffraction Inc.)

Surface Area Analysis. Nitrogen sorption analysis was performed on a Quantachrome Instruments NOVA 2000 high-speed surface area BET analyzer at a temperature of 77 K. Prior to measurements, the samples were degassed in vacuum for a minimum of 12 hours at room temperature. The specific surface area was calculated using the BET method from the nitrogen adsorption data in the relative pressure range (P/P_0) of 0.05 to 0.30

Electron Microscopy. Scanning (transmission) electron microscopy (SEM/STEM) was performed with a Hitachi S-5500 using a 30 kV accelerating voltage

and a probe current of 20 μA . The bare perovskite powder was deposited from a dilute ethanol suspension onto a 300 mesh copper grid coated with lacey carbon or Formvar (Electron Microscopy Sciences).

3.2.3 Electrochemical Characterization

Catalyst inks were prepared by adding 1 mL of a NaOH neutralized 0.05 wt% Nafion solution²⁹ to 1 mg of catalyst powder and bath sonicated for 30 minutes. A volume of ink (10 μL) was drop cast onto a clean 5 mm (0.196 cm^2 , Pine Instruments) glassy carbon (GC) electrodes and dried at ambient conditions. The GC electrodes were cleaned prior to drop casting by sonication in a 1:1 DI water:ethanol solution. The GC electrodes were then polished using 0.05 μm alumina powder, sonicated in a fresh DI water:ethanol solution, and dried in ambient air. All electrochemical tests were performed on GC electrodes prepared by this method, obtaining a composite catalyst loading of 51 $\mu\text{g}/\text{cm}^2$ (15.3 $\mu\text{g}_{\text{perovskite}}/\text{cm}^2$ for carbon supported catalysts). Electrochemical testing was performed on either a CH Instruments CHI832a or a Metrohm Autolab PGSTAT302N potentiostat, both equipped with high speed rotators from Pine Instruments. All testing was done at room temperature in 0.1 M KOH (measured pH \approx 12.6). The current interrupt and positive feedback methods were used to determine electrolyte resistance (50 Ω) and all data was iR compensated after testing. Each measurement was performed in a standard 3 electrode cell using a Hg/HgO (1 M KOH) reference electrode, a Pt wire counter electrode, and a film of catalyst ink on GC as the working electrode. All potentials are reported versus the regular hydrogen electrode (RHE), which is +0.843 V vs. Hg/HgO (Hg/HgO (1 M KOH) + 0.1 V) = NHE; $\text{NHE} + 0.059 \cdot \text{pH} = \text{RHE}$).

Quantification of Oxygen Reduction Activities. The electrolyte was saturated with oxygen by bubbling for a minimum of 10 minutes. ORR activity measurements were

taken by rotating the electrode at 1600 rpm and performing a linear sweep from 1.043 V to 0.243 V RHE at 5 mV/s. Kinetic currents were used to evaluate mass activities for the ORR and were taken at 0.693 V RHE from the polarization curves. The kinetic ORR current was calculated according to the equation: $i^{-1} = i_d^{-1} + i_k^{-1}$. Data reported herein are the average mass activity taken from cathodic scans of multiple electrodes.

Quantification of Oxygen Evolution Activities. All OER testing was performed on a new electrode which had not undergone previous testing. It should be noted that kinetic OER currents could not be calculated due to the lack of a well-defined diffusion limited regime as the result of interference from the oxygen bubbles and the degradation of the carbon support at anodic potentials. Cyclic scans were performed from 0.9 V to 1.943 V at 10 mV/s with a rotation rate of 1600 rpm in O₂ saturated 0.1 M KOH. The current at 1.56 V was selected from the polarization curves to compare the OER activities to values reported in literature. Note that at potentials above 1.6 V in oxygen saturated media, visible oxygen bubble formation on the electrode surface likely interfered with the ability to accurately measure the activity. Data reported herein is the average mass activity taken from anodic scans of multiple electrodes.

3.3 RESULTS AND DISCUSSION

LaNiO₃, LaNi_{0.75}Fe_{0.25}O₃, LaCoO₃, and LaMnO₃ were synthesized by the calcination of amorphous mixed metal hydroxide precursors that had undergone rapid freeze drying, as shown in Figure 3.1a-d.¹¹ The formation of amorphous nanoparticle precursors was enabled by the rapid, simultaneous hydrolysis of metal and rare earth nitrates, resulting in a dispersion of amorphous hydroxide nanoparticles. In this reverse phase arrested growth coprecipitation scheme, the formation of nanoparticles was facilitated by the use of tetrapropylammonium bromide (TPAB), of which the cation

provided electrostatic and steric stabilization. In addition to providing colloidal stabilization, particle growth was also arrested which enabled formation of stable dispersions of 20 - 30 nm particles, as measured by DLS and summarized in Table C.1 (Appendix C). The dispersions, when rapidly freeze dried, resulted in a highly open, low fractal dimension nanoparticulate powders.³⁴

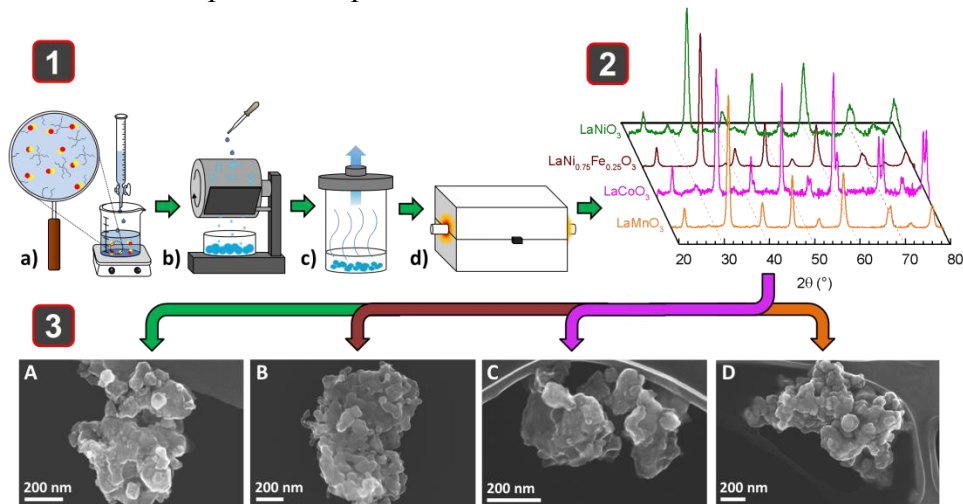


Figure 3.1: Generalized synthetic route to form phase pure nanostructured perovskites

1a) arrested growth coprecipitation of hydroxide nanoparticles, 1b) thin film freezing of metal hydroxides sols, 1c) lyophilization of frozen sol powder and 1d) calcination of metal hydroxide powder. 2) X-ray diffraction patterns shown phase pure LaNiO_3 , $\text{LaNi}_{0.75}\text{Fe}_{0.25}\text{O}_3$, LaCoO_3 and LaMnO_3 . 3A-D: scanning electron micrographs of 3A) LaNiO_3 , 3B) $\text{LaNi}_{0.75}\text{Fe}_{0.25}\text{O}_3$, 3C) LaCoO_3 and 3D) LaMnO_3 .

Figure 3.1.2 shows the XRD patterns resulting from the calcination of LaNiO_3 , $\text{LaNi}_{0.75}\text{Fe}_{0.25}\text{O}_3$, LaCoO_3 , and LaMnO_3 precursor powders at 700°C . All perovskites show similar phase purity, characteristic of the adequate intermixing of elements during hydrolysis. LaNiO_3 was indexed to the stoichiometric rhombohedral (R-3c) phase, $\text{LaNi}_{0.75}\text{Fe}_{0.25}\text{O}_3$ was found to most closely match that of rhombohedral $\text{LaNi}_{0.6}\text{Fe}_{0.4}\text{O}_3$, LaCoO_3 was assigned to the stoichiometric rhombohedral phase, and LaMnO_3 was

indexed to the orthorhombic (Pnma) oxygen excess $\text{La}_{0.97}\text{Mn}_{0.97}\text{O}_3$ phase. Complete phase assignments, including PDF#, are available in Appendix C. Scherrer analysis was also performed on the most intense diffraction peak due to a single crystalline plane, {024} for all systems, to determine crystallite sizes. For LaNiO_3 , $\text{LaNi}_{0.75}\text{Fe}_{0.25}\text{O}_3$, LaCoO_3 , and LaMnO_3 crystallite sizes of 12 nm, 14 nm, 20 nm and 15 nm were calculated, respectively. Due to all the perovskites being formed by the calcination of 20 – 30 nm hydroxide precursors, this size range is expected given the colloidal precursor sizes.

As crystallite size is not indicative of particle size or surface area, Brunauer-Emmett-Teller (BET) theory was used in conjunction with nitrogen sorption experiments to determine the surface area of each perovskite catalysts, and it was found that all perovskites have similar surface areas of 11 to 14 m^2/g . Figure 3.1.3A-D shows representative SEM images for LaNiO_3 , $\text{LaNi}_{0.75}\text{Fe}_{0.25}\text{O}_3$, LaCoO_3 , and LaMnO_3 , in which the nanoparticulate processing history of the catalyst can clearly be seen. The calcined perovskites form a network of moderately sintered 20 to 50 nm primary particles. Both 2D sheet-like and 3D globular morphologies are observed, with no clear morphological distinction between the different perovskite systems. All physical characterization (DLS, XRD, BET) results are summarized and provided in Table C.1 located in Appendix C. The general synthesis produces high phase purity, crystallinity, surface areas and morphologies that are essentially invariant among the different perovskite catalysts reported herein. This enables the systematic investigation of each perovskite as OER and ORR electrocatalysts. To provide enhanced electrical conductivity and introduce new chemical functionality, two high surface-area carbon supports were chosen to support the perovskites. Activated microwave exfoliated, mildly oxidized graphene (G) was selected as the unfunctionalized support³³ and nitrogen-doped

mesoporous carbon (NC) was chosen for the functionalized support, due to the high relative proportion of pyridinic nitrogen incorporated into the carbon (XPS spectra of both supports available in Appendix C, Figure C.1).³²

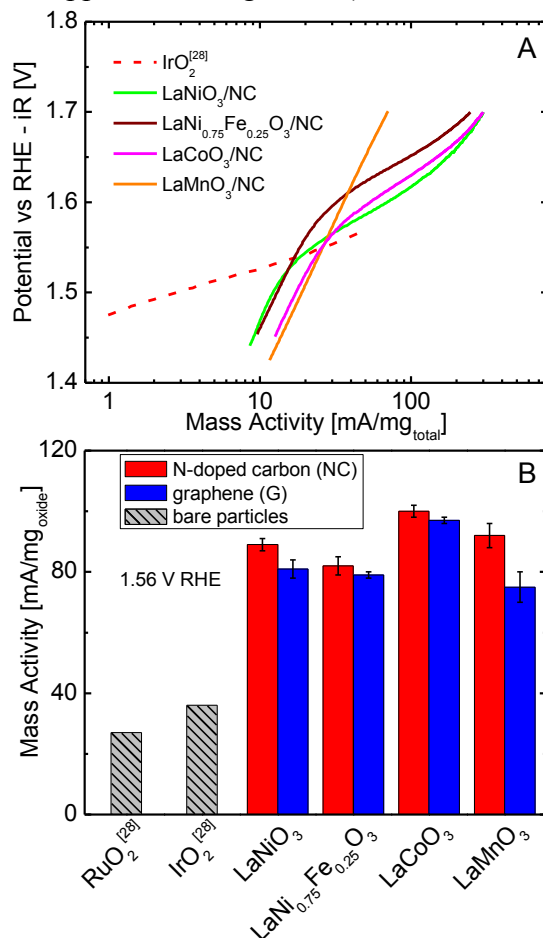


Figure 3.2: Electrochemical OER testing of perovskites

Tafel plot and B) catalyst mass activities for the oxygen evolution reaction. All data were taken in O₂ saturated 0.1 M KOH at 1600 rpm and 10 mV/s.

To determine the effect of perovskite transition metal species and the impact of a nitrogen functionalized carbon support, OER mass activities were quantified for LaNiO₃,

LaNi_{0.75}Fe_{0.25}O₃, LaCoO₃, and LaMnO₃ by measuring polarization curves in O₂ saturated 0.1 M KOH at 1600 rpm and are presented in Figure 3.2. Each perovskite was physically mixed (30 wt% perovskite) with either nitrogen doped carbon (NC, 1080 m²/g) or activated microwave exfoliated graphene oxide (G, ~2500 m²/g). The inclusion of a carbon support is necessary due to perovskite conductivity being one or more orders of magnitude less than metals, depending on the system. Without the use of carbon (or another equally conductive support), electrical contact with the electrode is by way of point contacts and little to no catalytic activity is observed.^{11,20,27} Additionally, negligible hysteresis is observed for the catalysts,¹¹ such that current contributions due to carbon oxidation are negligent. The potential of 1.56 V RHE-iR was selected for determination of mass activities, which enables comparison with recent studies.¹¹⁻¹³ As seen in Figure 3.2B, perovskites supported on nitrogen-doped carbon achieved 3 to 23% greater mass activity than those supported on G. Within the set of perovskites supported on NC, LaCoO₃ displayed the highest mass activity (100 mA/mg_{oxide}), followed by LaMnO₃ (92 mA/mg_{oxide}), LaNiO₃ (89 mA/mg_{oxide}) and LaNi_{0.75}Fe_{0.25}O₃ (82 mA/mg_{oxide}). A similar trend was observed for perovskites supported on G, in which LaCoO₃ was the most active (97 mA/mg_{oxide}), followed by LaNiO₃ (81 mA/mg_{oxide}), LaNi_{0.75}Fe_{0.25}O₃ (79 mA/mg_{oxide}) and LaMnO₃ (75 mA/mg_{oxide}). Remarkably, each perovskite was more active than IrO₂ and RuO₂ on a mass basis, regardless of the carbon support, and LaCoO₃/NC was 2.8 and 3.7 times as active as IrO₂ and RuO₂, respectively.³⁵ IrO₂ and RuO₂ were chosen for comparison due to their widespread use, but other, more active catalysts such as electrodeposited Co₃O₄ and iron doped nickel oxyhydroxide thin films have also been identified.^{36,37} The Tafel slopes for LaNiO₃, LaNi_{0.75}Fe_{0.25}O₃, LaCoO₃ and LaMnO₃ supported on NC were calculated and found to be 42 mV/dec, 44 mV/dec, 51 mV/dec and 145 mV/dec, respectively. Noting that reported tafel slope values for these systems

vary widely in the literature, there is general agreement with the values published by Bockris and Otagawa.³

Clearly, catalytic activity increases when using a nitrogen-doped carbon support with a high proportion of pyridinic functionality, but the mechanism responsible for the observed increase has not previously been investigated for the OER. Presumably the ability of a support to disproportionate hydroperoxide (HOO^-), an OER intermediate, can influence the activity.

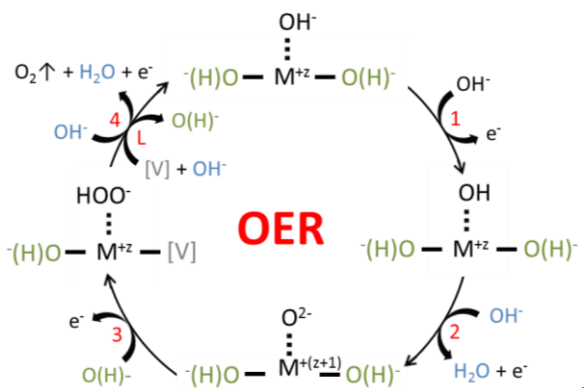


Figure 3.3: Oxygen evolution cycle utilizing lattice oxygen

Proposed oxygen evolution cycle, wherein lattice (hydr)oxide is utilized in the formation of the O-O bond in HOO^- .

Figure 3.2A shows a Tafel plot containing the total mass activity ($\text{mA}/\text{mg}_{\text{total}}$) of each NC supported perovskite to that of highly active 6 nm IrO_2 . For all perovskites studied, with the exception of LaMnO_3 , there is a sharp change in the slope of data, indicating a changing mechanism during water oxidation. LaMnO_3 is also the catalyst that benefits the most from the NC support, gaining 23% more mass activity. Conversely, LaCoO_3 benefits the least from the NC support (3%). These disparate differences can be understood by considering the role of chemical steps in the OER cycle, particularly each

catalyst's ability to decompose peroxide. Figure 3.3 shows a generalized version of the OER cycle,¹¹ in which lattice (hydr)oxide can participate in the formation of the O-O bond in OOH^- , commonly identified as the rate determining OER step.^{2,4,38,39} For catalysts where Step 4 in Figure 3.3 proceeds sluggishly, chemical disproportionation of the HOO^- intermediate (Eqn. 4) will still result in the formation of O_2 , circumventing Step 4. This chemical functionality is an intrinsic property of perovskites, and can also be imparted through support functionalization, as previously discussed. LaMnO_3 is a poor peroxide disproportionation catalyst, which is likely the reason for its anomalous Tafel slope, and the 23% increase in current observed when it is supported on NC.⁴⁰ This hypothesis is further confirmed by the results for LaCoO_3 and $\text{LaNi}_{0.75}\text{Fe}_{0.25}\text{O}_3$,^{41,42} for which the difference in mass activity between NC and G supports are the lowest, at 3% and 4%, respectively. The rate limiting OER step for Co oxides has been identified as either Step 1 or Step 3.² Therefore, the addition of peroxide disproportionation functionality has negligible effect. $\text{LaNi}_{0.75}\text{Fe}_{0.25}\text{O}_3$ is a highly active peroxide disproportionation catalyst, so in an argument similar to that for LaCoO_3 , the additional functionality provided by the NC support has little effect.⁴² The lower absolute mass activity of $\text{LaNi}_{0.75}\text{Fe}_{0.25}\text{O}_3$ is rationalized by the lower surface area of the catalyst, and the lower amount of valence electrons for $\text{Fe}^{(\text{IV})}$ as compared to $\text{Ni}^{(\text{III})}$ (4 vs. 7). This is crucial for several reasons. As electron density decreases, so too does the adsorption energy for all intermediates.¹⁴ Intermediates that are too weakly bound will diffuse away or participate in unwanted side reactions. $\text{Fe}^{(\text{IV})}$ also must now be oxidized during the OER (Figure 3.3, Step 2), but has a higher energetic barrier to overcome than $\text{Ni}^{(\text{III})}$. It also should be noted that there is a decrease in electronic conductivity (as compared to LaNiO_3) resulting from the substitution of Fe for Ni.⁴² The role of nitrogen-doped carbon and peroxide disproportionation will be revisited later in this article, but these results

clearly show the importance of understanding material-specific catalytic pathways and how addition of chemical functionalities in graphitic carbon can result in significant (23%) improvements in catalytic activity.

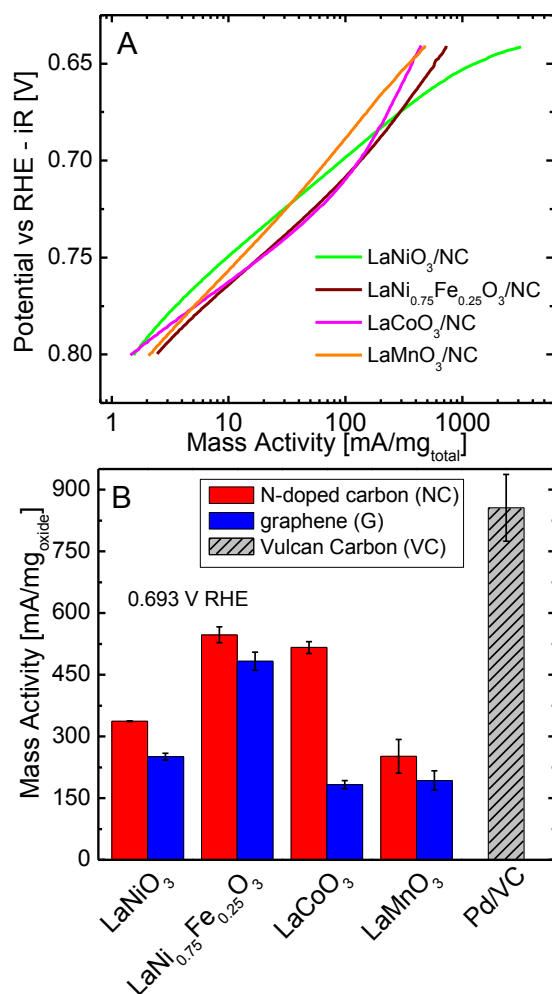


Figure 3.4: Electrochem ORR characterization of perovskites

A) Tafel plots and B) catalyst mass activities for the oxygen reduction reaction. All data was taken in O₂ saturated 0.1 M KOH at 1600 rpm and 5 mV/s. The mass activity of a commercial 20 wt% Pd catalyst supported on XC72 Vulcan Carbon (VC) is shown for comparison.

The influence of carbon support functionality on LaNiO_3 , $\text{LaNi}_{0.75}\text{Fe}_{0.25}\text{O}_3$, LaCoO_3 , and LaMnO_3 catalysis of the ORR was examined by performing RDE experiments in O_2 saturated 0.1 M KOH at 1600 rpm and 5 mV/s (polarization curves, including those of NC and G, are available in Appendix C). Kinetic currents were calculated at 0.693 V, such that all currents were taken below the half-wave potential of each polarization curve, with the exception of Pd/VC.⁴³ Kinetic currents that have been normalized with respect to the perovskite mass loading are presented in Figure 3.4B. Of the catalyst supported on nitrogen-doped carbon, $\text{LaNi}_{0.75}\text{Fe}_{0.25}\text{O}_3/\text{NC}$ is the most active of the series (547 mA/mg_{oxide}), followed by LaCoO_3/NC (516 mA/mg_{oxide}), LaNiO_3/NC (337 mA/mg_{oxide}) and LaMnO_3/NC (252 mA/mg_{oxide}). Also, it is remarkable to note that $\text{LaNi}_{0.75}\text{Fe}_{0.25}\text{O}_3/\text{NC}$ possesses 60% of the mass activity of commercial Pd supported on XC72 Vulcan Carbon (Pd/VC), a leading precious metal catalyst. When examining the perovskite catalysts supported on G, the activity of each decreased, similar to the results for the OER. $\text{LaNi}_{0.75}\text{Fe}_{0.25}\text{O}_3$ remained the most active (483 mA/mg_{oxide}) followed by LaNiO_3 (251 mA/mg_{oxide}), LaMnO_3 (193 mA/mg_{oxide}) and LaCoO_3 (121 mA/mg_{oxide}). The mass activity of the bare NC and G supports at 0.693 V are 17 and 43 mA/mg_{total}, respectively. These trends ($\text{LaNi}_{0.75}\text{Fe}_{0.25}\text{O}_3$ will be covered later), devoid of any additional support functionality, are the most telling. Using e_g filling as a descriptor, one would not expect such different results. For the ORR in solid oxide fuel cells, activity has been correlated to the oxygen p-band relative to the transition metal, strength of metal-adsorbate interaction, surface oxygen exchange and the energetic barrier to vacancy formation.^{14,16,44} These results, in which $\text{Ni} > \text{Co} \sim \text{Mn}$, are also the same trend for the ease of formation of surface oxygen vacancies.⁴⁴ To better understand why $\text{LaNi}_{0.75}\text{Fe}_{0.25}\text{O}_3$ is so active, and hopefully achieve a greater understanding of each

catalyst's response to the peroxide disproportionation functionality, we focused on the ORR pathways and the effect of hydroperoxide specifically.

The use of the NC support has been shown to improve the activity catalysts for both the ORR and OER. Furthermore, previous work has shown that the alkaline OER on perovskites proceeds via the hydroperoxide intermediate, HOO^- .^{3,13,28} We hypothesize that the intrinsic ability for each perovskite to chemically disproportionate peroxide is a key step in understanding the observed activity trends. To probe the ability of each catalyst to disproportionate peroxide, argon was vigorously bubbled through 0.1 M KOH such that all oxygen was flushed from the system. After removal of oxygen from the electrolyte was complete, an argon blanket was placed over top and 5 mM of H_2O_2 was injected. Immediately following injection, cyclic voltammetry (CV) was performed over the same potential window as used in the ORR polarization tests. In these anoxic conditions, any oxygen reduction wave that arises must be from oxygen that is produced through peroxide disproportionation. Figure 3.5 shows the results of these tests, in which clear oxygen reduction waves can be seen for all catalysts, despite the *absence* of oxygen prior to peroxide injection. The bare NC carbon in Figure 3.5A shows a sharp oxygen reduction peak at ~ 0.7 V, while the graphene oxide (Figure 3.5B) has a much broader peak centered at ~ 0.685 V. Despite the qualitative nature of this analysis, the trends shown in Figure 3.5A,B follow the general trend of Figure 3.4B.

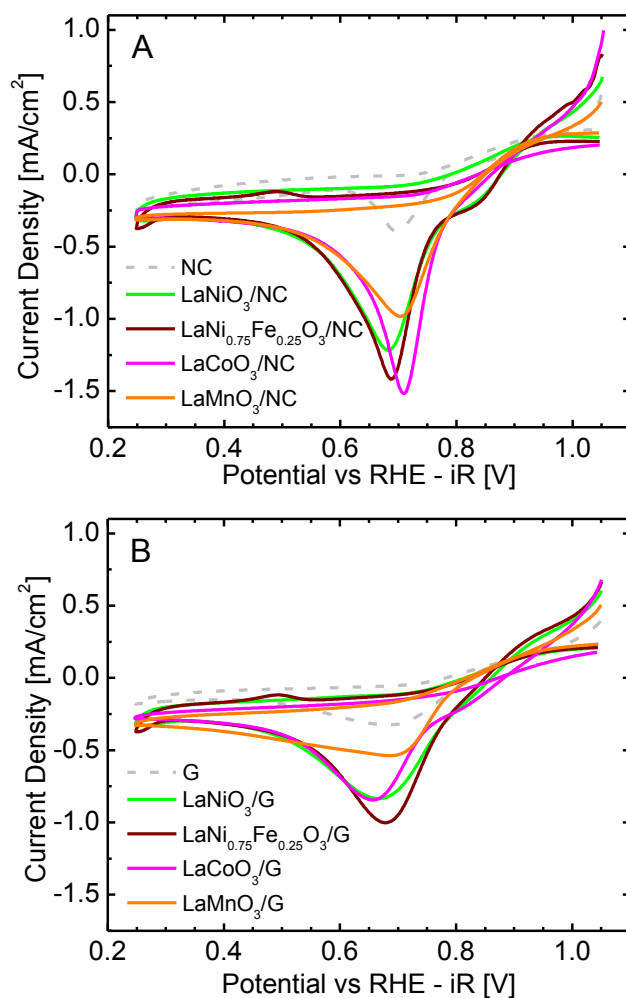


Figure 3.5: Oxygen reduction waves observed by cyclic voltammetry at 5 mV/s in deoxygenated 0.1 M KOH after injection of 5 mM H_2O_2 .

A) Bare NC and NC supported perovskite catalysts and B) bare G and G supported perovskite catalysts.

For catalysts supported on NC, $\text{LaNi}_{0.75}\text{Fe}_{0.25}\text{O}_3$ is nearly equivalent to LaCoO_3 , followed by LaNiO_3 and LaMnO_3 . For catalysts supported on G, $\text{LaNi}_{0.75}\text{Fe}_{0.25}\text{O}_3$ is producing and reducing the most oxygen, followed by LaNiO_3 , LaCoO_3 and LaMnO_3 . Furthermore, the large discrepancy amongst LaCoO_3 supported on G and NC in Figure

3.4B explained by examining Figure 3.5A,B. LaCoO_3/NC has a tall, sharp oxygen reduction peak, but when supported on G, the CV response flattens dramatically, resulting in the largest negative $E_{1/2}$ shift (13 mV) exhibited by any of the catalysts. All catalysts, regardless of carbon support, disproportionate peroxide. Indeed, the relative peak areas due to oxygen reduction qualitatively follow the observed activity trends, indicating that this chemical functionality could be crucial to the design of active ORR catalysts, as seen in the model $\text{LaNi}_{0.75}\text{Fe}_{0.25}\text{O}_3$ system.

We have shown that $\text{LaNi}_{0.75}\text{Fe}_{0.25}\text{O}_3$ remains highly active for the ORR on either NC or G support, despite reduced conductivity and surface area as compared to LaNiO_3 , due in part to its inherent ability to rapidly disproportionate peroxide.⁴² What then is the role of nitrogen doped carbon in the OER? This is a question that demands further study, but for nitrogen doped carbon containing a relatively high amount of pyridinic nitrogen (~65 rel. at.% as determined by XPS, Figure C.1), we believe that the lone pair of electrons on the pyridinic nitrogen functionality are also able to stabilize the perovskite catalyst during the OER, and that oxidative stability is partly responsible for the increase in activity seen for all catalysts supported on NC. To test the idea that pyridinic nitrogen contributes to oxidative stability, preliminary stability testing was done on perovskite-free NC and G carbon supports, under a constant galvanostatic discharge of 10 A/g. The potential was monitored as a function of time and is shown in Figure 6. Testing was stopped when the potential required to draw 10 A/g exceeded 1.9 V. While further testing is needed, these initial results indicate that the NC support is more stable under oxidizing conditions than the G support, having lasted more than twice as long at high current density. Other possible interactions between the pyridinic nitrogen centers and perovskite catalysts, such as a dual-site mechanism, are discussed Appendix C.

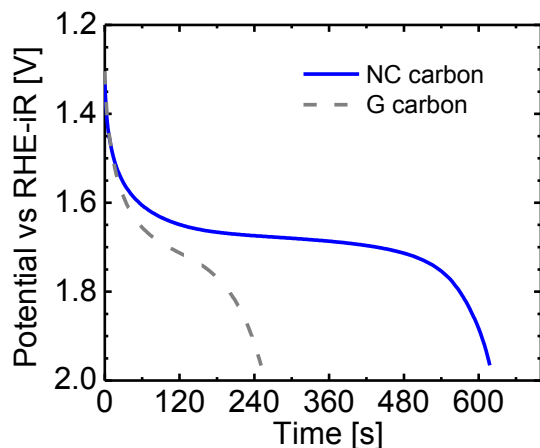


Figure 3.6: Stability Comparison with Carbon

Voltage-time trace showing the stability of the NC and G supports, drawing a constant current of 10 A/g in O₂ saturated 0.1 M KOH at 1600 rpm.

To assess the suitability of the perovskite electrocatalysts as bifunctional metal-air battery electrodes, the difference in potential between the ORR at -3 mA/cm^2 and the OER at 10 mA/cm^2 (ΔE), current densities of practical importance for electrochemical and photoelectrochemical applications, are compared below in Table 3.1 in addition to several precious metal benchmarks.⁴⁵ ΔE is simply the sum of the overpotentials for the two reactions. LaCoO₃/NC exhibits the lowest total overpotential ($\Delta E = 1.00 \text{ V}$), followed by LaNi_{0.75}Fe_{0.25}O₃ and LaNiO₃ which are 10 and 20 mV greater, respectively. LaCoO₃/NC has a lower total overpotential between reactions than both Pt ($\Delta E = 1.16 \text{ V}$) and Ru ($\Delta E = 1.01 \text{ V}$), while only 80 mV greater than Ir ($\Delta E = 0.92 \text{ V}$). Note that this comparison is not assuming ideal ORR or OER materials, simply comparing some of the most active catalysts. LaMnO₃ was omitted from this comparison due to insufficient OER current density. It should also be noted that while Pt is a highly active ORR catalyst, it

forms an inactive oxide skin at anodic potentials. The low total overpotential between both reactions for LaCoO_3/NC , $\text{LaNi}_{0.75}\text{Fe}_{0.25}\text{O}_3/\text{NC}$ and LaNiO_3/NC indicates that they are suitable for bifunctional air electrodes, but the long-term stability (durability) of each catalyst still needs to be investigated.

Table 3.1: Perovskite Catalyst Bifunctionality

Catalyst	ORR Potential (V) vs RHE @ - 3 mA/cm ²	OER Potential (V) vs RHE @ 10 mA/cm ²	ΔE (V)
LaCoO_3/NC	0.64	1.64	1.00
$\text{LaNi}_{0.75}\text{Fe}_{0.25}\text{O}_3/\text{NC}$	0.67	1.68	1.01
LaNiO_3/NC	0.64	1.66	1.02
20 wt% Ir/C ⁴⁵	0.69	1.61	0.92
20 wt% Ru/C ⁴⁵	0.61	1.62	1.01
20 wt% Pt/C ⁴⁵	0.86	2.02	1.16

Note: OER data for Ir, Pt and Ru were taken at 5 mV/s, whereas all perovskite OER data is at 10 mV/s.

3.4 CONCLUSIONS

In conclusion, a series of phase pure perovskite electrocatalysts having modest surface area ($\sim 11 \text{ m}^2/\text{g}$) have been synthesized using a robust synthetic process in which colloidal mixed metal hydroxides are formed by reverse phase arrested growth coprecipitation. Phase purity is enabled by the rapid simultaneous hydrolysis of nitrate salts, forming sols of perovskite precursor nanoparticles. When these particles are freeze dried and calcined, a series of perovskites having nearly identical morphology and

surface area are formed. These perovskite catalysts, when supported on nitrogen doped carbon or activated microwave exfoliated graphene oxide displayed high activities for both the OER and ORR, with LaCoO_3/NC having $\sim 4\times$ the OER mass activity of the precious metal oxide benchmark IrO_2 , and $\text{LaNi}_{0.75}\text{Fe}_{0.25}\text{O}_3/\text{NC}$ having comparable ORR activity as Pd/VC . This demonstrates that the high specific ($\mu\text{A}/\text{cm}^2_{\text{ox}}$) activity of perovskites can be translated into highly active and bifunctional oxygen catalysts. Through tuning of the carbon support functionalization, rate limiting steps were identified and bypassed by successful incorporation of peroxide disproportionation into the catalyst itself, which was achieved through selective doping. $\text{LaNi}_{0.75}\text{Fe}_{0.25}\text{O}_3$ exceptional ORR activity is in part rationalized by the catalyst's ability to bypass the traditional rate determining ORR step of peroxide reduction by disproportionation of HOO^- into O_2 and OH^- , enabling a pseudo four electron ORR pathway. This work attempts to look beyond the choice of bulk electrical properties or use of single catalytic descriptors such as e_g filling, while providing a catalyst-specific understanding of the importance of peroxide oxidation or reduction on perovskites during the OER and ORR. This mechanistic understanding is crucial for enabling the continued improvement of nonprecious metal water oxidation and oxygen reduction catalysis.

3.5 ADDITIONAL INFORMATION

Material summary table including XRD phase identification, DLS colloid size, BET surface area, and crystallite size. XPS of the N 1s core region of the carbon supports, and electrochemical polarization curves used to calculate mass activities are provided in Appendix C

3.6 REFERENCES

- (1) Nørskov, J. K.; Rossmeisl, J.; Logadottir, A.; Lindqvist, L.; Kitchin, J. R.; Bligaard, T.; Jonsson, H. *The Journal of Physical Chemistry B* **2004**, *108*, 17886.

- (2) Bajdich, M.; García-Mota, M.; Vojvodic, A.; Norskov, J. K.; Bell, A. T. *J Am Chem Soc* **2013**.
- (3) Bockris, J. O.; Otagawa, T. *J Phys Chem* **1983**, *87*, 2960.
- (4) Dau, H.; Limberg, C.; Reier, T.; Risch, M.; Roggan, S.; Strasser, P. *Chemcatchem* **2010**, *2*, 724.
- (5) Wiggins-Camacho, J. D.; Stevenson, K. J. *J Phys Chem C* **2011**, *115*, 20002.
- (6) Sepa, D.; Vojnovic, M.; Damjanovic, A. *Electrochim Acta* **1981**, *26*, 781.
- (7) Spendelow, J. S.; Wieckowski, A. *Phys Chem Chem Phys* **2007**, *9*, 2654.
- (8) Neburchilov, V.; Wang, H.; Martin, J. J.; Qu, W. *J Power Sources* **2010**, *195*, 1271.
- (9) Cheng, F. Y.; Chen, J. *Chem Soc Rev* **2012**, *41*, 2172.
- (10) Lee, J. S.; Kim, S. T.; Cao, R.; Choi, N. S.; Liu, M.; Lee, K. T.; Cho, J. *Adv Energy Mater* **2011**, *1*, 34.
- (11) Hardin, W. G.; Slanac, D. A.; Wang, X.; Dai, S.; Johnston, K. P.; Stevenson, K. J. *The Journal of Physical Chemistry Letters* **2013**, *4*, 1254.
- (12) Suntivich, J.; Gasteiger, H. A.; Yabuuchi, N.; Nakanishi, H.; Goodenough, J. B.; Shao-Horn, Y. *Nat Chem* **2011**, *3*, 546.
- (13) Suntivich, J.; May, K. J.; Gasteiger, H. A.; Goodenough, J. B.; Shao-Horn, Y. *Science* **2011**, *334*, 1383.
- (14) Calle-Vallejo, F.; Inoglu, N. G.; Su, H.-Y.; Martinez, J. I.; Man, I. C.; Koper, M. T. M.; Kitchin, J. R.; Rossmeisl, J. *Chemical Science* **2013**, *4*, 1245.
- (15) Vojvodic, A.; Calle-Vallejo, F.; Guo, W.; Wang, S.; Toftelund, A.; Studt, F.; Martinez, J. I.; Shen, J.; Man, I. C.; Rossmeisl, J. *The Journal of chemical physics* **2011**, *134*, 244509.
- (16) Lee, Y.-L.; Kleis, J.; Rossmeisl, J.; Shao-Horn, Y.; Morgan, D. *Energy Environ. Sci.* **2011**, *4*, 3966.
- (17) Markovic, N.; Gasteiger, H.; Ross, P. N. *J Electrochem Soc* **1997**, *144*, 1591.
- (18) Maldonado, S.; Stevenson, K. J. *J Phys Chem B* **2005**, *109*, 4707.
- (19) Liang, Y. Y.; Li, Y. G.; Wang, H. L.; Zhou, J. G.; Wang, J.; Regier, T.; Dai, H. J. *Nat Mater* **2011**, *10*, 780.
- (20) Poux, T.; Napolskiy, F.; Dintzer, T.; Kéranguéven, G.; Istomin, S. Y.; Tsirlina, G.; Antipov, E.; Savinova, E. *Catal Today* **2012**, *189*, 83.
- (21) Bielański, A. *Oxygen in catalysis*; CRC Press, 1991; Vol. 43.
- (22) Burke, L. D.; Murphy, O. J.; O'Neill, J. F.; Venkatesan, S. *J. Chem. Soc., Faraday Trans. 1* **1977**, *73*, 1659.

- (23) Fierro, S.; Nagel, T.; Baltruschat, H.; Comninellis, C. *Electrochem Commun* **2007**, *9*, 1969.
- (24) Lee, C.; Riga, A.; Yeager, E. In *Mass Transport Phenomena in Ceramics*; Gordon, R. S., Cooper, A. R., Heuer, A. H., Eds.; Plenum Press: New York, 1975, p 489.
- (25) Macounová, K.; Jirkovský, J.; Makarova, M. V.; Franc, J.; Krtíl, P. *J Solid State Electrochem* **2009**, *13*, 959.
- (26) Wohlfahrt-Mehrens, M.; Heitbaum, J. *Journal of Electroanalytical Chemistry and Interfacial Electrochemistry* **1987**, *237*, 251.
- (27) Karlsson, G. *Electrochim Acta* **1985**, *30*, 1555.
- (28) Sunarso, J.; Torriero, A. A. J.; Zhou, W.; Howlett, P. C.; Forsyth, M. *J Phys Chem C* **2012**, *116*, 5827.
- (29) Suntivich, J.; Gasteiger, H. A.; Yabuuchi, N.; Shao-Horn, Y. *J Electrochem Soc* **2010**, *157*, B1263.
- (30) Twu, J.; Gallagher, P. K. In *Properties and Applications of Perovskite-Type Oxides*; L.G. Tejuca, J. L. G. F., Ed.; Marcel Dekker, Inc.: New York, 1993.
- (31) Mefford, J. T.; Hardin, W. G.; Dai, S.; Johnston, K. P.; Stevenson, K. J. *Nat Mater* **in press**.
- (32) Wang, X. Q.; Lee, J. S.; Zhu, Q.; Liu, J.; Wang, Y.; Dai, S. *Chem Mater* **2010**, *22*, 2178.
- (33) Zhu, Y.; Murali, S.; Stoller, M. D.; Ganesh, K. J.; Cai, W.; Ferreira, P. J.; Pirkle, A.; Wallace, R. M.; Cychosz, K. A.; Thommes, M.; Su, D.; Stach, E. A.; Ruoff, R. S. *Science* **2011**, *332*, 1537.
- (34) Engstrom, J. D.; Lai, E. S.; Ludher, B. S.; Chen, B.; Milner, T. E.; Williams, R. O.; Kitto, G. B.; Johnston, K. P. *Pharm Res* **2008**, *25*, 1334.
- (35) Lee, Y.; Suntivich, J.; May, K. J.; Perry, E. E.; Shao-Horn, Y. *J Phys Chem Lett* **2012**, *3*, 399.
- (36) Koza, J. A.; He, Z.; Miller, A. S.; Switzer, J. A. *Chem Mater* **2012**, *24*, 3567.
- (37) Trotochaud, L.; Ranney, J. K.; Williams, K. N.; Boettcher, S. W. *J Am Chem Soc* **2012**, *134*, 17253.
- (38) Man, I. C.; Su, H. Y.; Calle-Vallejo, F.; Hansen, H. A.; Martinez, J. I.; Inoglu, N. G.; Kitchin, J.; Jaramillo, T. F.; Nørskov, J. K.; Rossmeisl, J. *Chemcatchem* **2011**, *3*, 1159.
- (39) Rossmeisl, J.; Qu, Z. W.; Zhu, H.; Kroes, G. J.; Nørskov, J. K. *J Electroanal Chem* **2007**, *607*, 83.
- (40) Lee, Y. N.; Lago, R. M.; Fierro, J. L. G.; González, J. *Applied Catalysis A: General* **2001**, *215*, 245.

- (41) Read, M. S.; Islam, M. S.; Watson, G. W.; King, F.; Hancock, F. E. *J Mater Chem* **2000**, *10*, 2298.
- (42) Falcon, H.; Carbonio, R.; Fierro, J. *J Catal* **2001**, *203*, 264.
- (43) Wiberg, G. K. H.; Mayrhofer, K. J. J.; Arenz, M. *Fuel Cells* **2010**, *10*, 575.
- (44) Lee, Y.-L.; Kleis, J.; Rossmeisl, J.; Morgan, D. *Physical Review B* **2009**, *80*, 224101.
- (45) Gorlin, Y.; Jaramillo, T. F. *J Am Chem Soc* **2010**, *132*, 13612.

Chapter 4: Exceptional Electrocatalytic Oxygen Evolution Via Tunable Charge Transfer Interactions in $\text{La}_{0.5}\text{Sr}_{1.5}\text{Ni}_{1-x}\text{Fe}_x\text{O}_{4+\delta}$ Ruddlesden-Popper Oxides³

4.1 INTRODUCTION

Increasing global energy demand requires greater efficiency in water electrolyzers for low cost hydrogen generation and rechargeable metal-air batteries to enable pragmatic development of these key technologies. Given that the efficiencies of these technologies are limited primarily by the sluggish kinetics of the oxygen evolution reaction (OER, $4\text{OH}^- \rightarrow \text{O}_2 + 2\text{H}_2\text{O} + 4\text{e}^-$), extensive efforts have been made to reduce the overpotential for the OER in alkaline media with advanced catalysts.¹ Whereas precious metals such as Ir and Ru are standard OER catalysts in acidic electrolytes, alkaline electrolytes enable the use of earth-abundant, non-precious metals. For example, Ni-M oxyhydroxides such as $\text{Ni}_{1-x}\text{Fe}_x\text{OOH}$ are known to be very active for the OER; however, lack of long-range order and uncontrolled electronic structure stemming from different synthetic methods² complicates elucidation of the mechanism(s) by which OER activity is improved.^{3, 4, 5} In fact, recent reports question whether Fe is part of the catalytic cycle or if Fe promotes partial charge transfer between Ni and Fe metal centers.^{2, 4, 6} Only recently has it been revealed that as much as 50% of the measured current (catalytic activity) for carbon-supported Ni-Fe oxyhydroxides is not due to the OER.⁷ Collectively, the large variations in electronic configuration and the resulting catalytic activity in these studies complicate establishment of precise structure-property correlations for Ni-Fe oxyhydroxides.^{2, 5, 8}

In contrast, perovskite oxides having the nominal formula $\text{ABO}_{3\pm\delta}$, in which A is a rare-earth or alkaline earth element and B is a transition metal, have recently been shown to promote OER catalysis through high ionic and electronic conductivities, good

³ Large parts of this chapter have been submitted to *Nature Materials* on March 31st, 2017.

structural stability, and synthetic versatility, all of which enable the development of rational catalyst design criteria.^{9, 10, 11} Importantly, the ability to substitute elements of varying valence, electronegativity, or ionic size into A and B-sites directly influences the resultant properties of these catalysts.^{1, 12} Recently, we demonstrated that highly covalent Co 3*d* – O 2*p* bonding in SrCoO_{2.7} improved OER activity via a more energetically favorable lattice oxygen mediated (LOM) reaction pathway, consistent with prior reports and theory.^{13, 14, 15} This LOM mechanism does not require the redox switching of transition metal sites, but rather utilizes lattice oxygen in the OER when the Fermi level, E_F^0 , crosses the transition metal 3*d* - O 2*p* hybridized bands. This results in ligand holes that activate lattice oxygen which may combine with chemisorbed OH to produce O₂⁻. In a separate report, SrNiO₃ was predicted to be more covalent and thus be more catalytically active than SrCoO₃.¹⁶ Unfortunately, this prediction is hard to validate experimentally as SrNiO₃ adopts a non-perovskite structure based on a hexagonal close packing of Sr and O atoms.¹⁷ In addition, it is known that the substitution of Sr into LaNiO₃ is limited to ~5-20% after which phase impurities appear, which result in poor catalytic activity.^{18, 19} To overcome this limitation, we investigate an alternative crystal structure to the perovskite-phase SrNiO₃ that promotes high OER activity but does not suffer from limited Sr solubility and can stabilize highly oxidized, covalently bound Ni.

In this report, we utilize a precise synthetic approach to explore the influence of Sr and Fe substitution on Ni-based electrocatalysts by exploiting the crystalline Ruddlesden-Popper phase to study the influence of atomic and electronic configurations that are unrealizable in other electrocatalyst systems. The Ruddlesden-Popper (RP) crystal structure is represented as A_{*n*+1}B_{*n*}O_{3*n*+1} or equivalently (AO)(ABO_{3±δ})_{*n*}, wherein perovskite layers with a thickness of *n* (BO₆) octahedra are separated by rocksalt (AO)(OA) double layers. This RP phase can accommodate all the elemental substitutions

available to perovskites as well as additional compositions that are not stable in the perovskite structure.²⁰ While Ruddlesden-Popper materials have been explored as solid oxide fuel cell cathodes owing to their chemical flexibility and labile lattice oxygen, they have not been fully examined for room temperature water oxidation.^{21, 22, 23, 24, 25, 26, 27}

Herein, we report a series of $\text{La}_{0.5}\text{Sr}_{1.5}\text{Ni}_{1-x}\text{Fe}_x\text{O}_{4+\delta}$ (LSNF, $x = 0$ to 1) OER catalysts that have enabled us to achieve exceptionally high catalytic activities at low overpotentials with small OER Tafel slopes. In particular, we show that Sr substitution promotes high catalytic activity by further oxidizing Ni via charge compensation, enhancing Ni-O covalency and electronic conductivity. Chemical substitution of Fe for Ni introduces and tunes the overlap between the Ni and Fe $3d$ bands and the O $2p$ band. Density functional theory (DFT) modeling confirms that cross-gap hybridization between $e_g(\text{Ni})$, $p(\text{O})$ and $e_g(\text{Fe})$ bands across the Fermi level enhances charge transfer interactions across Fe-O-Ni bridges and the bandwidth available for electrode-adsorbate electron transfer. We propose the concept of cross-gap hybridization²⁸ of transition metal $3d$ states and O $2p$ orbitals as an effective new catalyst design criteria for improving OER activity. Furthermore, our work illustrates the remarkable catalytic activity of the RP LSNF series that encompasses a range of chemical substitutions and electronic configurations that are not fully-realizable in perovskite electrocatalysts or other crystalline metal oxide phases. This precise synthesis of RP compositions enables the elucidation of crucial structural-chemical-electronic relationships that have not been possible with Ni-M oxyhydroxides and other reported metal oxide catalysts for OER. Yet by analogy, cross gap hybridization of $3d$ states with O $2p$ possibly explains the reported high OER activity for Fe-doped Ni- and Co-based oxide systems.

4.2 RESULTS AND DISCUSSION

4.2.1 Material Characterization

$\text{La}_{0.5}\text{Sr}_{1.5}\text{Ni}_{1-x}\text{Fe}_x\text{O}_{4+\delta}$ (LSNF, $x = 0$ to 1) samples were synthesized using a modified Pechini method²⁹ followed by crystallization and annealing, details of which are found in the methods section. Electron diffraction and powder X-ray diffraction (PXRD) patterns correspond to a body-centered tetragonal unit cell with the $I4/mmm$ space group, characteristic of the $n = 1$ Ruddlesden-Popper (RP) crystal structure (Figure 4.1a,c and Figure D.1). No superlattice reflections were detected that could be attributed to the La/Sr or Fe/Ni ordering, ordering of hyperstoichiometric oxygen atoms, or lattice distortions. The a and c unit cell parameters (Figure 4.1b) and unit cell volume (Figure D.2) increase almost linearly with Fe substitution reflecting that the $\text{La}_{0.5}\text{Sr}_{1.5}\text{Ni}_{1-x}\text{Fe}_x\text{O}_{4+\delta}$ solid solution is homogeneous over the entire substitutional range. The $I4/mmm$ structure has been confirmed with Rietveld refinement from PXRD data (Table D.1, Figure D.3, D.4). Unit cell volume increases with Fe substitution are in agreement with the increasing fraction of Fe cations that have larger ionic radii than Ni cations ($r(\text{Fe}^{3+}, \text{HS}) = 0.645 \text{ \AA}$, $r(\text{Fe}^{4+}, \text{HS}) = 0.585 \text{ \AA}$, $r(\text{Ni}^{3+}, \text{LS}) = 0.56 \text{ \AA}$, $r(\text{Ni}^{4+}, \text{LS}) = 0.48 \text{ \AA}$).³⁰ The ratio of the apical to equatorial Ni/Fe – O distances increases from 1.038 in LSN to 1.073 in LSF, which correlates with an increasing fraction of Jahn-Teller Fe^{4+} (HS) cations in the Ni/Fe position $2a$, promoting the apical elongation of the (Ni/Fe) O_6 octahedra. The $I4/mmm$ crystal structure is also directly viewed with annular bright field scanning transmission electron microscopy (ABF-STEM, Figure 4.1d), which visualizes heavier cations and lighter oxygen anions simultaneously. The ABF-STEM image shows perfect stacking of the perovskite (BO_2) ($B = \text{Ni}, \text{Fe}$) layers and the rock salt (AO)(OA) ($A = \text{La}, \text{Sr}$) layers without stacking faults. The crystal structure propagates to the surface without noticeable traces of amorphization.

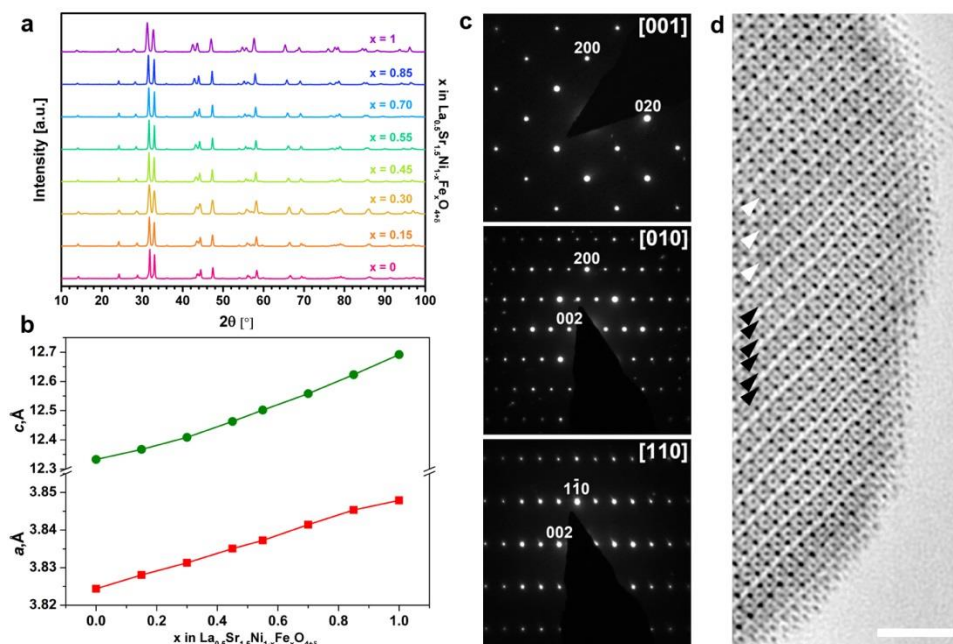


Figure 4.1: Crystallographic characterization of the $\text{La}_{0.5}\text{Sr}_{1.5}\text{Ni}_{1-x}\text{Fe}_x\text{O}_{4+\delta}$ series

a) PXRD patterns of $\text{La}_{0.5}\text{Sr}_{1.5}\text{Ni}_{1-x}\text{Fe}_x\text{O}_{4+\delta}$ demonstrate all compositions have the tetragonal $n = 1$ Ruddlesden-Popper $I4/mmm$ structure. b) Compositional dependence of a and c unit cell parameters showing $0 \leq x \leq 1$ homogeneity range. c) Electron diffraction patterns of LSNF30 confirm the absence of cation and/or anion ordering. d) [100] ABF-STEM image of LSNF30 directly visualizes the stacking of the (BO)₂ octahedra (white arrowheads, B = Ni, Fe) and (AO)(OA) layers (black arrowheads, A = La, Sr) in the Ruddlesden-Popper structure. The scale bar is 2 nm.

The consistent morphology of catalysts is crucial to the analytical comparison of electrochemical OER activity. High-angle annular dark-field scanning transmission electron microscopy (HAADF-STEM) and Brunauer-Emmet-Teller (BET) surface area analysis were performed on the LSNF series. The results, presented in Figures D.5 and D.6, indicate similar morphology across the series regardless of Fe substitution. All compositions consist of 50 – 300 nm crystallites loosely sintered into agglomerates that

are up to several microns in size. This morphological similarity is reinforced by BET surface area results which range from 3.3 to 6.8 m² g⁻¹ (Figure D.6).

4.2.2 Electrochemistry

The La_{0.5}Sr_{1.5}Ni_{1-x}Fe_xO_{4+δ} (LSNF) series was tested for the OER and the results are presented in Figure 4.2. Representative polarization curves for all compositions are shown in Figures 4.2a and D.7. For all amounts of Fe substitution, with the exception of 100% (LSF), the onset potential for the OER decreases and the corresponding catalytic activity increases significantly compared to LSN. Merely 15% replacement of Ni with Fe increases the specific activity (mA cm⁻²_{oxide}) by over an order of magnitude at 1.63 V vs RHE-iR, as seen in Figure 4.2b. Further substitution of Fe for Ni yields a volcano-like catalytic trend, with LSNF30 being the most active composition. LSNF30 displays exceptionally high catalytic activities of 32.7 mA cm⁻²_{oxide} and 1930 mA mg⁻¹_{oxide} at 1.63 V, over 20 and 40 times higher than the respective values for LSN, and achieves the common benchmark of 10 mA cm⁻²_{geo} at only a 360 mV overpotential. The catalytic activity of VC is negligible, contributing only 7 mA mg⁻¹ (Figures D.7 and D.8a-b) at 1.63 V. Figures 4.2c-d demonstrate the significantly high mass and specific activity of LSNF30 compared to other leading metal oxide OER catalysts. As the figures show, LSNF30 is over 5 times more active than the recently reported SrCoO_{2.7} (1930 vs 332 mA mg⁻¹_{oxide}) and over an order of magnitude more active than IrO₂ (173 mA mg⁻¹_{oxide}), a leading precious-metal oxide benchmark catalyst. LSNF30 generates 3 times as much current per surface area as SrCoO_{2.7} (Figure 4.2d, 32.7 vs 9.2 mA cm⁻²_{oxide}), over an order of magnitude more than IrO₂ (1.2 mA cm⁻²_{oxide}) at 1.63 V, has a Tafel slope of 44 mV dec⁻¹, and sustains 10 A g⁻¹_{ox} for over 24 hours without failure (Figure D.9). Table D.2 summarizes the catalytic activities of other promising catalysts to enable comparison with

LSNF30 using multiple metrics. Examined in the context of precious- and non-precious metal OER catalysts, LSNF30 is one of the most active OER catalysts ever reported to our knowledge.

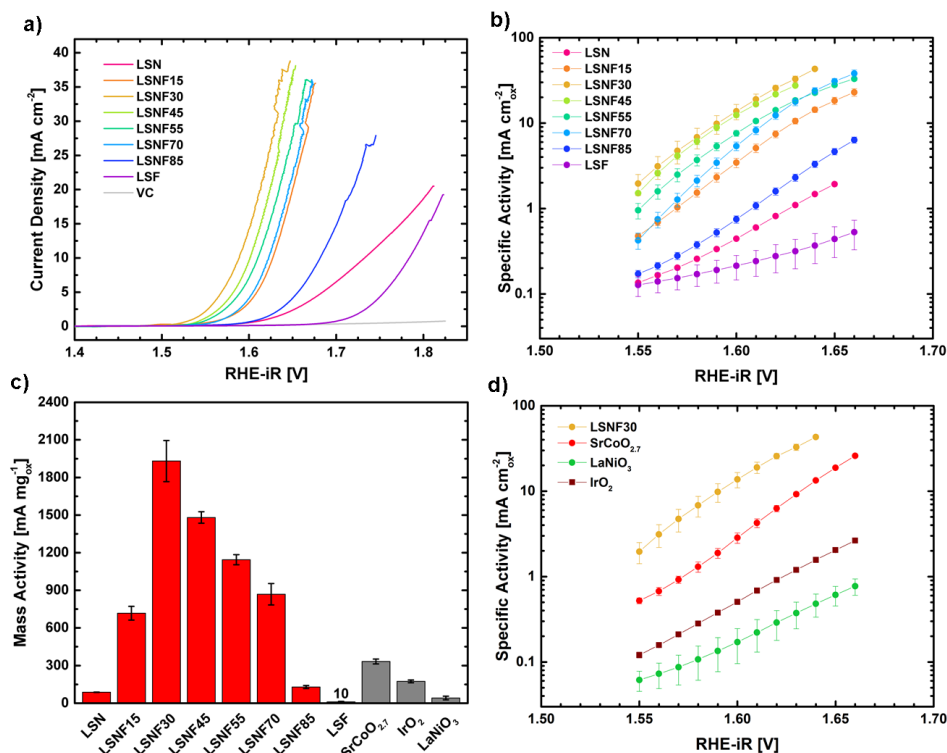


Figure 4.2: Oxygen evolution results and catalytic activities for the LSNF series taken in O_2 saturated 0.1 M KOH at 10 mV s^{-1} and 1600 rpm

a) Averaged (anodic and cathodic) OER polarization curves presented in geometric current density (5 mm GCE , $A = 0.196 \text{ cm}^2$). b) Tafel plots of the specific activity of each LSNF catalyst, c) oxide mass activity of the LSNF series at 1.63 V vs RHE-iR compared to leading OER catalysts $\text{SrCoO}_{2.7}$, LaNiO_3 and IrO_2 on XC72 Vulcan Carbon (VC). d) Specific activities of leading OER catalysts compared to LSNF30, the most active composition of the series. All catalysts are 30 wt\% oxide on VC, except for IrO_2 which is 20 wt\% on VC. Electrode loading is fixed at $51 \mu\text{g}_{\text{total}} \text{ cm}^{-2}_{\text{geo}}$ for all tests.

The $\text{Ni}^{2+/3+}$ redox couple in LSNF is observed to shift to more positive potentials with Fe substitution, indicating a direct modulation of Ni's reactivity with Fe substitution. This redox couple exists in the incipient OER region, as indicated in the reversible cyclic voltammetry (CV) peaks in Figure 4.3a. The potential range over which the redox peaks are observed is consistent with prior studies of Ni-based electrocatalysts^{3, 31, 32} with Fe substitution shifting the peak potential (E_p) of $\text{Ni}^{2+/3+}$ oxidation as documented with Ni-Fe oxyhydroxides.^{3, 4, 31} The features in Figure 4.3c arise from electroactive Ni, as indicated by integration of the oxidation waves (Figures D.10 and D.11) which reveal that the specific oxidative charge ($\mu\text{C cm}^{-2}_{\text{oxide}}$) transferred during oxidation/intercalation is consistently reduced upon increasing Fe substitution with the exception of the initial introduction of Fe in LSNF15 (Figures 4.3d). Similar behavior was reported earlier for 10% Fe substitution into NiOOH hydroxide electrodes³ and is speculated to be due to increased oxygen and electrolyte diffusivity. Such an interpretation is supported by the increased electrochemical oxygen diffusion rate in LSNF15 as compared to LSN ($1.04\text{E}^{-12} \text{ cm}^2 \text{ s}^{-1}$ vs $8.03\text{E}^{-13} \text{ cm}^2 \text{ s}^{-1}$; Figure D.12 and Table D.3).

Oxygen intercalation concomitant with Ni redox is likely given the labile nature of oxygen in $\text{La}_2\text{NiO}_{4+\delta}$. This is further suggested by the observation that the pH dependence of the $\text{Ni}^{2+/3+}$ oxidation E_p in Figure 4.3b behaves like a Nernstian pseudocapacitor using OH^- as the intercalating ion.^{13, 33, 34, 35} Beyond apparent oxygen intercalation in LSNF30, consistent modulation of Ni's reactivity is evidenced by the anodic shift in E_p with increasing Fe substitution, as seen in Figure 4.3c and summarized in Figure D.8c.

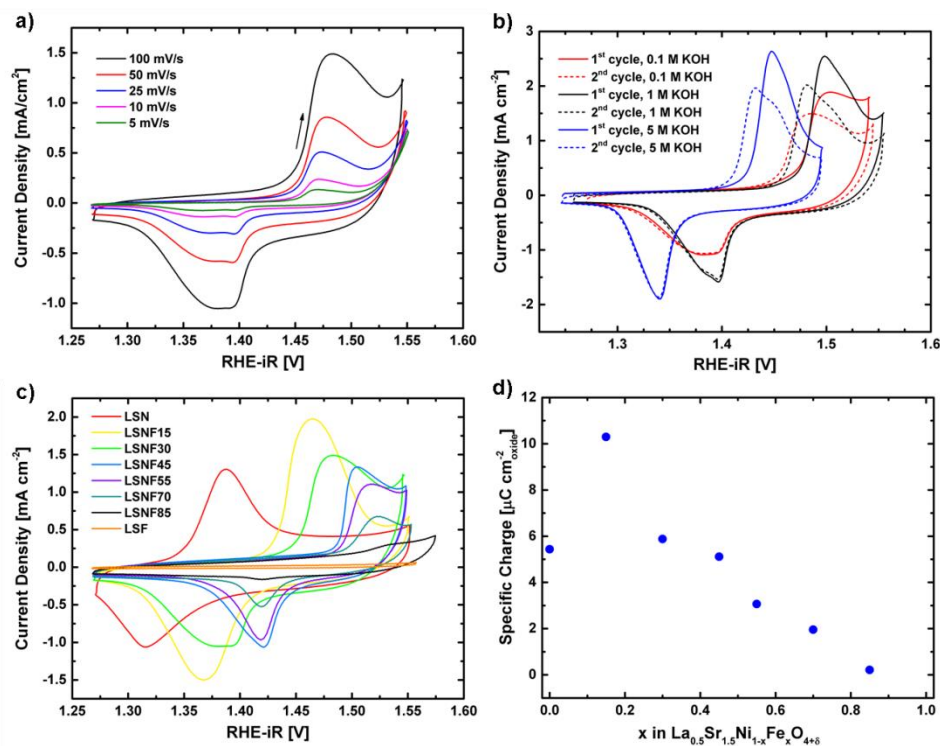


Figure 4.3: Cyclic voltammetry (CV) of LSNF catalysts in O₂ saturated 0.1 M KOH unless otherwise specified.

a) CVs in the incipient OER region for LSNF30 demonstrating both reversibility and peak potential dependence on scan rate. CVs from 5 to 100 mV s⁻¹ for the entire LSNF series are available in Figure D.9. b) CVs of LSNF30 in 0.1 M, 1 M and 5 M KOH demonstrates pH dependence on the oxidation wave peak potential (E_p), consistent with OH⁻ intercalation, while shifts between the first and second cycle suggest catalyst surface restructuring upon initial cycling. c) CVs of LSNF at 100 mV s⁻¹ revealing a systematic anodic shift in Ni^{2+/3+} oxidation/intercalation potentials with increasing Fe substitution. CVs at 100 mV s⁻¹, taken after 3 to 4 cycles to ensure peaks occur at a stable position, are depicted to aid the reader in distinguishing peak potential shifts and relative areas, but at 100 mV s⁻¹ contributions to E_p from capacitance and mass transport resistance cannot be ignored. To address this, peak potentials reported in Figure D.8c were taken from stable CVs at 10 mV s⁻¹. d) Specific oxidative charge (μC cm⁻²_{oxide}) resulting from the integration of oxidation waves. Integrations were performed using specific current density (μA cm⁻²_{oxide}) to normalize differences in catalyst surface area (Figure D.8d). The OER baselines for stable CVs at 10 mV s⁻¹ were fit and subtracted. Figure D.11 contains the CVs used for integration.

4.2.3 Chemical States and Electronic Structure

Remarkable improvement of the catalytic activity of LSN upon Fe substitution for Ni may be explained by the impact of the Fe 3*d* states on the electronic structure of LSNF. Figure 4.4 presents a schematic of the expected evolution of the band structure as first Sr and then Fe are substituted into the La₂NiO_{4+δ} host lattice. It is known that over 50% Sr substitution for La induces metal-like conductivity^{23, 36} in the charge transfer insulator La₂NiO_{4+δ} due to hole doping in the O 2*p* band.³⁷ Earlier studies of the electronic structure of La_{1.1}Sr_{0.9}Ni_{0.8}Fe_{0.2}O_{4+δ} with resonant photoemission spectroscopy suggest that the Fe 3*d* states make a substantial contribution to the valence band near the Fermi level (E_F) by strongly hybridizing with the O 2*p* and Ni 3*d* states²⁶ which facilitates cation oxidation and redox processes. The lower electronegativity of Fe compared to Ni dictates that the Fe 3*d* σ^* band should be higher in energy than the Ni 3*d* σ^* band. The mixed Fe 3*d* and Ni 3*d* bands pinned at E_F in close proximity to the O 2*p* band should give rise to a mixture of Ni^{3+/4+} and Fe^{3+/4+} where the relative proportion of oxidation states changes with the amount of Fe substitution.^{25, 27, 38}

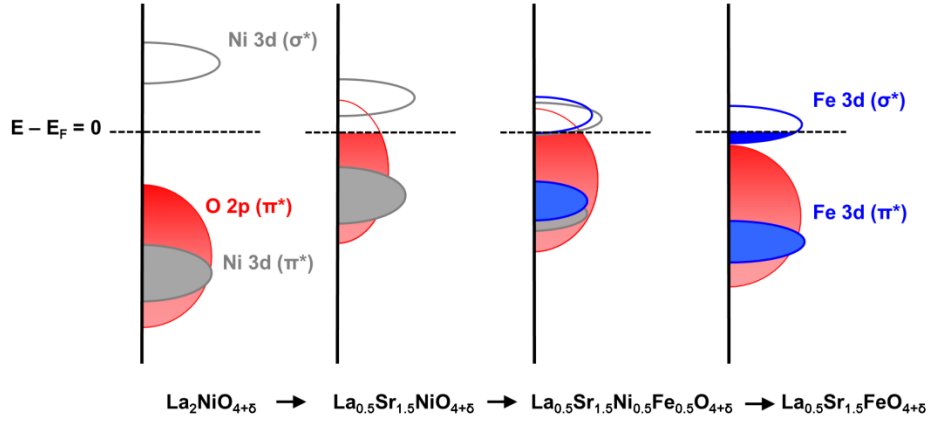


Figure 4.4: Schematic evolution of the electronic structure of semiconducting $\text{La}_2\text{NiO}_{4+\delta}$ as Sr and Fe are substituted into it. The substitution of La^{3+} by Sr^{2+} shifts the O $2p$ band towards the Fermi level (E_F), giving rise to metal-like conductivity in LSN from hole injection into O $2p$ π^* and overlap with Ni $3d$ σ^* . Next, substitution of the less electronegative Fe for Ni introduces a Fe $3d$ σ^* band that overlaps with Ni $3d$ σ^* while shifting the O $2p$ π^* down relative to LSN. LSNF is predicted to exhibit a continuum of Ni/Fe $3d$ σ^* bands that overlap with the O $2p$ above the E_F . Complete replacement of Ni with Fe results in $\text{La}_{0.5}\text{Sr}_{1.5}\text{FeO}_{4+\delta}$ ³⁹.

The average Ni and Fe oxidation states were determined by *ex-situ* room temperature Mössbauer spectroscopy (Figure D.13) in conjunction with iodometric titrations. Table 4.1 contains the results of this analysis wherein the average oxidation state of Ni increases with increasing Fe content from +3.54 to +3.95, as does the oxygen hyperstoichiometry (δ) and the average B-site oxidation state. The increase in the oxidation state of Ni is supported by the observation that the Ni $3p$ spectrum, obtained by X-ray photoelectron spectroscopy (XPS), shifts to higher binding energies with increasing Fe content (Figure D.14) as well as the positive potential shifting of the $\text{Ni}^{2+/3+}$ redox features (Figure 4.3c)

Table 4.1: Oxygen hyperstoichiometry (δ) in $\text{La}_{0.5}\text{Sr}_{1.5}\text{Ni}_{1-x}\text{Fe}_x\text{O}_{4+\delta}$, average B-site oxidation states determined by iodometry, the results of Mössbauer spectroscopy and the calculated average Ni oxidation state

Catalyst	Fe sub.	δ , hyperst.	δ st. dev	B^+ avg	B^+ st. dev	Fe^{4+} (Moss.)	Fe^{3+} (Moss.)	Ni^{x+} avg	Ni^{x+} st. dev
LSN	0%	0.018	0.013	3.54	0.03	-	-	3.54	0.03
LSNF15	15%	0.046	0.007	3.59	0.01	73%	27%	3.57	0.02
LSNF30	30%	0.042	0.010	3.58	0.02	62%	38%	3.57	0.03
LSNF45	45%	0.065	0.027	3.63	0.05	57%	43%	3.68	0.10
LSNF55	55%	0.088	0.011	3.68	0.02	58%	42%	3.80	0.05
LSNF70	70%	0.076	0.022	3.65	0.04	58%	42%	3.82	0.14
LSNF85	85%	0.081	0.036	3.66	0.07	61%	39%	3.95	0.48
LSF	100%	0.143	0.037	3.79	0.07	62%	38%	-	-

To further understand the electronic structure evolution across the LSNF series and its implications for the OER activity, as well as confirm the results of the Mössbauer spectroscopy and iodometric titrations, we model the bulk phase of LSNF by density functional theory (DFT). A series of LSNF compositions are modeled by 2x2x1 primitive unit cells allowing for unit compositions of $\text{La}_{0.5}\text{Sr}_{1.5}\text{NiO}_4$ (LSN), $\text{La}_{0.5}\text{Sr}_{1.5}\text{Ni}_{0.75}\text{Fe}_{0.25}\text{O}_4$ (LSNF25), LSNF50, LSNF75 and LSF. Details regarding cell formation and magnetic investigation are given in Appendix D.

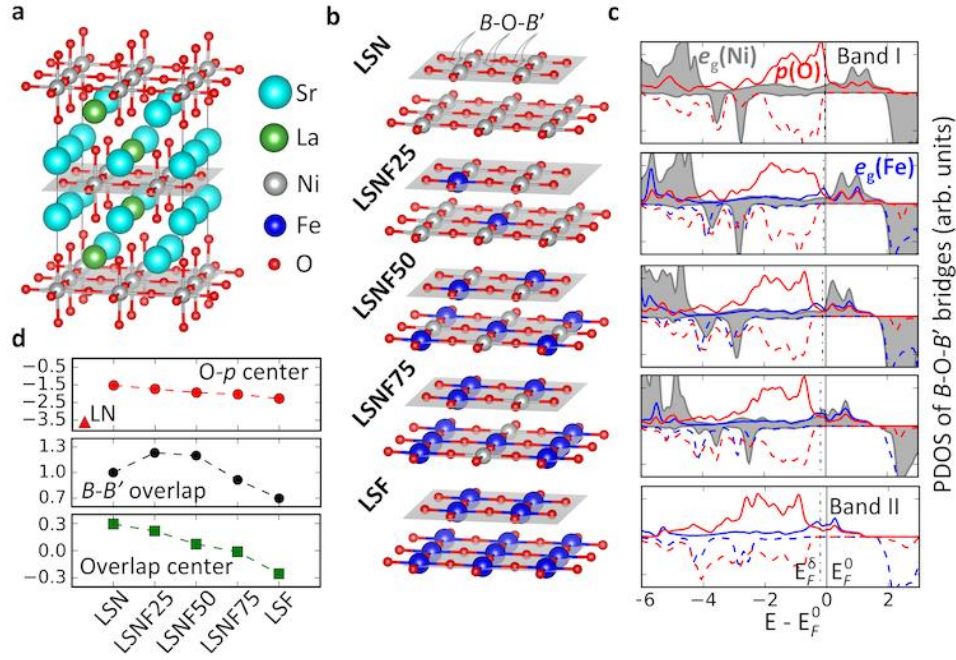


Figure 4.5: Density functional theory modeling of atomic and electronic structures of bulk LSNF in ferromagnetic configuration.

(a) The ground-state $2 \times 2 \times 1$ cell of $\text{La}_{0.5}\text{Sr}_{1.5}\text{NiO}_4$, with uniformly distributed La in each $[001]$ AO layer. (b) Representations of the two $B(B')\text{O}_2$ layers for each ground state $\text{La}_{0.5}\text{Sr}_{1.5}\text{Ni}_{1-x}\text{Fe}_x\text{O}_4$, with x at 0, 0.25, 0.5, 0.75 and 1; for each x , the ground state Fe arrangement is characterized by equal numbers of Fe in the two $B(B')\text{O}_2$ layers, with the Fe in each layer arranged to maximize the number of Fe-O-Ni bridges. (c) The corresponding spin polarized PDOS of e_g (Ni: grey shaded area, and Fe: blue line) and $2p$ (O: red line) with respect to Fermi level (E_F^0) for the $B\text{-O-B'}$ bridges; the PDOS are the average of existing $B\text{-O-B'}$ bridges; the adapted Fermi level (E_F^δ) to oxygen hyperstoichiometry is estimated via the rigid band model, with $E_F^\delta = E_F^0 - 2e^- \delta / \text{DOS}(E_F^0)$, where $\text{DOS}(E_F^0)$ is the total density of states at E_F^0 per formula unit of LSNF. (d) Top: Computed values of the O- p band center (top panel), with La_2NiO_4 (LN) calculated as reference. Middle: The magnitude of band overlap, determined by the integration of maximum PDOS between $e_g(B)$ and $e_g(B')$ from -2 to 2 eV, normalized to $e_g(\text{Ni})$ in LSN. Bottom: The corresponding overlap center (centroid) of maximum PDOS between $e_g(B)$ and $e_g(B')$.

Figures 4.5a-b show the (001) atomic layers of the most stable LSNF structures based on our screening. For LSN (Figure 4.5a), we find a uniform, proportional distribution of La/Sr.⁴⁰ Using this La/Sr distribution, we determine the minimum energy Ni/Fe ordering which results in two key features governing the Fe arrangement in LSNF (Figure 4.5b). First, each of the two $B(B')\text{O}_2$ layers has an equal number of Fe cations in order to prevent an unbalanced charge distribution between them. Second, the Fe cations in each $B(B')\text{O}_2$ plane are distributed such that the number of Fe-O-Ni bridges is maximized.² This arrangement mitigates the effects of the induced O $2p$ electron hole at Ni-O-Ni bridges due to more effective electron donation by Fe at Fe-O-Ni bridges, which increases stability.¹⁶ Compared with Fe-O-Fe bridges, the Fe-O-Ni bridges induce shorter Fe-O bond lengths and thus indicate higher Fe oxidation states. This observation agrees with the experimentally observed predominance of Fe^{4+} over Fe^{3+} at low Fe substitution.

The computed projected density of state (PDOS) of the Fe-O-Ni bridges confirms that the Ni cations are in the low-spin state, with fully occupied t_{2g}^{\downarrow} states (Figure D.15d), while the Fe cations are in the high-spin state, with mostly unoccupied t_{2g}^{\downarrow} states for all LSNF.⁴¹ These spin states lead to e_g bands positioned around the Fermi level, E_F^0 , thus becoming the most relevant for Fe-O-Ni interactions and the focus of our study.

Inspection of the Fe-O-Ni bridges reveals significant overlap of O $2p$, Ni e_g^{\uparrow} and Fe e_g^{\uparrow} bands for all compositions in the LSNF series (Figure 4.5c) as suggested in Figure 4.4. This overlap leads to two important observations. First, the unoccupied O $2p^{\uparrow}$ states indicate oxygen electron holes with finite PDOS across E_F^0 , thus bridging charge transfer between neighboring cations.^{30, 41} Second, the similar energies of the Ni and Fe e_g^{\uparrow} states (denoted Band I and Band II in the following) open up the possibility of electron exchange through oxygen. These two factors govern the evolution of the PDOS from LSN to LSF. On one hand, the substitution of Ni by less electronegative Fe stabilizes O

2*p* electrons and increases the Ni-O distances, shifting the O 2*p* band center downwards relative to E_F (Figure 4.5d) and decreasing the bandwidth⁴¹ which reduces electron holes and charge transfer ability.⁴² This condition is consistent with the experimentally observed increase in oxygen hyperstoichiometry in going from LSN to LSF. On the other hand, the partially filled Band II (Fe) significantly hybridizes with both O 2*p* and Band I (Ni), driving the latter towards E_F^0 . Both Bands I and II make significant contributions to the occupied (valence) and unoccupied (conduction) states, respectively, and this dramatically increases the bandwidth of the triple band overlap,²⁶. These observations are consistent with Figure 4.4 and previous work demonstrating similar changes to the O 2*p* band center when less electronegative elements are substituted in $\text{Sr}_{2-x}\text{La}_x\text{MO}_{4+\delta}$.⁴³ As Figure 4.5d shows, from LSN to LSNF50, the magnitude of overlap electron density dramatically increases with its center approaching E_F^0 , suggesting a significantly lower energetic cost to accept/donate electrons. The increased Fe concentration in LSNF75, however, drives Band I (Ni) into the similar distribution of Band II (Fe) and reduces the overlap magnitude. This suggests that the optimal OER activity will occur for a composition between LSNF25 and LSNF50, which is consistent with experimental observations. More discussion on band movement due to oxygen hyperstoichiometry can be found in Appendix D.

The triple band overlap increases the bandwidth available for charge transfer at the adsorbate-catalyst interface, and therefore should increase the rate of reaction according to the Gerischer-Marcus model of electron transfer.⁴⁴ A larger bandwidth implies a higher density of both occupied and unoccupied states around the Fermi level, which are able to accommodate surface redox reactions via only a slight Fermi level shift, thus requiring less energetic cost. This model is also consistent with the *d* band theory,⁴⁵ which suggests the optimal metal catalyst as one with desirable bonding (occupied) and

anti-bonding (mostly unoccupied) states, so as to attain an intermediate bond strength at the adsorbate-metal interface.

The effects of band overlap on activity can be further understood with respect to the adsorption energy of reaction intermediates and bulk catalyst stability. On one hand, comparison between the LSNF activity volcano (Figure 4.2c) and the DFT computed volcano described by Man¹⁵ indicate binding character that is too weak on LSN and too strong on LSF. Too high an oxidation state on the B-site cation, as is the case at higher Fe contents, favors adsorption of O while too low an oxidation state, present at lower levels of Fe substitution, favors adsorption of OH.^{13, 15, 16} We propose that significant mediation between the two end-member compounds via electron exchange and hybridization across Ni-O-Fe bridges produces an intermediate adsorption strength stemming from these exchange interactions that may play a significant role. On the other hand, the catalyst stability is reduced from LSF to LSN due to formation of more oxygen electron holes, which may favor rapid subtraction and direct participation of surface lattice oxygen into the OER via the LOM mechanism.¹⁶ The observed OER activity for the LSNF RP series and its correlation with the electronic structure calculations and oxygen diffusion rates suggest that the series follows the LOM pathway as we have previously proposed.^{13, 16} A full rationalization supporting this hypothesis is included in Appendix D.

4.3 CONCLUSIONS

We have precisely synthesized a series of RP catalysts having highly oxidized and covalent Ni 3*d* - O 2*p* - Fe 3*d* bonds that give rise to exceptional OER activity. To increase the oxidation state and Ni-O covalency, Sr substitution into LaNiO₃ has previously been proposed but not fully realized. Inactive secondary phases resulting from poor solubility of Sr in the perovskite phase were avoided through utilization of the RP

crystal structure. Using $\text{La}_{0.5}\text{Sr}_{1.5}\text{NiO}_{4\pm\delta}$ as the host lattice, we achieved complete substitution of Fe for Ni across the entire compositional range, while crystalline periodicity of the RP phase enabled precise study of the impact of Fe substitution on the chemical and electronic properties of the LSNF series. Iodometric titrations coupled with Mössbauer spectroscopy indicate that the average Ni oxidation state in the LSNF series increases from +3.46 to +3.95 with increasing Fe substitution while the $\text{Ni}^{2+/3+}$ redox peaks also shift to more positive potentials, consistent with Ni developing a more oxidized character. The influence of Fe substitution extends beyond increasing the oxidative strength of Ni, however, as the electrocatalytic activity increases by over an order of magnitude from LSN to LSNF30, despite possessing statistically equivalent Ni oxidation states. DFT calculations reveal that Fe substitution results in cross-gap hybridization where the Fe $3d\ e_g$ band is hybridized with both the Ni $3d\ e_g$ and top of the O $2p$ density of states across the Fermi level. The increased covalency of the Ni-O bonds as well as facile charge transfer through Fe-O-Ni bridges due to incorporation of Fe explains the enhanced catalytic activity going from LSN to LSNF30. This methodology to promote cross-gap hybridization via selective substitution of A and B-site elements in RP oxides represents a new set of design principles for the optimization of metal oxide catalysts and reveals important fundamental aspects related to their structure and electrocatalytic activity.

4.4 METHODS

All chemicals were used as received. Lanthanum(III) nitrate hexahydrate (99.995%), strontium(II) nitrate hexahydrate (99%), nickel(II) nitrate hexahydrate (99%), iron(III) nitrate non-hydrate (99.99%), tetramethylammonium hydroxide pentahydrate (TMAOH, 99%), diethylene glycol (DEG, 99.99%), citric acid monohydrate, 2-propanol,

ethylenediaminetetraacetic acid, and potassium hydroxide were obtained from Fisher Scientific. Ethanol (Absolute 200 proof) was obtained from Aaper Alcohol. 5 wt % Nafion solution in lower alcohols and IrO₂ powder were purchased from Sigma-Aldrich. Millipore high purity water (DI water, 18 MΩ) was used. Oxygen (research grade, 99.999% purity) and argon (research grade, 99.999% purity) were obtained from Praxair. Vulcan XC72 carbon (VC) was purchased from Cabot Corporation and ball-milled prior to use.

Catalyst Synthesis

La_{0.5}Sr_{1.5}Ni_{1-x}Fe_xO_{4±δ} (LSNF, x = 0 to 1) samples were synthesized using a modified Pechini method²⁹ followed by crystallization and annealing. A- and B-site nitrate salts, in stoichiometric ratios, were dissolved in water to create a solution with a total metal salt concentration of 0.1 M. Citric acid and EDTA were added to the solution each at a concentration of 0.1 M as well. TMAOH was added dropwise to the solution until the pH had reached 7.5 in order to deprotonate and dissolve the EDTA. DEG was then added to the solution at a concentration of 0.067 M and the solution was heated to 85° C while stirring. The EDTA and citric acid were both added to ensure complete chelation of the metal cations, preventing agglomerations or particle formations that may lead to catalyst inhomogeneity. DEG and heat were added to the solution to drive a dehydration reaction between the polyhydroxyl alcohol and the carboxylic acid groups of the chelates to form a polyester gel. Once all of the water had been evaporated the gel was combusted on a hot plate at 350° C to form mixed metal oxide precursor particles. This step was performed on a hot place and not in a sealed tube furnace to avoid possible explosions from rapid evolution of gasses upon combustion. Finally, precursor particles were crystallized at 950° C (heated at 20° C min⁻¹) for 5 hours, then cooled to 400° C and left to anneal for 6 hours in a tube furnace. The entire crystallization and annealing

routine was done under pure O₂ flowing at 200 mL min⁻¹. Catalysts were recovered and immediately stored under Ar gas to prevent catalyst surface amorphization. Total catalyst yields per synthesis ranged from 500 to 750 mg. More details regarding the synthesis can be found in Masato et al.²⁹

SrCoO_{2.7} and LaNiO₃ were synthesized via a coprecipitation method previously reported elsewhere^{13, 46} in which A and B-site nitrate salts in a 1:1 ratio were dissolved in a 1 wt% solution of TMAOH containing an equimolar amount of TPAB to the total moles of metal cations in order to form mixed metal hydroxide precursor particles. These solutions were flash-frozen on a rotating metal drum at cryogenic temperatures and collected before lyophilization to remove water. The precursor particles were then calcined at 700° C (LaNiO₃) or 950° C (SrCoO_{2.7}) to form the perovskite phase.

Electrochemical Characterization

Catalyst inks were prepared by adding 2 mL of a NaOH neutralized 0.05 wt% Nafion solution⁴⁷ to 2 mg of catalyst powder and bath sonicated for at least one hour. A volume of ink (10 µL) was drop cast onto a clean 5 mm (0.196 cm², Pine Instruments) glassy carbon electrode and dried under ambient conditions overnight. The glassy carbon electrodes were cleaned prior to drop casting by sonication in a 1:1 DI water:ethanol solution. The electrode was then polished using 0.05 µm alumina powder, sonicated in a fresh DI water:ethanol solution, and dried in ambient air. All electrochemical tests were performed on electrodes prepared by this method, obtaining a composite catalyst loading of 51 µg_{total} cm⁻²_{geo}, yielding 15.3 µg_{oxide} cm⁻²_{geo} for catalysis and intercalation tests (30 wt% on carbon).

Electrochemical testing was performed on either a CH Instruments CHI832a or a Metrohm Autolab PGSTAT302N potentiostat, both equipped with high speed rotators from Pine Instruments. All testing was done at room temperature in 0.1 M KOH

(measured pH \approx 12.8). Current interrupt and positive feedback methods were used to determine electrolyte resistance (46 Ω) and all data was iR compensated after testing unless stated otherwise. Each test was performed in a standard 3 electrode cell using a CH Instruments Hg/HgO (1 M KOH) reference electrode, a Pt or Au wire counter electrode, and a film of catalyst ink on glassy carbon as the working electrode. All potentials are reported versus the regular hydrogen electrode (RHE), which was determined experimentally to be +0.8976 V vs. Hg/HgO (1 M KOH). Figure D.16 contains the RHE calibration data.

Quantification of Oxygen Evolution Activities. All OER testing was performed on newly dropcast electrodes which had not undergone previous testing, drop-cast with 30 wt% catalyst on VC (15.3 $\mu\text{g}_{\text{oxide}} \text{cm}^{-2}_{\text{geo}}$). Cyclic voltammetry scans were performed from 1 to 2 V vs RHE at 10 mV/s with a rotation rate of 1600 rpm in O₂-saturated 0.1 M KOH. The anodic and cathodic scans were averaged and iR corrected, and the current at 1.63 V vs RHE-iR was selected from the polarization curves to compare OER activities. Scatter in the data at high current densities is due to oxygen bubble formation and desorption on the electrode surface. Data reported herein is the average taken from at least three tests on fresh electrodes.

Oxygen Intercalation Cyclic Voltammetry (CV). All CVs were taken on fresh electrodes of 30 wt% oxide on VC. All catalysts were first conditioned by performing 20 cycles from 1.26 to 1.55 V vs RHE at 100 mV s⁻¹. Immediately following, 3 cycles at 100, 50, 25, 10 and 5 mV s⁻¹ were collected. Unless otherwise stated, all cycles shown are the third cycle at a given scan rate. For samples containing more than 50% Fe substitution, it was necessary to perform 4 cycles at each scan rate. Additionally, LSNF85 had to be cycled to 1.575 V before any oxidative features were observed.

For comparison of charge passed for all oxidative waves, the last cycle at 10 mV s⁻¹ was used to compute specific current density. The baseline of each CV was fit and subtracted from the specific current density. The background subtracted CVs (Figure D.11) were then integrated to find the total charge transferred.

Oxygen Diffusion Rate Determination. All oxygen diffusion tests were performed in argon-saturated, 1 M KOH on fresh 85 wt% oxide films. Each LSNF composition was cycled at 20 mV s⁻¹ until the oxidative peak potential did not change upon further cycling. Chronoamperometry was then performed at potentials 10 mV more anodic than E_p to ensure diffusion-limited intercalation. Linear regression was performed as described elsewhere^{48, 49} to determine the diffusion rate. Particle sizes were estimated using the surface area calculated from BET measurements and densities determined by Rietveld analysis. All values reported are the average of at least three tests.

Iodometric Titrations

Iodometric titrations were performed according to the referenced procedure.¹³ 3 mL of deoxygenated 2 M KI solution was added to a flask containing 15 – 20 mg of perovskite under an argon atmosphere and allowed to disperse for three minutes. After a few minutes 25 ml of 1 M HCl was added and the perovskite was allowed to dissolve. This solution was then titrated to a faint golden color with a solution of ~26 mM solution of Na₂S₂O₃ that had been pre-standardized with 0.1 N KIO₃. Starch indicator was then added and the solution was titrated until clear, marking the end point.

Catalyst Preparation and Support

Fresh, Ar-sealed catalysts were ball milled for three minutes using a Wig-L-Bug spectroscopic grinding mill. To support the catalysts onto Vulcan carbon, the correct amounts of pre-ground catalyst and pre-ground VC were measured into the grinding mill's vial and ball milled for three minutes.

Powder X-ray Diffraction (PXRD)

Catalyst structure was probed by X-ray diffraction using a Rigaku MiniFlex600 Diffractometer at 298 K in ambient conditions, utilizing Cu K α radiation (1.54 Å wavelength) operating at 40 kV and 15 mA. For all tests, argon-sealed catalyst powder was exposed to ambient air and scanned over 10 - 100° 2 θ in 0.01° increments with a dwell time of 0.35 seconds per step. PXRD patterns for the Rietveld refinement were taken with a Huber G670 Guinier diffractometer (Cu K α_1 radiation; curved Ge(111) monochromator; image plate). The refinement was done with the JANA2006 package.⁵⁰ As the electron diffraction patterns of all compositions revealed no deviation from the R \bar{P} n = 1 *I4/mmm* structure, the La₂NiO₄ structure⁵¹ was used as a starting model. The La/Sr occupancy factors of the A positions were refined; the Fe/Ni occupancy factors for the B positions were assigned according to the results of the EDX analysis. The crystallographic data, positional and atomic displacement parameters, interatomic distances and reliability factors are listed in Table D.1 of Appendix D.

Surface Area Analysis

Nitrogen sorption analysis was performed on a Quantachrome Instruments NOVA 2000 high-speed surface area BET analyzer at a temperature of 77 K. Prior to measurements, the samples were ball milled for three minutes followed by degassing in vacuum for a minimum of 12 hours at room temperature. The specific surface area was calculated using the BET method from the nitrogen adsorption data in the relative pressure range (P/P₀) of 0.05 to 0.30, with a minimum R² of 0.995 and C value of 20.

Transmission Electron Microscopy (TEM)

The TEM samples were prepared by crushing the crystals in a mortar in ethanol and depositing drops of suspension onto holey carbon grid. Electron diffraction patterns, TEM images, high angle annular dark field scanning TEM (HAADF-STEM) images,

annular bright field scanning TEM (ABF-STEM) images and energy dispersive X-ray (EDX) spectra were obtained with an aberration-corrected Titan G³ electron microscope equipped with a Super-X EDX system, operated at 200 kV using a convergence semi-angle of 21.6 mrad.

Mössbauer Spectroscopy

⁵⁷Fe Mössbauer spectroscopy was performed in a transmission mode using a constant acceleration spectrometer MS1104 (Rostov-na-Donu, RF). A ⁵⁷Co/Rh γ -ray source was used for the measurements. The spectrometer was calibrated with standard α -Fe or sodium nitroprusside absorbers. All isomer shift values (IS) are referred to α -Fe at room temperature. The spectra evaluation was carried out using “UnivemMS” (Rostov-na-Donu, RF) and custom least squares fitting software with Lorentzian- Gaussian line shapes. Details regarding the deconvolution of the spectra are found in the text accompanying Figure D.12.

Density Functional Theory (DFT) modeling

Spin polarized calculations are performed using the Vienna *Ab initio* Simulation Package (VASP),⁵² the PAW pseudopotentials⁵³ and the exchange-correlation functional of Perdew-Burke-Ernzerhof (PBE),⁵⁴ with the effective Hubbard U_{eff} of 5.3 (Fe)⁵⁵ and 6.2 eV (Ni)⁵⁶ respectively. The Ruddlesden-Popper bulk phase is modeled by fully relaxing a 2x2x1 primitive unit cell, La(Sr)₁₆Ni(Fe)₈O₃₂, with a plane wave cutoff energy of 520 eV, Monkhorst-Pack k -point of 4x4x2, forces convergence criterion of 10⁻⁴ eV/Å and Gaussian smearing, where the smearing width is 0.1 eV. All models follow ferromagnetic ordering, as our calculations indicate its lower energy than those of nonmagnetic and antiferromagnetic orderings (A, C and G type). Details regarding the determinations of effective Hubbard U_{eff} , atomic, magnetic and electronic structures, and oxygen hyperstoichiometry effects are provided in Appendix D.

X-ray Photoelectron Spectroscopy

Chemical states were characterized by a Kratos AXIS Ultra DLD XPS in 0.1 eV steps using a dwell time of 4 s per step and a monochromatic Al X-ray source (Al α , 1.4866 eV). Charge compensation was used for all samples. Binding energies were for all spectra were calibrated against the adventitious carbon peak at 285 eV. CasaXPS was used for all data analysis and deconvolution. Details regarding the deconvolution of the Ni 3p spectrum are found in the text accompanying Figure D.13.

Determination of Ni and Fe oxidation states

Together, the iodometric titrations and the Mössbauer spectroscopy enable the calculation of Ni's average oxidation state and the relative percentage of Fe^{3+/4+}. Figure D.12 contains the deconvolution method and Mössbauer spectra.

4.5 ADDITIONAL INFORMATION

Extensive characterization and notes are in Appendix D

4.6 REFERENCES

1. Zhu H, Zhang P, Dai S. Recent Advances of Lanthanum-Based Perovskite Oxides for Catalysis. *ACS Catal* 2015, **5**(11): 6370-6385.
2. Conesa JC. Electronic Structure of the (Undoped and Fe-Doped) NiOOH O₂ Evolution Electrocatalyst. *J Phys Chem C* 2016, **120**(34): 18999-19010.
3. Corrigan DA. The Catalysis of the Oxygen Evolution Reaction by Iron Impurities in Thin Film Nickel Oxide Electrodes. *J Electrochem Soc* 1987, **134**(2): 377-384.
4. Trotochaud L, Young SL, Ranney JK, Boettcher SW. Nickel–Iron Oxyhydroxide Oxygen-Evolution Electrocatalysts: The Role of Intentional and Incidental Iron Incorporation. *J Am Chem Soc* 2014, **136**(18): 6744-6753.

5. Dionigi F, Strasser P. NiFe-Based (Oxy)hydroxide Catalysts for Oxygen Evolution Reaction in Non-Acidic Electrolytes. *Advanced Energy Materials* 2016, **6**(23): 1600621-n/a.
6. Chen JYC, Dang L, Liang H, Bi W, Gerken JB, Jin S, *et al.* Operando Analysis of NiFe and Fe Oxyhydroxide Electrocatalysts for Water Oxidation: Detection of Fe⁴⁺ by Mössbauer Spectroscopy. *J Am Chem Soc* 2015, **137**(48): 15090-15093.
7. Görlin M, Ferreira de Araújo J, Schmies H, Bernsmeier D, Dresch S, Gliech M, *et al.* Tracking Catalyst Redox States and Reaction Dynamics in Ni–Fe Oxyhydroxide Oxygen Evolution Reaction Electrocatalysts: The Role of Catalyst Support and Electrolyte pH. *J Am Chem Soc* 2017, **139**(5): 2070-2082.
8. Hunter BM, Gray HB, Müller AM. Earth-Abundant Heterogeneous Water Oxidation Catalysts. *Chem Rev* 2016, **116**(22): 14120-14136.
9. Bockris JO, Otagawa T. Mechanism of oxygen evolution on perovskites. *J Phys Chem* 1983, **87**(15): 2960-2971.
10. Suntivich J, May KJ, Gasteiger HA, Goodenough JB, Shao-Horn Y. A Perovskite Oxide Optimized for Oxygen Evolution Catalysis from Molecular Orbital Principles. *Science* 2011, **334**(6061): 1383-1385.
11. Hardin WG, Mefford JT, Slanac DA, Patel BB, Wang X, Dai S, *et al.* Tuning the Electrocatalytic Activity of Perovskites through Active Site Variation and Support Interactions. *Chem Mater* 2014, **26**(11): 3368-3376.
12. Galasso FS. *Structure, Properties and Preparation of Perovskite-Type Compounds*, vol. 5. Pergamon Press, 1969.
13. Mefford JT, Rong X, Abakumov AM, Hardin WG, Dai S, Kolpak AM, *et al.* Water electrolysis on La_{1-x}Sr_xCoO_{3-δ} perovskite electrocatalysts. *Nature Communications* 2016, **7**: 11053.

14. Zhou W, Zhao M, Liang F, Smith SC, Zhu Z. High activity and durability of novel perovskite electrocatalysts for water oxidation. *Mater Horiz* 2015, **2**(5): 495-501.
15. Man IC, Su H-Y, Calle-Vallejo F, Hansen HA, Martínez JI, Inoglu NG, *et al.* Universality in Oxygen Evolution Electrocatalysis on Oxide Surfaces. *ChemCatChem* 2011, **3**(7): 1159-1165.
16. Rong X, Parolin J, Kolpak AM. A Fundamental Relationship between Reaction Mechanism and Stability in Metal Oxide Catalysts for Oxygen Evolution. *ACS Catal* 2016, **6**(2): 1153-1158.
17. Takeda Y, Hashino T, Miyamoto H, Kanamaru F, Kume S, Koizumi M. Synthesis of SrNiO₃ and related compound, Sr₂Ni₂O₅. *Journal of Inorganic and Nuclear Chemistry* 1972, **34**(5): 1599-1601.
18. Oliveira FS, Pimentel PM, Oliveira RMPB, Melo DMA, Melo MAF. Effect of lanthanum replacement by strontium in lanthanum nickelate crystals synthesized using gelatin as organic precursor. *Materials Letters* 2010, **64**(24): 2700-2703.
19. Seki H, Saito T, Shimakawa Y. High Pressure Synthesis of SrFe_{1-x}Ni_xO₃. *Journal of the Japan Society of Powder and Powder Metallurgy* 2016, **63**(7): 609-612.
20. Sharma IB, Singh D. Solid state chemistry of Ruddlesden-Popper type complex oxides. *Bulletin of Materials Science* 1998, **21**(5): 363-374.
21. Amow G, Davidson IJ, Skinner SJ. A comparative study of the Ruddlesden-Popper series, La_{n+1}Ni_nO_{3n+1} (n = 1, 2 and 3), for solid-oxide fuel-cell cathode applications. *Solid State Ionics* 2006, **177**(13-14): 1205-1210.
22. Zhang Z, Greenblatt M. Synthesis, Structure, and Properties of Ln₄Ni₃O_{10-δ} (Ln = La, Pr, and Nd). *Journal of Solid State Chemistry* 1995, **117**(2): 236-246.

23. Takeda Y, Kanno R, Sakano M, Yamamoto O, Takano M, Bando Y, *et al.* Crystal chemistry and physical properties of $\text{La}_{2-x}\text{Sr}_x\text{NiO}_4$ ($0 \leq x \leq 1.6$). *Materials Research Bulletin* 1990, **25**(3): 293-306.
24. Benloucif R, Nguyen N, Greneche JM, Raveau B. $\text{La}_{2-2x}\text{Sr}_{2x}\text{Ni}_{1-x}\text{Fe}_x\text{O}_{4-(x/2)+\delta}$: Magnetic and electron transport properties. *Journal of Physics and Chemistry of Solids* 1989, **50**(4): 435-440.
25. Rao CNR, Ganguly P, Singh KK, Ram RAM. A comparative study of the magnetic and electrical properties of perovskite oxides and the corresponding two-dimensional oxides of K_2NiF_4 structure. *Journal of Solid State Chemistry* 1988, **72**(1): 14-23.
26. Howlett JF, Flavell WR, Thomas AG, Hollingworth J, Warren S, Hashim Z, *et al.* Electronic structure, reactivity and solid-state chemistry of $\text{La}_{2-x}\text{Sr}_x\text{Ni}_{1-x}\text{Fe}_x\text{O}_{4-\delta}$. *Faraday Discussions* 1996, **105**(0): 337-354.
27. Gilev AR, Kiselev EA, Cherepanov VA. Homogeneity range, oxygen nonstoichiometry, thermal expansion and transport properties of $\text{La}_{2-x}\text{Sr}_x\text{Ni}_{1-y}\text{Fe}_y\text{O}_{4+\delta}$. *RSC Adv* 2016, **6**(77): 72905-72917.
28. Cohen RE. Origin of ferroelectricity in perovskite oxides. *Nature* 1992, **358**(6382): 136-138.
29. Masato K, Masahiro Y. Synthesis and Characteristics of Complex Multicomponent Oxides Prepared by Polymer Complex Method. *Bulletin of the Chemical Society of Japan* 1999, **72**(7): 1427-1443.
30. Erat S, Braun A, Piamonteze C, Liu Z, Ovalle A, Schindler H, *et al.* Entanglement of charge transfer, hole doping, exchange interaction, and octahedron tilting angle and their influence on the conductivity of $\text{La}_{1-x}\text{Sr}_x\text{Fe}_{0.75}\text{Ni}_{0.25}\text{O}_{3-\delta}$: A combination of x-ray spectroscopy and diffraction. *Journal of Applied Physics* 2010, **108**(12): 124906.

31. Louie MW, Bell AT. An Investigation of Thin-Film Ni–Fe Oxide Catalysts for the Electrochemical Evolution of Oxygen. *J Am Chem Soc* 2013, **135**(33): 12329-12337.
32. Forslund RP, Mefford JT, Hardin WG, Alexander CT, Johnston KP, Stevenson KJ. Nanostructured LaNiO₃ Perovskite Electrocatalyst for Enhanced Urea Oxidation. *ACS Catal* 2016, **6**(8): 5044-5051.
33. Bhavaraju S, DiCarlo JF, Scarfe DP, Jacobson AJ, Buttrey DJ. Electrochemical oxygen intercalation in La₂NiO₄ + δ crystals. *Solid State Ionics* 1996, **86**: 825-831.
34. Conway BE. *Electrochemical Supercapacitors*. Springer US: Boston, MA, 1999.
35. Mefford JT, Hardin WG, Dai S, Johnston KP, Stevenson KJ. Anion charge storage through oxygen intercalation in LaMnO₃ perovskite pseudocapacitor electrodes. *Nat Mater* 2014, **13**(7): 726-732.
36. Sreedhar K, Honig JM. Low-Temperature Electron Transport Properties of La_{2-x}Sr_xNiO₄ with $0.5 \leq x \leq 1.3$. *Journal of Solid State Chemistry* 1994, **111**(1): 147-150.
37. Anisimov VI, Bukhvalov D, Rice TM. Electronic structure of possible nickelate analogs to the cuprates. *Physical Review B* 1999, **59**(12): 7901-7906.
38. Falcón H, Carbonio RE, Fierro JLG. Correlation of Oxidation States in LaFe_xNi_{1-x}O_{3+ δ} Oxides with Catalytic Activity for H₂O₂ Decomposition. *Journal of Catalysis* 2001, **203**(2): 264-272.
39. Rozenberg GK, Milner AP, Pasternak MP, Hearne GR, Taylor RD. Experimental confirmation of a *p*–*p* intraband gap in Sr₂FeO₄. *Physical Review B* 1998, **58**(16): 10283-10287.

40. Ritzmann AM, Muñoz-García AB, Pavone M, Keith JA, Carter EA. Ab Initio DFT+U Analysis of Oxygen Vacancy Formation and Migration in $\text{La}_{1-x}\text{Sr}_x\text{FeO}_{3-\delta}$ ($x = 0, 0.25, 0.50$). *Chem Mater* 2013, **25**(15): 3011-3019.
41. Mogni L, Prado F, Ascolani H, Abbate M, Moreno MS, Manthiram A, *et al.* Synthesis, crystal chemistry and physical properties of the Ruddlesden–Popper phases $\text{Sr}_3\text{Fe}_{2-x}\text{Ni}_x\text{O}_{7-\delta}$ ($0 \leq x \leq 1.0$). *Journal of Solid State Chemistry* 2005, **178**(5): 1559-1568.
42. Torrance JB, Lacorre P, Nazzari AI, Ansaldo EJ, Niedermayer C. Systematic study of insulator-metal transitions in perovskites RNiO_3 ($R=\text{Pr}, \text{Nd}, \text{Sm}, \text{Eu}$) due to closing of charge-transfer gap. *Physical Review B* 1992, **45**(14): 8209-8212.
43. Lee Y-L, Lee D, Wang XR, Lee HN, Morgan D, Shao-Horn Y. Kinetics of Oxygen Surface Exchange on Epitaxial Ruddlesden–Popper Phases and Correlations to First-Principles Descriptors. *J Phys Chem Lett* 2016, **7**(2): 244-249.
44. Bard AJ, Faulkner LR. Kinetics of Electrode Reactions. *Electrochemical Methods: Fundamentals and Applications*, 2nd edn. John Wiley & Sons, Inc.: New York, NY, 2001, pp 124-132.
45. Nørskov JK, Abild-Pedersen F, Studt F, Bligaard T. Density functional theory in surface chemistry and catalysis. *Proceedings of the National Academy of Sciences* 2011, **108**(3): 937-943.
46. Hardin WG, Slanac DA, Wang X, Dai S, Johnston KP, Stevenson KJ. Highly Active, Nonprecious Metal Perovskite Electrocatalysts for Bifunctional Metal–Air Battery Electrodes. *J Phys Chem Lett* 2013, **4**(8): 1254-1259.
47. Suntivich J, Gasteiger HA, Yabuuchi N, Shao-Horn Y. Electrocatalytic Measurement Methodology of Oxide Catalysts Using a Thin-Film Rotating Disk Electrode. *J Electrochem Soc* 2010, **157**(8): B1263-B1268.
48. Kobussen AGC, van Buren FR, Broers GHJ. The influence of the particle size distribution on the measurement of oxygen ion diffusion coefficients in

- La_{0.50}Sr_{0.50}CoO_{3-y}. *Journal of Electroanalytical Chemistry and Interfacial Electrochemistry* 1978, **91**(2): 211-217.
49. Van Buren FR, Broers GHJ, Bouman AJ, Boesveld C. An electrochemical method for the determination of oxygen ion diffusion coefficients in La_{1-x}Sr_xCoO_{3-y} compounds. *Journal of Electroanalytical Chemistry and Interfacial Electrochemistry* 1978, **87**(3): 389-394.
 50. Petříček V, Dušek M, Palatinus L. Crystallographic Computing System JANA2006: General features. *Zeitschrift für Kristallographie*; 2014. p. 345.
 51. Goodenough JB, Ramasesha S. Further evidence for the coexistence of localized and itinerant 3d electrons in La₂NiO₄. *Materials Research Bulletin* 1982, **17**(3): 383-390.
 52. Kresse G, Furthmüller J. Efficient iterative schemes for *ab initio* total-energy calculations using a plane-wave basis set. *Physical Review B* 1996, **54**(16): 11169-11186.
 53. Blöchl PE. Projector augmented-wave method. *Physical Review B* 1994, **50**(24): 17953-17979.
 54. Perdew JP, Burke K, Ernzerhof M. Generalized Gradient Approximation Made Simple. *Physical Review Letters* 1996, **77**(18): 3865-3868.
 55. Gou G, Grinberg I, Rappe AM, Rondinelli JM. Lattice normal modes and electronic properties of the correlated metal LaNiO₃. *Physical Review B* 2011, **84**(14): 144101.
 56. Shein IR, Shein KI, Kozhevnikov VL, Ivanovskii AL. Band structure and the magnetic and elastic properties of SrFeO₃ and LaFeO₃ perovskites. *Physics of the Solid State* 2005, **47**(11): 2082-2088.

Chapter 5: Highly Active Perovskite and Ruddlesden-Popper Composite Electrocatalysts for Water Oxidation

5.1 INTRODUCTION

For renewable solar and wind energy, strategies are needed to address the intermittency of energy generation combined with peak demand schedules. One proposed solution to this problem is to store the excess energy in the form of chemical fuels by splitting water into H_2 and O_2 . Unfortunately, the efficiency of water splitting remains a large technological barrier due to the slow kinetics of the oxygen evolution reaction (OER, $4\text{OH}^- \rightarrow \text{O}_2 + 2\text{H}_2\text{O} + 4\text{e}^-$). Even with precious-metal oxide catalysts such as IrO_2 and RuO_2 ,² a large (≥ 400 mV) overpotential is required.³ Many studies have attempted to reduce the overpotential required for the OER not only to promote inexpensive hydrogen generation, but to also improve the efficiency of metal-air batteries and regenerative fuel-cells.⁴ To reduce the cost of electrode materials and improve catalytic efficiencies, non-precious metal oxides which are stable in alkaline conditions have recently been the focus of extensive research.⁵ For the perovskite family of oxides^{3, 6} very high specific ($\text{mA cm}^{-2}_{\text{oxide}}$) and mass ($\text{mA mg}^{-1}_{\text{oxide}}$) activities have been reported,^{7, 8} with overpotentials below 400 mV to achieve 10 mA cm^{-2} .^{1, 8}

The perovskite crystal structure accommodates a large variety of elements and elemental substitutions, which allows for the precise synthetic tuning of the physical, chemical and electronic properties⁹ to promote oxygen electrocatalysis.^{6, 10, 11} Perovskites have the nominal formula $\text{ABO}_{3\pm\delta}$, where A is typically a rare-earth or alkaline ion, and B is a transition metal ion.^{6, 10, 11} The oxygen content (δ) can also be regulated by chemical substitution of lower-valence A site ions, such as in $\text{La}_{1-x}\text{Sr}_x\text{CoO}_{3-\delta}$,⁸ to create oxygen vacancies. These vacancies promote a more energetically favorable lattice-oxygen mediated (LOM) OER mechanism, relative to the adsorbate evolution mechanism.^{8, 12}

Building upon theoretical^{2, 12} and experimental^{8, 13} work that demonstrated that oxygen vacancies and highly covalent Co 3*d* - O 2 2*p* bonding was responsible for the exceptional catalytic activity of SrCoO_{2.7}, it was predicted that SrNiO₃ would be more covalent and thus more catalytically active.¹² Unfortunately, this material does not form a perovskite phase at room temperature,¹⁴ and Sr solubility in LaNiO₃ has been reported to be limited to ~20%¹⁵ before catalytically inactive secondary phases form.¹⁶ In contrast, the *n*=1 Ruddlesden-Popper (RP) crystal structure (A_{*n*+1}BO_{3*n*+1}) was demonstrated to accommodate 75% or more Sr substitution¹⁷ and electronic structures that are not realizable in perovskites.^{1, 18} To take advantage of these observations, a series of highly active La_{0.5}Sr_{1.5}Ni_{1-x}Fe_xO_{4+δ} electrocatalysts was synthesized by calcination at high temperature of a charred polyester gel (polymerizable complex) method for *x* = 0 to 1. On the basis of experimental and DFT calculations, it was observed that cross-gap hybridization between Ni and Fe 3*d* and O 2*p* orbitals gave rise to exceptional catalytic activity at *x* = 0.3 (1930 mA mg⁻¹_{ox}), wherein Ni-O-Fe bridges were maximized.¹

The morphology and surface functionality of nanostructured catalysts from sol-gel synthesis may in principle be quite different than those from solid state synthesis and the polymerizable complex method¹ described above. Metal and metal-oxide nanostructured catalysts have been synthesized in reverse phase water-in-oil microemulsions, in which nanometer-sized water droplets are stabilized in an oil phase with a surfactant and cosolvent, to tune the surface functionality and catalytic activity.^{19, 20, 21, 22} Nanoparticle nucleation and growth is spatially confined within a micellar or bicontinuous water phase, the shape of which is typically controlled by varying the ratio of water-to-surfactant and oil, and the chemical structure of the oil and surfactant.^{23, 24, 25} Morphological control of metal oxides can promote preferential crystalline facets, such as {001}, that increases the active-site density, oxygen diffusion and exchange, and surface

moieties that enhance catalysis.^{26, 27} Reverse phase microemulsions were used to synthesize $\text{La}_{0.5}\text{Sr}_{0.5}\text{CoO}_{3-\delta}$ nanowires which increased the number of catalytically active sites, as compared to spheres, and improved their OER activity.²² Similarly, the oxygen diffusivity and resulting oxygen electrocatalysis rates were increased for $\text{La}_2\text{NiO}_{4\pm\delta}$ nanorods synthesized in reverse micelles.^{20, 21} The method used to synthesize complex metal oxide catalysts can significantly impact their catalytic activity for a fixed elemental precursor stoichiometry.²⁸ Therefore, novel synthetic methods would be of interest to form highly active perovskite⁸ and RP¹ electrocatalysts, which used controlled precipitation and charring of a polymerized complex, respectively.

Herein, we introduce new highly active electrocatalysts for the OER, a nickel-based perovskite $\text{La}_{0.4}\text{Sr}_{0.6}\text{Ni}_{0.8}\text{Fe}_{0.2}\text{O}_{3\pm\delta}$ (LSNF) and a La-free Ruddlesden-Popper (RP) oxide $\text{Sr}_4\text{Ni}_{2.4}\text{Fe}_{0.6}\text{O}_{10\pm\delta}$ (SNF), both synthesized in reverse microemulsions. Whereas modest phase impurities were present, they were significantly less prevalent than for the charred polymerized complex method*ref ours and classical*. To promote high catalytic activities and utilize the more energetically favorable lattice oxygen mediated OER mechanism,⁸ elemental substitution of 60% Sr for La in LaNiO_3 was performed to increase Ni-O bond covalency¹² in the perovskite phase. Complete Sr substitution for La and targeting of the $n=3$ RP phase was performed to maximize Ni-O bond covalency in the RP phase and triple the amount of perovskite units as compared to the $n=1$ phase.²⁹ Fe was substituted for 20% Ni in LSNF and SNF to introduce triple band overlap of Fe and Ni 3d orbitals with O 2p, which was previously demonstrated to significantly enhance the OER activity for other RP catalysts.^{1, 30, 31} We demonstrate that these elemental substitutions result in exceptional catalytic enhancement and small Tafel slopes compared to LaNiO_3 , wherein the mass activity is increased by over 30 fold for SNF (1541 vs 40 $\text{mA mg}^{-1}_{\text{ox}}$).

All chemicals were used as-received. Isooctane (2,2,4-trimethylpentane, $\geq 99\%$), 1-butanol ($\geq 99\%$), cetrimonium bromide (CTAB, $\geq 99\%$), and 5 wt% Nafion solution in lower alcohols were purchased from Sigma-Aldrich. Lanthanum(III) nitrate hexahydrate (99.995%), strontium(II) nitrate hexahydrate (99%), nickel(II) nitrate hexahydrate (99%), iron(III) nitrate non-anhydrate (99.99%), cobalt(II) hexahydrate ($\geq 99\%$), tetramethylammonium hydroxide pentahydrate (TMAOH, 99%), and potassium hydroxide ($\geq 85\%$) were obtained from Fisher Scientific. Millipore high purity water (DI water, 18 M Ω) was used. Oxygen (research grade, 99.999% purity) and argon (research grade, 99.999% purity) were obtained from Praxair. Ethanol (Absolute 200 proof) was obtained from Aaper Alcohol. Vulcan XC72 carbon (VC) was purchased from Cabot Corporation and ball-milled prior to use.

5.2 RESULTS AND DISCUSSION

$\text{LaNiO}_{3\pm\delta}$ (LNO), $\text{La}_{0.4}\text{Sr}_{0.6}\text{Ni}_{0.6}\text{Fe}_{0.4}\text{O}_{3\pm\delta}$ (LSNF) and $\text{Sr}_3\text{Ni}_{2.4}\text{Fe}_{0.6}\text{O}_{10\pm\delta}$ (SNF) were synthesized using a modified reverse phase water-in-oil microemulsion²² followed by crystallization and annealing. These stoichiometries are based on the feed ratio of elements into each synthesis. Reverse microemulsions containing the hydrolysis agent and required cations were each prepared (solutions abbreviated as HYD and CAT, respectively) by adding 3 g of CTAB to a mixture of 15 mL of isooctane and 3 mL of 1-butanol. The solutions were stirred to break up aggregated CTAB particles such that upon addition of water, all CTAB is easily solvated. A turbid, homogenous solution in which no bulk particles of CTAB are visible indicated that the CTAB was adequately dispersed. 4 mL of 1 M KOH (4 mmol) was added to the HYD solution, under stirring, after which the solution rapidly became clear which indicated successful formation of the water-in-oil

microemulsion. Separately, 4 mL of a variable molarity (0.327 M total for LNO, 0.356 M for LSNF and 0.348 M for SNF) alkali and metal nitrate solution is added to the CAT solution under stirring, transforming it from turbid to clear almost immediately. The same ratio of hydroxide ions in the HYD solution ($[\text{OH}^-]$), to cations in the CAT solution ($[\text{M}]$) as Zhao et al.²² used, modified to account for the average oxidation state (z) of cations in the nitrate salts, $\text{M}(\text{NO}_3)_z$, such that $[\text{OH}^-]:z[\text{M}] = 11/9$ was maintained.

The HYD and CAT solutions were left stirring for an hour after becoming transparent, to ensure complete formation of the reverse microemulsion phase. After one hour, the CAT solution was added drop-wise, over the course of 1 - 2 minutes, to the vigorously stirring (~ 1200 rpm) HYD solution. 10 minutes after the CAT solution was completely transferred, the HYD solution stir-rate was reduced to 600 rpm to minimize micellar collision and potential nanoparticle aggregation or Ostwald ripening. Shortly after addition of the CAT solution, the reverse microemulsion becomes colored and turbid, indicating the onset of nanoparticle nucleation via hydrolysis, and likely transformation of the spherical water-in-oil micelles to a bicontinuous micellar structure.^{23, 26} The reactant solution was left to stir for 6 hours, and then let statically age (no stirring) for 18 - 24 hours to decrease hydroxide nanoparticle size and improve phase purity.³²

After aging, hydroxide precipitate was collected via antisolvent precipitation using EtOH and washed via centrifugation as previously reported.²¹ After washing, the particles are suspended in DI water, probe sonicated, nebulized into liquid N_2 using a commercial spray bottle, followed by lyophilization at -10°C and ~ 50 mTorr to facilitate complete sublimation of the ice.³³ Finally, the dried nanoparticle powder is crystallized in a tube furnace under 200 sccm of flowing, dehumidified, O_2 . LaNiO_3 was crystallized at 650°C under pure O_2 with a hold of only 30 minutes, while $\text{La}_{0.6}\text{Sr}_{0.4}\text{Ni}_{0.6}\text{Fe}_{0.4}\text{O}_3$ was

crystallized at 825°C and held there for 5 hours. All catalyst compositions are furnace-cooled to room temperature under their respective flowing gas.

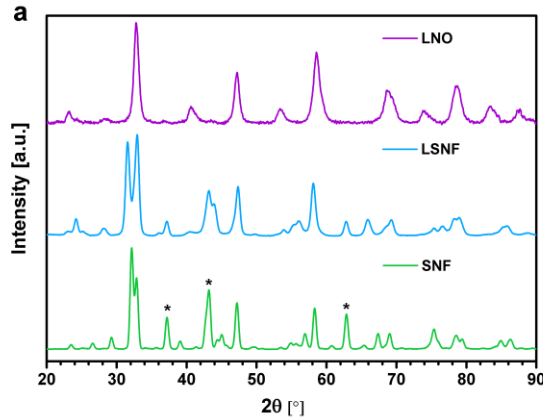


Figure 5.1: X-ray diffraction patterns of SNF, LSNF and LNO electrocatalysts

X-ray diffraction, shown in Figure 5.1a, indicates that LNO is a phase pure, $R\bar{3}c$ rhombohedral perovskite with a crystallite size of ~ 11 nm calculated on the most intense reflection arising from a single crystallographic plane, $\{024\}$. The XRD pattern for LSNF indicates a multi-phase system in which NiO and the perovskite phase are present. The XRD pattern for SNF reveals that it crystallized in the $n=1$ RP phase ($\text{Sr}_2(\text{Ni,Fe})\text{O}_{4\pm\delta}$) occupying the $I4/mmm$ space group,³⁴ with ~ 15 wt% NiO in addition. The NiO spectrum is characterized by the intense reflections seen at 35° , 42.5° , and 62.5° in Figure 5.1a. The existence of NiO impurities is consistent with the formation of the $n=1$ RP phase, rather than the $n=3$, as the excess Ni would have precipitated out of the crystal structure and oxidized. The crystallite size of each sample was estimated using the Scherrer equation to be 11, 12 and 14 nm, for LNO, LSNF and SNF, respectively. These sizes are consistent with the increasing crystallization temperatures used for the nickelates (650, 825 and 950°C), and thus increased sintering. To contrast the capabilities of the reverse-

phase water-in-oil microemulsion synthesis to successfully incorporate Sr, Ni and Fe into the RP crystal structure, LSNF and SNF were also synthesized using a modified Pechini method¹ which does not involve aqueous hydrolysis or the formation of hydroxide precursor particles.³⁵ The resulting XRD patterns are shown in Appendix E (Figure E.1) wherein it is unclear if any perovskite or RP phase formed due the large amount of untargeted secondary phases present. Transmission electron microscopy in conjunction with EDX was used to examine the atomic-scale crystal structure and elemental homogeneity, and is shown in Figure 5.1b,c.

5.3 ELECTROCHEMICAL CHARACTERIZATION AND DISCUSSION

All electrochemical characterization and preparation of catalyst inks were performed as previously outlined.¹ Briefly, inks were prepared by adding 2 mL of a NaOH neutralized³⁶ 0.05 wt% Nafion solution to 2 mg of catalyst powder, bath sonicated for ≥ 1 hour, and 10 μL was drop cast onto a clean 5 mm (0.196 cm^2 , Pine Instruments) glassy carbon electrode (GCE) which was dried overnight. This resulted in a composite catalyst loading of $51\text{ }\mu\text{g}_{\text{total}}\text{ cm}^{-2}_{\text{geo}}$, yielding $15.3\text{ }\mu\text{g}_{\text{oxide}}\text{ cm}^{-2}_{\text{geo}}$ for catalysis tests (30 wt% on Vulcan Carbon, VC). All tests were carried out at room temperature in 0.1 M KOH (measured pH ≈ 12.8), performed in a standard 3 electrode cell using a CH Instruments Hg/HgO (1 M KOH) reference electrode, a Pt or Au wire counter electrode, and a film of catalyst ink on glassy carbon as the working electrode. All data were iR compensated to account for the electrolyte resistance ($46\text{ }\Omega$). Potentials are reported versus the regular hydrogen electrode (RHE), determined experimentally to be +0.8976 V vs. Hg/HgO (1 M KOH). OER testing was performed on pristine drop-cast electrodes using cyclic voltammetry (CV) by applying a potential from 1 to 2 V vs RHE at 10 mV/s

with a rotation rate of 1600 rpm in O₂-saturated 0.1 M KOH. The anodic and cathodic scans were averaged and iR corrected, and all data reported is the average of at least three independent tests, and representative polarization curves are shown in Figure E.2 in Appendix E.

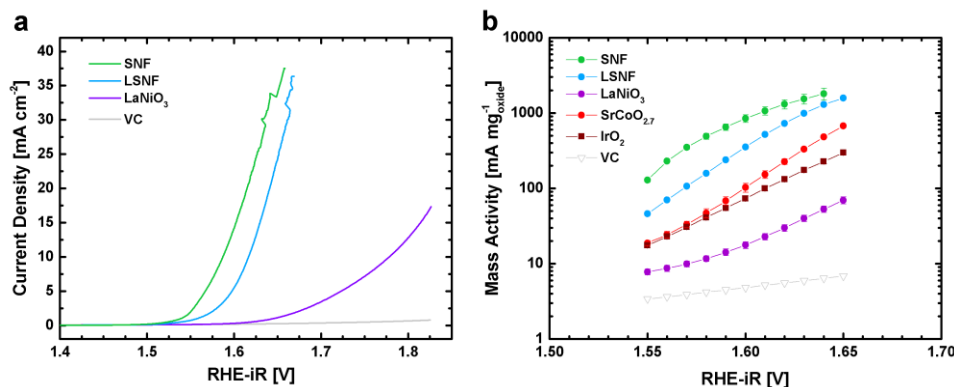


Figure 5.2: Electrochemical characterization of the SNF, LSNF and LNO composites and comparison to recently reported non-precious metal oxide catalysts.

a) Representative OER polarization curves of geometric current density ($\text{mA cm}^{-2}_{\text{geo}}$; $A_{\text{GCE}} = 0.196 \text{ cm}^2$) and b) Tafel presentation of catalyst mass activity ($\text{mA mg}^{-1}_{\text{ox}}$) compared to other leading oxides. {Hardin, 2017 #167} All tests are performed in O₂ saturated 0.1 M KOH at 10 mV s^{-1} and 1600 rpm. All values shown are the results of at least three independent tests, and all catalysts are 30 wt% on VC with a total electrode loading of $51 \text{ ug cm}^{-2}_{\text{geo}}$, yielding $15.3 \text{ ug}_{\text{ox}} \text{ cm}^{-2}_{\text{geo}}$, with the exception of IrO₂ which was tested at 20 wt% on VC ($10.2 \text{ ug}_{\text{ox}} \text{ cm}^{-2}_{\text{geo}}$). VC is Cabot XC72 Vulcan Carbon.

Electrocatalysis of the OER is shown for SNF, LSNF and LNO in Figure 5.2. Upon 60% Sr substitution for La, and 20% Fe substitution for Ni, the mass activity of LSNF increased by approximately an order of magnitude as compared to LNO (Figure 5.2b). Complete Sr substitution for La in the RP phase SNF catalyst further increased the mass activity by ~50% to $1541 \text{ mA mg}^{-1}_{\text{ox}}$ at 1.63 V vs RHE-iR. Catalysis with SNF also

exhibits a small Tafel slope of 55 mV dec^{-1} and reaches a benchmark current density of $10 \text{ mA cm}^{-2}_{\text{geo}}$ at only 361 mV overpotential, compared to 388 and 552 mV for LSNF and LNO, respectively. Figure 5.2b clearly illustrates that at all potentials, the nickelate activity trend is $\text{SNF} > \text{LSNF} > \text{LNO}$. The activity mass activity of SNF is superior to that of leading OER catalysts, IrO_2 and $\text{SrCoO}_{2.7}$. The precious metal oxide IrO_2 is widely used commercially given its high activity and stability in both acid and alkaline environments despite the high cost.³⁷ Furthermore, the perovskite-phase $\text{SrCoO}_{2.7}$ possess highly covalent Co $3d$ - O $2p$ interactions² that promote an energetically favorable OER mechanism¹² wherein lattice oxygen participates⁸ in the formation of O_2^- .

Figure 5.3 compares the mass activity of the nickelate catalysts to IrO_2 and $\text{SrCoO}_{2.7}$ at 1.63 V vs RHE-iR. Remarkably, SNF is more than 4 and 8 times as active as $\text{SrCoO}_{2.7}$ and IrO_2 , respectively. In fact, the activity of SNF (1541 mA mg^{-1}) approaches that of one of the most active known crystalline catalysts, $n=1$ RP $\text{La}_{0.5}\text{Sr}_{1.5}\text{Ni}_{0.7}\text{Fe}_{0.3}\text{O}_{4+\delta}$ (1930 vs $1541 \text{ mA mg}^{-1}_{\text{ox}}$).¹ Likewise, LSNF ($991 \text{ mA mg}^{-1}_{\text{ox}}$) is one of the most active perovskites for the OER, by mass, ever reported, with an activity of about half of that of the above RP phase

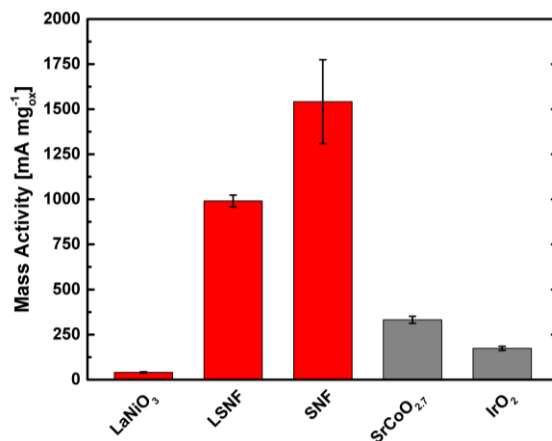


Figure 5.3: Selected catalyst mass activities at 1.63 V vs RHE-iR

The values for SrCoO_{2.7} and IrO₂ are taken from Hardin et al.

In our recent work, the high activity of LSNF was explained in terms of cross-gap hybridization between Fe and Ni 3d with the O 2p band based on experimental and DFT results. Building on this study, an analogous schematic band diagram of the expected partial density of states (PDOS) for the LSNF electrocatalyst is presented in Figure 5.4. LaNiO₃ exists at room temperature in the distorted rhombohedral crystal structure and is a metal-like conductor with significantly covalent O 2p - Ni 3d character near the Fermi level (E_F).^{12, 38, 39} The absolutely limit of Sr substitution into LaNiO₃ before the hexagonal phase occurs¹⁴ is not known, but the band structures of SrNiO₃,⁴⁰ La_{1-x}Sr_xMnO₃,^{41, 42} and La_{1-x}Sr_xFeO₃⁴¹ provide instructive examples. Complete Sr substitution for La results in significant hole doping of the O 2p band, with slight Ni character existing around E_F , but mostly above it.⁴⁰ 60% Sr substitution for La in La_{0.4}Sr_{0.6}MnO_{3±δ} shifts E_F down relative to the O 2p, also resulting in hole injection. This is reflected in the middle panel of Figure 5.4, where the O 2p level exists across E_F , and the Ni 3d σ* level has been oxidized. In this case, there is charge compensation in La_{1-x}Sr_xNiO_{3±δ} by both

oxygen vacancy formation, and partial Ni^{3+} oxidation. As Ni in LaNiO_3 is in a low-spin $t_{2g}^6 e_g^1$ configuration,⁴³ partial Ni oxidation will remove electron density from the σ^* band. As Fe is less electronegative and exists in a high-spin $t_{2g}^3 e_g^2$ configuration,⁴¹ the greater crystal field splitting and lesser electronegativity will create Fe σ^* at or above the Ni σ^* band, while the Fe π^* band will exist below nickel's. This effect of Fe is shown schematically in the right-most panel in Figure 5.4. The resulting schematic band structure suggested for LSNF is similar to that for highly active Ni-Fe oxyhydroxides,³⁰ $\text{Ba}_{0.5}\text{Sr}_{0.5}\text{Co}_{0.8}\text{Fe}_{0.2}\text{O}_{3-\delta}$ (BSCF),³¹ and $\text{La}_{0.5}\text{Sr}_{1.5}\text{Ni}_{0.7}\text{Fe}_{0.3}\text{O}_{4+\delta}$.¹ Thus, we expect that cross-gap hybridization across the Ni-Fe-O bridge in the LSNF perovskite creates a large amount of bandwidth near E_F to easily facilitate redox switching between the catalyst and OER intermediates, resulting in an exceptional catalytic activity.

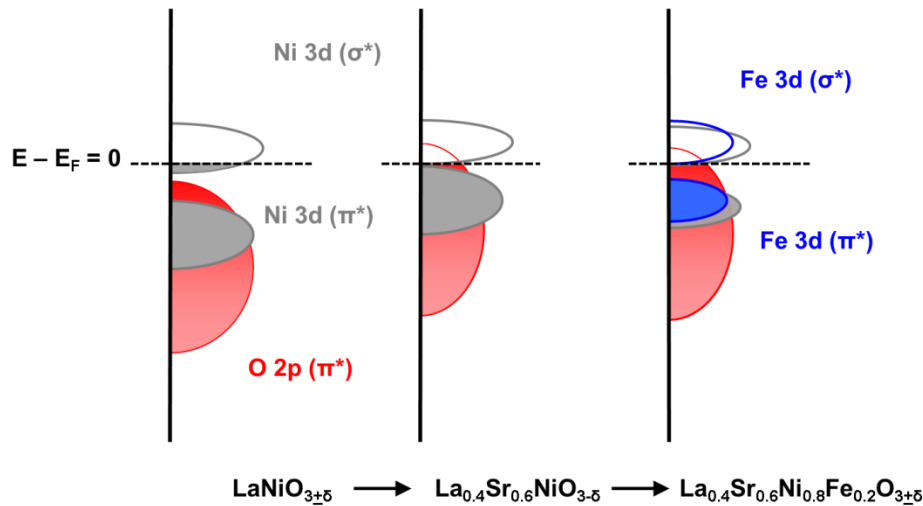


Figure 5.1: Schematic of the expected band diagram of $\text{LaNiO}_{3\pm\delta}$ as first Sr and then Fe are substituted into it

As Sr^{2+} is substituted for La^{3+} , the relative position of the O $2p$ band and the Ni $3d$ band will rise relative to the fermi level, consistent with Ni taking on a more oxidized character through charge compensation. Likely hole doping of the O $2p$ should results in oxygen vacancy formation. The

elemental substitution of Fe for Ni will introduce new Fe 3d π^* and σ^* bands, with strong covalent hybridization between $e_g(\text{Ni})$, $p(\text{O})$ and $e_g(\text{Fe})$ bands near the Fermi level.

The remarkable activities seen for the LSNF perovskite as a consequence of the electronic structure of the catalyst also depend upon the effect of the crystal structure and surface composition, which are influenced in part by the nucleation and growth in the microemulsion prior to calcination. The formation of metal oxide precursor particles by aqueous hydrolysis can impart distinct, beneficial surface moieties in the final crystalline oxide,²⁸ such as hydroxylated lattice oxygen which has been suggested to enhance the OER.³³ Upon addition of the CAT solution to the HYD solution, the aqueous micelles containing the precipitation agent (KOH) and cations (La^{3+} , Sr^{2+} , Ni^{2+} , Fe^{2+}) begin to collide, fuse and exchange their contents before separating.²⁴ Upon exchange of micellar content, hydrolysis of the cations occurs and hydroxide nanoparticles begin to nucleate and grow within the aqueous micelles. The rate of hydrolysis is governed by the Pourbaix behavior of the cations for a given local pH and cation concentration within the micelles,⁴⁴ so addition of the CAT to the rapidly stirring HYD is required ensure good micellar exchange and equilibrium solution conditions for hydrolysis.

Additionally, the hydroxide nanoparticles that form within the micellar network can exhibit preferential shape control directed by the type and concentration of ligands that are present within the micelle, such as the CTA^+ cation which will be electrostatically attracted to the anionic hydroxide surfaces. Furthermore, the presence of surfactants can also direct the aggregation and assembly nuclei, giving rise to unique morphologies such as nanorods^{20, 22} or mesoporous metal oxides.⁴⁵ These morphologies often promote specific crystalline facets, such as the $\{001\}$,²¹ and surface chemistries (facile surface oxygen exchange, etc)^{19, 20} which are capable of enhancing catalytic processes. While aqueous hydrolysis of cations possessing significantly different

hydrolysis rates can cause compositional stratification from the core to the surface of hydroxide precursor particles, leading to compositional inhomogeneity in the final crystalline phase, the formation of small amounts of secondary phases such as NiO and Fe_xO_y can actually enhance the OER activity, as seen in raney nickel.⁴⁶ In our case, the amounts of the impurity phases were estimated to be 15 wt%.

5.4 CONCLUSIONS

We have demonstrated that the reverse microemulsion synthetic scheme produces highly active OER catalyst phases with smaller amounts of unwanted secondary phases than the charred polymerized complex method. Despite the impurity phases, the mass activities among the highest reported for any perovskite or RP electrocatalysts. *The reverse microemulsion method produced precursor particles that crystallized into these mixtures containing highly covalent Ni-rich oxides for both SNF and LSNF.* The SNF RP catalyst is 38 fold more active than LaNiO_3 (1541 vs 40 $\text{mA mg}^{-1}_{\text{ox}}$), and generates over 8 times more current per mass than IrO_2 (174 $\text{mA mg}^{-1}_{\text{ox}}$) with a low Tafel slope of 55 mV dec^{-1} . These exceptional catalytic activities are further enabled by chemical substitution wherein Sr and Fe are substituted for La and Ni. Sr substitution increases the average oxidation state of Ni, while substitution of the less electronegative Fe introduces new Fe 3d orbitals at or above the Fermi level, to facilitate easy charge transfer between the catalyst and adsorbate via cross-gap hybridization.

5.5 ADDITIONAL INFORMATION

Additional Information Additional Information Additional Information Additional Information Additional Information Additional Information are provided in Appendix m


5.6 REFERENCES

1. Hardin WG, Forslund RP, Abakumov AM, Rong X, Filimonov D, Alexander CT, *et al.* Exceptional Electrocatalytic Oxygen Evolution Via Tunable Charge Transfer Interactions in $\text{La}_{0.5}\text{Sr}_{1.5}\text{Ni}_{1-x}\text{Fe}_x\text{O}_{4+\delta}$ Ruddlesden-Popper Oxides. *Nat Mater* 2017.
2. Man IC, Su H-Y, Calle-Vallejo F, Hansen HA, Martínez JI, Inoglu NG, *et al.* Universality in Oxygen Evolution Electrocatalysis on Oxide Surfaces. *ChemCatChem* 2011, **3**(7): 1159-1165.
3. Zhu H, Zhang P, Dai S. Recent Advances of Lanthanum-Based Perovskite Oxides for Catalysis. *ACS Catal* 2015, **5**(11): 6370-6385.
4. Chen D, Chen C, Baiye ZM, Shao Z, Ciucci F. Nonstoichiometric Oxides as Low-Cost and Highly-Efficient Oxygen Reduction/Evolution Catalysts for Low-Temperature Electrochemical Devices. *Chem Rev* 2015, **115**(18): 9869-9921.
5. Hunter BM, Gray HB, Müller AM. Earth-Abundant Heterogeneous Water Oxidation Catalysts. *Chem Rev* 2016, **116**(22): 14120-14136.
6. Suntivich J, May KJ, Gasteiger HA, Goodenough JB, Shao-Horn Y. A Perovskite Oxide Optimized for Oxygen Evolution Catalysis from Molecular Orbital Principles. *Science* 2011, **334**(6061): 1383-1385.
7. Seitz LC, Dickens CF, Nishio K, Hikita Y, Montoya J, Doyle A, *et al.* A highly active and stable $\text{IrO}_x/\text{SrIrO}_3$ catalyst for the oxygen evolution reaction. *Science* 2016, **353**(6303): 1011-1014.
8. Mefford JT, Rong X, Abakumov AM, Hardin WG, Dai S, Kolpak AM, *et al.* Water electrolysis on $\text{La}_{1-x}\text{Sr}_x\text{CoO}_{3-\delta}$ perovskite electrocatalysts. *Nature Communications* 2016, **7**: 11053.
9. Galasso FS. *Structure, Properties and Preparation of Perovskite-Type Compounds*, vol. 5. Pergamon Press, 1969.

10. Bockris JO, Otagawa T. Mechanism of oxygen evolution on perovskites. *J Phys Chem* 1983, **87**(15): 2960-2971.
11. Hardin WG, Mefford JT, Slanac DA, Patel BB, Wang X, Dai S, *et al.* Tuning the Electrocatalytic Activity of Perovskites through Active Site Variation and Support Interactions. *Chem Mater* 2014, **26**(11): 3368-3376.
12. Rong X, Parolin J, Kolpak AM. A Fundamental Relationship between Reaction Mechanism and Stability in Metal Oxide Catalysts for Oxygen Evolution. *ACS Catal* 2016, **6**(2): 1153-1158.
13. Yagi S, Yamada I, Tsukasaki H, Seno A, Murakami M, Fujii H, *et al.* Covalency-reinforced oxygen evolution reaction catalyst. *Nature Communications* 2015, **6**: 8249.
14. Takeda Y, Hashino T, Miyamoto H, Kanamaru F, Kume S, Koizumi M. Synthesis of SrNiO₃ and related compound, Sr₂Ni₂O₅. *Journal of Inorganic and Nuclear Chemistry* 1972, **34**(5): 1599-1601.
15. Oliveira FS, Pimentel PM, Oliveira RMPB, Melo DMA, Melo MAF. Effect of lanthanum replacement by strontium in lanthanum nickelate crystals synthesized using gelatin as organic precursor. *Materials Letters* 2010, **64**(24): 2700-2703.
16. Seki H, Saito T, Shimakawa Y. High Pressure Synthesis of SrFe_{1-x}Ni_xO₃. *Journal of the Japan Society of Powder and Powder Metallurgy* 2016, **63**(7): 609-612.
17. Takeda Y, Kanno R, Sakano M, Yamamoto O, Takano M, Bando Y, *et al.* Crystal chemistry and physical properties of La_{2-x}Sr_xNiO₄ (0 ≤ x ≤ 1.6). *Materials Research Bulletin* 1990, **25**(3): 293-306.
18. Gilev AR, Kiselev EA, Cherepanov VA. Homogeneity range, oxygen nonstoichiometry, thermal expansion and transport properties of La_{2-x}Sr_xNi_{1-y}Fe_yO_{4+δ}. *RSC Adv* 2016, **6**(77): 72905-72917.

19. Das A, Xhafa E, Nikolla E. Electro- and thermal-catalysis by layered, first series Ruddlesden-Popper oxides. *Catalysis Today* 2016, **277, Part 2**: 214-226.
20. Ma X, Carneiro JSA, Gu X-K, Qin H, Xin H, Sun K, *et al.* Engineering Complex, Layered Metal Oxides: High-Performance Nickelate Oxide Nanostructures for Oxygen Exchange and Reduction. *ACS Catal* 2015, **5(7)**: 4013-4019.
21. Ma X, Wang B, Xhafa E, Sun K, Nikolla E. Synthesis of shape-controlled $\text{La}_2\text{NiO}_{4+\delta}$ nanostructures and their anisotropic properties for oxygen diffusion. *Chem Commun* 2015, **51(1)**: 137-140.
22. Zhao Y, Xu L, Mai L, Han C, An Q, Xu X, *et al.* Hierarchical mesoporous perovskite $\text{La}_{0.5}\text{Sr}_{0.5}\text{CoO}_{2.91}$ nanowires with ultrahigh capacity for Li-air batteries. *Proceedings of the National Academy of Sciences* 2012, **109(48)**: 19569-19574.
23. Pileni M-P. The role of soft colloidal templates in controlling the size and shape of inorganic nanocrystals. *Nat Mater* 2003, **2(3)**: 145-150.
24. Eastoe J, Hollamby MJ, Hudson L. Recent advances in nanoparticle synthesis with reversed micelles. *Advances in Colloid and Interface Science* 2006, **128–130**: 5-15.
25. Ganguli AK, Ganguly A, Vaidya S. Microemulsion-based synthesis of nanocrystalline materials. *Chemical Society Reviews* 2010, **39(2)**: 474-485.
26. Giannakas AE, Ladavos AK, Pomonis PJ. Preparation, characterization and investigation of catalytic activity for NO+CO reaction of LaMnO_3 and LaFeO_3 perovskites prepared via microemulsion method. *Applied Catalysis B: Environmental* 2004, **49(3)**: 147-158.
27. Garg N, Basu M, Upadhyaya K, Shivaprasad SM, Ganguli AK. Controlling the aspect ratio and electrocatalytic properties of nickel cobaltite nanorods. *RSC Adv* 2013, **3(46)**: 24328-24336.

28. Bell RJ, Millar GJ, Drennan J. Influence of synthesis route on the catalytic properties of $\text{La}_{1-x}\text{Sr}_x\text{MnO}_3$. *Solid State Ionics* 2000, **131**(3–4): 211-220.
29. Zhang Z, Greenblatt M. Synthesis, Structure, and Properties of $\text{Ln}_4\text{Ni}_3\text{O}_{10-\delta}$ (Ln = La, Pr, and Nd). *Journal of Solid State Chemistry* 1995, **117**(2): 236-246.
30. Conesa JC. Electronic Structure of the (Undoped and Fe-Doped) NiOOH O_2 Evolution Electrocatalyst. *J Phys Chem C* 2016, **120**(34): 18999-19010.
31. Merkle R, Mastrikov YA, Kotomin EA, Kuklja MM, Maier J. First Principles Calculations of Oxygen Vacancy Formation and Migration in $\text{Ba}_{1-x}\text{Sr}_x\text{Co}_{1-y}\text{Fe}_y\text{O}_{3-\delta}$ Perovskites. *J Electrochem Soc* 2011, **159**(2): B219-B226.
32. Soleymani M, Edrissi M. Preparation of manganese-based perovskite nanoparticles using a reverse microemulsion method: biomedical applications. *Bulletin of Materials Science* 2016, **39**(2): 487-490.
33. Hardin WG, Slanac DA, Wang X, Dai S, Johnston KP, Stevenson KJ. Highly Active, Nonprecious Metal Perovskite Electrocatalysts for Bifunctional Metal–Air Battery Electrodes. *J Phys Chem Lett* 2013, **4**(8): 1254-1259.
34. Takeda Y, Imayoshi K, Imanishi N, Yamamoto O, Takano M. Preparation and characterization of $\text{Sr}_{2-x}\text{La}_x\text{FeO}_4$ ($0 \leq x \leq 1$). *Journal of Materials Chemistry* 1994, **4**(1): 19-22.
35. Masato K, Masahiro Y. Synthesis and Characteristics of Complex Multicomponent Oxides Prepared by Polymer Complex Method. *Bulletin of the Chemical Society of Japan* 1999, **72**(7): 1427-1443.
36. Suntivich J, Gasteiger HA, Yabuuchi N, Shao-Horn Y. Electrocatalytic Measurement Methodology of Oxide Catalysts Using a Thin-Film Rotating Disk Electrode. *J Electrochem Soc* 2010, **157**(8): B1263-B1268.

37. Lee Y, Suntivich J, May KJ, Perry EE, Shao-Horn Y. Synthesis and Activities of Rutile IrO₂ and RuO₂ Nanoparticles for Oxygen Evolution in Acid and Alkaline Solutions. *J Phys Chem Lett* 2012, **3**(3): 399-404.
38. María Luisa M. Structural, magnetic and electronic properties of  perovskites (R = rare earth). *Journal of Physics: Condensed Matter* 1997, **9**(8): 1679.
[http://ej.iop.org/images/0953-8984/9/8/003/toc_img1.gif]
39. Zhou JS, Goodenough JB, Dabrowski B. Transition from Curie-Weiss to enhanced Pauli paramagnetism in RNiO₃ (R = La, Pr,...Gd). *Physical Review B* 2003, **67**(2): 020404.
40. Chen G-Y, Ma C-L, Chen D, Zhu Y. Robust half-metallicity of hexagonal SrNiO₃. *Journal of Solid State Chemistry* 2016, **233**: 438-443.
41. Abbate M, de Groot FMF, Fuggle JC, Fujimori A, Strebel O, Lopez F, *et al.* Controlled-valence properties of La_{1-x}Sr_xFeO₃ and La_{1-x}Sr_xMnO₃ studied by soft-x-ray absorption spectroscopy. *Physical Review B* 1992, **46**(8): 4511-4519.
42. Saitoh T, Bocquet AE, Mizokawa T, Namatame H, Fujimori A, Abbate M, *et al.* Electronic structure of La_{1-x}Sr_xMnO₃ studied by photoemission and x-ray-absorption spectroscopy. *Physical Review B* 1995, **51**(20): 13942-13951.
43. Zhang D, Song Y, Du Z, Wang L, Li Y, Goodenough JB. Active LaNi_{1-x}Fe_xO₃ bifunctional catalysts for air cathodes in alkaline media. *J Mater Chem A* 2015, **3**(18): 9421-9426.
44. Cushing BL, Kolesnichenko VL, O'Connor CJ. Recent Advances in the Liquid-Phase Syntheses of Inorganic Nanoparticles. *Chem Rev* 2004, **104**(9): 3893-3946.
45. Holmberg K. Surfactant-templated nanomaterials synthesis. *Journal of Colloid and Interface Science* 2004, **274**(2): 355-364.

46. Bates MK, Jia Q, Doan H, Liang W, Mukerjee S. Charge-Transfer Effects in Ni–Fe and Ni–Fe–Co Mixed-Metal Oxides for the Alkaline Oxygen Evolution Reaction. *ACS Catal* 2016, **6**(1): 155-161.

Chapter 6: Anion charge storage through oxygen intercalation in LaMnO_3 perovskite pseudocapacitor electrodes⁴

6.1 INTRODUCTION

Perovskite oxides have attracted significant attention as energy conversion materials for metal-air battery and solid oxide fuel cell electrodes due to their unique physical and electronic properties. Amongst these unique properties is the structural stability of the cation array in perovskites which can accommodate mobile oxygen ions under electrical polarization. However, while oxygen ion mobility and vacancies have been shown to play an important role in catalysis, their role in charge storage has yet to be explored. Herein we investigate the mechanism of oxygen vacancy mediated redox pseudocapacitance for a nanostructured lanthanum based perovskite, LaMnO_3 . This is the first example of anion-based intercalation pseudocapacitance as well as the first time oxygen intercalation has been exploited for fast energy storage. Whereas previous pseudocapacitor and rechargeable battery charge storage studies have focused on cation intercalation, the anion based mechanism presented here offers a new paradigm for electrochemical energy storage.

Carbon electric double-layer supercapacitors and the analogous metal-based pseudocapacitors play an intermediate role between traditional electrostatic capacitors and batteries in terms of energy density and power density.¹ As their charge and discharge rates are orders of magnitude faster than batteries, there have been considerable efforts to increase the energy densities of pseudocapacitor materials.² Metal oxides have gained significant interest due to their reversible faradaic surface reactions that allow for up to an order of magnitude greater energy storage than carbon based electric double layer

⁴Large parts of this chapter have been published as Mefford JT, Hardin WG, Dai S, Johnston KP, Stevenson KJ. Anion charge storage through oxygen intercalation in LaMnO_3 perovskite pseudocapacitor electrodes. *Nat Mater* 2014, **13**(7): 726-732.

capacitors. However, classic pseudocapacitor materials including RuO_2 , MnO_2 , and Ni(OH)_2 are limited by high cost, low capacities, or limited potential windows, respectively.³⁻⁵ For materials to exhibit high pseudocapacitance, fast, reversible faradaic redox reactions must occur at the electrode-electrolyte interface leading to a change in the extent of accumulated charge, Q , as a function of the potential, according to equation (6.1):

$$Q = C\Delta V \quad (6.1)$$

where ΔV is the potential change (V) and C is the pseudocapacitance (F).¹ The specific capacitance, C_s (F g^{-1}), of an electrode material can be evaluated using cyclic voltammetry (CV) from the area under the current-voltage curve during the cathodic sweep using equation (6.2):

$$C_s = \frac{1}{mv|V_c - V_a|} \int_{V_a}^{V_c} i(V) dV \quad (6.2)$$

where m is the mass loading of the electroactive material on the electrode (g), v is the scan rate for the measurement (V s^{-1}), V_c and V_a are the cathodic and anodic potentials respectively (V), and $i(V)$ is the current response (A) at potential V (V).¹

Currently, there are three accepted mechanisms of charge storage for pseudocapacitor electrodes.¹ The first, which is generally accepted to occur for all charged metal or metal oxide surfaces, involves the adsorption of ions from the electrolyte as a monolayer on the electrode surface. This effect may be manifested through the underpotential deposition of cations or through partial charge transfer between the metal centers of the electrode and electrolyte anions, the so called “electrosorption valency”.^{6,7} The second mechanism of pseudocapacitance involves redox reactions at the surface of the electrode such as proton exchange in the amorphous surface of RuO_2 ,³ and the third relies on the fast reversible intercalation of ions into the bulk of the material.^{8,9} While all of these mechanisms can be described as

pseudocapacitive due to changes in the oxidation state of the transition metal, only electrosorption valency has been demonstrated as an anion effect. A recent paper by Hahn *et al.* explored the role of cation vacancies in MnO_2 , demonstrating increased charge storage at faster rates through cation insertion into Mn vacancies.¹⁰ The question then arises, if materials with inherent cation vacancies can be exploited to increase charge storage through electrolyte cations, can materials with anion vacancies also be exploited to store charge through electrolyte anions?

Perovskite-type oxides, with the nominal formula ABO_3 , where A is a lanthanide or alkali earth element and B is a transition metal, have traditionally been studied as electrodes and oxide ion conducting electrolytes for solid oxide fuel cells (SOFCs) due to their structural stability at high temperatures and inherent nature to contain oxygen vacancies.¹¹ Further, the ability to aliovalently substitute ions with varying oxidation states at both the A and B sites allows a high amount of synthetic control over the electronic and physical properties of the material.¹¹⁻¹⁴ While these materials have been extensively investigated as energy conversion materials, few studies have demonstrated charge storage in perovskite structured materials.^{9,12-16} As such, this study aims to investigate the role of anion vacancies as charge storage sites for pseudocapacitive applications.

It is known that as the dimensions of metal oxide crystals are reduced, their pseudocapacitive responses increase dramatically.¹⁷ Further, nanoscale materials with oxygen vacancies demonstrate greater oxygen diffusion rates due to decreased transport lengths and larger potential gradients across the particles.¹⁸ However, traditional solid-state methods to synthesize perovskites yield microscale particles, limiting their applications to high-temperature SOFCs where conduction and oxygen diffusion rates are improved.¹¹ Using a colloidal synthetic scheme we have demonstrated the ability to

synthesize nanostructured perovskites with increased particle surface area and controlled crystallinity.¹⁹ In this study, we focus on the perovskite $\text{LaMnO}_{3+\delta}$ as an oxygen intercalation compound, because of its nature to accommodate both substoichiometric and superstoichiometric oxygen content, i.e. $-0.25 \lesssim \delta \gtrsim 0.25$.²⁰⁻²² The electrochemical role of oxygen vacancies in perovskites is investigated and compared between two LaMnO_3 samples—one containing a deficit of oxygen ions and one with a slight excess.

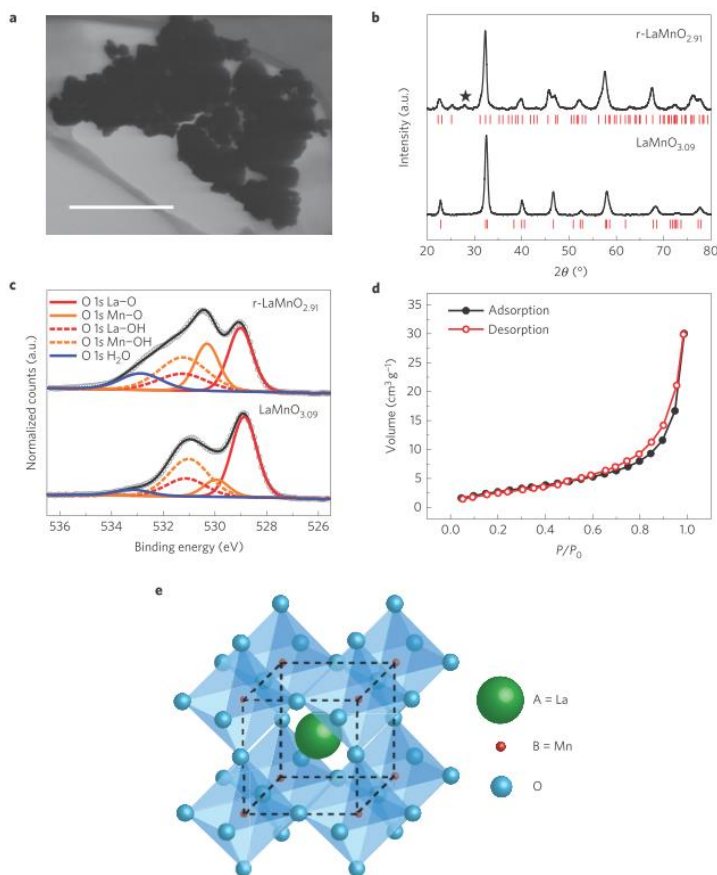


Figure 6.1: Nanocrystal morphology of $\text{LaMnO}_{3.09}$

(a), Dark-field scanning electron micrograph showing the small ($\sim 20\text{--}50\text{ nm}$) nanocrystals of $\text{LaMnO}_{3.09}$ that sinter into agglomerated particles after the calcination step. Scale bar, 500 nm. (b), X-ray diffraction spectra of $\text{LaMnO}_{3.09}$ and $r\text{-LaMnO}_{2.91}$ showing the conversion from rhombohedral to orthorhombic structure and high phase purities of the samples. The impurity peak at $\sim 28^\circ$ is a result of carbon products produced from the decomposition of the capping ligands from the precursor mixed hydroxides. (c), XPS O 1s spectra of $\text{LaMnO}_{3.09}$ and $r\text{-LaMnO}_{2.91}$ showing high degrees of surface hydroxylation in both samples. (d), N_2 BET data corresponding to a surface area of $10.6\text{ m}^2\text{ g}^{-1}$. (e), Idealized cubic ABO_3 perovskite structure

6.2 NANOSCALE PEROVSKITES

To obtain nanostructured particles, LaMnO_3 was synthesized using a previously developed reverse phase hydrolysis approach.¹⁵ The morphology of the nanocrystalline material can be seen in Figure 6.1a. Initially, dynamic light scattering (DLS) indicates small ~ 25 nm mixed La and Mn hydroxides are formed (Supplementary Figure F.1) which, when heated to 700°C in dry air, sinter to form larger agglomerates of nanocrystals with a Brunauer-Emmet-Teller (BET) surface area of $10.6\text{ m}^2\text{ g}^{-1}$ (Figure 6.1d). Although the overall particle size is larger than that of other thin film and powder pseudocapacitor electrodes, the porosity caused by sintering of the nanoparticle precursors in the LaMnO_3 powder allows for a high concentration of grain boundaries and defect sites which will be shown below to result in high material utilization. Iodometric titrations were performed to determine the average oxygen content of the $\text{LaMnO}_{3+\delta}$, yielding a value of $\delta = 0.09 \pm 0.02$.²¹ A reduced sample of $\text{r-LaMnO}_{3-\delta}$ was synthesized by taking the oxygen excess material and exposing it to 7% H_2 in Ar gas at 400°C . Iodometric titration of the reduced sample showed an oxygen vacancy content of $\delta = -0.09 \pm 0.02$. X-ray diffraction (XRD) indicated high purity for both samples, with the oxygen excess $\text{LaMnO}_{3.09}$ sample (PDF 01-073-8342 ICDD, 2004) converting from a rhombohedral to orthorhombic structure upon thermal reduction to $\text{r-LaMnO}_{2.91}$ (PDF 01-087-2014 ICDD, 1997). Scherrer analysis of the peak at 46.7° determined an average crystalline domain of 12 nm for $\text{LaMnO}_{3.09}$ which is similar to the precursor mixed hydroxide particle sizes. X-ray photoelectron spectroscopy (XPS) was used to characterize the chemical nature of the $\text{LaMnO}_{3\pm\delta}$ samples, where the oxygen 1s spectra are presented in Figure 6.1c. In both samples there exists a high degree of surface hydroxylation due to the Lewis acidity of oxygen vacancy sites as is commonly observed

in metal oxides.²³ However, if one neglects the contribution of adsorbed water on the surface of the material, the oxygen content of r-LaMnO_{3-δ} is ~12% less than LaMnO_{3+δ}.

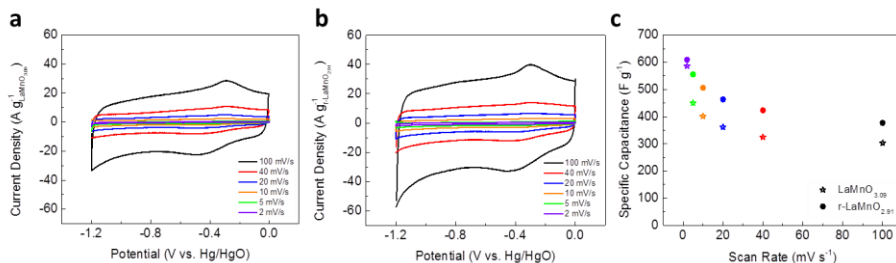


Figure 6.2: Electrochemical characterization of LaMnO_{3±δ}

a, b. Cyclic voltammograms for oxygen excess LaMnO_{3.09} (a) and oxygen deficient r-LaMnO_{2.91} (b) in Ar saturated 1M KOH at various scan rates. The redox peak at ~-0.3V vs Hg/HgO is indicative of the intercalation of OH⁻ ions into both samples. c, Specific capacitance versus scan rate for the 2 materials. *In all of these figures, the current and capacitance contributions of the carbon support have been subtracted out to clearly demonstrate the electrochemical characteristics of LaMnO_{3±δ}.

6.3 ELECTROCHEMICAL CHARACTERIZATION

The pseudocapacitive response of LaMnO_{3±δ} was characterized using cyclic voltammetry in 1M KOH. In order to explore the mechanistic aspects of charge storage, thin films of 0.051 mg_{composite} cm⁻² with LaMnO_{3±δ} loadings of 30 wt% on mesoporous carbon were used. Although low for practical pseudocapacitive applications, thin films are ideal for studying the mechanisms of charge storage, where the effects of grain boundaries, surface defects, and vacancies can be more clearly investigated.²⁴⁻²⁶ Figure 6.2a and 6.2b shows nearly rectangular current-voltage curves for LaMnO_{3.09} and r-LaMnO_{2.91} respectively, characteristic of an ideal pseudocapacitive response with redox peaks appearing near E_{1/2} = -0.3 V for both materials. As can be seen from the specific capacitance versus scan rate presented in Figure 6.2c, the capacitive envelope of the

cyclic voltammograms and the specific capacitance increases with an increase in oxygen vacancies in LaMnO_3 . However, at sufficiently low scan rates, the specific capacitance of the two materials approaches each other, with high specific capacitances of 586.7 F g^{-1} and 609.8 F g^{-1} for the oxygen excess and oxygen deficient samples, respectively. Interestingly, the increase in capacitance for the oxygen deficient sample of $\sim 4\%$ is similar to the 6% percent difference in oxygen content between the two materials. Considering the low surface area of the material, the high specific capacitances and remarkable response of the samples to increased oxygen vacancies as charge storage sites indicate that pseudocapacitive charge storage in $\text{LaMnO}_{3\pm\delta}$ extends into the bulk structure through a mechanism of oxygen intercalation as described below.

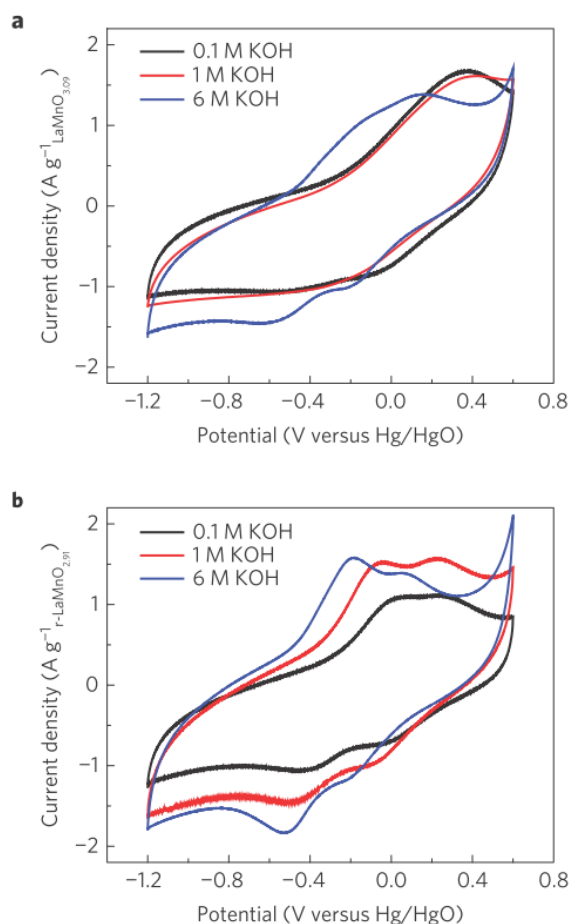


Figure 6.3: Effect of Electrolyte Concentration on Redox Reactions $\text{LaMnO}_{3\pm\delta}$

a, b. Cyclic voltammograms at a scan rate of 40 mV s^{-1} for unsupported $\text{LaMnO}_{3.09}$ (a) and $\text{r-LaMnO}_{2.91}$ (b). The charge stored increases and the position of the redox peaks shift to more negative potentials with increasing pH. Both peaks are therefore related to oxygen intercalation, with the peak centered at -0.4 V corresponding to $\text{Mn}^{2+} \leftrightarrow \text{Mn}^{3+}$ as oxygen vacancy sites are filled, and the peak at 0 V corresponding to $\text{Mn}^{3+} \leftrightarrow \text{Mn}^{4+}$ as excess oxygen is intercalated into the structure.

6.4 OXYGEN INTERCALATION

The idea of electrochemical oxygen intercalation was developed during the early *chimie douce* movement of the 1990s involving topotactic reactions whereby structural

elements are preserved during the reaction despite changes in chemical composition. Kudo *et al.* first demonstrated the reversible electrochemical intercalation of oxygen into a perovskite in alkaline conditions with room-temperature diffusion rates of up to $10^{-11} \text{ cm}^2 \text{ s}^{-1}$.²⁷ Since then, the reversible topotactic intercalation of oxygen has become a well-established phenomenon for perovskites and perovskite-derived structures.²⁷⁻³³ Mahesh *et al.* demonstrated that a high degree of oxygen intercalation can be exhibited even in oxygen excess $\text{LaMnO}_{3+\delta}$ to yield the cubic structure.³² However, until now the *chimie douce* oxygen intercalation method has generally been reserved as a synthesis procedure for high oxidation state transition metal oxides. Only one report takes advantage of the potential dependence of oxygen content in perovskites to make a low voltage rocking battery based on the shuttling of oxygen ions between perovskite electrodes.¹⁵ The results presented here for $\text{LaMnO}_{3\pm\delta}$ represent the first example of oxygen intercalation in high rate energy storage, as well as the first example of anion-based intercalation pseudocapacitance.

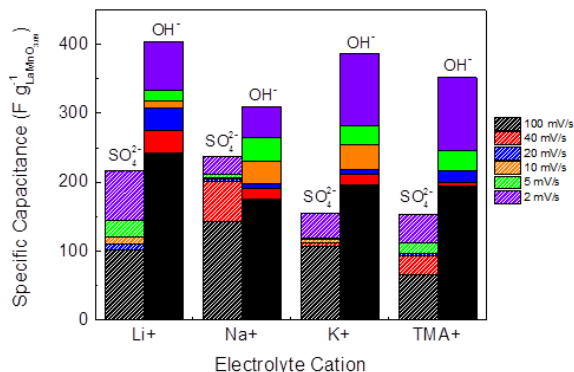


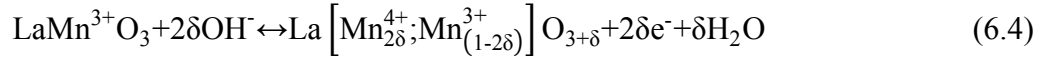
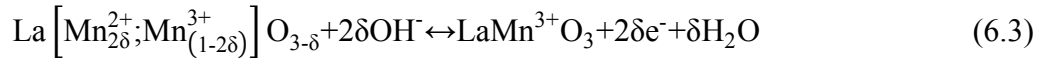
Figure 6.4: Electrolyte Studies of LaMnO_{3.09}

Specific capacitances for composite electrodes in neutral SO₄²⁻ electrolytes and alkaline electrolytes with varying sizes of cations (Electrolyte concentration = 0.1 N based on the anion contribution). The bars show the incremental addition of capacitance as the scan rate is reduced. LaMnO_{3+δ} exhibits a higher capacitance at all scan rates for alkaline electrolytes than for neutral electrolytes regardless of the cation size. The current and capacitance contributions of the carbon support have been subtracted out to elucidate the dominant charge storage species in LaMnO_{3.09}.

In order to elucidate the redox features of oxygen intercalation in LaMnO_{3±δ}, cyclic voltammetry was performed on unsupported samples in potassium based electrolytes of varying pH. Figures 6.3a and 6.3b show the electrochemical response of LaMnO_{3.09} and r-LaMnO_{2.91}, respectively, to the increase in concentration of hydroxide ions. The CVs of the reduced sample exhibit a separate peak at more negative potentials corresponding to oxidation of lower oxidation state Mn²⁺ through oxygen intercalation into vacancy sites. Further, the peak's growth with increasing pH and shift to more negative potentials demonstrate the role of OH⁻ concentration on charge storage. As the pH increases, the shift in potential results in a greater facility for oxygen intercalation. Importantly, at high pH, the two peaks begin to resolve on the anodic scan, indicating that even in the oxygen excess LaMnO_{3.09} sample there exist surface anion vacancies that can

participate in charge storage. The second peak is the further oxidation of Mn^{3+} to Mn^{4+} as excess oxygen is intercalated into the structure. The intercalation of oxygen ions into vacancy sites is accompanied by proton transfer to electrolyte hydroxide ions yielding water as a product.

The nature of the oxygen intercalation species is still a matter of debate, as the large size of the O^{2-} ion should meet a substantial resistance to insertion into the densely packed perovskite structure at room temperature. It is hypothesized that for oxygen to be inserted into oxygen vacancies, the adsorbed hydroxide ion should transfer its proton to a neighboring lattice oxide and then may be oxidized into a peroxide type species, O_2^{2-} .^{28,31} However, the extent of the oxidation of the adsorbed oxygen ion is strongly dependent on the covalency of the oxygen-transition metal bond in perovskites and the degree of hybridization between the transition metal 3d and oxygen 2p band.^{13,34} In general, late transition metal perovskites exhibit an increased covalency and more metallic character. Because of this, in perovskites such as LaNiO_3 , if the oxidation of oxide ions to peroxide species occurs, a redox event should appear during electrochemical measurements. In a series of tests on the perovskite LaNiO_3 , the presence of a reduction peak for the peroxide species was observed at $\sim E_{1/2} = -0.6\text{V}$ vs. Hg/HgO (Supplementary Figure F.3). As such, it is proposed that the intercalation of oxygen in highly covalent perovskites proceeds likely through a peroxide pathway, as has been shown in previous oxygen intercalation materials.²⁷⁻³³ However, the lack of an observed reduction or oxidation peak for a peroxide type species in the cyclic voltammograms of $\text{LaMnO}_{3\pm\delta}$ suggest that oxygen intercalation in Mn based perovskites does not involve a peroxide type species, and thus is direct intercalation of electrolyte oxygen ions mediated through oxidation of the manganese centers. This mechanism is described through the following reactions (equations (6.3) and (6.4)) and diagrammed in Figure 6.5:



To probe the change in oxidation state of manganese as oxygen is intercalated in $\text{LaMnO}_{3\pm\delta}$ more directly, ex-situ XPS was performed on carbon-free electrodes of $\text{LaMnO}_{3.09}$ and $\text{r-LaMnO}_{2.91}$ after 25, 100 and 500 cycles (Supplementary Figure F.4). The distribution of manganese oxidation states and surface composition was compared to the neat, as-synthesized materials. For $\text{LaMnO}_{3.09}$, the manganese centers were found to initially undergo oxidation after 25 cycles, with a decrease of 17 relative atomic percent in Mn^{3+} concomitant with a 6 relative atomic percent increase in Mn^{4+} and an 11 relative atomic percent increase in satellite peak components. Following this, there was a 6% increase in Mn^{3+} from 17% to 23% going from 25 to 500 cycles, and a 3% decrease in Mn^{4+} and satellite components. Thus, there was a net Mn^{3+} decrease of 10 atomic percent as compared to the uncycled material, and an increase in both Mn^{4+} and satellite peaks. Similar trends were observed for $\text{r-LaMnO}_{2.91}$. There was a net oxidation of manganese centers over 500 cycles, resulting in a 6 relative atomic percent increase in Mn^{4+} and a decrease in both Mn^{3+} and satellite components. After only 25 cycles it was found that Mn^{3+} was oxidized such that there was a 6% increase in Mn^{4+} to 52%, solely at the expense of Mn^{3+} . As the number of cycles increased from 25 to 500, the proportion of Mn^{4+} remained unchanged while a 4% increase in Mn^{3+} from 26% to 30% was observed, due to oxidation of lower binding energy species. This trend corresponds to the loss of capacitance over cycling as oxygen vacancies become filled and can no longer be reversibly extracted. To determine if any lanthanum or manganese surface segregation occurred during cycling, the La 4p 3/2 core region was also examined. Unreduced $\text{LaMnO}_{3.09}$ was found to undergo a 20% enrichment in surface manganese, from 28 to

34% (relative atomic percent to lanthanum) over 500 cycles, while reduced $\text{r-LaMnO}_{2.91}$ showed a two-fold enrichment in surface manganese, from 27 to 54 at. % over 500 cycles. This surface enrichment of manganese is expected to be beneficial to the longer-term pseudocapacitive charge storage capabilities of $\text{r-LaMnO}_{2.91}$, as it results in more redox-active metal centers at the electrode-electrolyte interface.

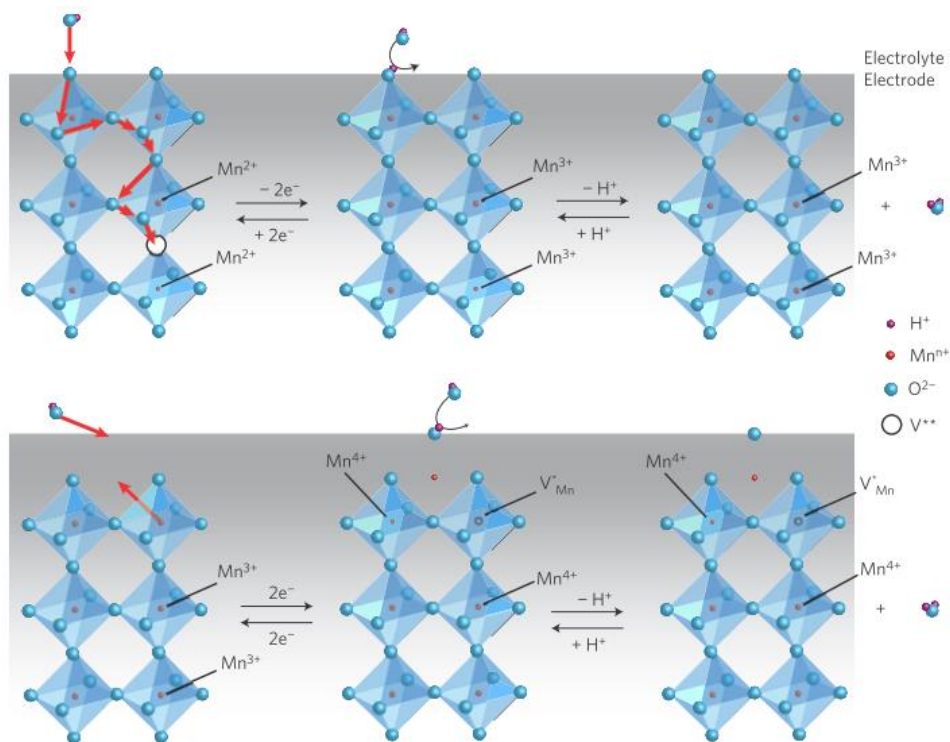


Figure 6.5: Mechanism of oxygen intercalation into $\text{LaMnO}_{3\pm\delta}$

Initially oxygen vacancies are filled through intercalation of an electrolyte oxygen ion and diffusion of O^{2-} along octahedral edges through the crystal concomitant with the oxidation of two Mn^{2+} centres to two Mn^{3+} . In the next step of the reaction, excess oxygen is intercalated at the surface through diffusion of manganese to the surface and oxidation of two Mn^{3+} centres to two Mn^{4+} .

To understand why $\text{LaMnO}_{3\pm\delta}$ stores charge capacitively rather than purely faradaically, the diffusion rate of oxygen was measured. Nemudry *et al.* investigated the underlying factors that influence the diffusion rate of oxygen through perovskites at low temperatures.³³ They propose that perovskite materials with substantial heterogeneous microstructures provide high diffusivity pathways along crystal domain boundaries, allowing for diffusion rates of up to $10^{-9} \text{ cm}^2 \text{ s}^{-1}$ in oxygen intercalation materials. Using an approach developed by Hibino *et al.* the diffusion rate of O^{2-} in $\text{LaMnO}_{3.09}$ was approximated as $5.6 \times 10^{-12} \text{ cm}^2 \text{ s}^{-1}$. With the introduction of oxygen vacancies, the diffusion rate doubled to $1.2 \times 10^{-11} \text{ cm}^2 \text{ s}^{-1}$ in r- $\text{LaMnO}_{2.91}$ (Figures F.5 and F.6).¹⁶ This diffusion rate is similar to those found in high temperature SOFC applications and for Li^+ in common lithium-ion intercalation materials.^{35,36} Thus, the sintering of the initial particles into larger structures with 12 nm crystal domains provides for a high density of boundaries and therefore pathways for fast diffusion, even at room temperature. Further, as the degree of non-stoichiometry is increased, the heterogeneity of the system increases as does the diffusion rate leading to an increased utilization of the bulk structure of $\text{LaMnO}_{3\pm\delta}$. This result is also supported through XRD after cycling which demonstrated the diffusion along oxygen dense planes (Supplementary Figure F.7).

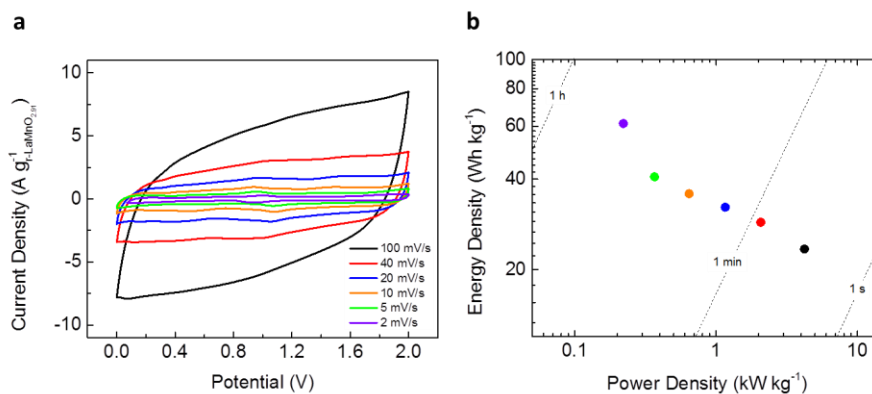


Figure 6.6: Symmetric Cell Cyclic Voltammetry of r-LaMnO_{2.91}

(a), Cyclic voltammograms at various scan rates for symmetric 2-electrode cell in Ar saturated 1 M KOH. The current density is scaled by the mass loading of r-LaMnO_{2.91} after the contribution of the carbon, N-OMC, to the current has been removed. (b), Ragone Plot for the symmetric cell. The Ragone Plot represents the performance of the composite system and thus is not normalized by the mass loading of r-LaMnO_{2.91}.

6.5 PRACTICAL APPLICATIONS OF LaMnO₃ PSEUDOCAPACITORS

In order to test the practicality of LaMnO₃ as a pseudocapacitive system, a symmetric cell of 30 wt% r-LaMnO_{2.91} on mesoporous carbon composite at a loading of 1 mg cm⁻² on Ni foam was constructed and tested in an Ar saturated 1 M KOH electrolyte. This mass loading was chosen after performing a power-law analysis on the capacitive current with variable carbon mass loadings (Figures F.8 and F.9). Figure 6.5a shows the cyclic voltammogram of the resulting cell across a 2 V window. The rectangular shape of the symmetric cell is indicative of ideal capacitive behavior. The energy densities of the cell were evaluated using equation (6.5),

$$U = \frac{1}{2}CV^2 \quad (6.5)$$

where U corresponds to the potential energy density (Wh kg⁻¹), C is the capacitance of the material (F) and V is the potential window of the cell (V).¹ This data is presented in a Ragone plot of the symmetric cell's performance, Figure 6.5b, which demonstrates the promising performance of r-LaMnO_{2.91} even at practical mass loadings. At a high power density of 4214 W kg⁻¹ r-LaMnO_{2.91} exhibits an energy density 23.4 Wh kg⁻¹ which increases to 61.2 Wh kg⁻¹ at a lower power density of 220.4 W kg⁻¹. As such, the role of oxygen intercalation into anion vacancies in LaMnO₃ can be seen as a new paradigm for oxygen ion based charge storage that may be exploited for high energy density and power density applications.

6.6 CONCLUSIONS

As pseudocapacitor and rechargeable battery research has long focused on cation intercalation, the anion based charge storage mechanism presented here opens the door to a new energy storage concept possessing high specific capacitance and affordability. In addition, the oxygen intercalation mechanism appears to be universal with other lanthanum based perovskites such as LaNiO_3 , which exhibits similar charge storage behavior. The wide range of possibilities to modify the electronic and physical properties of perovskites and perovskite-derived structures will likely lead to materials with high energy densities that also utilize anion based mechanisms of energy storage. Further it is likely that similar anion based mechanisms may be found to contribute substantial energy densities to other systems containing oxygen vacancies.

6.7 METHODS

*Synthesis of $\text{LaMnO}_{3+\delta}$:*¹⁵ Initially mixed metal hydroxides were prepared by reverse-phase hydrolysis of La and Mn nitrates in the presence of an equimolar amount of tetrapropylammonium bromide dissolved in 1 wt% tetramethylammonium hydroxide (TMAOH). An ~10 mM solution of mixed metal nitrates was added dropwise to 200 mL of TMAOH. The resulting suspension was collected by centrifugation and washed with DI water, followed by re-suspension in DI water through probe sonication. The solution was frozen as a thin film on rotating steel drum at cryogenic temperatures, and then lyophilized at -10 °C at a fixed pressure of ~50 mTorr for 20h. The lyophilized powder was calcined at 700 °C for 4 h under dehumidified air. Following calcination, the particles were washed with EtOH and filtered. $\text{LaCoO}_{3-\delta}$ and $\text{LaNiO}_{3-\delta}$ were synthesized following a similar procedure.

Synthesis of $\text{LaMnO}_{3-\delta}$: ~100 mg of pre-synthesized $\text{LaMnO}_{3+\delta}$ was thermally reduced topotactically in an environment of 7% H_2 in Ar reforming gas at a temperature of 400 °C for 1 h and cooled naturally to room temperature.

3-Electrode Cell Electrode Preparation: All perovskite nanopowders were loaded to 30%wt by mass of perovskite on nitrogen doped ordered mesoporous carbon (N-OMC) by mixing with ball milling. The perovskite/carbon mixture was dispersed in EtOH containing 0.05 wt% Na-substituted Nafion in a ratio of 1 mg mL^{-1} and sonicated for 30 min. 10 μL of this solution was spuncast at 700 rpm onto a glassy carbon electrode (0.196 cm^2 , Pine Instruments) yielding an perovskite loading of 15.3 $\mu\text{g cm}^{-2}$ for N-OMC supported LaMnO_3 and a total mass loading of 51.0 $\mu\text{g cm}^{-2}$. Spincasting is important to get consistent thin films across a series of measurements.²⁷ Electrodes of neat N-OMC at a mass loading of 35.7 $\mu\text{g cm}^{-2}$ were also made with the same procedure. The current contribution from N-OMC was subtracted out of the data to more clearly present the electrochemistry of $\text{LaMnO}_{3\pm\delta}$. The synthesis of N-OMC is described elsewhere.³⁸

2-Electrode Cell Electrode Preparation: 30 wt% r- $\text{LaMnO}_{2.91}$ composite electrodes of 1 mg cm^{-2} total loading were made by dropcasting the same inks described in the 3-electrode cell section onto Ni foam (2 mm thick, 100 ppi, 95% porosity, Marketch). The electrodes were then dried at 80 °C for 20 min. and manually pressed to a thickness of ~ 0.5 mm.

Materials Characterization: Structural information about the resulting oxides was obtained using wide-angle X-ray diffraction (Rigaku Spider, Cu $\text{K}\alpha$ radiation, $\lambda = 1.5418$ Å) and analyzed with JADE software (Molecular Diffraction Inc.). Scanning (transmission) electron microscopy (SEM/STEM) was performed using a Hitachi S-5500 with a 30 kV accelerating voltage and 20 μA probe current. $\text{LaMnO}_{3.09}$ was deposited from a dilute ethanol suspension onto a 200 mesh copper grid coated with lacey carbon.

Chemical states were characterized by X-ray photoelectron spectroscopy (XPS, Kratos AXIS Ultra DLD) in 0.1 eV steps using a dwell time of 4 seconds per step and a monochromatic Al X-ray source (Al α , 1.4866 eV). Brunauer-Emmett-Teller surface area measurements were performed through nitrogen sorption on a Quantachrome Instruments NOVA 2000 high-speed surface area BET analyzer at a temperature of 77K. The hydrodynamic diameter (D_H) of as-synthesized hydrolysis particles was measured via dynamic light scattering (DLS, Brookhaven ZetaPALS instrument) and fit with the CONTIN routine. Iodometric titrations were performed following the procedure developed by Laiho *et al.*²¹ In a sealed 2-neck round bottom flask under Ar atmosphere, ~10-15 mg of LaMnO₃ was dissolved in 5.5 mL of 4M HCl followed by dilution with 10 mL of pre-boiled DI water and degassed with Ar for 15 min. Then 7.2mL of a 1M KI solution made in pre-boiled DI water was injected into the cell. The solution was immediately titrated with a solution of 0.015M Na₂S₂O₃ that had standardized against a 0.1M KIO₃ standard solution. The perovskite solution was titrated to a faint golden color, then ~0.5 mL of starch indicator was added. The solution was titrated until the color changed from deep purple to clear.

Electrochemical testing was performed on a CH Instruments CHI832a potentiostat. The tests were performed in a standard 3 electrode cell using a Hg/HgO (1M KOH) reference electrode, a Pt wire counter electrode, and a film of the pseudocapacitor material on glassy carbon as the active electrode. The potential of the reference electrode was measured prior to testing against a standardized Hg/HgO (1M KOH) electrode that was never used during testing. Electrolyte solutions were degassed with Ar for at least 15 minutes before testing to ensure that no oxygen reduction current would be observed during cyclic voltammetry. Further, the tests were performed under a blanket of Ar. Two electrode cell tests were also performed in an Ar saturated 1M KOH electrolyte. In the 2-

electrode testing, one r-LaMnO_{2.91}/N-OMC composite electrode served as the reference and counter electrode and the other served as the working electrode.

6.8 ADDITIONAL INFORMATION

Appendix F contains details regarding the experimental methods, supporting materials characterization, and analysis.

6.9 REFERENCES

1. Conway, B. E. *Electrochemical Supercapacitors* (Kluwer–Academic, 1999).
2. Arico, A. S., Bruce, P., Scrosati, B., Tarascon, J. & Van Schalkwijk, W. Nanostructured materials for advanced energy conversion and storage devices. *Nature Mater.* 4, 366-377 (2005).
3. Zheng, J. P. & Jow, T. R. A New Charge Storage Mechanism for Electrochemical Capacitors. *J. Electrochem. Soc.* 142, 6-8 (1995).
4. Patel, M. N. *et al.* High pseudocapacitance of MnO₂ nanoparticles in graphitic disordered mesoporous carbon at high scan rates. *J. Mater. Chem.* 22, 3160-3169 (2012).
5. Wang, H.; Sanchez Casalongue, H.; Liang, Y. & Dai, H. Ni(OH)₂ Nanoplates Grown on Graphene as Advanced Electrochemical Pseudocapacitor Materials *J. Am. Chem. Soc.* 132, 7472-7477(2010).
6. Herrero, E., Buller, L. J. & Abruña, H. D. Underpotential deposition at single crystal surfaces of Au, Pt, Ag and other materials. *Chem. Rev.* 101, 1897-1930 (2001).
7. Guidelli, R. & Schmickler, W. Electrosorption Valency and Partial Charge Transfer. In *Modern Aspects of Electrochemistry* 38, 303-371 (Springer, 2005).
8. Augustyn, V. *et al.* High-rate electrochemical energy storage through Li⁺ intercalation pseudocapacitance. *Nature Mater.* 12, 518-522 (2013).
9. Brezesinski, T., Wang, J., Tolbert, S. H. & Dunn, B. Ordered mesoporous α -MoO₃ with iso-oriented nanocrystalline walls for thin-film pseudocapacitors. *Nature Mater.* 9, 146-151 (2010).
10. Hahn, B. P., Long, J. W. & Rolison, D. R. Something from Nothing: Enhancing Electrochemical Charge Storage with Cation Vacancies. *Acc. Chem. Res.* 46, 1181-1191 (2013).

11. Ishihara, T. *Perovskite Oxide for Solid Oxide Fuel Cells* (Springer, 2009).
12. Wilde, P. M., Guther, T. J., Oesten, R. & Garche, J. Strontium ruthenate perovskite as the active material for supercapacitors. *J. Electroanal. Chem.* 461, 154-160 (1999).
13. Suntivich, J., May, K. J., Gasteiger, H. A., Goodenough, J. B. & Shao-Horn, Y. A Perovskite Oxide Optimized for Oxygen Evolution Catalysis from Molecular Orbital Principles. *Science* 334, 1383-1385 (2011).
14. Suntivich, J. *et al.* Design principles for oxygen-reduction activity on perovskite oxide catalysts for fuel cells and metal-air batteries. *Nature Chem.* 3, 546-550 (2011).
15. Wohlfahrt-Mehrens, M. *et al.* New materials for supercapacitors. *J. Power Sources* 105, 182-188 (2002).
16. Hibino, M., Kimura, T., Suga, Y., Kudo, T. & Mizuno, N. Oxygen rocking aqueous batteries utilizing reversible *topotactic* oxygen insertion/extraction in iron-based perovskite oxides $\text{Ca}_{1-x}\text{La}_x\text{FeO}_{3-\delta}$. *Sci. Rep.* 2, 601-605 (2012).
17. Wang, J., Polleux, J., Lim, J., & Dunn, B. Pseudocapacitive contributions to electrochemical energy storage in TiO_2 (anatase) nanoparticles. *J. Phys. Chem. C* 111, 14925-14931 (2007).
18. Kalinin, S. V., Borisevich, A. & Fong, D. Beyond Condensed Matter Physics on the Nanoscale: The Role of Ionic and Electrochemical Phenomena in the Physical Functionalities of Oxide Materials. *ACS Nano* 6, 10423-10437 (2012).
19. Hardin, W. G. *et al.* Highly Active, Nonprecious Metal Perovskite Electrocatalysts for Bifunctional Metal-Air Battery Electrodes. *J. Phys. Chem. Lett.* 4, 1254-1259 (2013).
20. Cortés-Gil, R. *et al.* Evolution of magnetic behavior in oxygen deficient $\text{LaMnO}_{3-\delta}$. *J. Phys. Chem. Solids* 67, 579-582 (2006).
21. Laiho, R. *et al.* Low-field magnetic properties of $\text{LaMnO}_{3+\delta}$ with $0.065 \leq \delta \leq 0.154$. *J. Phys. Chem. Solids* 64, 2313-2319 (2003).
22. Ruiz-González, L., Cortés-Gil, R., Alonso, J. M., González-Calbet, J. M. & Vallet-Regí, M. Revisiting the Role of Vacancies in Manganese Related Perovskites. *The Open Inorganic Chemistry Journal* 1, 37-46 (2007).
23. Boehm, H. P. Acidic and Basic Properties of Hydroxylated Metal Oxide Surfaces. *Discuss. Faraday Soc.* 52, 264-275 (1971).
24. Schmidt, T. J. *et al.* Characterization of High-Surface-Area Electrocatalysts Using a Rotating Disk Electrode Configuration. *J. Electrochem. Soc.* 145, 2354-2358 (1998).

25. Wiberg, G. K. H., Mayrhofer, K. J. J. & Arenz, M. Investigation of the Oxygen Reduction Activity on Silver – A Rotating Disc Electrode Study. *Fuel Cells* 10, 575-581 (2010).
26. Garsany, Y., Singer, I. L. & Swider-Lyons, K. E. Impact of film drying procedures on RDE characterization of Pt/VC electrocatalysis. *J. Electroanal. Chem.* 662, 396-406 (2011).
27. Kudo, T., Obayashi, H. & Gejo, T. Electrochemical Behavior of the Perovskite-Type $\text{Nd}_{1-x}\text{Sr}_x\text{CoO}_3$ in an Aqueous Alkaline Solution. *J. Electrochem. Soc.* 122, 159-163 (1975).
28. Grenier, J. C., Pouchard, M. & Wattiaux, A. Electrochemical synthesis: oxygen intercalation. *Curr. Opin. Solid State Mater. Sci.* 1, 233-240 (1996).
29. Piovano, A. *et al.* Time Resolved in Situ XAFS Study of the Electrochemical Oxygen Intercalation in $\text{SrFeO}_{2.5}$ Brownmillerite Structure: Comparison with the Homologous $\text{SrCoO}_{2.5}$ System. *J. Phys. Chem. C* 115, 1311-1322 (2011).
30. Karvonen, L. *et al.* O-K and Co-L XANES Study on Oxygen Intercalation in Perovskite $\text{SrCoO}_{3-\delta}$ *Chem. Mater.* 22, 70-76 (2010).
31. Wattiaux, A. *et al.* A Novel Preparation Method of the SrFeO_3 Cubic Perovskite by Electrochemical Means. *Solid State Comm.* 77, 489-493 (1991).
32. Mahesh, R., Kannan, K. R. & Rao, C. N. R. Electrochemical Synthesis of Ferromagnetic LaMnO_3 and Metallic NdNiO_3 . *J. Solid State Chem.* 114, 294-296 (1995).
33. Nemudry, A., Goldberg, E. L., Aguirre, M. & Alario-Franco, M. Á. Electrochemical Topotactic Oxidation of Nonstoichiometric Perovskites at Ambient Temperature. *Solid State Sci.* 4, 677-690 (2002).
34. Abbate, M. *et al.* Controlled-valence properties of $\text{La}_{1-x}\text{Sr}_x\text{FeO}_3$ and $\text{La}_{1-x}\text{Sr}_x\text{MnO}_3$ studied by soft x-ray absorption spectroscopy. *Phys. Rev. B.* 46, 4511-4519 (1992).
35. Manthiram, A., Kuo, J. F. & Goodenough, J. B. Characterization of Oxygen Deficient Perovskites as Oxide Ion Electrolytes. *Solid State Ionics* 52, 225-234 (1993).
36. Thomas, M. G. S. R., Bruce, P. G. & Goodenough, J. B. Lithium Mobility in the Layered Lithium Cobalt Oxide ($\text{Li}_{1-x}\text{CoO}_2$). *Solid State Ionics* 17, 13-19 (1985).
37. Wang, X. Q. *et al.* Ammonia Treated Ordered Mesoporous Carbons as Catalytic Materials for Oxygen Reduction Reaction. *Chem. Mater.* 22, 2178-2180 (2010).

Chapter 7: Conclusions

7.1 CONCLUSIONS

7.1.1 Highly Active, Non-precious Metal Perovskite Electrocatalysts for Bifunctional Metal Air Battery Electrodes

We demonstrated that LaNiO_3 nanocrystalline aggregates on nitrogen doped carbon exhibit extremely high activity for the OER ($90 \text{ mA mg}^{-1}_{\text{ox}}$ @ 1.56 V vs RHE-iR) and strong OER/ORR bifunctional character (1.02 V ΔE between 3 mA cm^{-2} ORR and 10 mA cm^{-2} OER), as a result of high phase purity, lattice hydroxylation and increased surface area ($11 \text{ m}^2 \text{ g}^{-1}$). This bifunctional character is crucial to the development of inexpensive aqueous metal-air batteries, fuel cells and electrolyzers. This highly active morphology is produced by rapid, simultaneous hydrolysis of La^{3+} and Ni^{2+} nitrates during reverse phase arrested growth precipitation, followed by rapid drying. This synthetic concept to generate precursors that are calcined to form phase pure nanocrystalline aggregates is general and thus a directly applicable route to prepare a wide variety of nonprecious metal, nanocrystalline perovskites as highly active catalysts.

7.1.2 Tuning the Electrocatalytic Activity of Perovskites Through Active Site Variation and Support Interactions

We showed how a series of phase pure perovskite electrocatalysts were made using a robust synthetic process in which colloidal mixed metal hydroxides are formed by reverse phase arrested growth coprecipitation. These perovskite catalysts, when supported on nitrogen doped carbon or reduced graphene oxide displayed high activities for both the OER and ORR, with LaCoO_3/NC having $\sim 4\times$ the OER mass activity ($100 \text{ mA mg}^{-1}_{\text{ox}}$) of the precious metal oxide benchmark IrO_2 , and $\text{LaNi}_{0.75}\text{Fe}_{0.25}\text{O}_3/\text{NC}$ having comparable ORR activity ($547 \text{ mA mg}^{-1}_{\text{ox}}$) as Pd/VC . This demonstrates that the high

specific ($\mu\text{A}/\text{cm}^2_{\text{ox}}$) activity of perovskites can be translated into highly active and bifunctional oxygen catalysts. Through tuning of the carbon support functionalization, rate limiting steps were identified and bypassed by successful incorporation of peroxide disproportionation into the catalyst itself, which was achieved through selective doping. $\text{LaNi}_{0.75}\text{Fe}_{0.25}\text{O}_3$ exceptional ORR activity is in part rationalized by the catalyst's ability to bypass the traditional rate determining ORR step of peroxide reduction by disproportionation of HOO^- into O_2 and OH^- , enabling a pseudo four electron ORR pathway. This work attempts to look beyond the choice of bulk electrical properties or use of single catalytic descriptors such as e_g filling, while providing a catalyst-specific understanding of the importance of peroxide oxidation or reduction on perovskites during the OER and ORR.

7.1.3 Exceptional Electrocatalytic Oxygen Evolution Via Tunable Charge Transfer Interactions in $\text{La}_{0.5}\text{Sr}_{1.5}\text{Ni}_{1-x}\text{Fe}_x\text{O}_{4+\delta}$ Ruddlesden-Popper Oxides

We have precisely synthesized a series of RP catalysts having highly oxidized and covalent Ni $3d$ - O $2p$ - Fe $3d$ bonds that give rise to exceptional OER activity. To increase the oxidation state and Ni-O covalency, Sr substitution into LaNiO_3 has previously been proposed but not fully realized. Inactive secondary phases resulting from poor solubility of Sr in the perovskite phase were avoided through utilization of the RP crystal structure. Using $\text{La}_{0.5}\text{Sr}_{1.5}\text{NiO}_{4+\delta}$ as the host lattice, we achieved complete substitution of Fe for Ni across the entire compositional range, while crystalline periodicity of the RP phase enabled precise study of the impact of Fe substitution on the chemical and electronic properties of the LSNF series. Iodometric titrations coupled with Mössbauer spectroscopy indicate that the average Ni oxidation state in the LSNF series increases from +3.46 to +3.95 with increasing Fe substitution while the $\text{Ni}^{2+/3+}$ redox

peaks also shift to more positive potentials, consistent with Ni developing a more oxidized character. The influence of Fe substitution extends beyond increasing the oxidative strength of Ni, however, as the electrocatalytic activity increases by over an order of magnitude from LSN to LSNF30 (88 vs 1931 mA mg⁻¹_{ox}, respectively), despite possessing statistically equivalent Ni oxidation states. DFT calculations reveal that Fe substitution results in cross-gap hybridization where the Fe 3d e_g band is hybridized with both the Ni 3d e_g and top of the O 2p density of states across the Fermi level. The increased covalency of the Ni-O bonds as well as facile charge transfer through Fe-O-Ni bridges due to incorporation of Fe explains the enhanced catalytic activity going from LSN to LSNF30. This methodology to promote cross-gap hybridization via selective substitution of A and B-site elements in RP oxides represents a new set of design principles for the optimization of metal oxide catalysts and reveals important fundamental aspects related to their structure and electrocatalytic activity.

7.1.4 Highly Active Perovskite and Ruddlesden-Popper Composite Electrocatalysts for Water Oxidation

We have demonstrated that the reverse microemulsion synthetic scheme produces highly active OER catalyst phases with smaller amounts of unwanted secondary phases than the charred polymerized complex method. Despite the impurity phases, the mass activities among the highest reported for any perovskite or RP electrocatalysts. The reverse microemulsion method produced precursor particles that crystallized into these mixtures containing highly covalent Ni-rich oxides for both SNF and LSNF. The SNF RP catalyst is 38 fold more active than LaNiO₃ (1541 vs 40 mA mg⁻¹_{ox}), and generates over 8 times more current per mass than IrO₂ (174 mA mg⁻¹_{ox}) with a low Tafel slope of 55 mV dec⁻¹. These exceptional catalytic activities are further enabled by chemical substitution

wherein Sr and Fe are substituted for La and Ni. Sr substitution should increase the average oxidation state of Ni, while substitution of the less electronegative Fe introduces new Fe 3d orbitals at or above the Fermi level, to facilitate easy charge transfer between the catalyst and adsorbate via cross-gap hybridization.

7.1.5 Anion charge storage through oxygen intercalation in LaMnO₃ perovskite pseudocapacitor electrodes

Herein we proposed the mechanism of oxygen vacancy mediated redox pseudocapacitance for a nanostructured lanthanum based perovskite, LaMnO_{3±δ}. We demonstrated that OH⁻ is reversibly intercalated into LaMnO_{3±δ} at room temperature in 0.1 M KOH, and results in large faradaic pseudocapacitance, up to ~600 F g⁻¹ which retained ~95% of the capacitance over 500 cycles. By examination of other, bulkier anions and a series of common intercalating cations (K⁺, Na⁺), we have demonstrated the first example of anion-based intercalation pseudocapacitance as well as the first time oxygen intercalation has been exploited for fast energy storage. This was further supported by the introduction of oxygen vacancies through the topotactic reduction of LaMnO_{3.09} to LaMnO_{2.91}, and subsequent increase in charge-storage capacity. Whereas previous pseudocapacitor and rechargeable battery charge storage studies have focused on cation intercalation, the anion based mechanism presented here offers a new paradigm for electrochemical energy storage.

7.2 RECOMMENDATIONS

The robust phase space that perovskite and Ruddlesden-Popper oxides exist in offer many opportunities for tuning their chemical, electronic and structural properties for

enhanced ORR and OER, but future work surrounding these oxides must address long-term stability of the catalyst and support, especially the carbon. The support interactions between perovskite and carbons have previously been examined¹, but it is still unclear the mechanism responsible for the synergistic enhancement towards the OER observed for perovskites on N-doped carbon. Furthermore, the long term oxidative stability of carbon and catalyst must be quantified and measured. Thermodynamically, carbon will oxidize at all potentials required for the OER. The kinetics of carbon corrosion must be decreased by increasing the oxidation-resistant graphitic character of the carbon,² while maximizing beneficial support interactions to lower the total overpotential required for the OER, and thus reducing the corrosion potential that carbon experiences.

To address catalyst stability, the surface Pourbaix behavior of the most promising catalysts should be calculated, and stability metrics better defined. We have used a 10 A g⁻¹_{ox} galvanostatic hold, and comparing the time until failure before reaching unsafe potentials, defined as ≥ 2 V vs RHE-iR.^{1, 3, 4} These tests are phenomenological though, and true durability testing should also encompass cyclic oscillations of potential between operational and open circuit, to better represent all modes of operation. The quantification of degradation products in the electrolyte through ICP-OER is needed to corroborate theoretical surface Pourbaix behavior, to understand the kinetics of catalyst corrosion.

The strength of the metal oxide work I have participated in is firmly rooted in the work of pioneering solid state chemists and physicists of past decades, such as John B. Goodenough. A more thorough reviewing of this literature would surely yield more examples of band structures that promote the OER. Elemental substitution into perovskite and RP structures has yielded very large catalytic enhancements, and I firmly believe through reading of the old literature and insights gained through the current Ni-Fe-M oxyhydroxides literature, there is room for further improvement. The exertion of

synthetic control over the shape, size, and crystalline facets will undoubtedly improve the OER for perovskites and RPs, although the exertion of such control is made more difficult by the high temperatures required for crystallization.

Octahedral coordination of transition metal ions, combined with a relatively large amount of active sites per mass, passable conductivity, and their robust ability to accept substituted elements has made perovskites and RPs host oxides for developing new design criteria and examining catalytic mechanisms. Yet, there exist many other crystalline metal oxide phases with octahedral coordination, such as pyrochlores and ilmenites, that have yet to be examined in any serious fashion for the OER.^{5, 6}

7.3 REFERENCES

1. Hardin WG, Mefford JT, Slanac DA, Patel BB, Wang X, Dai S, *et al.* Tuning the Electrocatalytic Activity of Perovskites through Active Site Variation and Support Interactions. *Chem Mater* 2014, 26(11): 3368-3376.
2. Staud N, Sokol H, Ross PN. The Corrosion of Carbon Black Anodes in Alkaline Electrolyte: IV . Current Efficiencies for Oxygen Evolution from Metal Oxide-Impregnated Graphitized Furnace Blacks. *J Electrochem Soc* 1989, 136(12): 3570-3576.
3. Hardin WG, Slanac DA, Wang X, Dai S, Johnston KP, Stevenson KJ. Highly Active, Nonprecious Metal Perovskite Electrocatalysts for Bifunctional Metal–Air Battery Electrodes. *J Phys Chem Lett* 2013, 4(8): 1254-1259.
4. Mefford JT, Rong X, Abakumov AM, Hardin WG, Dai S, Kolpak AM, *et al.* Water electrolysis on $\text{La}_{1-x}\text{Sr}_x\text{CoO}_{3-\delta}$ perovskite electrocatalysts. *Nature Communications* 2016, 7: 11053.
5. Patzke GR, Zhou Y, Kontic R, Conrad F. Oxide Nanomaterials: Synthetic Developments, Mechanistic Studies, and Technological Innovations. *Angewandte Chemie International Edition* 2011, 50(4): 826-859.

6. Hunter BM, Gray HB, Müller AM. Earth-Abundant Heterogeneous Water Oxidation Catalysts. *Chem Rev* 2016, 116(22): 14120-14136.

Appendix A: Atomic Ensemble and Electronic Effects in Ag-Rich AgPd Nanoalloy Catalysts for Oxygen Reduction in Alkaline Media⁵

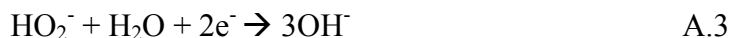
A.1 INTRODUCTION

Bimetallic catalysts have garnered considerable interest since they exhibit distinctly different and often superior activity for many chemical transformations compared to pure monometallic systems as determined via DFT calculations¹⁻³ and experimental studies.⁴⁻⁷ The enhanced performance of bimetallic catalysts may be rationalized by a combination of ligand, geometric and/or ensemble effects.^{1,8,9} Ligand effects, namely charge transfer between nearest neighbor atoms, and geometric effects, primarily compressive or tensile strain, generally influence the strength of interactions of reactants, intermediates and products. Ensemble effects result when more than one reactive site, composed of different metal atoms or clusters of atoms, catalyze distinct steps in a reaction mechanism. Whereas ensemble effects are well known in gas phase heterogeneous catalysis,⁸⁻¹¹ they have received limited attention in electrocatalysis.¹²⁻¹⁴

To understand how to employ ligand, geometric, and/or ensemble effects to achieve high catalyst activity, we have chosen the oxygen reduction reaction (ORR) as a model system. The kinetic limitations in the ORR are a major concern for both metal-air batteries and low-temperature fuel cells.¹⁵⁻²¹ In base, the two main pathways for the ORR are the direct 4 electron transfer:



and a 2 by 2 electron (stepwise) pathway,



⁵Large portions of this appendix have been published as Slanac, D. A.; Hardin, W. G.; Johnston, K. P.; Stevenson, K. J. *Journal of the American Chemical Society* **2012**, *134*, 9812.

which goes through a hydroperoxide intermediate (HO_2^-). The combination of reactions A.2a and A.2b yield reaction A.1, though the kinetics of reaction A.3.2b can be limiting. Furthermore, the HO_2^- intermediate can undergo disproportionation according to:



Bimetallic catalysts may be designed to efficiently target this set of reaction pathways to achieve high synergy among the various metal atoms.

For core-shell catalysts, the combination of ligand and geometric effects provides exceptionally high ORR activity.^{6,22-24} Here an electronic shift and geometric strain in the shell, due to the underlying core, favorably modify the binding energies of reaction intermediates, particularly in the direct 4 electron transfer. For example, a Pt or Pd monolayer shell deposited on a transition metal core produced activities per mass of noble metal up to 8x times relative to the pure noble metal.^{22,25} However, when the diameter of a core-shell catalyst becomes <5 nm, a monolayer shell would comprise greater than >30% of the total atoms in the particle. In contrast, even lower precious metal concentrations are possible for homogenous bimetallic nanoalloys. Furthermore, the large number of contacts between dissimilar metals promotes ensemble effects, as well as ligand effects. However, for ORR nanoparticle catalysts, precious noble metal contents are typically >50% due to challenges in synthesis.^{4,5,7,26}

To design an active nanoalloy catalyst with a low content of a highly active precious noble metal and a second less active metal, it would be desirable to achieve strong ligand and ensemble effects. For the ORR in alkaline media, less-expensive precious metals such as Ag exhibit good ORR activity, especially for HO_2^- disproportionation²⁷, and are more stable^{20,21,28,29} than in acid, enabling them to be used in nanoalloys with Pd³⁰⁻³⁴. Since the cost ratio of Pd:Ag is ~22:1, it would be economically desirable to utilize both metals in a bifunctional manner to raise activity

and improve stability. However, for a case where the Pd level was only 20 mol% (Ag_4Pd), the activity was not above the level expected from a linear combination of activities of the pure components.³⁰ To design structure and atomic surface arrangements of bimetallic nanoalloys for ligand and ensemble effects, improved synthetic methods are needed for controlling composition, morphology and architecture (e.g. random-alloy vs core-shell). Alloy nanoparticles have been pre-synthesized in the presence of stabilizing ligands by arrested growth precipitation^{13,35-37} or in microemulsions^{38,39} and then later adsorbed onto the catalyst support. Dendrimer encapsulated nanoparticles have been synthesized with controlled alloy formation, for example with Pd compositions just below 50 mol% ($\text{Pd}_{36}\text{Cu}_{64}$).⁴⁰ Recently, large 40 nm Au_4Pd alloy nanoparticles have been shown to exhibit higher activity than their core-shell morphologies, as a result of strong ensemble effects.¹³ However, we are not aware of small nanoalloys (<5 nm) with low amounts of a precious metal in the surface, where electronic and ensemble effects produce high activities.

Herein, we synthesize uniform bimetallic nanoalloy catalyst (~5nm), with as little as ~10 mol% Pd (Ag_9Pd), to achieve high activity for the oxygen reduction reaction (ORR) in alkaline media. To control the distribution of the Pd and Ag on the surface, the nanoalloys with Ag compositions from ~40% up to ~90% were synthesized by co-reduction of Ag and Pd carboxylic acid complexes precursors at similar rates⁴¹ in the presence of stabilizing ligands. The nanoparticles were found to be uniformly alloyed, displaying a single alloy composition among the particles, as shown by a combination of X-ray diffraction (XRD), cyclic voltammetry (CV) and X-ray photoelectron spectroscopy (XPS). Furthermore detailed probe-corrected scanning transmission electron microscopy (pcSTEM) analysis is presented for the Ag_9Pd catalyst. As a consequence of the low overall Pd content for $\text{Ag}_{\geq 4}\text{Pd}$ and the uniformity of the alloying, the Pd atoms on the

surface were surrounded primarily by Ag atoms, as characterized by the surface sensitive electrochemical techniques, cyclic voltammetry and CO stripping measurements. Our hypothesis is that nearly all of the contacts of the more active metal Pd will be with Ag for $\text{Ag}_{\geq 4}\text{Pd}$, and these unlike interactions will enhance catalyst activity through electronic interactions (ligand effect), as was observed by the binding energy shift from XPS, and the cooperation of each metal towards various ORR reaction steps (ensemble effect). We found that the activities for Ag_9Pd and Ag_4Pd were up to 2.7 and 3.2 fold above the value expected from the pure metals, a large non-linear enhancement for ORR. Furthermore, the total metal mass activity for the AgPd_2 catalyst is 60% higher than for pure Pd, suggesting high synergy is also present for alloys with higher Pd loading. These results are compared to those of pure Ag and pure Pd nanoparticles of similar size on carbon. Furthermore, it appears that the sintering of pure Ag particles during calcination is mitigated by the addition of a small amount (10 mol%) of Pd in the alloy, again illustrating cooperative effects for the uniform alloy. Ultimately, the ability to disperse small amounts of a highly active precious metal within a less active metal on a nanoalloy surface is a general strategy that may offer significant benefit for scientific and practical advancement in catalysis.

A.2 EXPERIMENTAL

All chemicals were used as received. Silver nitrate, palladium acetate, tripropylamine, anhydrous ethanol, tetradecanoic acid, and 5 wt % nafion solution in lower alcohols were purchased from Sigma-Aldrich. Hexane (99.9%) and potassium hydroxide were obtained from Fisher Scientific, and ethanol (Absolute 200 proof) from Aaper alcohol. Millipore high purity water (18 M Ω) was used. Vulcan XC72 (VC) carbon was obtained from Cabot Corporation. Oxygen (research grade, 99.999% purity),

argon (research grade, 99.999% purity) and CO (99.9%) were obtained from Praxair. Commercial 20% Pd/VC was obtained from ETEK.

A.2.1 Catalyst Synthesis

A.2.1.1 Particle Synthesis

Pd-tetradecanoate (Pd-TDOA) and Ag-tetradecanoate (Ag-TDOA) precursor powders were synthesized from palladium acetate and silver nitrate salts in organic and aqueous ligand substitution reactions, respectively, as reported previously.^{41,42}

The total concentration of metal atoms in syntheses of both alloy and pure component nanoparticles was controlled to 0.71 M. The desired molar ratio of Ag-TDOA or Pd-TDOA was added to a 10 mL round bottom reaction flask with 1.414 mL of tripropylamine.⁴¹ The solution was slowly heated under argon to 100 °C while vigorously stirring. The solution was left at 100°C for 1 hour, and then cooled to room temperature. Acetone was then added in excess, and the solution was centrifuged for 5 minutes 2000 rpm. This washing step was done three times, discarding the supernatant and replacing it with fresh acetone after each wash. Finally, the particles were added to hexane and centrifuged for 2 minutes at 10,000 rpm to narrow the size distribution. The hexane was evaporated and the yield of nanoparticles was quantified. Finally, the particles were suspended in n-hexane to a 10 mg/mL concentration which was black in color.

A.2.1.2 Adsorption of particles onto carbon support.

Aside from the commercial Pd/VC, all catalyst powders were prepared via adsorption of pre-synthesized nanoparticles onto Vulcan carbon. Vulcan XC72 carbon was mixed with an appropriate volume of nanoparticle solution (10mg/mL in hexane) to achieve a loading of 20 wt% metal (assuming 100% adsorption of the particles). The

carbon and nanoparticle solution was stirred for 1 hour. The mixture was vacuum filtered. The color of the filtrate came out clear, indicating essentially complete adsorption of the particles on the carbon. The catalyst powder was calcined at 450 °C under forming gas, in a quartz tube furnace. The furnace was held at room temperature for 30 minutes, ramped to the desired temperature over 2 hours and held at 450 °C for 2 hours. However, for the 10nm Ag/VC catalysts, the same calcination procedure was used but with a maximum temperature of 210°C. The calcined catalyst powder was then washed with 100 mL of EtOH, dried at 60 °C for 20 minutes, and stored under ambient conditions.

A.2.2 Electron Microscopy

A.2.2.1 Transmission Electron Microscopy (TEM)

Low-mag TEM was conducted on an FEI Tecnai 20 BioTwin microscope using an 80 kV accelerating voltage. The carbon supported catalysts were deposited from a dilute ethanol suspension onto a 200 mesh copper grid coated with lacey carbon (Electron Microscopy Sciences). Average particle sizes were calculated from measurements of ~100 particles using ImageJ.

A.2.2.2 Scanning Transmission Electron Microscopy (STEM)

High resolution probe corrected STEM (pcSTEM) imaging was performed on a JOEL JEM-ARM200F probe aberration corrected electron microscope, operated at 200 kV. The probe size used was of 0.08 nm with a current of 24 pA. The spherical aberration was reduced with a dodecapole corrector (CEOS). Calibration was done using standard Si[110] and Au nanoparticles to align the corrector with CESCOR software. Images were recorded in STEM mode by simultaneously collecting bright field and high angle annular dark field (HAADF) images from scans of 12 to 16 seconds with a probe size of 0.08Å.

To determine the extent of alloying in the Ag₉Pd particles, energy dispersive X-ray spectroscopic (EDS) line scans were performed on individual particles using a probe size of ~1.3 Å, a step size of 2 Å, and a dwell time of 5 seconds, while correcting for spatial drift.

A.2.3 X-ray Diffraction (XRD)

Wide-angle X-ray diffraction was performed on a film of carbon supported catalyst powders on a quartz slide with a Bruker Nokius instrument using Cu K α radiation (1.54 Å wavelength). Samples were scanned from 10 to 90 degrees in 0.02 degree increments with a dwell time of 10 seconds. The average nanoparticle size was estimated from the Scherrer equation in JADE software (Molecular Diffraction Inc.). Background correction, fitting, and deconvolution were done using JADE software. The d-spacing is calculated from $d_{hkl} = \lambda / (2 \sin \theta)$, while the lattice parameter is calculated according to $a = d_{hkl} * \sqrt{h^2 + k^2 + l^2}$ where h,k, and l are the miller indices for the crystal plane, λ is the X-ray wavelength, and θ is the angle of the peak for the crystal plane reflection.

A.2.4 X-ray Photoelectron Spectroscopy (XPS)

XPS was acquired using a Kratos AXIS Ultra DLD spectrometer equipped with a monochromatic Al X-ray source (Al α , 1.4866 keV). High resolution elemental analysis was performed on the Pd 3d and Ag 3d regions with a 20eV pass energy, a 0.1 eV step, and an 4 s dwell time. Charge compensation was not used as each sample was conductive. All absolute energies were calibrated relative to gold, silver and graphite. The peak positions and areas are calculated using a standard Gaussian + Lorentzian fit with a Shirley background correction.

A.2.4 Thermogravimetric Analysis (TGA).

Thermogravimetric analysis was made with a Mettler Toledo TGA/DSC 1 STARe system equipped with a gas controller (GC 200) and a recirculating stage cooling bath set at 22°C (Julabo). A sample size of >2mg of carbon supported catalysts after calcination was used for analysis. The gas flow rate during the analysis was controlled at 60 mL_{air}/min. The catalysts were initially held at 110°C for 10 min to drive off any solvents. Next the catalysts were heated to directly to 900 at 20°C/min. The final mass remaining after the analysis was used to calculate the total metal loading (wt%).

A.2.4 Electrochemical Characterization

Catalyst inks were prepared by adding 1 mL of a 0.05 wt% Nafion solution to 1 mg of catalyst powder and sonicated for 30 minutes. 10 µL of ink was drop cast onto a clean 5mm (0.196 cm²) glassy carbon electrode and left to dry under a glass vial. The glassy carbon electrodes were cleaned prior to drop casting by sonication in a 1:1 DI water:ethanol solution. The electrode was then polished using 0.05 µm alumina powder, sonicated in a fresh DI water:ethanol solution, and dried in ambient air. All electrochemical tests were performed on electrodes prepared by this method, such that the metal loading for all catalysts was 10 µg/cm².

Electrochemical testing was performed on either a CH Instruments CHI832a or a Metrohm Autolab PGSTAT302N potentiostat, both equipped with high speed rotators from Pine Instruments. Each test was performed in a standard 3 electrode cell, with a Hg/HgO (1M KOH) reference electrode, a Pt wire counter electrode, and the catalyst ink film on glass carbon as the working electrode. All testing was done at room temperature in 0.1M KOH. The solution was deaerated by bubbling argon for at least 10 minutes. The catalyst was electrochemically cycled from -0.9 to 0.25 V (Hg/HgO) at 20 mV/s for 10 cycles to clean the surface. Immediately following the cleaning procedure, an

extended cyclic voltammogram (CV) from -0.9 to 0.55 V at 20 mV/S for 2 cycles was performed to identify the oxidation/reduction for both Ag and Pd. The total amount of charge to reduce the oxidized metal surface was used to estimate the surface composition of the catalyst. The oxidation of silver involves one electron per silver atom ($\text{Ag}_2\text{O} + \text{H}_2\text{O} + 2\text{e} \rightarrow 2\text{Ag} + 2\text{OH}^-$ or $\text{AgOH} + \text{e} \rightarrow \text{Ag} + \text{OH}^-$)⁴³ while the reduction of Pd oxide requires two electrons ($\text{Pd}(\text{OH})_2 + 2\text{e} \rightarrow \text{Pd} + 2\text{OH}^-$).⁴⁴ The electrolyte was then saturated with oxygen by bubbling for a minimum of 10 minutes. ORR activity measurements were taken by rotating the electrode at 1600 rpm and performing a linear sweep from 0.2 to -0.6 V at 5 mV/s. Kinetic currents were used to evaluate mass activities and were taken at -0.05V vs NHE from the polarization curves. The kinetic current was calculated according to the Koutecky-Levich equation: $\frac{1}{i} = \frac{1}{i_d} + \frac{1}{i_k}$. The number of electrons transferred, n , for the ORR was calculated based on the diffusion limited current according to the Levich equation: $i_d = 0.620nFAD^{\frac{2}{3}}\omega^{\frac{1}{2}}\nu^{\frac{-1}{6}}C$, where F is Faraday's constant (96485 C/mol), A is electrode area (0.196cm²), D is diffusion coefficient for dissolved oxygen (2x10⁻⁵ cm²/s), ω is scan rate (1600 rpm or 167.7 rad/s), ν is kinematic viscosity (0.01 cm²/s), and C is the saturated oxygen concentration in 0.1 M KOH at an oxygen partial pressure of 1 atm (1.2x10⁻⁶ mol/cm³).²¹

CO stripping was performed to determine the surface composition of the catalyst. The solution was saturated with CO by bubbling for 30 min. The potential of the electrode was held at -0.8 V (Hg/HgO) for 15 min. The solution was then purged with Ar while still holding the potential at -0.8 V (Hg/HgO) for 20 min. The potential was then cycled 3 times between -0.8V and 0.3 V (Hg/HgO).

A.3 RESULTS AND DISCUSSION

To realize the electronic and ensemble effects, the catalyst composition and morphology were controlled via thermolysis of organometallic precursors in the presence of capping ligands to arrest particle growth, as demonstrated for other alloy systems.^{35-37,45} Ag and Pd were separately complexed to tetradecanoic acid, which acted as a capping agent to arrest the growth of the particles after reduction by tripropylamine.⁴¹ The similar reduction rates of the complexes yielded small ($\sim 3\text{-}5$ nm), relatively monodisperse sizes for the AgPd alloys and pure Ag nanoparticles determined via TEM and shown by micrographs for Ag₉Pd ($3.2\pm 0.6\text{ nm}$) and Ag ($4.3\pm 0.7\text{ nm}$) in Figures A.5A,D and A.6A,D, respectively. The alloy particles (for Ag₉Pd) after adsorption onto the carbon support and removal of the ligands at 450°C in nitrogen remain small and uniformly dispersed on the carbon (5.3 nm Figures A.1A, A.5B, and A.5E), as is also seen for the commercial Pd particles (5.7 nm, Figure A.5C,F). Similar sizes were obtained for the other AgPd alloy ratios in Table A.1. With only 10 mol% Pd, the nanoalloy particles were resistant to sintering at 450°C , whereas the pure Ag particles coalesced to 19 nm (Figure A.6C,F). The Pd acts to effectively lower bulk atomic mobility and movement of the particles on the support during calcination, thereby strongly anchoring the particles and mitigating thermal sintering.⁴⁶ For a lower calcination temperature of 210°C , the degree of sintering for pure Ag is mitigated, yielding a final particle size of 10 nm (Figure A.6B). The alloy particles displayed an FCC crystal structure as shown by the characteristic $\{111\}$, $\{200\}$, $\{220\}$, $\{311\}$, and $\{222\}$ reflections in their XRD spectrum (Figure A.1B, A.7). This structure is expected as both Pd and Ag are FCC crystalline materials. Scherrer analysis was performed on the $\{111\}$ reflections to calculate crystallite sizes. The values span from $\sim 4\text{-}8$ nm as summarized in Table A.1, consistent with the values measured via TEM. Probe-

corrected STEM was performed on the Ag₉Pd catalyst, clearly showing the crystalline nature of the particle (Figure A.1C). Electron diffraction reveals that the particle surface is dominated by {111} planes and contains twinning, common among Ag nanoparticles.⁴⁷

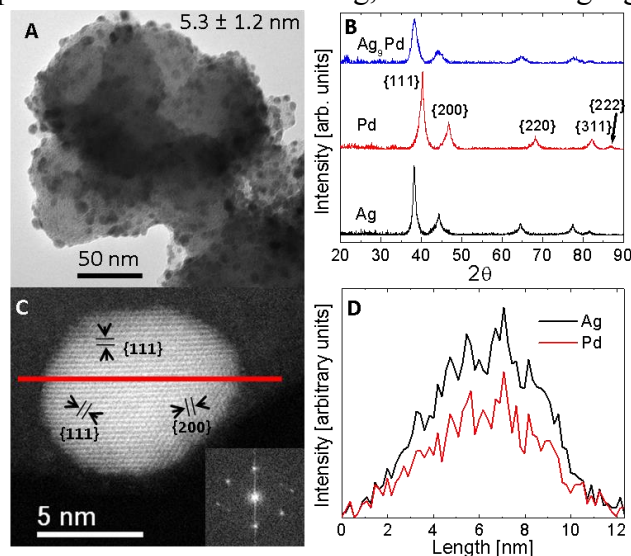


Figure A.1. Ag₉Pd nanoparticles supported on Vulcan XC72 carbon after calcination at 350°C in N₂

as shown by (A) TEM and (B) XRD. The TEM shows that the particles are uniformly distributed over VC with an average particle size of 5.3 ± 1.2 nm. The peak for {111} is located between both pure Pd and Ag due to the alloying with 10 mol% Pd (as confirmed by Vegard's law). The lack of additional peak shoulders suggests that the particles are composed of a single alloy phase, Ag₉Pd. The uniform composition is confirmed by the STEM EDS line scan (C,D). Furthermore, the particles are shown to be composed primarily of {111} facets (C insert), along with twinning for the {111}.

Uniform alloying among the particles was achieved by the simultaneous reduction of Ag and Pd at similar rates, as a consequence of the same tetradecanoate complex for each metal.⁴¹ The lack of peak shoulders for the crystalline reflections from XRD

suggests a uniform alloy composition among particles (Figure A.1B, A.7). The alloy composition can be estimated according to Vegard's Law^{48,49} for an unstrained alloy. Here, the composition of the alloy follows a simple linear relationship based on the shift in lattice constant of the alloy from that of either of the pure components. The compositions correspond closely to the starting precursor ratios as shown in Table A.1. For example, the atomic percentages calculated using Vegard's Law for Ag₉Pd and Ag₄Pd are 90% and 78% Ag, respectively. The compositions measured by XPS shown in Figure A.2, are in agreement with the less quantitative results calculated from Vegard's law. Furthermore, a probe-corrected STEM-EDS line scan across a single Ag₉Pd alloy nanocrystal (Figures A.1C,D) directly shows the uniformity of the alloy throughout the particle. Both Ag and Pd have the same signal ratio from the edge to the center of the particle, indicating little intraparticle segregation of metals. It should be noted that due to the significant overlap of the Pd and Ag EDS spectra, which makes deconvolution impractical, this method cannot be used to determine alloy composition quantitatively.

Table A.1. Summary of catalyst loading, morphology and composition.

Catalyst	wt% loading	Size [nm]	XRD Size [nm]	Vegard's Law Ag mol%	XPS Ag mol%
Ag	28	10.1	11.8	100	100
Ag	28	19.0	--	--	100
Ag ₉ Pd	23	5.3	A.0	90	91
Ag ₄ Pd	23	5.1	4.4	78	83
Ag ₂ Pd	24	6.8	3.7	55	65
AgPd ₂	25	6.6	6.8	36	38
Pd	19	5.7	7.7	~0	~0

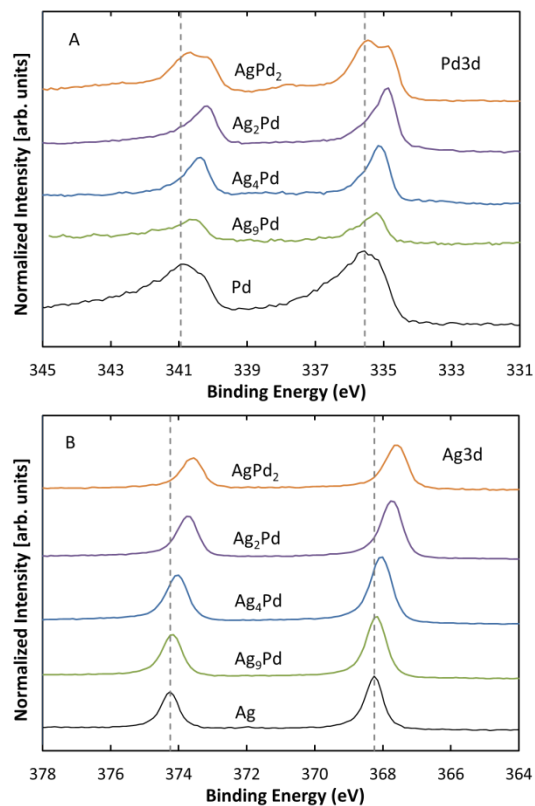


Figure A.2. XPS spectra for the (A) Pd3d and (B) Ag3d regions for all Pd:Ag alloy ratios as well as the pure metals.

The Pd peaks are shifted negatively for all alloy ratios, as the Pd atoms always have a significant number of Ag atoms with which to interact. However, the Ag peaks only show a shift when the alloy ratio is $\text{Ag}_{\leq 4}\text{Pd}$, when there are enough Pd atoms in the particles to sufficiently disturb the Ag-Ag interactions.

The polarization curves for the most active ORR alloys (Ag_9Pd and Ag_4Pd alloys) are shown along with the pure metal components in Figure A.3A. Kinetic current densities are measured at -0.05 V vs NHE from the linear sweep voltammograms and

calculated according to the Koutechy-Levich equation. Catalyst loadings on Vulcan XC72 carbon were 22 wt%, 24 wt%, and 23 wt% for Ag₉Pd, Ag₄Pd, and Ag, respectively, as measured by TGA (Figure A.8), comparable to the 20 wt% commercial Pd on Vulcan XC72 for a meaningful comparison of activities. Additional polarization curves and activities are provided in the supplemental section (Figure A.9 and Table A.2), indicating a non-linear enhancement, with the largest activity boost occurring for Ag₉Pd and Ag₄Pd. The synergy in the activity is depicted for all of the catalysts in Figure A.3B. Here, all of the activities lie above the line drawn between the pure components. The overall activity of AgPd₂ is actually 60% higher than for Pd. A factor of 3.2 above the linear combination in activities was achieved for Ag₄Pd, as shown in Table A.2, suggesting that the presence of both Ag and Pd provide synergistic enhancement. An activity of ~207 mA/mg_{Ag+Pd} would be expected for an alloy with 80 mol% Ag (~60 mA/mg_{Ag}) and 20 mol% Pd (~799 mA/mg_{Pd}), assuming a linear combination of pure component activities. However, the measured activity was ~598 mA/mg_{Ag+Pd} for the Ag₄Pd catalyst, 3.2x above this prediction. Similar trends are observed for other Ag-rich alloys are observed, including a 2.7 fold increase Ag₉Pd, whereas for alloy ratios of Ag₂Pd and AgPd₂, the enhancement is slightly lower (ca. 2.3x). The Pd based mass activities are summarized in the histograms in Figure A.3C and Table A.2. By mass of Pd, the alloy is up to 4.7x more active than pure Pd, with a value of 3778 mA/mg_{Pd} for Ag₉Pd versus 799 mA/mg_{Pd} for pure Pd/VC. Based on the size of the nanoparticles as measured from TEM, an estimated specific activity was calculated and summarized in Table A.2, and plotted in Figure A.3D. The specific activity increases monotonically with increasing Pd composition, reaching a maximum of 2.6x above the expected value for the linear combination of pure metal specific activities. Due to the difference in particle size for pure silver (19nm or 10 nm) vs the other

catalysts in this study (~ 5 nm), it may be reasonable to assume that the Ag mass activity could increase if it were ~ 5 nm, due to an increased surface to mass ratio. However, a slower rate of 4 electron reduction was observed for 20 nm Ag particles relative to 100 nm particles, which was attributed to fewer of the more active terrace sites on the smaller particles.^{20,50} In our study, we observed specific activities of 106 mA/cm^2 and 151 mA/cm^2 for 10 nm and 19 nm Ag particles, respectively. Therefore, it is unclear that smaller particles of Ag would demonstrate higher activity, however, 10 nm Ag is used for comparison in the synergy plots for both mass and specific activity.

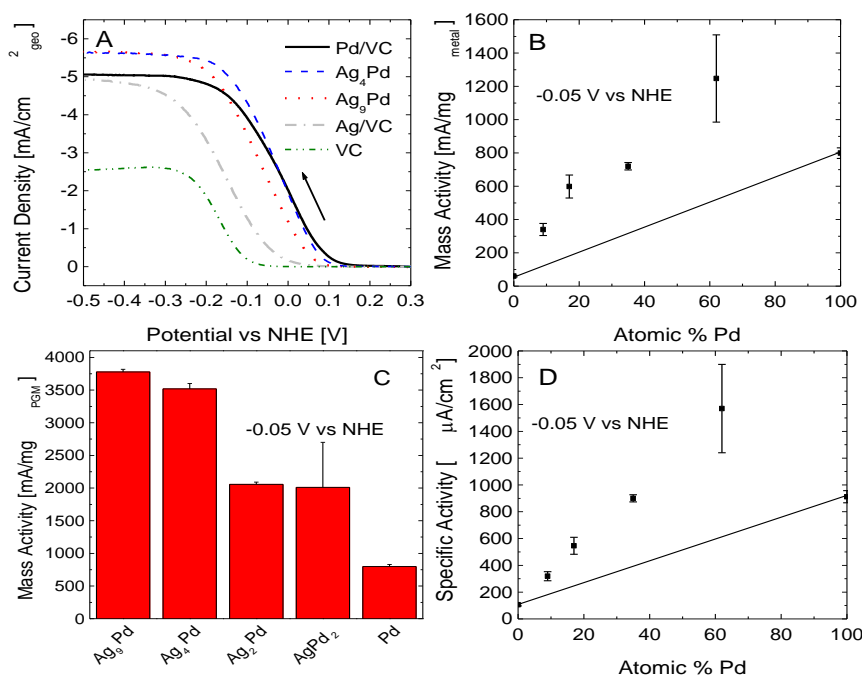


Figure A.3. Oxygen reduction activity comparison between Ag-rich alloys and pure components.

(A) Linear sweep voltammograms from a rotating disk electrode measurement in O₂ saturated 0.1 M KOH. The diffusion limited current density for the alloy corresponds to a 4 electron process, higher than either pure Ag or Pd (3.4). (B) Synergy plot of mass activity normalized by total metal loading versus Pd composition. The solid line indicates the linear combination of activities between the pure Ag and Pd components. All of the activities lie above the solid line, indicating a synergy in ORR activities across the compositional range. (C) Bar plot summarizing the ORR activity per Pd loading. The synergy between the Ag and Pd in the alloy achieves a Pd mass normalized activity of 4.7x over the commercial Pd/VC and up to 3.2x over the linear combination of mass activities for pure Ag and Pd. (D) Synergy plot of specific activity, where the solid line indicates a linear combination of pure component specific activities. Currents were normalized by metal particle surface areas based on measured TEM diameters.

Table A.2. Summary of ORR Activity for AgPd alloy compositions and pure component benchmarks at -0.05 V vs NHE.

Catalyst	Total Mass Activity [mA/mg _{total metal}]	Synergy Factor for Total Mass Activity	PGM Mass Activity [mA/mg _{Pd}]	Specific Activity [$\mu\text{A}/\text{cm}^2$]	Synergy Factor for Specific Activity	# of electrons
Ag (10 nm)	60	1.0	--	106	1.0	3.4
Ag ₉ Pd	340	2.7	3778	319	1.8	4
Ag ₄ Pd	598	3.2	3518	546	2.2	3.7
Ag ₂ Pd	720	2.3	2057	900	2.3	3.6
AgPd ₂	1247	2.4	2011	1570	2.6	3.7
Pd	799	1.0	799	912	1.0	3.4
VC	0.50	--	--	--	--	1.7

The onset potential for the ORR is ~20mV for Ag compared to ~130mV for pure Pd (Figure A.3A). For the Ag₉Pd alloy, the onset potential is shifted positively ~100mV, despite only 10 mol% Pd incorporated in the Ag. This shift is significantly greater than the potential of 31 mV expected for a linear combination from the pure metals. For the Ag₄Pd alloy, the calculated number of electrons transferred for the ORR, from the Levich equation, based on the diffusion limited currents was higher than the value of 3.4 observed for both Ag and Pd (Figure A.3, Table A.2). At a ratio of Ag₉Pd, the electron transfer number reached 4, indicating high efficiency for the full reduction of oxygen.⁵¹ The synergy from alloy Ag and Pd suggests that ligand and atomic ensemble effects are at play, as we elaborate below.

Cyclic voltammetry (CV) was used to probe the surface composition of the nanoalloys (Figures A.4 and A.11). The CV for pure Pd in Figure A.4 contains the expected adsorption and desorption of H_{upd} from -0.4V to -0.8V, along with the characteristic Pd oxide reduction at -0.15V. In contrast, for the pure Ag catalyst no

features are observed for adsorption and desorption of H^+ characteristic of pure Ag.²⁰ However, when the Ag catalyst is scanned positive of 0.35V vs NHE, three characteristic oxidation peaks develop at 0.37V, 0.45V, and 0.5V, corresponding to Ag₂O monolayer formation, AgOH bulk, and Ag₂O bulk, respectively.^{29,43} The reduction of silver oxide is observed to be reversible on the negative scan, at ~0.32V. The CV of the Ag₉Pd alloy catalysts shows oxide reduction peaks for both Pd (-0.17V) and Ag (0.25V), indicating that both metals are electroactive at the surface. However, it appears that the location of the metals in the surface has a profound effect on reaction characteristics. At negative potentials, associated with hydrogen adsorption/desorption, the alloy displays no peaks, similar to the response for a pure Ag surface. Previous reports on Pd-Au alloys also demonstrate this behavior, suggesting that a minimum cluster size of Pd dimers is required to show hydrogen adsorption/desorption. Similarly, our results suggest single Pd atoms are dispersed in the Ag rich surface domains.¹⁴

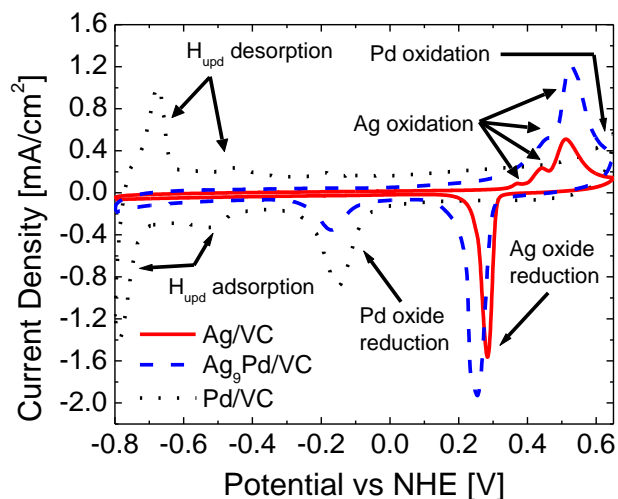


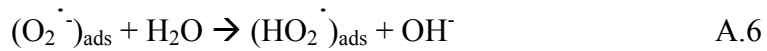
Figure A.4. Cyclic voltammograms showing the characteristic redox peaks for the alloy and pure metal catalysts supported on Vulcan XC72 carbon.

The presence of both Ag and Pd oxide reduction peaks shows that the surface is composed of both metals. However, the lack of H_{upd} for the alloy suggests that the Pd is dispersed primarily as single atomic sites. The silver oxidation peaks from 0.3 to 0.6 V shift slightly positive for the alloy catalyst, suggesting some resistance to oxidation due to the small amount of Pd. The large reduction peak of silver oxide is shifted negative, suggesting slightly more stable oxide formation.

For alloy ratios $\text{Ag}_{\leq 2}\text{Pd}$, the H_{upd} peaks, characteristic of pure Pd emerge, while the ratios of the peak intensities for Pd reduction versus Ag oxidation increase (Figure S6). At these high Pd levels, Pd-Pd contacts in the alloy surface are readily available to processes that depend upon contiguous Pd atoms. CO stripping experiments on the Ag_9Pd alloy (Figure A.11) support the evidence from CVs; that both Pd and Ag are present on the surface and that isolated Pd-Pd domains are negligible. Ag shows no peak

associated with CO oxidation (stripping),⁵² while Pd shows a sharp CO oxidation peak at $\sim 0.1\text{V}$. However, the alloy shows only two diffuse peaks at -0.05V and 0.2V again indicating an absence of Pd surface clusters with greater than three atoms. In summary, the absence of specific signatures in the CVs for adsorption of both H^+ and the Pd or Ag oxidation/reduction peaks indicates that the Pd is highly dispersed in the surface of the alloy, with minimal binary and higher Pd-Pd domains for $\text{Ag}_{\geq 4}\text{Pd}$. For all alloy systems, both Pd and Ag are well alloyed and available in the surface of the small nanoalloy particles for the ORR, which is essential for achieving enhanced catalytic activity from ligand and ensemble effects.

Insight into the ligand effect, where the electronic structure of the metals changes due to alloying, can be gleaned from the binding energy shifts in XPS^{1,3} and consideration of the reaction steps for the ORR. The binding energies for both Ag and Pd are shifted negatively (Figure A.2 Table A.3), consistent with observations for PdAg alloy films.¹⁰ For Ag_9Pd in Figure A.2, the peaks for the Pd 3d doublet are shifted by $\sim 0.4\text{ eV}$ to lower binding energies, while the Ag is shifted negative by only $\sim 0.1\text{ eV}$ (on the order of the instrument resolution). A smaller binding energy (BE) shift is observed for the Ag 3d doublet, as it is in 9 fold excess of the Pd, causing an attenuation of the shifted signal as seen for AgPd alloys containing a dilute amount of Pd.¹⁰ It has been reported that the BE shifts are due to a gain of charge density in the d-band, concomitant with a loss in the sp-band. According to DFT calculations, an up-shift in the d-band center can create a stronger bonding with the oxygen, thereby creating more favorable BE for the ORR intermediates to enhance activity.^{23,53,54} It has been well established that the 2x2 pathway which becomes available in basic media (Eq. A.2a) proceeds via a three-step surface mediated mechanism.⁵⁵



By increasing the d-band charge density, this may facilitate the initial electron transfer step (Eq. A.4a). As Ag has a significantly weaker oxygen binding than Pd⁵³, an up-shift in d-band is especially important for the Ag_{≥4}Pd catalysts to increase the oxygen binding affinity of the catalysts for facilitating the first electron transfer step. The uniform alloying among particles ensures that the entire catalyst experiences the d-band shift to achieve higher activities. Furthermore, low interaction energy between oxygen and Au has been shown to result from fully filled bonding and anti-bonding states.⁵⁶ As Ag and Au have similar electronic structures (with the addition of a filled f shell for Au), this may explain why Ag lies on the weak binding side of the volcano plot. However, when Pd was added to the Au, unoccupied oxygen-metal bonding states appear and contribute to strong oxygen binding, similar to the Pd in the Ag surface for the alloys in this study. However, this electronic ligand effect was shown to play a minor role next to the ensemble effects in PdAg films toward CO adsorption and oxidation.^{10,11} Thus, ligand effects alone are not responsible for the observed activity synergy for the AgPd alloys.

The data strongly support the existence of an ensemble effect, whereby a suitable geometric arrangement of Ag next to Pd surface atoms catalyzes ORR. Previous DFT calculations support this idea, as Ag has weak binding and Pd strong binding on a volcano of activity versus binding⁵³, suggesting a combination of the metals may result in higher activities.^{54,57} The stronger binding of hydroxyl species on Pd versus Ag has been shown to be the cause of hysteresis in polarization curves²⁰, and is evidenced in our

studies by the much larger double layer capacitance for pure Pd relative to Ag (Figure A.10). By creating an alloy surface, the Pd atoms may facilitate the initial oxygen binding (e.g. Eq. A.4), whereas the Ag may help to desorb the reaction products such as OH⁻, evidenced by the smaller double layer capacitances for the alloys versus Pd/VC. For Pd in an Au surface, DFT calculations suggest the most likely spot for oxygen adsorption to occur at the Pd sites, where one O atom binds atop and the other is coordinated in a hollow site.⁵⁶ Similarly, the oxygen may bind at the Pd sites, with one O atom “spilling over” onto the Ag site. When a reaction such as Eq. A.6 occurs, the hydroxyl species could easily leave the surface. This could then allow for the final electron transfer on the Pd site back to form the hydroperoxyl anion, followed by chemical disproportionation on the empty adjacent Ag site. In this way, the full 4 electron process can be achieved by combining the fast kinetics of Pd for the first 2 electron reduction (Eq. A.2a) with the rapid disproportionation on Ag (Eq. A.3). Recently, high ORR activity for a Pd-rich alloy film of Pd₃Fe²⁶ was attributed to the presence of a less active metal, Fe, in the surface to act as a binding center for ORR intermediates, highlighting the importance of ensemble effects. In contrast, in the current work the AgPd alloy is shown to exhibit a high level of synergy with a dilute amount of the more active metal, Pd, as well as for higher Pd contents. The high fraction of Pd-Ag versus Pd-Pd contacts for the low content Pd alloys would be expected to be highly beneficial for creating strong ligand and ensemble effects. Given the much higher cost and activity of Pd relative to Ag, this strategy has the potential to be of great practical benefit.

As far as the authors are aware, high catalytic activity and stability for oxygen reduction through ensemble effects with uniform nanoalloys containing extremely low concentrations of a highly active, precious metal has not been reported previously. The

high synergy achieved for the pre-synthesized Ag_{≥4}Pd uniform alloy morphology is in contrast to previous reports for Ag catalysts alloyed with a small amount of Pd or Pt, which have shown little to negative synergy in ORR activities.^{30,31,33,34} These AgPd nanoparticle alloys were synthesized by the typical approach of adsorption and reduction of metals salts in the presence of the support,^{30,31} which may lead to non-uniform compositions among particles as a result of the different nucleation and growth rates upon reduction of metal ions, as well as the diffusion and adsorption rates of the growing metal particles on the support.⁵⁸ The lack of intimate mixing between Ag and Pd may lead to decreased electronic and ensemble effects. Thus, it is essential to synthesize uniform nanoalloys to take advantage of low precious metal content by dispersing in throughout the surface of the particles to achieve strong ligand and ensemble effects, in our case producing a mass activity synergy factor up to 3.2 beyond the linear combination of Ag and Pd.

This strategy of enhancing catalyst activity by employing ensemble and ligand effects for a precious metal surrounded primarily by a large number of second metal atoms is a fundamentally different approach than in the case of core-shell nanoparticles.^{5,6,22,24,59,60} For the core-shell morphology, the more active metal is nearly all in the monolayer shell and available for surface reactions. However, the number of unlike metal contacts at the inside of the shell is lower than in the case of a uniform alloy with both metals at the surface. Both core-shell and alloy morphologies have been contrasted for ~40 nm PdAu catalyst for formic acid oxidation.¹³ Due to the presence of both metals in the surface for ensemble effects, the activity for formic acid oxidation was higher on the alloy surface than for the core shell particles, where unlike metal contacts and thus ensemble effects are weaker. Furthermore, for the smaller 5 nm nanocrystals in the current study, it would not be possible to achieve a low Pd content with a Pd

monolayer as in the case of the Ag₉Pd alloy. Thus, the nanoalloy approach is a highly complementary alternative to core-shell catalysts to achieve synergistic effects in catalysis.

A.4 CONCLUSIONS

A synthetic strategy has been demonstrated to produce uniform ~5 nm AgPd alloy nanoparticles across a wide compositional range via arrested growth during the simultaneous thermolysis of metal precursors to gain fundamental insight into catalytic mechanisms. The compositions of the particles were tuned to control the fraction of the Pd-Pd versus Ag-Pd contacts on the surface. For alloys of Ag_{≥4}Pd, the surface contained single Pd atoms surrounded by Ag atoms, which maximized the ability of a hetero-atomic site to amplify the activity of each Pd atom. Determination of atomic ensembles in the surface was accomplished with cyclic voltammetry and CO stripping, electrochemical techniques sensitive to the local environment of atoms in the surface. This level of atomic information is typically not available for the dominant nanoscale characterization techniques (TEM or STEM). In addition to the geometric structure of the surface, the electronic structure of the alloy was shown to shift according to XPS, contributing to enhance ORR activities. While synergy in activity was present for all alloy ratios, it reached as much as 3.2 for Ag₄Pd relative to the linear combination of the pure components, and the Pd normalized mass activity was as much as 4.7 times that of pure Pd. Furthermore, the overall mass activity per total metal was 60% higher for AgPd₂, which equates to a reduction in cost (\$/A) by a factor of 2.3. For low Pd content alloys, the synergy in activity was favored by the high degree Pd-Ag versus Pd-Pd contacts, which modified the Pd electronic structure, and by ensemble effects, evidenced by CV and CO stripping measurements which show the involvement of distinct mechanistic

steps the Ag and Pd domains in the alloys. The synergy factor for $\text{Ag}_{\leq 2}\text{Pd}$ may result from ensemble effects from larger domains of Pd surrounded by Ag. These studies provide a general approach for understanding and achieving high synergy in catalyst activity via electronic and ensemble effects.

A.5 ADDITIONAL INFORMATION

TEM, cyclic voltammograms, linear sweep voltammograms, XRD, and XPS of other alloy ratios and pure metal standards, as well as CO stripping for Pd, Ag, and Ag_9Pd are available in Appendix A.7.

A.6 REFERENCES

- (1) Liu, P.; Norskov, J. K. PCCP 2001, 3, 3814.
- (2) Mavrikakis, M.; Hammer, B.; Norskov, J. K. Phys. Rev. Lett. 1998, 81, 2819.
- (3) Rodriguez, J. A. Heterogen. Chem. Rev. 1996, 3, 17.
- (4) Fernandez, J. L.; Raghuvver, V.; Manthiram, A.; Bard, A. J. J. Am. Chem. Soc. 2005, 127, 13100.
- (5) Koh, S.; Strasser, P. J. Am. Chem. Soc. 2007, 129, 12624.
- (6) Sasaki, K.; Naohara, H.; Cai, Y.; Choi, Y. M.; Liu, P.; Vukmirovic, M. B.; Wang, J. X.; Adzic, R. R. Angew. Chem. Int. Ed. 2010, 49, 8602.
- (7) Stamenkovic, V. R.; Fowler, B.; Mun, B. S.; Wang, G.; Ross, P. N.; Lucas, C. A.; Markovic, N. M. Science 2007, 315, 493.
- (8) Chen, M.; Kumar, D.; Yi, C.-W.; Goodman, D. W. Science 2005, 310, 291.
- (9) Han, P.; Axnanda, S.; Lyubinetsky, I.; Goodman, D. W. J. Am. Chem. Soc. 2007, 129, 14355.
- (10) Ma, Y.; Bansmann, J.; Diemant, T.; Behm, R. J. Surf. Sci. 2009, 603, 1046.
- (11) Ma, Y.; Diemant, T.; Bansmann, J.; Behm, R. J. PCCP 2011, 13, 10741.
- (12) Cuesta, A. Chemphyschem 2011, 12, 2375.
- (13) Hong, J. W.; Kim, D.; Lee, Y. W.; Kim, M.; Kang, S. W.; Han, S. W. Angew. Chem. Int. Ed. 2011, 50, 8876.
- (14) Maroun, F.; Ozanam, F.; Magnussen, O. M.; Behm, R. J. Science 2001, 293, 1811.

- (15) Bruce, P. G.; Scrosati, B.; Tarascon, J.-M. *Angew. Chem. Int. Ed.* 2008, 47, 2930.
- (16) Girishkumar, G.; McCloskey, B.; Luntz, A. C.; Swanson, S.; Wilcke, W. J. *Phys. Chem. Lett.* 2010, 1, 2193.
- (17) Han, J. J.; Li, N.; Zhang, T. Y. *J. Power Sources* 2009, 193, 885.
- (18) Lu, Y.-C.; Xu, Z.; Gasteiger, H. A.; Chen, S.; Hamad-Schifferli, K.; Shao-Horn, Y. *J. Am. Chem. Soc.* 2010, 132, 12170.
- (19) Ogasawara, T.; Debart, A.; Holzapfel, M.; Novak, P.; Bruce, P. G. *J. Am. Chem. Soc.* 2006, 128, 1390.
- (20) Spendelow, J. S.; Wieckowski, A. *PCCP* 2007, 9, 2654.
- (21) Wiberg, G. K. H.; Mayrhofer, K. J. J.; Arenz, M. *ECS Trans.* 2009, 19, 37.
- (22) Adzic, R. R.; Zhang, J.; Sasaki, K.; Vukmirovic, M. B.; Shao, M.; Wang, J. X.; Nilekar, A. U.; Mavrikakis, M.; Valerio, J. A.; Uribe, F. *Top. Catal.* 2007, 46, 249.
- (23) Nilekar, A. U.; Xu, Y.; Zhang, J. L.; Vukmirovic, M. B.; Sasaki, K.; Adzic, R. R.; Mavrikakis, M. *Top. Catal.* 2007, 46, 276.
- (24) Shao, M. H.; Huang, T.; Liu, P.; Zhang, J.; Sasaki, K.; Vukmirovic, M. B.; Adzic, R. R. *Langmuir* 2006, 22, 10409.
- (25) Lima, F. H. B.; Zhang, J.; Shao, M. H.; Sasaki, K.; Vukmirovic, M. B.; Ticianelli, E. A.; Adzic, R. R. *J. Solid State Electrochem.* 2008, 12, 399.
- (26) Yang, X.; Hu, J.; Fu, J.; Wu, R.; Koel, B. E. *Angew. Chem. Int. Ed.* 2011, 50, 10182.
- (27) Kinoshita, K. *Carbon: Electrochemical and Physicochemical Properties*; John Wiley and Sons, 1988.
- (28) Blizanac, B. B.; Ross, P. N.; Markovic, N. M. *J. Phys. Chem. B* 2006, 110, 4735.
- (29) Guo, J.; Hsu, A.; Chu, D.; Chen, R. *J. Phys. Chem. C* 2010, 114, 4324.
- (30) Lee, C.-L.; Chiou, H.-P.; Chang, K.-C.; Huang, C.-H. *Int. J. Hydrogen Energy* 2011, 36, 2759.
- (31) Martinez-Casillas, D. C.; Vazquez-Huerta, G.; Perez-Robles, J. F.; Solorza-Feria, O. J. *New Mater. Electrochem. Syst.* 2010, 13, 163.
- (32) Oliveira, M. C.; Rego, R.; Fernandes, L. S.; Tavares, P. B. *J. Power Sources* 2011, 196, 6092.
- (33) Chatenet, M.; Aurousseau, M.; Durand, R.; Andolfatto, F. *J. Electrochem. Soc.* 2003, 150, D47.
- (34) Lima, F. H. B.; Sanches, C. D.; Ticianelli, E. A. *J. Electrochem. Soc.* 2005, 152, A1466.

- (35) Chen, W.; Kim, J.; Sun, S.; Chen, S. J. *Phys. Chem. C* 2008, 112, 3891.
- (36) Gupta, G.; Slanac, D. A.; Kumar, P.; Wiggins-Camacho, J. D.; Wang, X.; Swinnea, S.; More, K. L.; Dai, S.; Stevenson, K. J.; Johnston, K. P. *Chem. Mater.* 2009, 21, 4515.
- (37) Slanac, D. A.; Li, L.; Stevenson, K. J.; Johnston, K. *ECS Trans.* 2010, 33, 161.
- (38) Xiong, L. F.; Manthiram, A. J. *Mater. Chem.* 2004, 14, 1454.
- (39) Zhang, X.; Chan, K. Y. *Chem. Mater.* 2003, 15, 451.
- (40) Myers, S. V.; Frenkel, A. I.; Crooks, R. M. *Chem. Mater.* 2009, 21, 4824.
- (41) Yamamoto, M.; Kakiuchi, H.; Kashiwagi, Y.; Yoshida, Y.; Ohno, T.; Nakamoto, M. *Bull. Chem. Soc. Jpn.* 2010, 83, 1386.
- (42) Abe, K.; Hanada, T.; Yoshida, Y.; Tanigaki, N.; Takiguchi, H.; Nagasawa, H.; Nakamoto, M.; Yamaguchi, T.; Yase, K. *Thin Solid Films* 1998, 327, 524.
- (43) Hepel, M.; Tomkiewicz, M. J. *Electrochem. Soc.* 1984, 131, 1288.
- (44) Grden, M.; Lukaszewski, M.; Jerkiewicz, G.; Czerwinski, A. *Electrochim. Acta* 2008, 53, 7583.
- (45) Gupta, G.; Patel, M. N.; Ferrer, D.; Heitsch, A. T.; Korgel, B. A.; Johnston, K. P. *Chem. Mater.* 2008.
- (46) Luo, W.; Hu, W.; Xiao, S. J. *Phys. Chem. C* 2008, 112, 2359.
- (47) Wiley, B.; Sun, Y. G.; Mayers, B.; Xia, Y. N. *Chem.-Eur. J.* 2005, 11, 454.
- (48) Vegard, L. *Zeitschrift fuer Physik* 1921, 5, 17.
- (49) Vegard, L. *Zeitschrift fuer Physik* 1921, 5, 393.
- (50) Yang, Y.; Zhou, Y. J. *Electroanal. Chem.* 1995, 397, 271.
- (51) Bidault, F.; Brett, D. J. L.; Middleton, P. H.; Brandon, N. P. J. *Power Sources* 2009, 187, 39.
- (52) Nguyen, S. T.; Law, H. M.; Nguyen, H. T.; Kristian, N.; Wang, S.; Chan, S. H.; Wang, X. *App. Cat. B-Env.* 2009, 91, 507.
- (53) Lima, F. H. B.; Zhang, J.; Shao, M. H.; Sasaki, K.; Vukmirovic, M. B.; Ticianelli, E. A.; Adzic, R. R. J. *Phys. Chem. C* 2007, 111, 404.
- (54) Norskov, J. K.; Rossmeisl, J.; Logadottir, A.; Lindqvist, L.; Kitchin, J. R.; Bligaard, T.; Jonsson, H. J. *Phys. Chem. B* 2004, 108, 17886.
- (55) Wiggins-Camacho, J. D.; Stevenson, K. J. *J. Phys. Chem. C* 2011, 115, 20002.
- (56) Dhoubib, A.; Guesmi, H. *Chem. Phys. Lett.* 2012, 521, 98.
- (57) Fernandez, J. L.; Walsh, D. A.; Bard, A. J. *J. Am. Chem. Soc.* 2005, 127, 357.

- (58) Antolini, E. *Mater. Chem. Phys.* 2003, 78, 563.
- (59) Jiang, L.; Hsu, A.; Chu, D.; Chen, R. *Electrochim. Acta* 2010, 55, 4506.
- (60) Strasser, P.; Koh, S.; Anniyev, T.; Greeley, J.; More, K.; Yu, C. F.; Liu, Z. C.; Kaya, S.; Nordlund, D.; Ogasawara, H.; Toney, M. F.; Nilsson, A. *Nat. Chem.* 2010, 2, 454.

A.7 SUPPORTING INFORMATION

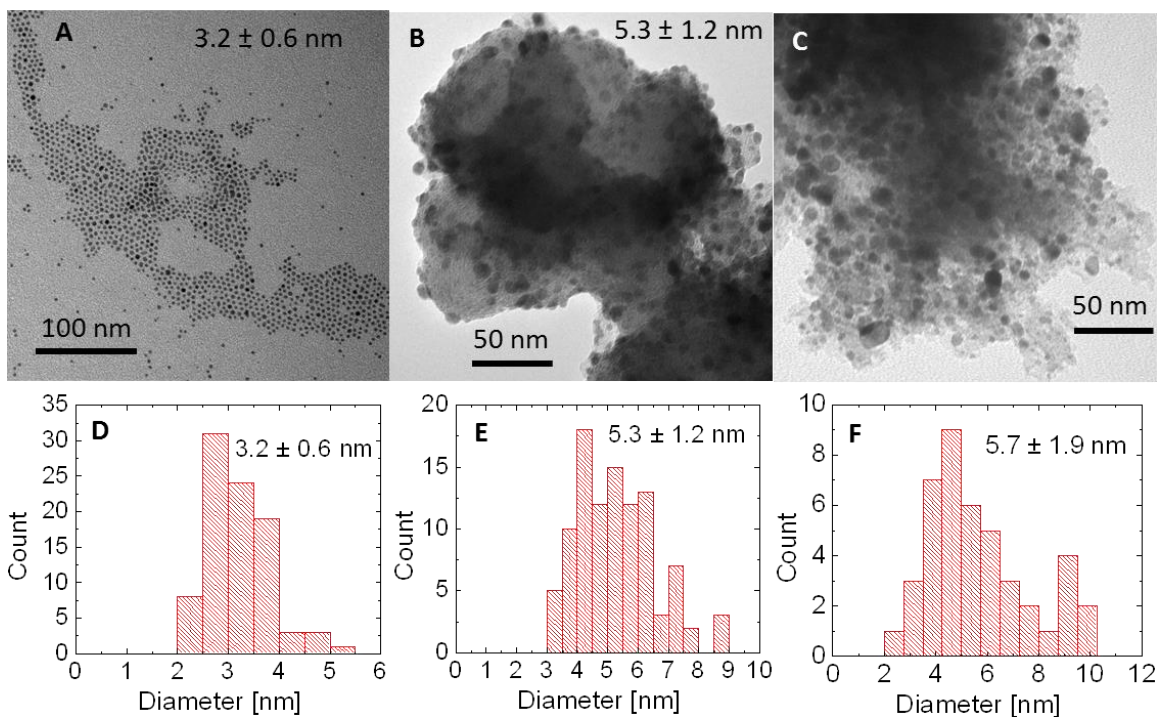


Figure A.5: Low mag TEM micrographs

of (A) as-synthesized Ag_9Pd nanoparticles, (B) Vulcan XC72 carbon supported Ag_9Pd particles after calcination at 450°C in N_2 , and (C) commercial Pd/VC calcined at 450°C in N_2 . The alloy particles undergo slight sintering from 3.2 to 5.3 nm. The similar size of the alloy and the commercial catalyst after calcination allows for meaningful comparison of activities based on their similar surface/volume ratio.

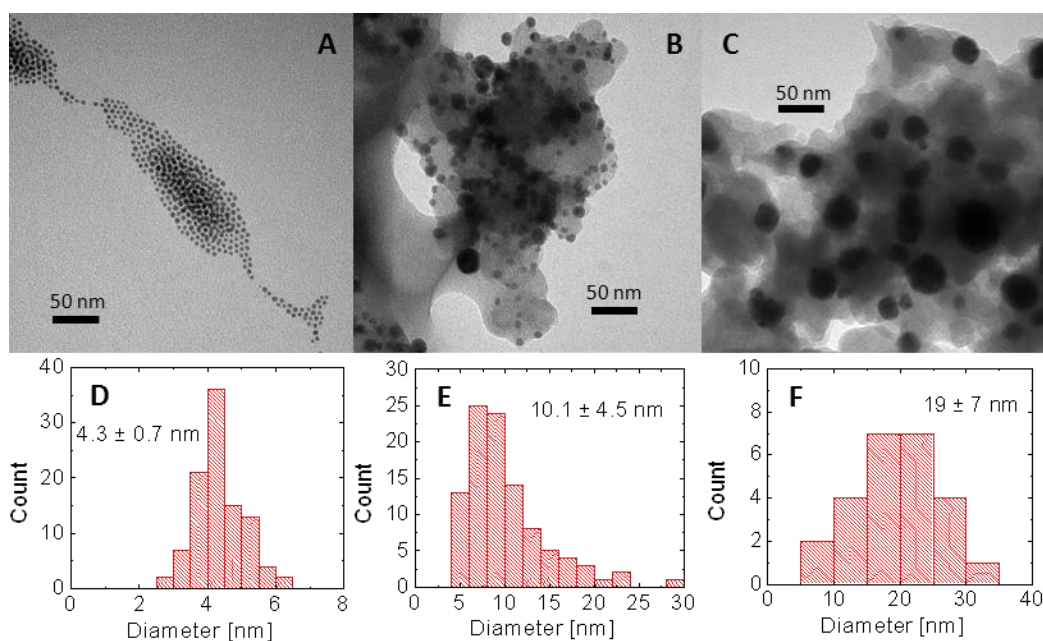


Figure A.6: TEM for pure Ag nanoparticles

(A) as-synthesized and after adsorption on Vulcan XC72 carbon and calcination at (B) 210°C in H₂/N₂ and (C) 450°C in N₂. The particles sinter significantly for calcination at 450°C as it is above the Tamman temperature for ~5nm Ag nanoparticles (220°C), {Luo, 2008 #70} where bulk diffusion becomes rapid.

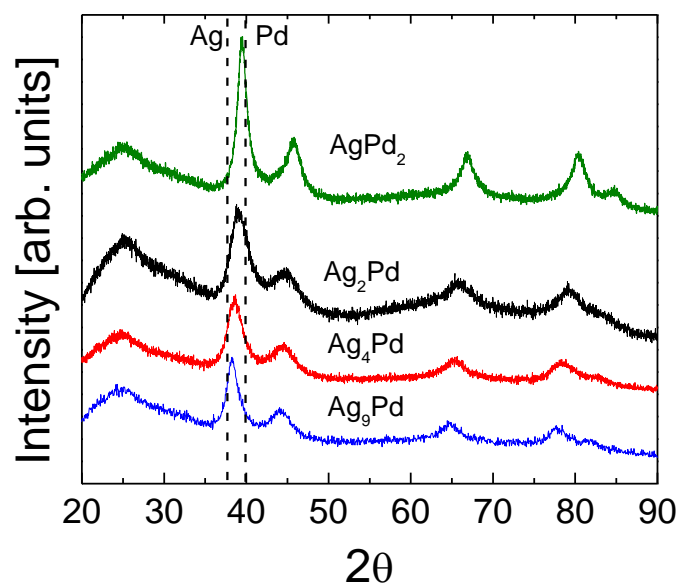


Figure A.7: X-ray diffraction for all Pd:Ag ratios.

The diffraction peaks shift linearly to higher two thetas as the amount of Pd increases in the alloy. The broad peaks from 20° to 30° correspond to the Vulcan XC72 carbon support. The particle sizes calculated from the (111) reflection with the Scherrer equation are summarized in Table 6.1.

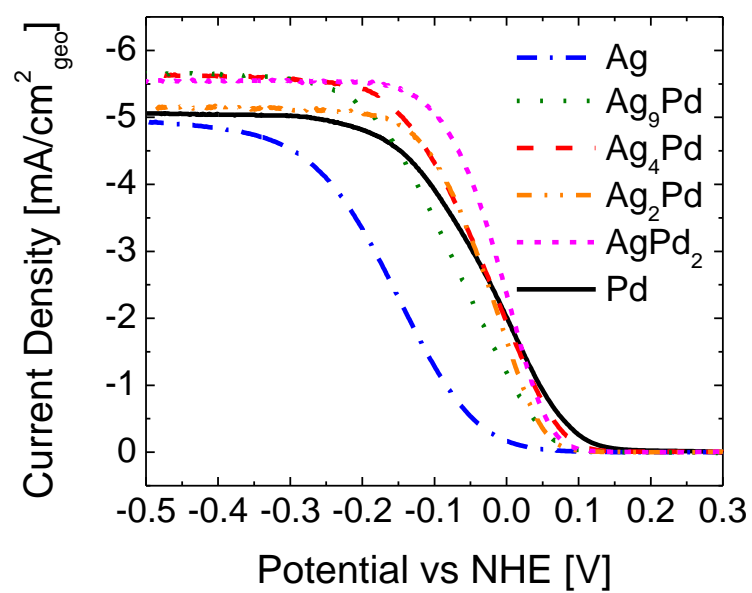


Figure A.9: Polarization curves for all alloy ratios studied as well as pure Ag and commercial Pd.

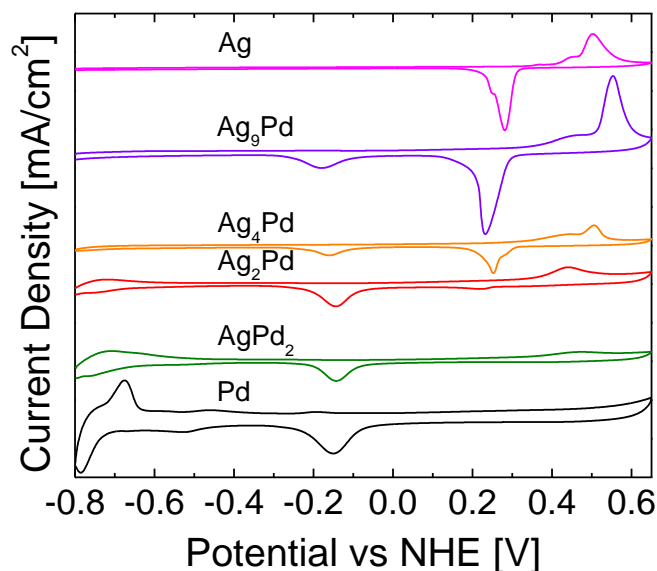


Figure A.10: Cyclic voltammograms for all Ag:Pd ratios in Ar purged 0.1 KOH.

The surface characteristics change as the more Pd is added to the alloy. For dilute $\text{Ag}_{\geq 4}\text{Pd}$, the CVs resemble that of pure Ag, with the addition of a small Pd oxide reduction peak at $\sim -0.2\text{V}$. For ratios of $\text{Ag}_{\leq 2}\text{Pd}$, the Ag oxidation peaks are diminished while the characteristic H_{upd} peaks ($\sim -0.6\text{V}$ to -0.8V) for pure Pd emerge. As a minimum of Pd dimers in the surface is required for this H_{upd} , the alloy surface can be characterized Pd monomers dispersed in Ag for $\text{Ag}_{\geq 4}\text{Pd}$, whereas Pd clusters in Ag are present for $\text{Ag}_{\leq 2}\text{Pd}$.

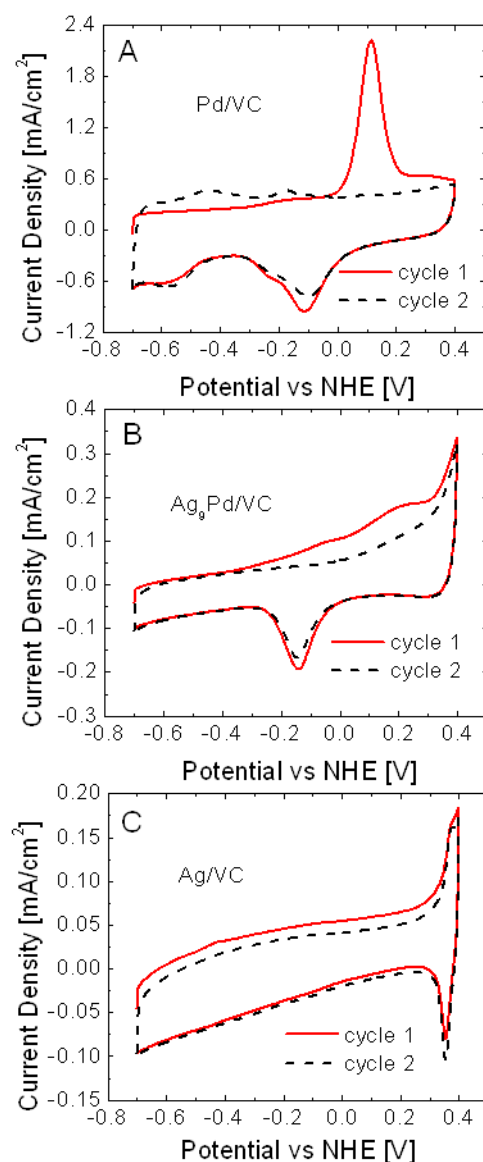


Figure A.11: CO stripping voltammograms of Vulcan XC72 carbon supported (A) Pd, (B) Ag₉Pd, and (C) Ag.

The stripping peak at ~0.12 V for pure Pd is not present for the pure Ag catalyst. The alloy catalyst displays a broad CO stripping curve from ~-0.1 V to 0.3V, indicating that the signal is not a combination of the pure components, but modified to a unique signature for the dilute Pd in Ag alloy surface.

Table A.3.1. XPS shifts for the various alloy ratios.

Catalyst	Pd 3d_{5/2} Peak [eV]	ΔPd_{5/2} [eV]	Ag 3d_{5/2} Peak [eV]	ΔAg_{5/2} [eV]
Ag	--	--	368.25	0
Pd	335.55	0	--	--
Ag₉Pd	335.2	0.35	368.15	0.1
Ag₄Pd	335.16	0.39	368.01	0.24
Ag₂Pd	334.86	0.69	367.76	0.49
AgPd₂	335.46	0.09	367.61	0.64

Appendix B: Highly Active, Non-precious Metal Perovskite Electrocatalysts for Bifunctional Metal Air Battery Electrodes⁶

B.1 EXPERIMENTAL

All chemicals were used as received. Anhydrous ethanol and 5 wt % nafion solution in lower alcohols were purchased from Sigma-Aldrich. Nickel(II) nitrate hexahydrate (99%), lanthanum(III) nitrate hexahydrate (99.999%), tetrapropylammonium bromide (TPAB, 98%), tetramethylammonium hydroxide pentahydrate (TMAOH, 99%), 2-propanol and potassium hydroxide were obtained from Fisher Scientific, and ethanol (Absolute 200 proof) from Aaper alcohol. Millipore high purity water (18 MΩ) was used. Oxygen (research grade, 99.999% purity) and argon (research grade, 99.999% purity) were obtained from Praxair. Nitrogen doped carbon (NC) was prepared as reported elsewhere.¹

B.2 CATALYST SYNTHESIS

B.2.1 Particle Synthesis

Amorphous particles composed of nickel and lanthanum hydroxides were prepared by slowly dripping (~2 mL/min) an aqueous metal nitrate solution into concentrated base containing dissolved TPAB, as reported previously.²⁻⁵ Briefly, equimolar amounts of $\text{La}(\text{NO}_3)_3$ and $\text{Ni}(\text{NO}_3)_2$ were dissolved under stirring in 50 mL of DI water, such that the total metal concentration was 9.9 mM. Separately, an equimolar amount of TPAB relative to metal nitrates was dissolved into 200 mL of 1 wt% TMAOH (pH 14) under vigorous stirring. The metal nitrate solution was slowly dripped (~2 mL/min) into the stirred base. The solution was left stirring for ~1 hour, collected and

⁶Large parts of this chapter have been published as Hardin WG, Slanac DA, Wang X, Dai S, Johnston KP, Stevenson KJ. Highly Active, Nonprecious Metal Perovskite Electrocatalysts for Bifunctional Metal–Air Battery Electrodes. *J Phys Chem Lett* 2013, 4(8): 1254-1259.

centrifuged at 8000 RPM for 4 min which resulted in a gelatinous green pellet. The gel was washed with DI water and centrifuged to obtain the final gel of amorphous particles.

B.2.2 Particle Harvesting and Crystallization

For oven dried samples, the washed hydroxide gel was spread over a glass dish and dried at 120°C under air for a minimum of 1 hour. The dried powder was collected and calcined at 700°C for 4 hours under flowing air (~120 mL/min). For samples harvested by thin film freezing (TFF), the washed hydroxide gel was dispersed in 100 mL of DI water and probe sonicated. The experimental apparatus for TFF has been described elsewhere.⁶ Briefly, a hollow metal drum was filled with dry ice and 2-propanol (~2:1 v/v) and rotated at 5 RPM. A metal plate with a tapered edge was fastened so that the plate edge grazed the drum surface. A recrystallization dish was placed directly under the plate and filled with liquid N₂. The particle solution was slowly pipetted (3 mL/min) onto the rotating drum, whereupon it froze and was subsequently scraped by the plate into the dish. Lyophilization was performed at -10°C and a fixed pressure of ~50 mTorr for 20 hours to remove all traces of water. The lyophilized powder was calcined at 700°C for 4 hours under flowing dehumidified air. Following calcination, all particles were washed with EtOH and filtered to obtain the final LaNiO₃ catalyst. All catalysts, except for those explicitly noted as unsupported, were loaded to 30wt% by mass of perovskite on nitrogen doped carbon (NC) by mixing with ball milling for 3 minutes using a Wig-L-Bug. The synthesis of the carbon composite is described elsewhere.¹

B.3 DYNAMIC LIGHT SCATTERING (DLS).

The hydrodynamic diameter (D_{Hs}) of as-synthesized hydrolysis particles was measured with a Brookhaven ZetaPALS instrument with the ZetaPlus option. Scattered light was collected with a 90° avalanche photodiode detector and all data were fit with

the CONTIN routine. The diameter of as-synthesized metal hydroxide particles were measured at a concentration of ~1 mg/mL in DI water. All measurements were made over a period of 3 min and repeated in triplicate.

B.4 X-RAY DIFFRACTION (XRD)

Wide-angle X-ray diffraction was performed on a compact powder of carbon supported catalyst on a quartz slide with a Bruker Nokius AXS D8 Advance instrument using Cu K α radiation (1.54 Å wavelength). Samples were scanned from 20 to 90 degrees in 0.02 degree increments with a dwell time of 4 seconds. The average crystallite size was estimated from the Scherrer equation. Background correction, fitting, and deconvolution were done using JADE software (Molecular Diffraction Inc.).

B.5 ELECTRON MICROSCOPY

Scanning (transmission) electron microscopy (SEM/STEM) was performed with a Hitachi S-5500 using a 30 kV accelerating voltage and a probe current of 20 μ A. The carbon supported catalysts were deposited from a dilute ethanol suspension onto a 200 mesh copper grid coated with lacey carbon or Formvar (Electron Microscopy Sciences).

B.6 SURFACE AREA ANALYSIS

Nitrogen sorption analysis was performed on a Quantachrome Instruments NOVA 2000 high-speed surface area BET analyzer at a temperature of 77 K. Prior to measurements, the samples were degassed in vacuum for a minimum of 12 hours at room temperature. The specific surface area was calculated using the BET method from the nitrogen adsorption data in the relative pressure range (P/P_0) of 0.05 to 0.30.

B.7 X-RAY PHOTOELECTRON SPECTROSCOPY (XPS)

XPS data was acquired using a Kratos AXIS Ultra DLD spectrometer equipped with a monochromatic Al X-ray source (Al α , 1.4866 keV). High resolution elemental analysis was performed on the N 1s, O 1s and La/Ni 3d core regions with a 20 eV pass energy, 0.1 eV steps, and a 4 second dwell time. Charge compensation was not used as each sample was conductive. All absolute energies were calibrated relative to gold, silver and graphite. The peak positions and areas are calculated using a standard sum Gaussian-Lorentzian fit with a linear (N, O) or Shirley (La/Ni) background correction.

B.8 ELECTROCHEMICAL CHARACTERIZATION

Catalyst inks were prepared by adding 1 mL of a NaOH neutralized 0.05 wt% Nafion solution⁷ to 1 mg of catalyst powder and bath sonicated for 30 minutes. A volume of ink (10 μ L) was drop cast onto a clean 5mm (0.196 cm², Pine Instruments) glassy carbon electrode and dried under a glass jar at ambient conditions. The glassy carbon electrodes were cleaned prior to drop casting by sonication in a 1:1 DI water:ethanol solution. The electrode was then polished using 0.05 μ m alumina powder, sonicated in a fresh DI water:ethanol solution, and dried in ambient air. All electrochemical tests were performed on electrodes prepared by this method, yielding a catalyst loading of 51 μ g/cm² (15.3 μ g_{oxide}/cm² for carbon supported LaNiO₃).

Electrochemical testing was performed on either a CH Instruments CHI832a or a Metrohm Autolab PGSTAT302N potentiostat, both equipped with high speed rotators from Pine Instruments. All testing was done at room temperature in 0.1 M KOH (measured pH \approx 12.6). The current interrupt and positive feedback methods were used to determine electrolyte resistance (50 Ω) and all data was iR compensated after testing. Each test was performed in a standard 3 electrode cell using a Hg/HgO (1 M KOH) reference electrode, a Pt wire counter electrode, and a film of catalyst ink on glassy

carbon as the working electrode. All potentials are reported versus the regular hydrogen electrode (RHE), which was shifted +0.843 V vs. Hg/HgO (Hg/HgO (1 M KOH) + 0.1 V = NHE; NHE + 0.059 * pH = RHE).

B.8.1 Quantification of Oxygen Reduction Activities

The electrolyte was saturated with oxygen by bubbling for a minimum of 10 minutes. ORR activity measurements were taken by rotating the electrode at 1600 rpm and performing a linear sweep from 1.043 V to 0.243 V RHE at 5 mV/s. Kinetic currents were used to evaluate mass activities for the ORR and were taken at 0.693 V RHE from the polarization curves. The kinetic ORR current was calculated according to the Koutecky-Levich equation: $\frac{1}{i} = \frac{1}{i_d} + \frac{1}{i_k}$. Data reported herein is the average mass activity taken from cathodic scans of multiple electrodes.

B.8.2 Quantification of Oxygen Evolution Activities

Immediately following ORR measurements, the electrolyte was saturated with argon by bubbling for a minimum of 10 minutes. OER activity measurements were taken upon rotating the electrode at 900 rpm and performing a linear sweep from -0.057 to 1.943 V at 50 mV/s.⁸ Kinetic OER currents could not be calculated due to the lack of a well-defined diffusion limited regime, as the result of interference from the oxygen bubbles. The current at 1.63 V (representing a 400 mV overpotential) was determined from the polarization curves and used to characterize the OER mass activity. To enable comparison with OER data in the literature, scans were also performed from 0.9 V to 1.943 V at 10 mV/s with a rotation rate of 1600 rpm in O₂ saturated 0.1 M KOH. O₂ saturated OER testing was performed on a new electrode which had not undergone any previous testing. The current at 1.56 V was taken from the polarization curves to compare the OER activities to values reported in literature. Note that at potentials above 1.6 V in

oxygen saturated media, visible oxygen bubble formation on the electrode surface interfered with the ability to accurately measure the activity. Data reported herein is the average mass activity taken from anodic scans of multiple electrodes.

B.9 BIFUNCTIONALITY COMPARISON

It should be noted that the OER data reported by Gorlin, et. al.⁹ for Ir/C and Pt/C was collected at 5 mV/s, whereas the OER data reported herein was taken at 10 mV/s. Capacitive current contributions in the LaNiO₃/NC system were found to be negligible, which enables a fair comparison. Figure A.4 shows the capacity corrected OER polarization curve, in which $j = 10 \text{ mA/cm}^2$ occurs at 1.660 V RHE.

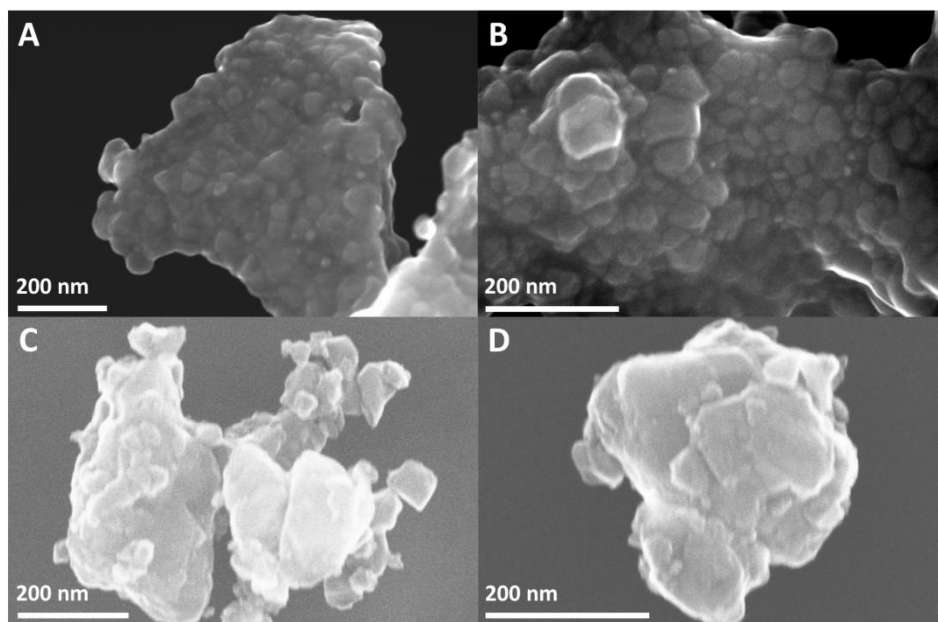


Figure B.1: SEM micrographs of particles calcined at 700°C in air.

These particles were crystallized from A/B) amorphous particles processed with thin film freezing followed by lyophilization ('freeze drying'), producing a thin film of sintered particles and C/D) amorphous particles dried in an oven at 120°C, resulting in larger particles with lower surface area.

Table B.1: Summary of particle size, size, crystallite size and BET measured surface area.

catalyst	DLS size [nm]*	SEM [nm]**	XRD [nm]***	BET [m ² /g]
LaNiO ₃	25 ± 5	20-400	15	6
nsLaNiO ₃	25 ± 5	~50	14	11

* As-synthesized amorphous precursor particle sizes

** After calcination, size of crystallites

*** Crystallite size after calcination, Scherrer analysis on {024} reflection

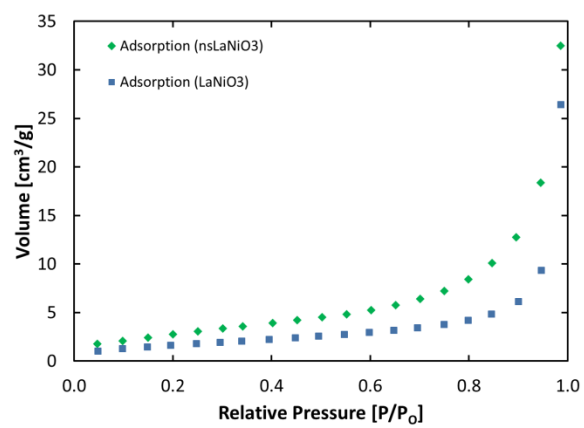


Figure B.2: BET adsorption curves for unsupported nsLaNiO₃ and LaNiO₃, used to calculate respective surface areas of 11 m²/g and 6 m²/g.

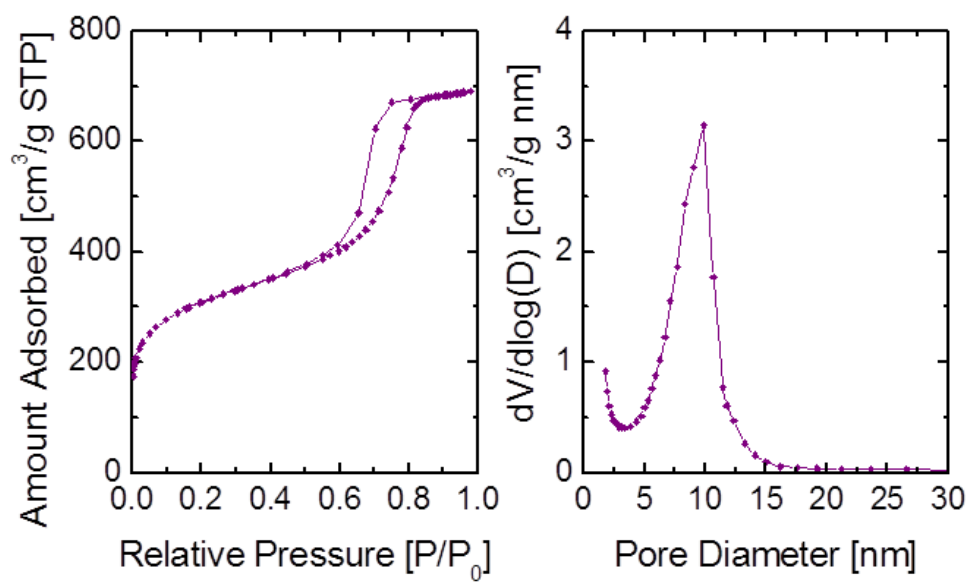


Figure B.3: BET adsorption curve and pore size distribution (PSD) for NC

Indicates a surface area of 1080 m²/g and pore volume 1.07 cm³/g. The PSD shows the carbon is primarily composed of mesopores in the range of ~10 nm.

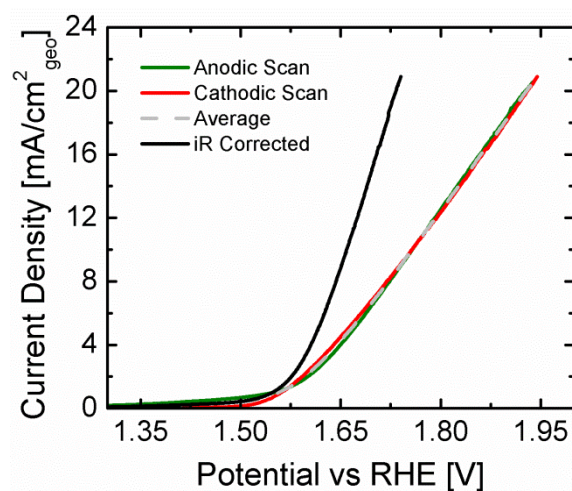


Figure B.4: OER polarization curves for both iR corrected and uncorrected nsLaNiO₃/NC in O₂ saturated 0.1 M KOH at 1600 rpm and 10 mV/s.

The anodic and cathodic scans (same electrode) are shown prior to iR correction, and the average of both scans has been taken and iR corrected to illustrate the lack of capacitive current contributions to the total observed current. The iR corrected average scan has an OER mass activity of 89 mA/mg_{oxide} at 1.56 V RHE, identical to corrected anodic and cathodic scans. Additionally, the potential at which $J = 10 \text{ mA/cm}^2$ is shifted by less than 0.5 mV when the iR corrected average scan is compared to either anodic or cathodic. Additionally, the lack of hysteresis indicates that the catalyst doesn't undergo any irreversible (electro)chemical changes during anodic cycling.

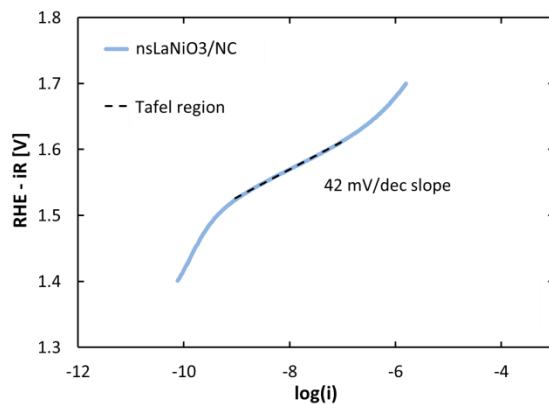


Figure B.5: Tafel plot of the iR corrected average OER polarization curve

From (Figure B.4) for nsLaNiO₃/NC in O₂ saturated 0.1 M KOH at 1600 rpm and 10 mV/s. Note that the linear fit was performed over the potential region of ~1.525 to 1.625 V, yielding a slope of 42 mV dec⁻¹ with a R² of 0.9994.

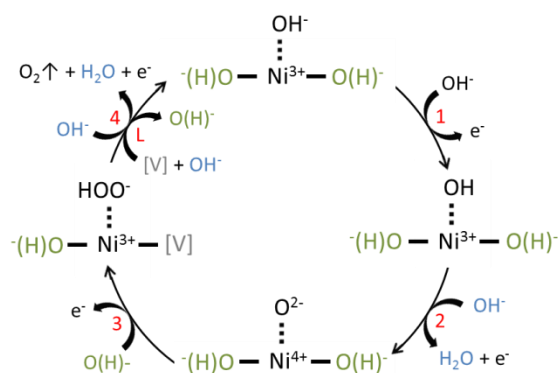


Figure B.6: The proposed alkaline oxygen evolution cycle on LaNiO_3

Includes the direct participation of lattice (hydr)oxide ions in the formation of surface hydroperoxide (step 3), resulting in a lattice vacancy that is subsequently replenished from the bulk electrolyte (step L). Surface lattice (hydr)oxides are distinguished from solution hydroxide ions by $(\text{H})\text{O}^-$, signifying their possible protonated state.

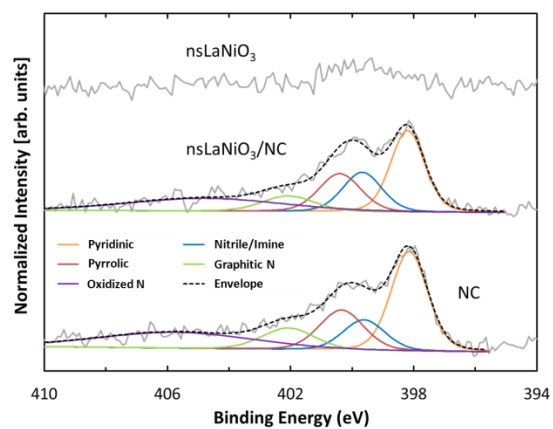


Figure B.7: High resolution XPS spectra of the N 1s core region

For neat nsLaNiO₃, nsLaNiO₃/NC and pure NC, which includes proposed peak deconvolution for pure NC and nsLaNiO₃/NC. Note the high percentage of pyridinic functionality in both spectra.

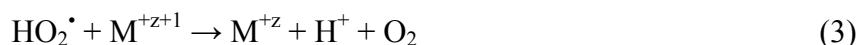
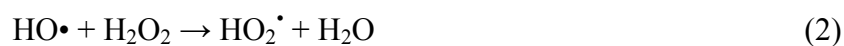
B.10 REFERENCES

- (1) Wang, X. Q.; Lee, J. S.; Zhu, Q.; Liu, J.; Wang, Y.; Dai, S. Ammonia-Treated Ordered Mesoporous Carbons as Catalytic Materials for Oxygen Reduction Reaction. *Chem. Mater.* **2010**, *22*, 2178-2180.
- (2) Imaizumi, S.; Shimanoe, K.; Teraoka, Y.; Miura, N.; Yamazoe, N. Preparation of Carbon-Supported Perovskite-Type Oxides $\text{LaMn}_{1-y}\text{Fe}_y\text{O}_{3+\Delta}$ Based on Reverse Homogeneous Precipitation Method. *J. Electrochem. Soc.* **2004**, *151*, A1559-A1564.
- (3) Imaizumi, S.; Shimanoe, K.; Teraoka, Y.; Yamazoe, N. Oxygen Reduction Property of Ultrafine LaMnO_3 Dispersed on Carbon Support. *Electrochem. Solid St.* **2005**, *8*, A270-A272.
- (4) Teraoka, Y.; Nanri, S.; Moriguchi, I.; Kagawa, S.; Shimanoe, K.; Yamazoe, N. Synthesis of Manganite Perovskites by Reverse Homogeneous Precipitation Method in the Presence of Alkylammonium Cations. *Chem. Lett.* **2000**, 1202-1203.
- (5) Yuasa, M.; Nishida, M.; Kida, T.; Yamazoe, N.; Shimanoe, K. Bi-Functional Oxygen Electrodes Using $\text{LaMnO}_3/\text{LaNiO}_3$ for Rechargeable Metal-Air Batteries. *J. Electrochem. Soc.* **2011**, *158*, A605-A610.
- (6) Engstrom, J. D.; Lai, E. S.; Ludher, B. S.; Chen, B.; Milner, T. E.; Williams, R. O.; Kitto, G. B.; Johnston, K. P. Formation of Stable Submicron Protein Particles by Thin Film Freezing. *Pharm. Res.* **2008**, *25*, 1334-1346.
- (7) Suntivich, J.; Gasteiger, H. A.; Yabuuchi, N.; Shao-Horn, Y. Electrocatalytic Measurement Methodology of Oxide Catalysts Using a Thin-Film Rotating Disk Electrode. *J. Electrochem. Soc.* **2010**, *157*, B1263-B1268.
- (8) Chen, Z.; Yu, A. P.; Higgins, D.; Li, H.; Wang, H. J.; Chen, Z. W. Highly Active and Durable Core-Corona Structured Bifunctional Catalyst for Rechargeable Metal-Air Battery Application. *Nano Lett.* **2012**, *12*, 1946-1952.
- (9) Gorlin, Y.; Jaramillo, T. F. A Bifunctional Nonprecious Metal Catalyst for Oxygen Reduction and Water Oxidation. *J. Am. Chem. Soc.* **2010**, *132*, 13612-13614.

Appendix C: Tuning the Electrocatalytic Activity of Perovskites Through Active Site Variation and Support Interactions⁷

C.1 NOTES ON $\text{LaNi}_{0.75}\text{Fe}_{0.25}\text{O}_3$ AND THE DUAL-SITE MECHANISM

$\text{LaNi}_{0.75}\text{Fe}_{0.25}\text{O}_3$ remains highly active for the ORR on either NC or G support due to its ability to disproportionate peroxide, making the additional functionality of NC redundant.¹ Two principal mechanisms for peroxide disproportionation have been proposed on perovskites: a surface transition metal mediated route in which HO^\bullet radicals scavenge oxygen from H_2O_2 (HOO^-), and a vacancy mediated route.² The transition metal mediated route is as follows:



and the suprafacial vacancy mediated route:



Previous work by Stevenson et al. has shown that peroxide disproportionation on nitrogen doped carbon occurs via a surface-mediated mechanism, resulting in a pseudo four electron ORR, in which the first two electrons are a result of the initial two electron reduction of O_2 :



while the second pair of electrons result from the hydroperoxide intermediate interacting with surface-bound Fe (oxy)hydroxide.^{3,4} Key to the dual site mechanism is the electron transfer involving surface mediated adsorption of HO_2^- onto hydroxylated Fe(III), forming Fe(II) and $\text{O}_2^{\bullet-}$ (site one), followed by the combination of $\text{O}_2^{\bullet-}$ with

⁷Large parts of this chapter have been published as Hardin WG, Mefford JT, Slanac DA, Patel BB, Wang X, Dai S, *et al.* Tuning the Electrocatalytic Activity of Perovskites through Active Site Variation and Support Interactions. *Chem Mater* 2014, **26**(11): 3368-3376.

HO₂• at Fe(III)-OH (site two). Presumably the stability imparted by the pyridinic nitrogen group in close proximity to the Fe (oxy)hydroxide that facilitates the dual site mechanism for the ORR. Of the LaNi_{1-x}Fe_xO₃ series, LaNi_{0.75}Fe_{0.25}O₃ is both the most active peroxide disproportionation catalyst and has the highest proportion of Ni(III)/Fe(IV).¹ To charge compensate for these high oxidation state species, Ni(II) and Fe(III) are then also generated in the same abundance and proportion. These species form a redox couple in which is thermodynamically capable of catalyzing peroxide disproportionation. Since transition metal oxide surfaces are well known to become hydroxylated when placed in aqueous alkaline solutions (i.e. forming Fe (oxy)hydroxide),^{1,5,6} an explanation of why LaNi_{0.75}Fe_{0.25}O₃ is so ORR active on both NC and G supports emerges. When LaNi_{0.75}Fe_{0.25}O₃ is supported on NC, the pyridinic nitrogen groups in the carbon interact with the perovskite such that HO₂⁻ is disproportionated into OH⁻ and O₂, following the dual site mechanism. When NC is replaced by G, pyridinic nitrogen is removed and the dual site mechanism becomes deactivated, or at least diminished, and an alternate disproportionation mechanism such as Eqn. 4 sustains the pseudo four electron ORR pathway.

Stability Testing

The stability of NC and G carbon supports was tested by preparing fresh electrodes as detailed in the experimental section, such that a total of 10 µg of carbon was deposited (51 µg/cm²). The electrode was rotated at 1600 rpm in O₂ saturated 0.1 M KOH and galvanostatically discharged at 10 A/g while the potential was continuously monitored. Testing was halted when the potential required to maintain the current exceeded 1.9 V

Bifunctionality Comparison

The data reported by Gorlin et. al.⁷ and used for comparison in Table 3.1 was taken at 5 mV/s, whereas the OER polarization curves taken here were at 10 mV/s. Capacitive current contributions from this increase in scan rate were found to be negligible,⁸ thus enabling a fair comparison.

Dissolved Oxygen Tests

To confirm the electrochemical generation of O₂, a fresh electrode of LaCoO₃/NC was prepared as detailed in the experimental section. To facilitate the detection of electrochemically produced oxygen, the 0.1 M KOH electrolyte was deoxygenated by bubbling of argon, after which an argon blanket was placed over the electrolyte and all openings were sealed. The electrode was held at open circuit for 15 minutes followed by a 5 minute pulse to 0.75 V (Hg/HgO in 1 M KOH). The concentration of dissolved oxygen was monitored in-situ using an Ocean Optics FOXY oxygen sensing system. To ensure that any detected oxygen was generated electrochemically, a control experiment was also performed. Deoxygenated 0.1 M KOH was prepared in an identical manner, and a flowing argon blanket was placed over the electrolyte while the dissolved oxygen levels were recorded.

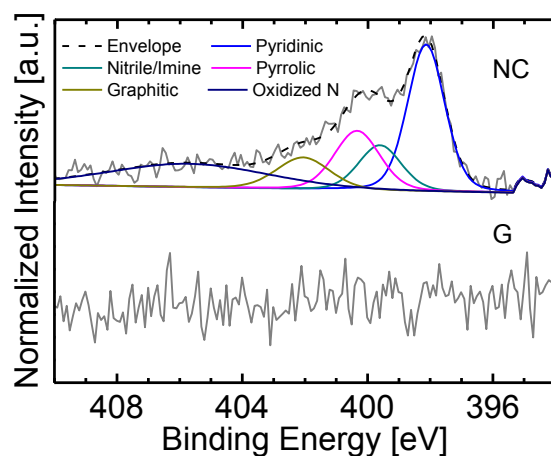


Figure C.1: High resolution XPS spectra

Of the N 1s core region for bare NC (top) and G (bottom) carbon supports. N content for G support is below detectable limits, while the NC support has contains ~ 1 at. % nitrogen, of which $\sim 65\%$ is pyridinic.

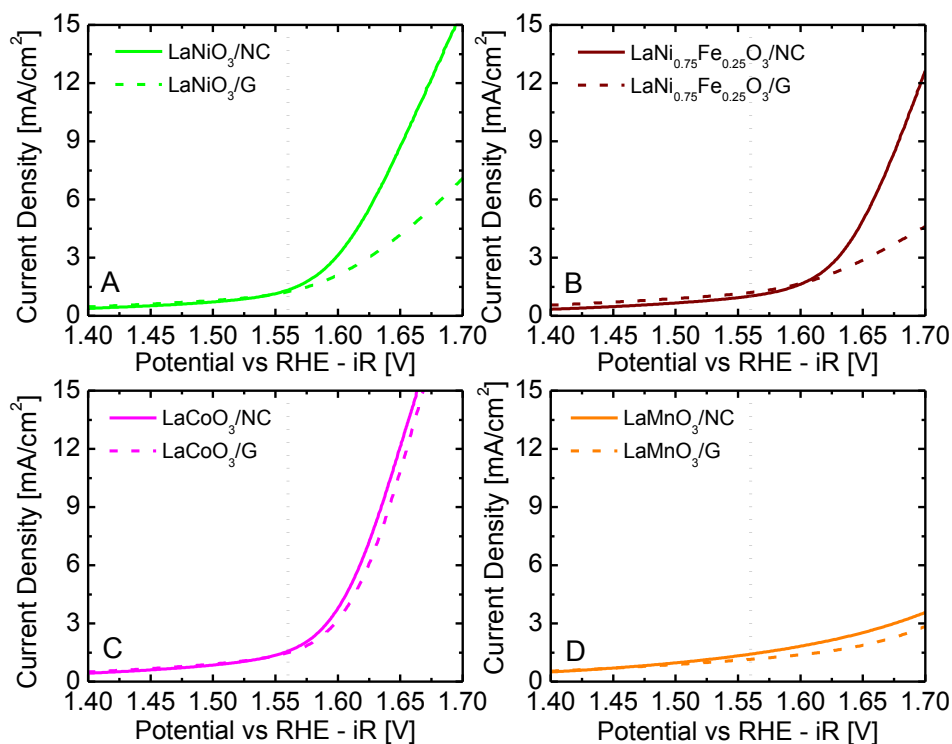


Figure C.2: Representative oxygen evolution rotating disk electrode polarization curves

A) LaNiO₃, B) LaNi_{0.75}Fe_{0.25}O₃, C) LaCoO₃ and D) LaMnO₃. All data were taken in O₂ saturated 0.1 M KOH at 1600 rpm and 10 mV/s, scanning anodically. The potential of 1.56 V was selected for the reporting of mass activities, and is represented in the above by a dashed gray line.

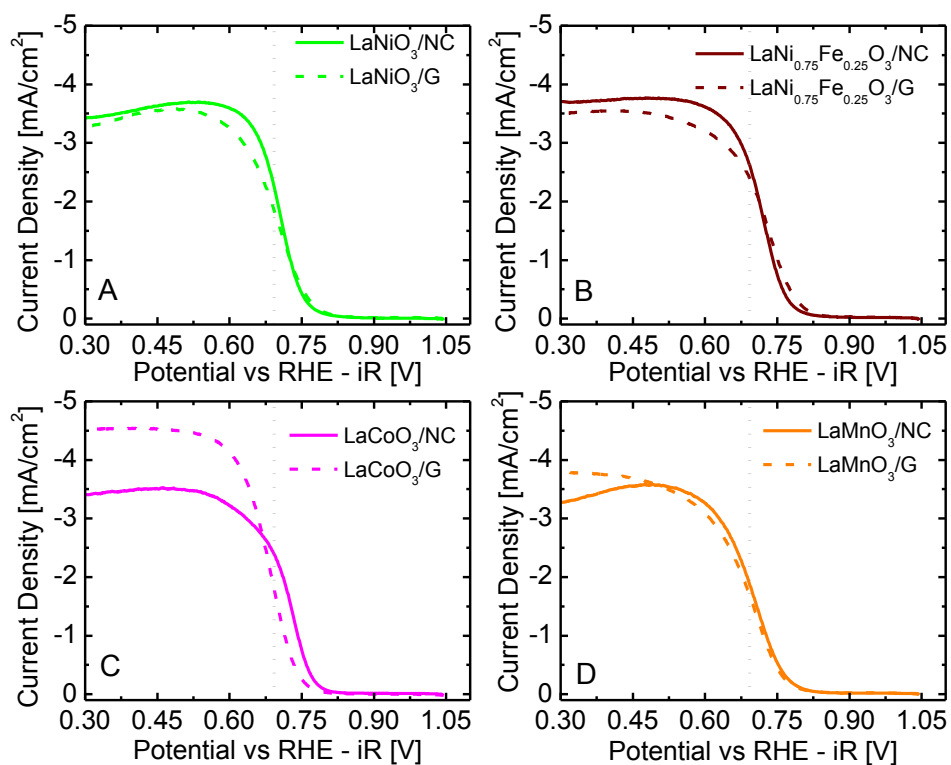


Figure C.3: Representative oxygen reduction rotating disk electrode polarization curves

A) LaNiO_3 , B) $\text{LaNi}_{0.75}\text{Fe}_{0.25}\text{O}_3$, C) LaCoO_3 and D) LaMnO_3 . All data were taken in O_2 saturated 0.1 M KOH at 1600 rpm and 5 mV/s, scanning cathodically. The potential of 0.693 V was selected for the reporting of mass activities, and is represented in the above by a dashed gray line.

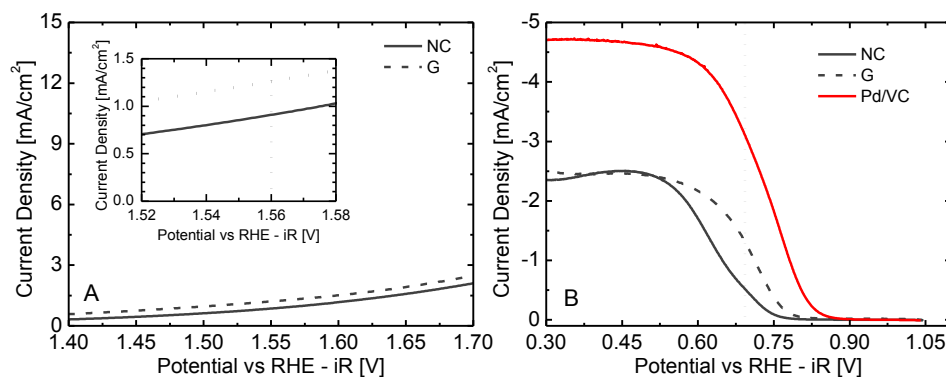


Figure C.4: Polarization curves taken in O₂ saturated 0.1 M KOH.

A) OER data for neat NC and G supports, taken at 10 mV/s (scanning anodically) and 1600 rpm. B) ORR data for NC and G supports, and 20 wt% Pd on XC 72 Vulcan Carbon (VC), taken at 5 mV/s and 1600 rpm (scanning cathodically). Experimental conditions for both A and B were identical to that of figures D.2 and D.3, including a carbon loading of 51 $\mu\text{g}/\text{cm}^2$ (10.2 $\mu\text{gPd}/\text{cm}^2$ for 20 wt% Pd/VC). The inset in A) highlights the current at 1.56 V.

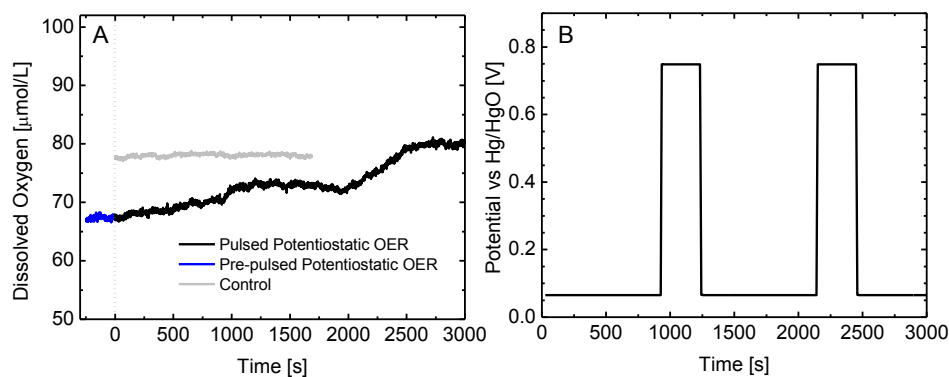


Figure C.5: Oxygen Probe Results

A) Dissolved oxygen concentrations measured prior to and during pulsed potentiostatic oxygen generation. B) Potential trace of LaCoO₃/NC, wherein the electrode is pulsed between the open circuit potential (0.065 V) and 0.750 V. The oxygen content is observed to increase when the potential is pulsed at 900 and 2100 s, while remaining relatively constant at open circuit. The initial rise from 0 to 900 s is attributed to a slow leak or incomplete purging of residual oxygen in the headspace of the cell, as is commonly observed for such tests. 9

Table C.1: DLS size, Crystallite size, BET surface area, XRD phase identification.

Material	hydrodynamic diameter [nm]	crystallite size [nm]	surface area [m ² /g]	XRD Phase Identification
LaNiO ₃	25 + 8	12	11	LaNiO ₃ , PDF# 01-088-0633
LaNi _{0.75} Fe _{0.25} O ₃	27 + 9	14	8	LaNi _{0.6} Fe _{0.4} O ₃ , PDF# 01-088-0637
LaCoO ₃	30 + 8	20	14	LaCoO ₃ , PDF# 01-084-0848
LaMnO ₃	27 + 7	15	11	La _{0.97} Mn _{0.97} O ₃ , PDF# 01-087-2015
NC	N/A	N/A	1080	
G	N/A	N/A	~2500	

C.2 REFERENCES

- (1) Falcon, H.; Carbonio, R.; Fierro, J. *J Catal* **2001**, *203*, 264.
- (2) Lee, Y. N.; Lago, R. M.; Fierro, J. L. G.; González, J. *Applied Catalysis A: General* **2001**, *215*, 245.
- (3) Maldonado, S.; Stevenson, K. J. *J Phys Chem B* **2005**, *109*, 4707.
- (4) Wiggins-Camacho, J. D.; Stevenson, K. J. *J Phys Chem C* **2011**, *115*, 20002.
- (5) Boehm, H. P. *Discuss Faraday Soc* **1971**, *52*, 264.
- (6) Pourbaix, M. *Atlas of Electrochemical Equilibria in Aqueous Solutions*; NACE International, 1974.
- (7) Gorlin, Y.; Jaramillo, T. F. *J Am Chem Soc* **2010**, *132*, 13612.
- (8) Hardin, W. G.; Slanac, D. A.; Wang, X.; Dai, S.; Johnston, K. P.; Stevenson, K. J. *The Journal of Physical Chemistry Letters* **2013**, *4*, 1254.
- (9) Seabold, J. A.; Choi, K.-S. *J Am Chem Soc* **2012**, *134*, 2186.

Appendix D: Exceptional Electrocatalytic Oxygen Evolution Via Tunable Charge Transfer Interactions in $\text{La}_{0.5}\text{Sr}_{1.5}\text{Ni}_{1-x}\text{Fe}_x\text{O}_{4+\delta}$ Ruddlesden-Popper Oxides⁸

D.1 NOTE ON OXYGEN HYPERSTOICHIOMETRY AND OXIDATION STATES

There are conflicting reports in the literature surrounding the average Ni oxidation state and oxygen hyperstoichiometry of $\text{La}_{2-x}\text{Sr}_x\text{NiO}_{4+\delta}$ and until the current study data were not available for $\text{La}_{0.5}\text{Sr}_{1.5}\text{Ni}_{1-x}\text{Fe}_x\text{O}_{4+\delta}$. The results in Table 4.1 indicate that Ni and Fe in Sr-nickelate are highly oxidized and the oxygen hyperstoichiometry increases as more Fe is substituted for Ni. However, others have observed increasing oxygen hyperstoichiometry at room temperature with increasing Fe content in La-rich $(\text{La,Sr})_2\text{Ni}_x\text{Fe}_{1-x}\text{O}_{4+\delta}$.^{1, 2} Medarde and Rodriguez-Carvajal found that ordered oxygen vacancies formed in $\text{La}_{2-x}\text{Sr}_x\text{NiO}_{4+\delta}$ when $x > 0.13$, while Aguadere and coworkers observed initial oxygen hyperstoichiometry when $x = 0.25$ in $\text{La}_{2-x}\text{Sr}_x\text{NiO}_{4+\delta}$, but find all samples to be oxygen deficient at $x \geq 0.5$, in contrast with our results.^{3, 4, 5} Other reports of $\text{La}_{2-x}\text{Sr}_x\text{NiO}_{4+\delta}$ demonstrate that Sr substitution increases the average oxidation state of Ni due to charge compensation, up to and including $\text{La}_{0.5}\text{Sr}_{1.5}\text{NiO}_{3.98}$ in which Ni has an average oxidation state of +3.46.^{6, 7, 8} Synthetic methodology and calcination temperature were both demonstrated to significantly affect the oxygen stoichiometry and crystal structure of $\text{La}_2\text{NiO}_{4+\delta}$,⁹ and a similar conclusion was reached by Inprasit in rationalizing their oxygen hyperstoichiometry in $\text{La}_{1.2}\text{Sr}_{0.8}\text{NiO}_{4.2}$.⁷ For $\text{La}_{2-x}\text{Sr}_x\text{NiO}_{4+\delta}$ synthesized using solid-state methods and crystallized at higher temperatures, lower Ni oxidation states and oxygen substoichiometry were observed.¹⁰ Thus, we rationalize that the good molecular intermixing promoted by the polymerizable complex synthesis, the pure oxygen calcination environment, and our relatively low crystallization temperature of

⁸Large parts of this chapter have been submitted to *Nature Materials* on March 31st, 2017.

950°C and subsequent 6 hour oxygen anneal at 400°C contribute to the high oxygen content and higher oxidation states in Figure 4.1, as has been seen for related materials elsewhere.^{10, 11} Finally, there is precedence for Fe substitution increasing the average oxidation state of a more electronegative B-site in a related $n=1$ RP system, $\text{NdSrCo}_{1-x}\text{Fe}_x\text{O}_{4+\delta}$.¹² Song et al found that increasing Fe substitution led to an increase in oxygen content and B-site oxidation state (measured by iodometry), which is logically consistent with our results as the band evolution upon Fe substitution may be expected to be similar to that of LSNF, shown in Figure 4.4.

D.2 NOTE ON BAND STRUCTURE AND CROSS-GAP HYBRIDIZATION

The computed band structure of LSNF is similar to that reported for other highly active OER catalysts such as $\text{Ba}_{0.5}\text{Sr}_{0.5}\text{Co}_{0.75}\text{Fe}_{0.25}\text{O}_{3+\delta}$ (BSCF).¹³ Merkle calculated the band diagram for BSCF and found a similar electronic configuration as in LSNF (Figure 4.4). Thus, it is possible that the high activity of BSCF may be rationalized not just by the covalent Co-O bonding, but also by the triply-overlapping Co and Fe $3d$ states with O $2p$ near E_F . We note that LSNF's band structure is also similar to that of highly active Ni-Fe layered double hydroxide (LDH) catalysts.¹⁴ Conesa calculated the DOS of one such polymorph, $\text{FeNi}_7\text{O}_8(\text{OH})_8$ in the $2H_C$ structure with Fe in $\text{O}_4(\text{OH})_2$ coordination and their result is strikingly similar to that of LSNF in that Ni and Fe $3d$ bands are strongly hybridized just above E_F . They concluded that Fe^{4+} is stabilized by induced charge transfer between Ni sites, and this explanation agrees with our observation of Fe in the $4+$ oxidation state in LSNF (Figure 4.1) which is also seen in Ni-Fe oxyhydroxides.¹⁵ The previously reported shifting of the $\text{Ni}^{2+/3+}$ redox couple in NiOOH upon incorporation of Fe that was concluded to result from partial charge transfer between Fe and/or Ni^{16, 17, 18} also occurs in our own work. A change in covalency by the introduction of FeO_6 units

into LSN must have an inductive effect on Ni through next nearest neighbor interactions via Fe-O-Ni bridges,¹⁹ which is consistent with the observation that our activity is maximized for the composition having the highest probability of Fe-O-Ni bridging interactions, LSNF30. Figure 4.2 clearly demonstrates that at greater than 30% Fe substitution the catalytic activity is reduced, concomitant with the increased probability of Fe-O-Fe bridges and decreased Ni site density.

D.3 NOTE ON BAND STRUCTURE AND OER MECHANISM(S)

Electron transfer between the transition metal sites of the catalysts and chemisorbed OER intermediates at the catalyst-adsorbate interface are driven by changes in the catalyst Fermi level due to applied potential or chemical steps between oxygen vacancies and solution hydroxides. The rate determining step(s) of the OER, regardless of mechanism, are usually associated with the highest free energy barrier to transformation of one intermediate to the next.^{20, 21} The band structure of LSNF accommodates surface redox reactions by easily shifting the Fermi level of the catalysts within the bandwidth immediately surrounding E_F in LSNF. Iodometric titration data coupled with Mössbauer spectroscopy indicate that the average oxidation state of Ni ranges from 3.46 to 3.95 with increasing Fe substitution, while the $\text{Ni}^{2+/3+}$ oxidation wave also shifts to more positive potentials, consistent with Ni developing a more oxidized character upon Fe substitution. However, as stated in the main text, the activity increases markedly from LSN to LSN30 despite having the same average oxidation state, thus Fe substitution must play a larger role than just increasing the average oxidation state of Ni.

As we have discussed in previous work, the OER can proceed by the adsorbate exchange mechanism (AEM) or the lattice oxygen mediated (LOM) mechanism.^{22, 23} In the AEM, chemisorbed intermediates undergo a series of electrochemical oxidations as

the transition metal active site undergoes oxidation and reduction. The demonstrated ability to tune the reactivity of the Ni and the increased bandwidth created around the Fermi level by substitution with Fe supports facile charge transfer at the adsorbate-catalyst interface and possibly the oxidation and reduction of transition metal active sites that occurs in the AEM. The lattice oxygen mediated (LOM) OER mechanism, on the other hand, does not require the redox switching of transition metal sites but instead requires the participation of lattice oxygen in the OER. Transition metal 3*d* bands that are highly covalent with O 2*p* bands and exist around E_F^0 support the LOM mechanism (Figure 4.5c) in which ligand holes activate lattice oxygen that combines with chemisorbed OH to produce O₂⁻. Triple overlap of $e_g(\text{Ni})$, $p(\text{O})$ and $e_g(\text{Fe})$ bands across E_F^0 that results in covalent hybridization of these bands is a requirement of this mechanism, which has been experimentally demonstrated elsewhere by the high diffusion rates of lattice oxygen.²² Indeed, electrochemical measurements indicate the highest oxygen diffusion rates for LSNF30 and LSNF45, the two most electrocatalytically active compositions (Figures D.12 and Table D.3). Thus the LOM mechanistic interpretation of the results is supported by both our electrochemical oxygen intercalation and diffusion measurements, our DFT modeling of the band structure of LSNF, and also the well-known surface oxygen exchange kinetics of the $n=1$ Sr-nickelate RP phase.^{24, 25}

D.4 NOTE ON DFT METHODS, MAGNETIC ORDERING AND OXYGEN CONTENT

Due to DFT self-interaction errors for strongly correlated materials,²⁶ the DFT+U method is employed to understand the electronic structures of LSNF. The values of U_{eff} of ~6.0 eV (Ni) and ~5.0 eV (Fe) are chosen based on previous work: In the case of Ni-containing perovskites, Gou et al. found that using U_{eff} (Ni) of ~6.0 eV gives a LaNiO₃ electronic structure closest to that obtained from hybrid functional methods and

experimental spectroscopic data.²⁷ Lee et al. showed that this choice of U_{eff} also gives the correct LaNiO_3 formation enthalpy.²⁸ For Fe-contained perovskites, Shein et al. used a $U_{eff}(\text{Fe})$ of ~ 5.0 eV to reproduce the experimental band gap for LaFeO_3 , as well as the experimental magnetic structures and moments for both LaFeO_3 and SrFeO_3 .²⁹ This choice of U_{eff} is also suggested by Ritzmann et al, particularly for those perovskites that exhibit some Fe(IV) character.^{30, 31} It is noteworthy that moderate adjustment of U_{eff} in a typical reported range may not significantly alter the density of states around Fermi level, as compared between several studies using $U_{eff}(\text{Ni})$ from 5.7 to 6.4 eV^{27, 28} and $U_{eff}(\text{Fe})$ from 4.3 to 5.4 eV^{28, 29, 30}.

We model the LSNF compounds using $2 \times 2 \times 1$ primitive unit cells, which enables the unit composition $\text{La}_{0.5}\text{Sr}_{1.5}\text{NiO}_{4+\delta}$ (LSN), $\text{La}_{0.5}\text{Sr}_{1.5}\text{Ni}_{0.75}\text{Fe}_{0.25}\text{O}_{4+\delta}$ (LSNF25), $\text{La}_{0.5}\text{Sr}_{1.5}\text{Ni}_{0.50}\text{Fe}_{0.50}\text{O}_{4+\delta}$ (LSNF50), $\text{La}_{0.5}\text{Sr}_{1.5}\text{Ni}_{0.25}\text{Fe}_{0.75}\text{O}_{4+\delta}$ (LSNF75), and $\text{La}_{0.5}\text{Sr}_{1.5}\text{FeO}_{4+\delta}$ (LSF). Starting from a $2 \times 2 \times 1$ cell of $I4/mmm$ La_2NiO_4 (LN, Figure D.15a), we first search for the ground state ordering of Sr substitutions for stoichiometric LSN through structural screening and relaxations. For the LSN, we find that La/Sr prefers a uniform (random) distribution with one La in each of the 4 AO layers, due to the ionic nature of La/Sr anions. We then perform a second round of screening to determine the minimum energy distributions of Fe substitutions for each stoichiometric LSNF composition.

Magnetic orderings, including ferromagnetic (FM), antiferromagnetic (AFM, A, C and G types) and non-magnetic structures are all investigated across the whole LSNF series to ensure that the magnetic ordering that gives rise to the lowest free energy structure is used in the calculation of PDOS diagrams. In the FM state, the overall spin directions of each individual B cation are aligned with each other. In the A-type AFM structure, the spins are parallel within each BO_2 layer, but antiparallel between

neighboring BO_2 layers, as illustrated in Figure D.17a. In the G-type AFM state, the spins of neighboring B atoms are aligned antiparallel both in the plane of each BO_2 layer and between the BO_2 planes, forming a checkerboard pattern. In this crystal structure, C-type and G-type AFM are identical. Figure D.17b shows the computed energies of the optimized LSNF cells with different magnetic states. As the figure shows, the FM and A-type AFM structures are very close in energy, while the G-type AFM and non-magnetic orderings are less stable across the whole LSNF series. This condition suggests that the large spatial separation leads to negligible dipole interactions between neighboring BO_2 layers. Thus, the in-plane charge density distribution is similar for the A-type AFM and FM cases, as shown by comparing the PDOS in Figure D.17c to that in Figure 4.5. Further investigation of the non-magnetic structure also reveals a similar trend in the $d(B)$ -to- $p(O)$ covalency from LSN to LSF, suggesting that characteristics of the PDOS for the FM state (shown in Figure 4.5 in the main text), are representative even above the Neel temperature.

We note that oxygen hyperstoichiometry effects either give rise to the emergence of bound states in conduction bands, a Fermi level shift, or a combination of the two.³² In the former case, the overall electronic structure is subject to negligible change due to the dilute and localized nature of interstitial oxygen and bound states. In the latter case, the magnitude of the Fermi level shift can be roughly estimated via the rigid band model to accommodate unoccupied band formation, which can be determined by $E_F^\delta = E_F^0 - 2e^- \delta / \text{DOS}(E_F^0)$, where $\text{DOS}(E_F^0)$ is the total density of states at E_F^0 per formula unit of LSNF. As Figure 4.5c shows, the slightly adapted Fermi level, E_F^δ , does not qualitatively alter our discussions and conclusions. This situation is due to the rich band distribution of O- p holes and B- d states around the Fermi level.

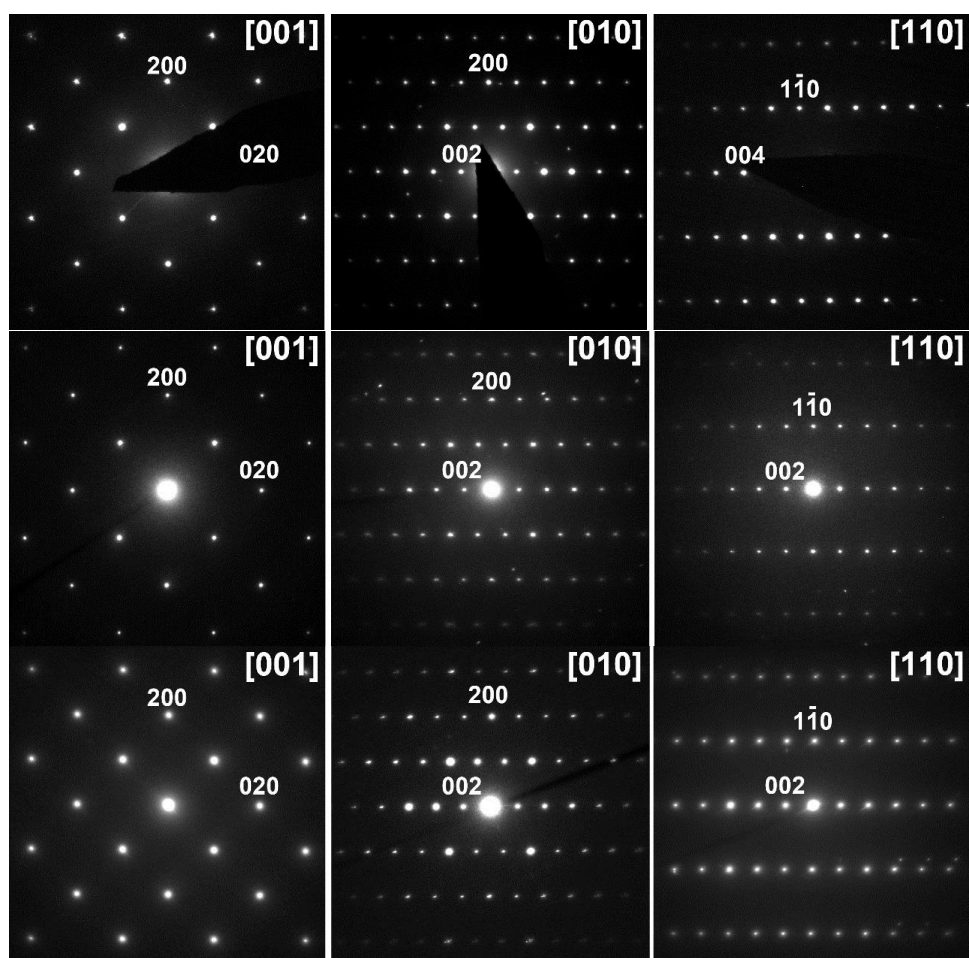


Figure D.1: Electron diffraction (ED) patterns

Of LSN (first row), LSNF45 (second row) and LSF (third row) (the ED patterns for LSNF30 are given in Figure 4.1 of the manuscript). The ED patterns are indexed in a body-centered tetragonal unit cell with the unit cell parameters listed in Table D.1.

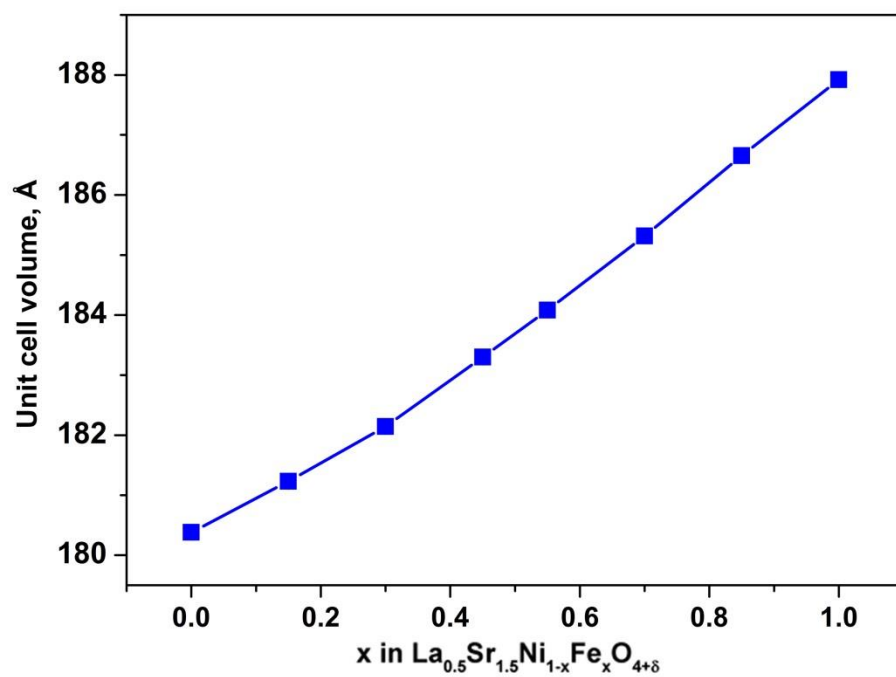


Figure D.2: Unit cell volume as a function of x in the $\text{La}_{0.5}\text{Sr}_{1.5}\text{Ni}_{1-x}\text{Fe}_x\text{O}_{4+\delta}$ solid solutions

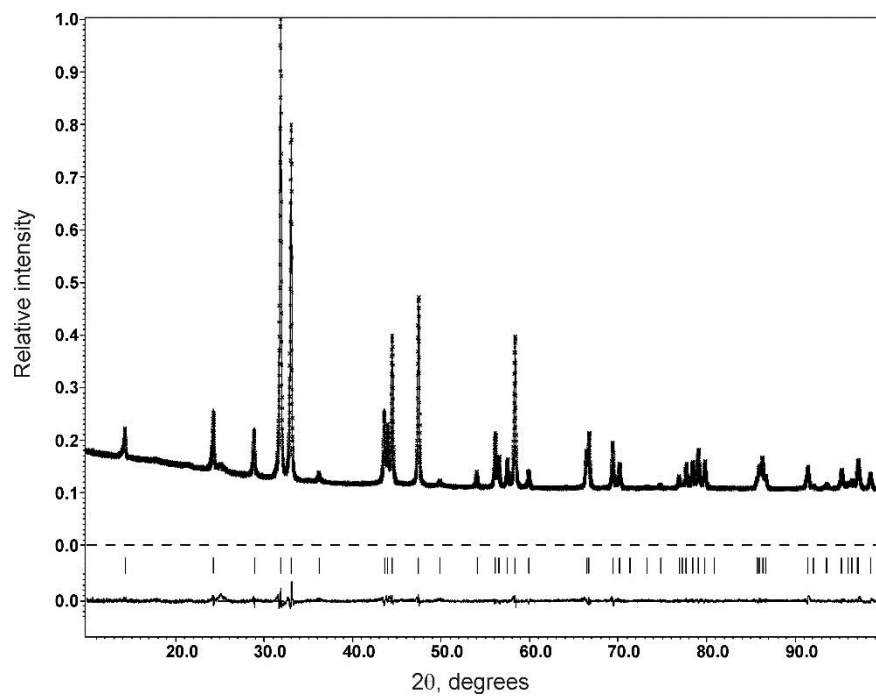


Figure D.3: Typical experimental, calculated and difference curves after the Rietveld refinement

Rietveld refinement of the $\text{La}_{0.5}\text{Sr}_{1.5}\text{Ni}_{1-x}\text{Fe}_x\text{O}_{4+\delta}$ structures (exemplified for LSNF30). The bars mark the reflection positions of the $I4/mmm$ structure.

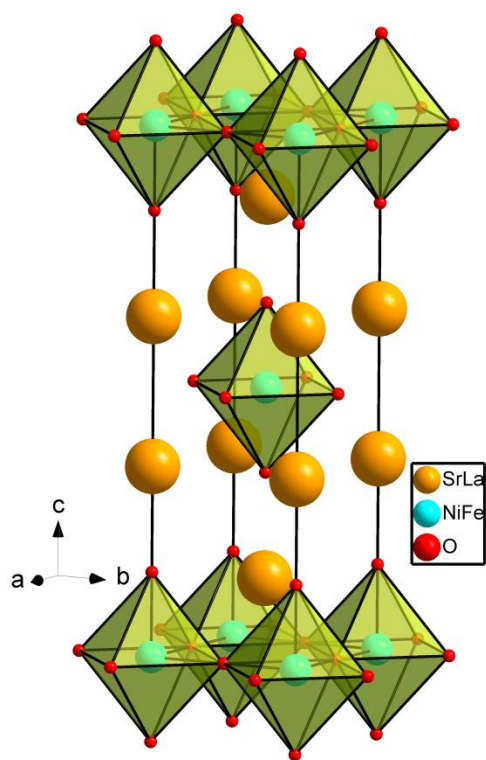


Figure D.4: The crystal structure of the $n=1$ Ruddlesden-Popper $\text{La}_{0.5}\text{Sr}_{1.5}\text{Ni}_{1-x}\text{Fe}_x\text{O}_{4+\delta}$ series.

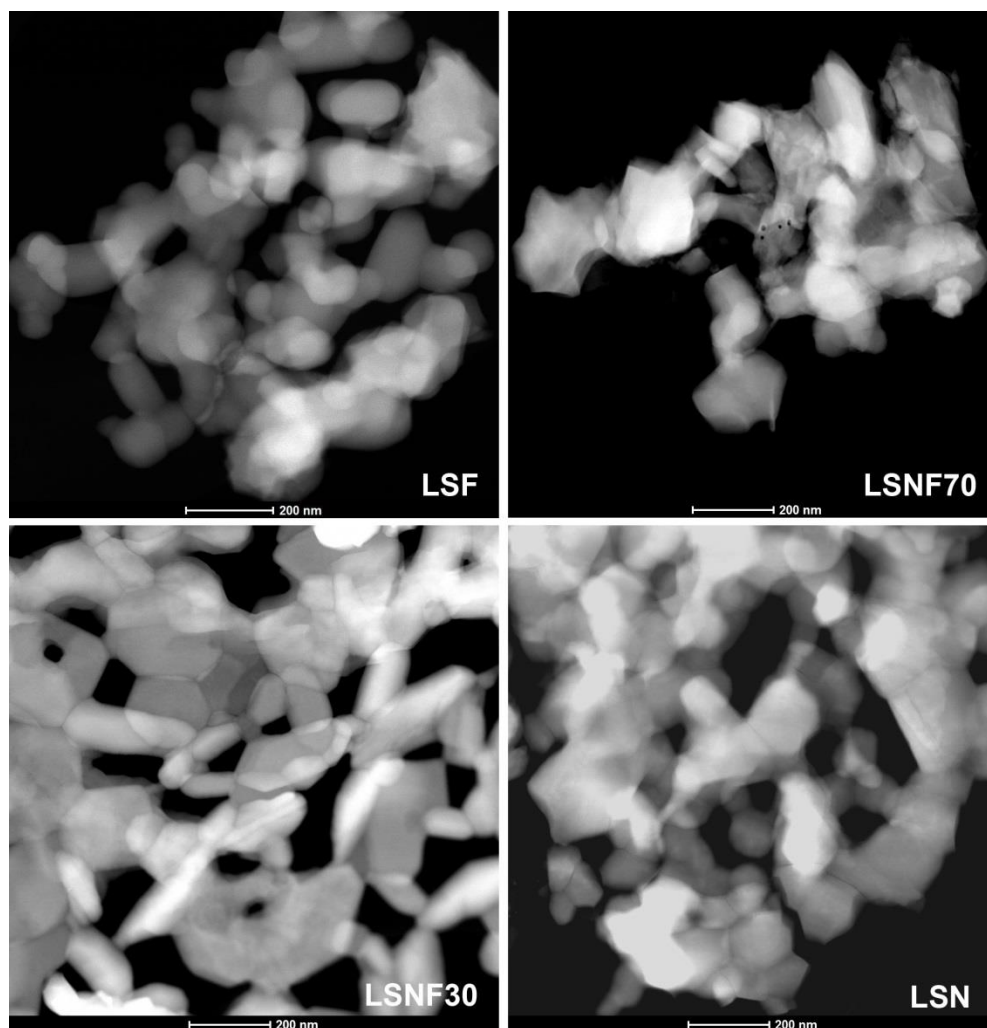


Figure D.5: HAADF-STEM images of $\text{La}_{0.5}\text{Sr}_{1.5}\text{Ni}_{1-x}\text{Fe}_x\text{O}_{4+\delta}$

Images demonstrate that the catalysts are comprised of similarly sized primary particles that form loosely sintered aggregates with well-developed porosity.

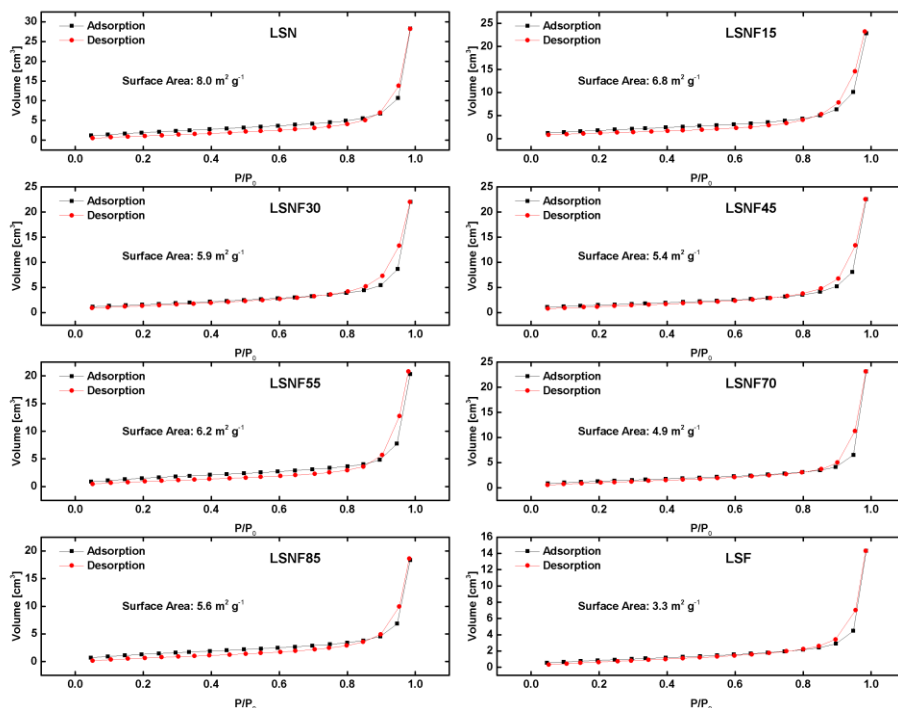


Figure D.6: Nitrogen sorption isotherms for BET surface area analysis of the $\text{La}_{0.5}\text{Sr}_{1.5}\text{Ni}_{1-x}\text{Fe}_x\text{O}_{4+\delta}$ series

Samples range in surface area from 3.3 to 8 $\text{m}^2 \text{g}^{-1}$. All samples underwent the same thermal treatments for mixed metal oxide precursor particle synthesis as well as crystallization and annealing.

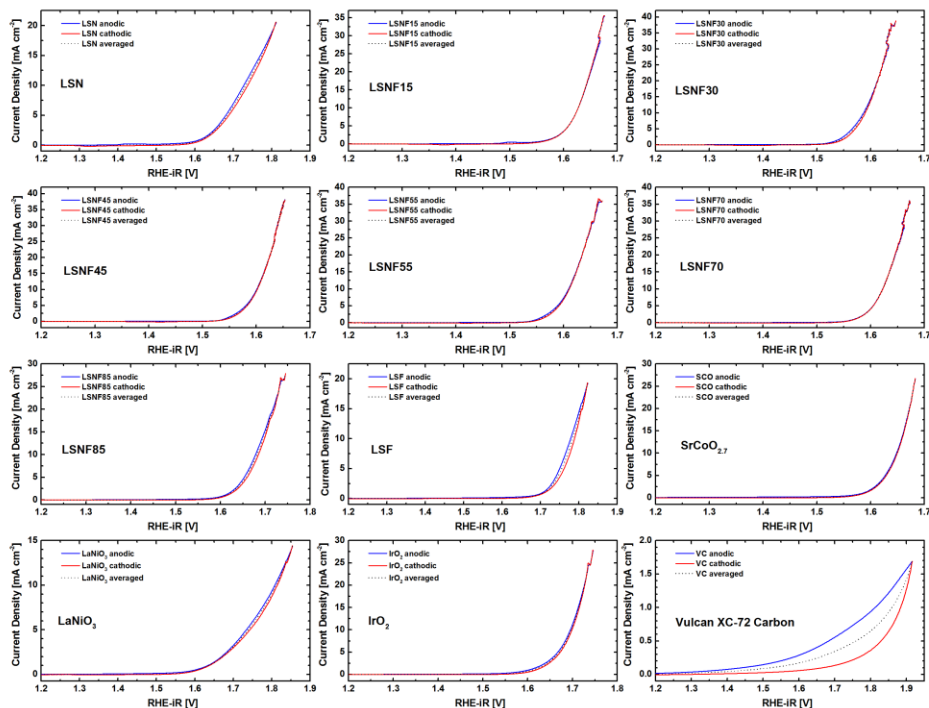


Figure D.7: Representative OER polarization curves

Taken in O₂ saturated 0.1 M KOH at 1600 rpm and 10 mV s⁻¹. Catalysts were first swept positive (anodic), then negative (cathodic), and the curves averaged before iR correction. Electrolyte resistance was measured to be 46 Ω. Total electrode loading is 51 μg_{total} cm⁻²_{geo} with 30 wt% LSNF, SrCoO_{2.7} or LaNiO₃ on XC72 Vulcan Carbon (VC), yielding 15.3 μg_{oxide} cm⁻²_{geo}. IrO₂ was tested at 20 wt% on VC (10.2 μg_{oxide} cm⁻²_{geo}) and neat VC was tested at 35.7 μg_{carbon} cm⁻²_{geo} (7 μg carbon, corresponding to the contribution to measured OER current for 30 wt% LSNF on VC). LaNiO₃ and SrCoO_{2.7} are the same materials as previously reported,^{22, 33} except supported on VC to only probe the effects of catalyst composition

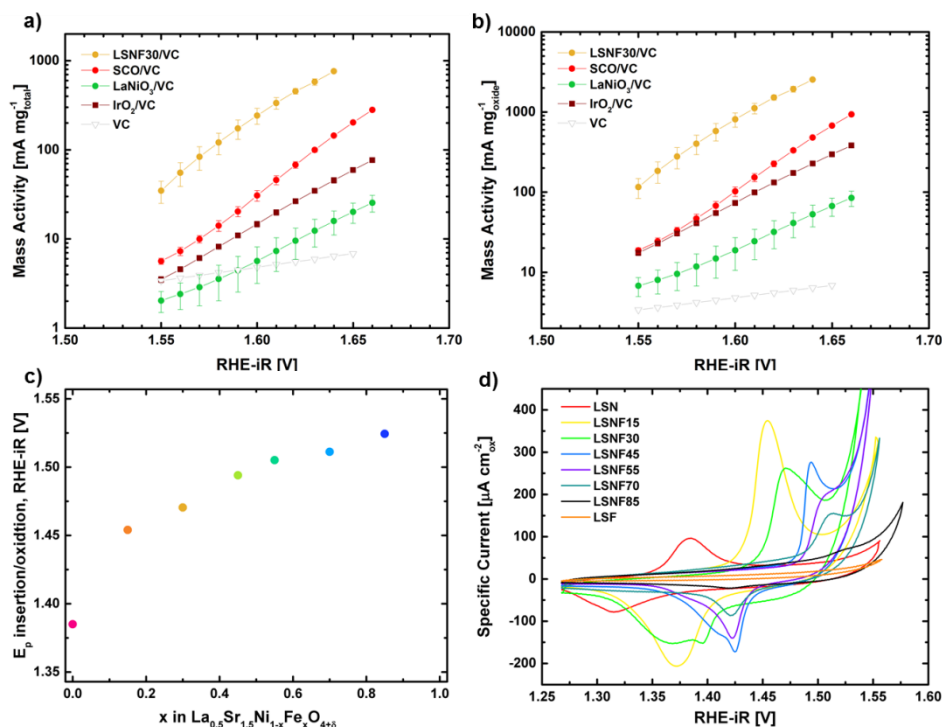


Figure D.8: OER tafel plots of LSNF30 and other leading metal oxide catalysts

a) total mass and b) catalyst mass basis. All data in a-b taken in oxygen saturated 0.1 M KOH at 10 mV/s and 1600 rpm. LSNF30, SCO and LaNiO₃ are 30 wt% on VC, IrO₂ is 20 wt%, all corresponding to 51 $\mu\text{g}_{\text{total}}/\text{cm}^2_{\text{geo}}$. VC is XC72 Vulcan Carbon. Pure VC is tested at 35.7 $\mu\text{g cm}^{-2}$, corresponding to the 70 wt% carbon used to support LSNF30, SCO and LaNiO₃. c) Shifting of the $\text{Ni}^{2+/3+}$ oxidation peak potential as a function of Fe substitution. All peak potentials were taken from stable CVs at 10 mV/s in oxygen saturated 0.1 M KOH. For LSNF55 and LSNF85, there was no local maximum at 10 mV/s and the peak potential was selected after the OER background was subtracted out, shown in Figure D.11. d) Stable intercalation CVs plotted in specific current density. All CVs are at 10 mV/s in O₂ saturated 0.1 M KOH.

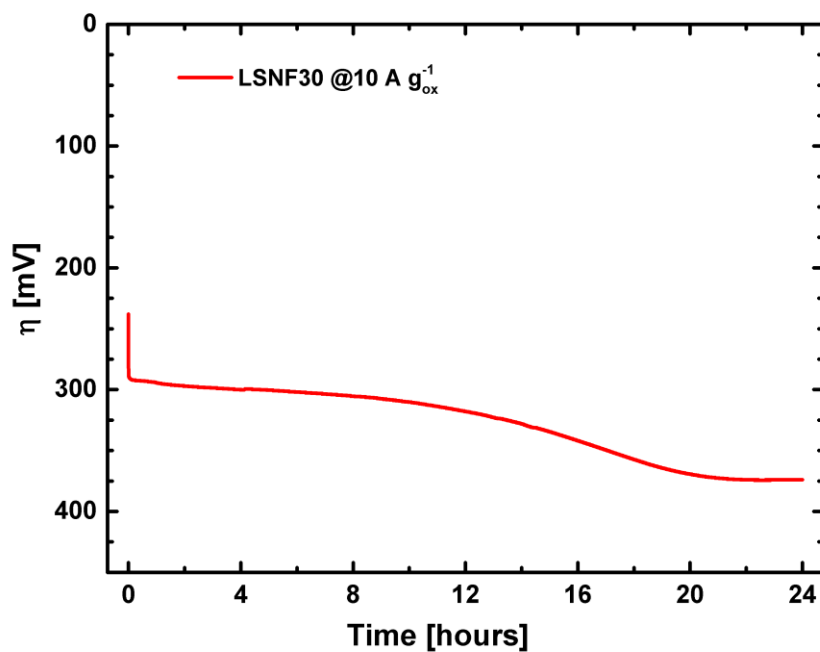


Figure D.9: Galvanostatic stability test of LSNF30

Galvanostatic stability test of LSNF30 at 10 A/g_{oxide} in O₂ saturated 0.1 M KOH at 1600 rpm. LSNF30 was supported at 30 wt% on XC72 VC and dropcast onto a 5 mm GCE for a total mass loading of 51 μg cm⁻²_{geo.}. η is calculated from the measured potential (RHE-iR) minus 1.229 V.

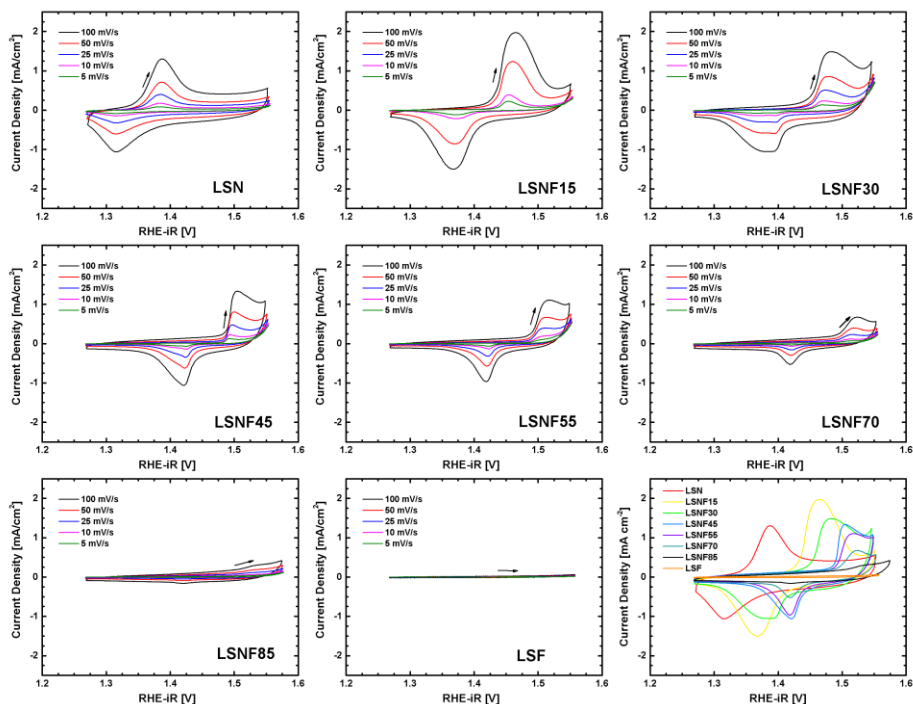


Figure D.10: Intercalation CVs

Taken in O_2 saturated 0.1 M KOH after 3 - 4 cycles so that oxidation peak potentials do not change upon subsequent cycling. CVs were taken on pristine electrodes that had been electrochemically preconditioned (see Methods for more information). Immediately following preconditioning, CVs were recorded for varying scan rates, descending from 100 mV s^{-1} to 5 mV s^{-1} , one electrode per material. All catalysts are 30 wt% oxide on VC. The bottom right-most panel is identical to that shown in Figure 4.3c in the main text, and is the overlay of the 100 mV s^{-1} scans for all catalysts.

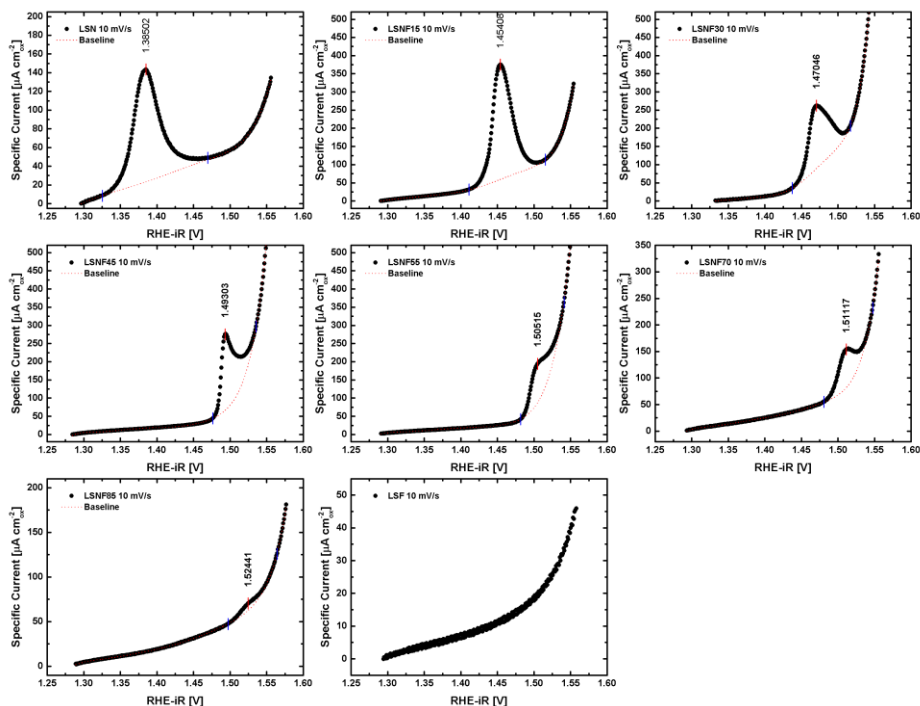


Figure D.11: Fitted intercalation CVs for $\text{La}_{0.5}\text{Sr}_{1.5}\text{Ni}_{1-x}\text{Fe}_x\text{O}_4$

The fitted baseline was subtracted prior to integration of peak areas. Currents were converted into specific current density ($\mu\text{A cm}^{-2}_{\text{ox}}$) activity to account for surface area differences between samples with varying Fe contents. All CVs are in O_2 saturated 0.1 M KOH and were taken at 10 mV s^{-1} . These are the same CVs from Figure D.10, meaning they were collected from a pristine electrode that was conditioned and cycled at 100, 50, and 25 mV s^{-1} . Consult the methods section for more information. Numbers are the computed peak maxima after baseline OER subtraction, used for determination of E_p in Figure D.8c for LSNF55 and LSNF85, in which no local maxima is observed prior to baseline subtraction.

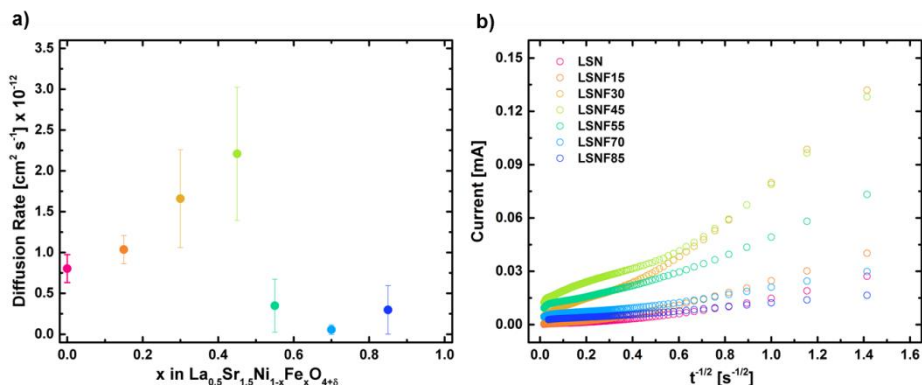


Figure D.12: Electrochemical diffusion rate data for the Sr-nickelate system

Taken in O_2 saturated 0.1 M KOH. a) Calculated oxygen diffusion rates for LSNF catalysts. b) Chronoamperometry data used for the calculation of diffusion rates in a). A linear regression was used on the linear, fast timescale portion of the current decay, and using the mathematical model referenced in the Methods section of the main text the diffusion rates were determined. Particle size was estimated from BET data and confirmed by the STEM images in Figure D.5. The shape factor (λ) was assumed to be 2 for all calculations. All materials are 85 wt% oxide on VC which were dropcast onto 5 mm glassy carbon electrodes (GCE) for a total loading of $51 \mu\text{g cm}^{-2}_{\text{geo}}$.

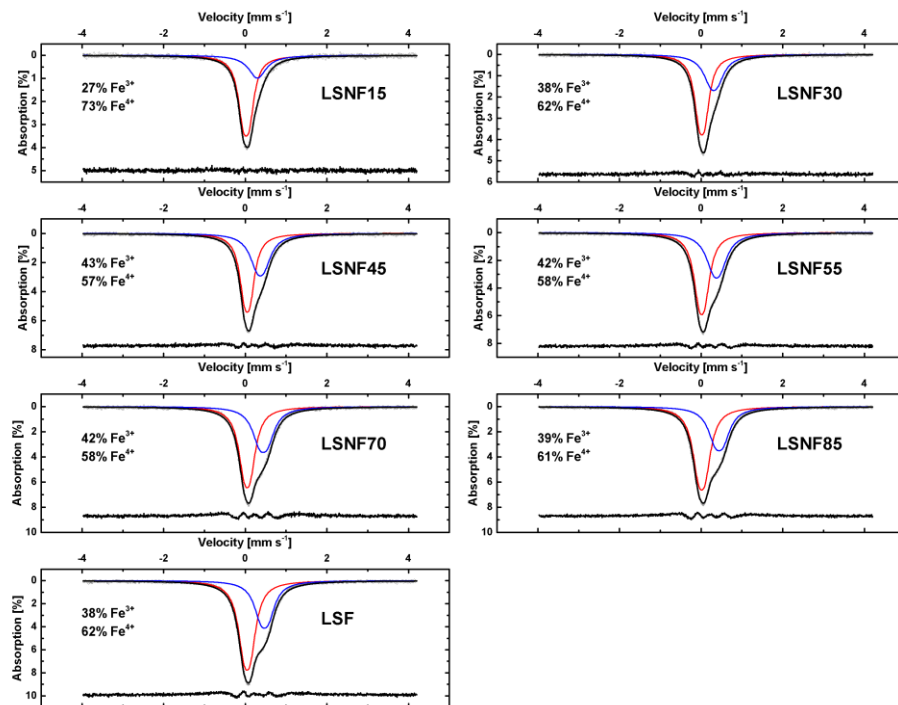


Figure D.13: Room temperature Mössbauer spectroscopy

Room temperature Mössbauer spectroscopy for the Sr-nickelate system. Fitted curves for Fe^{4+} depicted in red while fitted curves for Fe^{3+} are shown in blue. The spectra, measured at room temperature, were deconvoluted into two slightly overlapped paramagnetic doublets. According to their chemical isomer shifts (ISs), the doublets with smaller ISs of $\sim 0.32 - 0.4$ mm/s correspond to Fe^{4+} cations, while ones with larger ISs of $\sim 0.32 - 0.45$ mm/s correspond to Fe^{3+} cations. ³⁴ It was previously shown that values of quadrupole splitting (QSs) in the $\text{Sr}_{2-x}\text{La}_x\text{FeO}_{4\pm\delta}$ based solid solutions are highly dependent on La and O contents. ³⁵ The observed values of hyperfine parameters, viz. ISs and QSs, for the Sr-nickelate system investigated are consistent with the parameters reported for the related $\text{Sr}_{2-x}\text{La}_x\text{FeO}_{4\pm\delta}$ compounds with high oxygen content. ^{35, 36}

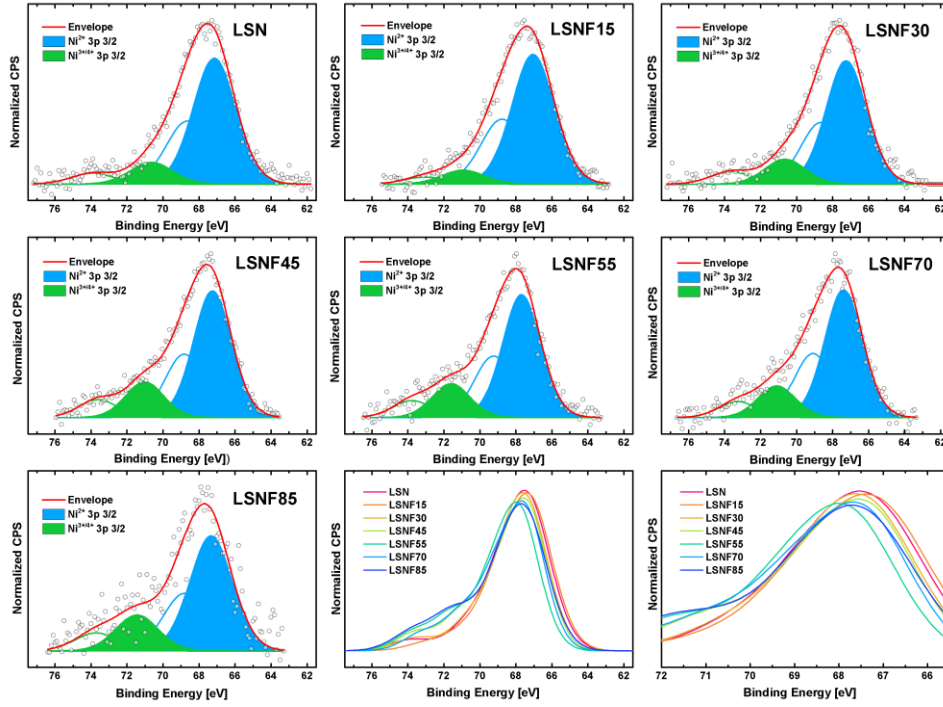


Figure D.14: XPS deconvolution of the Ni 3p spectra for $\text{La}_{0.5}\text{Sr}_{1.5}\text{Ni}_{1-x}\text{Fe}_x\text{O}_{4+\delta}$

Deconvolution performed by adaptation of the methods developed by Burriel et. al for $\text{La}_{2-x}\text{Sr}_x\text{NiO}_4$.³⁷ The Ni 3p spectrum was decomposed into 4 distinct components; Ni^{2+} and $\text{Ni}^{3+/4+}$ in both the $3p_{3/2}$ and $3p_{1/2}$ portions of the Ni doublet. Deconvolution was achieved by fitting error minimization on the 30% Gaussian/Lorentzian components using the Marquardt and Simplex methods within CasaXPS. To ensure self-consistency all components used the same FWHM and components assigned to Ni $3p_{1/2}$ were constricted to have exactly half the area of their counterparts in the Ni $3p_{3/2}$. Binding energy constraints were the same used by Burriel et. al, and the maximum allowed FWHM was increased to account for the multiple chemical states encompassed by the $\text{Ni}^{3+/4+}$ components.

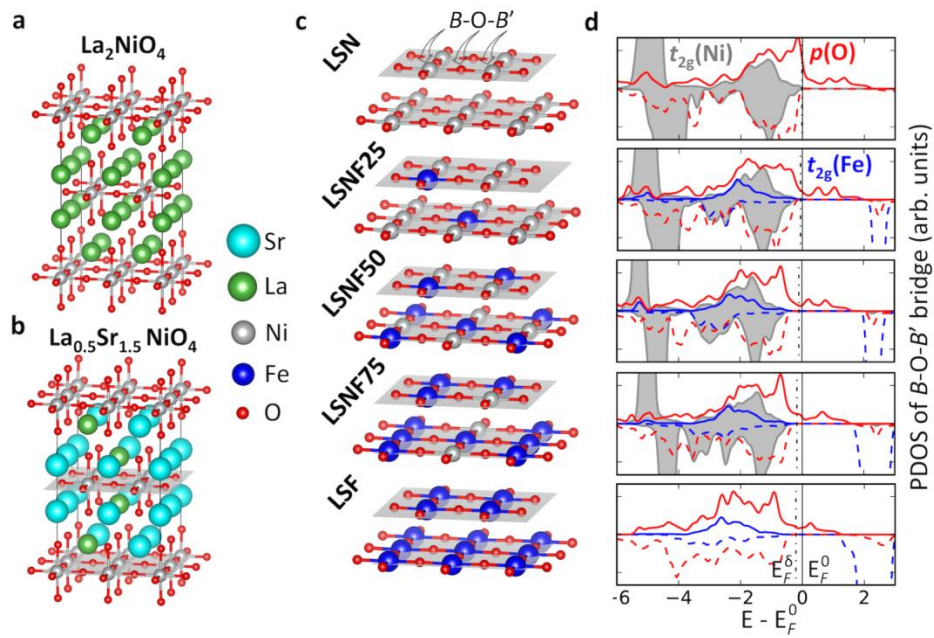


Figure D.15: DFT modeling of atomic and electronic structures of bulk LSNF

(a) The optimized atomic structure of $2 \times 2 \times 1$ La_2NiO_4 , as the initial structure for Sr substitution and relaxation. (b) and (c) follow the same as those in Figure 4.5. (d) The projected density of states (PDOS) of t_{2g} (Ni and Fe) and $2p$ (O) with respect to Fermi level for the $B\text{-O-}B'$ bridges; t_{2g} is shown not to come across Fermi level.

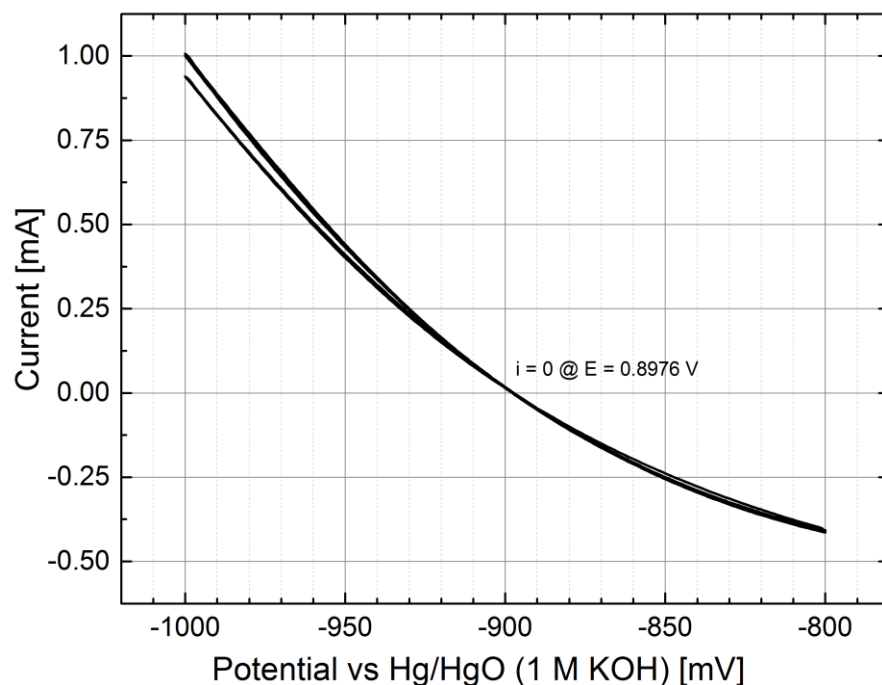


Figure D.16: Reversible hydrogen electrode (RHE) calibration

A Pt working electrode was cycled at 1 mV s^{-1} in H_2 saturated 0.1 M KOH using a Pt or Au counter electrode to standardize the Hg/HgO (1 M KOH) reference electrode against thermodynamic H_2 evolution and oxidation. The Hg/HgO conversion to RHE was determined by the average potential at which 0 current was measured, -0.8976 V vs Hg/HgO.

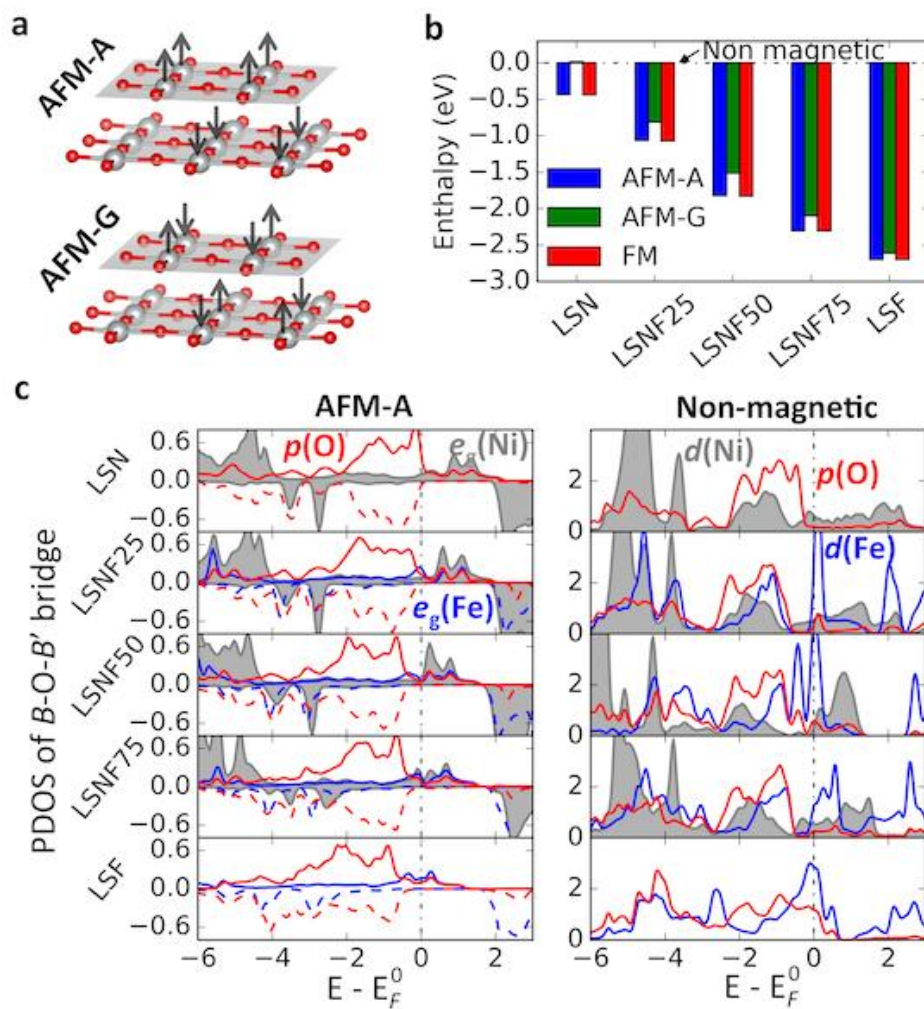


Figure D.17: Comparison of ferromagnetic, anti-ferromagnetic and non-magnetic structures from DFT modeling

(a) The structures of A-type antiferromagnetic (AFM-A) and G-type antiferromagnetic (AFM-G) orderings. In AFM-A, spin directions only differ between neighborhood BO_2 layers, while in AFM-G, spin directions differ between neighborhood B atoms; AFM-C is identical to AFM-G in this atomic structure. **(b)** Comparison of energetics per unit $La_{0.5}Sr_{1.5}Ni_{1-x}Fe_xO_4$, relative to the corresponding non-magnetic energy in each composition. The energetic comparison clearly indicates FM and AFM-A as more stable configurations. **(c)** The projected density of states (PDOS) of the $B-O-B'$ bridges for both AFM-A and non-magnetic structures. PDOS of AFM-A is shown to be similar to that of FM in Figure 4.5, while that of non-magnetic structure gives consistent trend of bands movement as described for Figure 4.5.

Table D.1: The results of Rietveld refinement for $\text{La}_{0.5}\text{Sr}_{1.5}\text{Ni}_{1-x}\text{Fe}_x\text{O}_{4+\delta}$.

Sample	a [Å]	c [Å]	V [Å ³]	Refined composition	z/c (La,Sr)	z/c (O2)	$d(\text{M-O})_{\text{eq}}$ [Å]	$d(\text{M-O})_{\text{ap}}$ [Å]	R_f, R_p, R_{wp}
LSN	3.82437(2)	12.3331(1)	180.382(2)	$\text{La}_{0.518(6)}\text{Sr}_{1.482(6)}\text{NiO}_4$	0.35979(3)	0.1608(2)	1.91219(2)	1.984(2)	0.013, 0.010, 0.014
LSNF15	3.82806(2)	12.3673(1)	181.231(2)	$\text{La}_{0.496(6)}\text{Sr}_{1.504(6)}\text{Ni}_{0.85}\text{Fe}_{0.15}\text{O}_4$	0.35951(3)	0.1609(2)	1.91403(2)	1.990(2)	0.015, 0.011, 0.016
LSNF30	3.83130(2)	12.4085(1)	182.143(3)	$\text{La}_{0.518(6)}\text{Sr}_{1.482(6)}\text{Ni}_{0.70}\text{Fe}_{0.30}\text{O}_4$	0.35924(3)	0.1619(2)	1.91565(2)	2.009(2)	0.020, 0.012, 0.018
LSNF45	3.83506(2)	12.4629(1)	183.300(1)	$\text{La}_{0.534(6)}\text{Sr}_{1.466(6)}\text{Ni}_{0.55}\text{Fe}_{0.45}\text{O}_4$	0.35863(3)	0.1619(2)	1.91753(2)	2.017(3)	0.018, 0.012, 0.017
LSNF55	3.83724(2)	12.5018(2)	184.082(3)	$\text{La}_{0.500(6)}\text{Sr}_{1.500(6)}\text{Ni}_{0.45}\text{Fe}_{0.55}\text{O}_4$	0.35821(4)	0.1605(2)	1.91862(2)	2.007(3)	0.022, 0.013, 0.017
LSNF70	3.84143(2)	12.5581(2)	185.315(3)	$\text{La}_{0.524(6)}\text{Sr}_{1.476(6)}\text{Ni}_{0.30}\text{Fe}_{0.70}\text{O}_4$	0.35773(4)	0.1613(2)	1.92071(2)	2.026(3)	0.021, 0.012, 0.017
LSNF85	3.84533(2)	12.6232(2)	186.654(3)	$\text{La}_{0.524(6)}\text{Sr}_{1.476(6)}\text{Ni}_{0.15}\text{Fe}_{0.85}\text{O}_4$	0.35748(4)	0.1615(2)	1.92267(2)	2.039(3)	0.019, 0.013, 0.017
LSF	3.84789(3)	12.6919(2)	187.920(3)	$\text{La}_{0.536(6)}\text{Sr}_{1.464(6)}\text{FeO}_4$	0.35704(4)	0.1626(2)	1.92394(2)	2.064(3)	0.017, 0.013, 0.018

The refinement was performed in the $I4/mmm$ space group with the atomic positions La,Sr $4e$ (0, 0, z), Ni,Fe $2a$ (0,0,0), O1 $4c$ (0, $\frac{1}{2}$, 0) and O2 $4e$ (0, 0, z).

Table D.2: Comparison of LSNF30 with other promising OER catalysts and accompanying notes

Catalyst	Support ^A	Surface Area [m ² /g]	Catalyst Loading [mg _{cat} /cm ² _{geo}]	η @ 10 mA/cm ² _{geo} [mV]	Specific Activity @ η = 400 mV [mA/cm ² _{ox}]	Mass Activity @ η = 400 mV [mA/mg _{cat}]	OER Tafel slope [mV/dec]	Testing Conditions	Ref.
La _{0.5} Sr _{1.5} Ni _{0.7} Fe _{0.3} O _{4.94}	VC	5.9	0.015	360	32.7	1930	44	0.1 M KOH, O ₂ sat, 10 mV/s at 1600 rpm; iR corrected	This work
SrCoO _{2.7}	VC	3.6	0.015	419	9.4	332	67	0.1 M KOH, O ₂ sat, 10 mV/s at 1600 rpm; iR corrected	This work
LaNiO ₃	VC	11	0.015	582	0.4	41	99	0.1 M KOH, O ₂ sat, 10 mV/s at 1600 rpm; iR corrected	This work
IrO ₂	VC	14.5	0.010	468	1.2	175	88	0.1 M KOH, O ₂ sat, 10 mV/s at 1600 rpm; iR corrected	This work
SrSe _{0.025} Nb _{0.025} Co _{0.95} O _{3.4}	C65	0.1	0.360	411	58	58	55-60	0.1 M KOH, O ₂ sat, 10 mV/s at 1600 rpm; iR corrected	38
BaNiO ₃ / Ba ₂ Ni ₂ O ₅	VC	0.3	0.295	421	4.2 (9.1) ^B	13 (27)	--	0.1 M KOH, O ₂ sat, 10 mV/s at 1600 rpm; iR corrected	39
Pr _{0.5} Ba _{0.5} CoO _{3.4}	AB	0.35	0.250	>381 ^C	9.1 ^D	31 ^E	60	0.1 M KOH, O ₂ sat, 10 mV/s at 1600 rpm; iR corrected	40
CaCu ₂ FeO ₁₂	AB	0.45	0.250	378	15.5	70	59 (44) ^B	0.1 M KOH, O ₂ sat, 10 mV/s at 1600 rpm; iR corrected	41
Ca _{1.75} Pr _{0.25} MnO _{4.5}	AB	1.8	0.400	>471 ^C	14.5E-3	0.26	86	0.1 M KOH, O ₂ sat, 10 mV/s at 1600 rpm; iR corrected	42
La _{1.2} Ca _{0.8} NiO ₄	C65	10.8	0.397	373	18.8	52.2	42	0.1 M KOH, O ₂ sat, 10 mV/s at 9 ^F rpm; iR corrected	43
La _{0.7} (Ba _{0.5} Sr _{0.5}) _{0.3} Co _{0.8} Fe _{0.2} O _{3.5}	KB	21.3	0.639	375	0.12	25	97	0.1 M KOH, O ₂ sat, 10 mV/s at 1600 rpm; iR corrected	44
Ni-Fe LDH (Ni:Fe 45:55)	--	27	0.051 ^G	311	~1.1 ^H	~295 ^I	37	0.1 M KOH, O ₂ sat, 2 mV/s at 1600 rpm; iR corrected	45

^A Supports: **VC** - Cabot XC-72 Vulcan Carbon; **C65** - TIMCAL Super C65; **AB** - Acetylene Black; **KB** - Ketjenblack EC-600JD

^B Results in () are after cycling

^C Current density did not reach 10 mA/cm²_{geo}, overpotential listed is maximum tested

^D Potential only reported to 1.61 V, LSNF30's corresponding value is 19 mA/cm²_{ox}

^E Potential only reported to 1.61 V, LSNF30's corresponding value is 1100 mA/mg_{ox}

^F Electrodes rotation rate not reported

^G Mass was determined only by metal weight, neglecting O(H) contributions. Calculated mass and specific activities will be larger than truly measured.

^H Current density only reported to ~1.55 V, LSNF30's corresponding value is 2.0 mA/cm²_{ox}

^I Current density only reported to ~1.55 V, LSNF30's corresponding value is 115 mA/mg_{ox}

Table D.3: Summary of the physical, chemical and electrochemical properties of the LSNF series

Sample	Surface Area [m ² /g]	Ni ²⁺ AVG ⁺	Oxygen Excess [δ]	E _p Ni ^{2+/3+} oxidation [V]	Electrochemical Oxygen Diffusion Rate [cm ² /s]	Specific Activity @ 1.63 V [mA/cm ² ox]	Mass Activity @ 1.63 V [mA/mg _{ox}]
LSN	8.0	3.54 ± 0.03	0.018 ± 0.013	1.385	8.0E-13 ± 1.7E-13	1.1 ± 0.0	87.7 ± 1.2
LSNF15	6.8	3.57 ± 0.02	0.046 ± 0.007	1.454	1.0E-12 ± 1.7E-13	10.6 ± 0.8	717.8 ± 54.6
LSNF30	5.9	3.57 ± 0.03	0.042 ± 0.010	1.470	1.7E-12 ± 6.0E-13	32.7 ± 2.8	1930.8 ± 164.0
LSNF45	5.4	3.68 ± 0.10	0.065 ± 0.027	1.494	2.2E-12 ± 8.2E-13	27.4 ± 0.8	1480.7 ± 45.7
LSNF55	6.2	3.80 ± 0.05	0.088 ± 0.011	1.505	3.5E-13 ± 3.2E-13	18.4 ± 0.6	1143.7 ± 40.2
LSNF70	4.9	3.82 ± 0.14	0.076 ± 0.022	1.511	5.6E-14 ± 6.0E-14	17.7 ± 1.7	868.4 ± 85.1
LSNF85	5.6	3.95 ± 0.48	0.081 ± 0.036	1.524	3.0E-13 ± 3.0E-13	2.3 ± 0.2	128.8 ± 12.3
LSF	3.3	--	0.143 ± 0.037	--	--	0.3 ± 0.1	10.4 ± 3.9

Surface area determined by multipoint BET measurements.

Average Ni oxidation state determined by a combination of iodometric titrations and deconvolution of room temperature Mössbauer spectroscopy.

Oxygen excess determined by iodometric titrations.

Peak potential for Ni^{2+/3+} oxidation determined from CVs taken at 10 mV/s and after iR correction applied.

Oxygen diffusion rates determined electrochemically as outlined in the Methods section of Chapter 4 and Appendix D.

D.5 REFERENCES

1. Benloucif R, Nguyen N, Greneche JM, Raveau B. $\text{La}_{2-2x}\text{Sr}_{2x}\text{Ni}_{1-x}\text{Fe}_x\text{O}_{4-(x/2)+\delta}$: Magnetic and electron transport properties. *Journal of Physics and Chemistry of Solids* 1989, **50**(4): 435-440.
2. Gilev AR, Kiselev EA, Cherepanov VA. Homogeneity range, oxygen nonstoichiometry, thermal expansion and transport properties of $\text{La}_{2-x}\text{Sr}_x\text{Ni}_{1-y}\text{Fe}_y\text{O}_{4+\delta}$. *RSC Adv* 2016, **6**(77): 72905-72917.
3. Medarde M, Rodríguez-Carvajal J. Oxygen vacancy ordering in $\text{La}_{2-x}\text{Sr}_x\text{NiO}_{4-\delta}$ ($0 \leq \delta \leq 0.5$): the crystal structure and defects investigated by neutron diffraction. *Z Phys B* 1997, **102**(3): 307-315.
4. Millburn JE, Green MA, Neumann DA, Rosseinsky MJ. Evolution of the Structure of the K_2NiF_4 Phases $\text{La}_{2-x}\text{Sr}_x\text{NiO}_{4+\delta}$ with Oxidation State: Octahedral Distortion and Phase Separation ($0.2 \leq x \leq 1.0$). *Journal of Solid State Chemistry* 1999, **145**(2): 401-420.
5. Aguadero A, Escudero MJ, Pérez M, Alonso JA, Pomjakushin V, Daza L. Effect of Sr content on the crystal structure and electrical properties of the system $\text{La}_{2-x}\text{Sr}_x\text{NiO}_{4+\delta}$ ($0 \leq x \leq 1$). *Dalton Trans* 2006(36): 4377-4383.
6. Takeda Y, Kanno R, Sakano M, Yamamoto O, Takano M, Bando Y, *et al.* Crystal chemistry and physical properties of $\text{La}_{2-x}\text{Sr}_x\text{NiO}_4$ ($0 \leq x \leq 1.6$). *Materials Research Bulletin* 1990, **25**(3): 293-306.
7. Inprasit T, Wongkasemjit S, Skinner SJ, Burriel M, Limthongkul P. Effect of Sr substituted $\text{La}_{2-x}\text{Sr}_x\text{NiO}_{4+\delta}$ ($x = 0, 0.2, 0.4, 0.6$, and 0.8) on oxygen stoichiometry and oxygen transport properties. *RSC Adv* 2014, **5**(4): 2486-2492.
8. Manthiram A, Tang JP, Manivannan V. Factors Influencing the Stabilization of Ni^+ in Perovskite-Related Oxides. *Journal of Solid State Chemistry* 1999, **148**(2): 499-507.

9. Fontaine M-L, Laberty-Robert C, Ansart F, Tailhades P. Elaboration and characterization of $\text{La}_2\text{NiO}_{4+\delta}$ powders and thin films via a modified sol-gel process. *Journal of Solid State Chemistry* 2004, **177**(4-5): 1471-1479.
10. Sharma IB, Singh D. Solid state chemistry of Ruddlesden-Popper type complex oxides. *Bulletin of Materials Science* 1998, **21**(5): 363-374.
11. Mogni L, Prado F, Ascolani H, Abbate M, Moreno MS, Manthiram A, *et al.* Synthesis, crystal chemistry and physical properties of the Ruddlesden-Popper phases $\text{Sr}_3\text{Fe}_{2-x}\text{Ni}_x\text{O}_{7-\delta}$ ($0 \leq x \leq 1.0$). *Journal of Solid State Chemistry* 2005, **178**(5): 1559-1568.
12. Song K-W, Lee K-T. Characterization of $\text{NdSrCo}_{1-x}\text{Fe}_x\text{O}_{4+\delta}$ ($0 \leq x \leq 1.0$) intergrowth oxide cathode materials for intermediate temperature solid oxide fuel cells. *Ceramics International* 2011, **37**(2): 573-577.
13. Merkle R, Mastrikov YA, Kotomin EA, Kuklja MM, Maier J. First Principles Calculations of Oxygen Vacancy Formation and Migration in $\text{Ba}_{1-x}\text{Sr}_x\text{Co}_{1-y}\text{Fe}_y\text{O}_{3-\delta}$ Perovskites. *J Electrochem Soc* 2011, **159**(2): B219-B226.
14. Conesa JC. Electronic Structure of the (Undoped and Fe-Doped) NiOOH O_2 Evolution Electrocatalyst. *J Phys Chem C* 2016, **120**(34): 18999-19010.
15. Chen JYC, Dang L, Liang H, Bi W, Gerken JB, Jin S, *et al.* Operando Analysis of NiFe and Fe Oxyhydroxide Electrocatalysts for Water Oxidation: Detection of Fe^{4+} by Mössbauer Spectroscopy. *J Am Chem Soc* 2015, **137**(48): 15090-15093.
16. Trotochaud L, Young SL, Ranney JK, Boettcher SW. Nickel-Iron Oxyhydroxide Oxygen-Evolution Electrocatalysts: The Role of Intentional and Incidental Iron Incorporation. *J Am Chem Soc* 2014, **136**(18): 6744-6753.
17. Corrigan DA, Conell RS, Fierro CA, Scherson DA. In-situ Moessbauer study of redox processes in a composite hydroxide of iron and nickel. *J Phys Chem* 1987, **91**(19): 5009-5011.

18. Dionigi F, Strasser P. NiFe-Based (Oxy)hydroxide Catalysts for Oxygen Evolution Reaction in Non-Acidic Electrolytes. *Advanced Energy Materials* 2016, **6**(23): 1600621-n/a.
19. Goodenough JB. Atomic Moments and Their Interactions. In: Cotton FA (ed). *Magnetism and the Chemical Bond*. Interscience Publishers: New York, NY, 1963, pp 249-295.
20. Dau H, Limberg C, Reier T, Risch M, Roggan S, Strasser P. The Mechanism of Water Oxidation: From Electrolysis via Homogeneous to Biological Catalysis. *ChemCatChem* 2010, **2**(7): 724-761.
21. Man IC, Su H-Y, Calle-Vallejo F, Hansen HA, Martínez JI, Inoglu NG, *et al.* Universality in Oxygen Evolution Electrocatalysis on Oxide Surfaces. *ChemCatChem* 2011, **3**(7): 1159-1165.
22. Mefford JT, Rong X, Abakumov AM, Hardin WG, Dai S, Kolpak AM, *et al.* Water electrolysis on $\text{La}_{1-x}\text{Sr}_x\text{CoO}_{3-\delta}$ perovskite electrocatalysts. *Nature Communications* 2016, **7**: 11053.
23. Rong X, Parolin J, Kolpak AM. A Fundamental Relationship between Reaction Mechanism and Stability in Metal Oxide Catalysts for Oxygen Evolution. *ACS Catal* 2016, **6**(2): 1153-1158.
24. Lee Y-L, Lee D, Wang XR, Lee HN, Morgan D, Shao-Horn Y. Kinetics of Oxygen Surface Exchange on Epitaxial Ruddlesden–Popper Phases and Correlations to First-Principles Descriptors. *J Phys Chem Lett* 2016, **7**(2): 244-249.
25. Das A, Xhafa E, Nikolla E. Electro- and thermal-catalysis by layered, first series Ruddlesden-Popper oxides. *Catalysis Today* 2016, **277, Part 2**: 214-226.
26. Vladimir IA, Aryasetiawan F, Lichtenstein AI. First-principles calculations of the electronic structure and spectra of strongly correlated systems: the LDA + U method. *Journal of Physics: Condensed Matter* 1997, **9**(4): 767.

27. Gou G, Grinberg I, Rappe AM, Rondinelli JM. Lattice normal modes and electronic properties of the correlated metal LaNiO_3 . *Physical Review B* 2011, **84**(14): 144101.
28. Lee Y-L, Kleis J, Rossmeisl J, Morgan D. *Ab initio* energetics of LaBO_3 (001) ($B = \text{Mn, Fe, Co, and Ni}$) for solid oxide fuel cell cathodes. *Physical Review B* 2009, **80**(22): 224101.
29. Shein IR, Shein KI, Kozhevnikov VL, Ivanovskii AL. Band structure and the magnetic and elastic properties of SrFeO_3 and LaFeO_3 perovskites. *Physics of the Solid State* 2005, **47**(11): 2082-2088.
30. Ritzmann AM, Muñoz-García AB, Pavone M, Keith JA, Carter EA. Ab Initio DFT+U Analysis of Oxygen Vacancy Formation and Migration in $\text{La}_{1-x}\text{Sr}_x\text{FeO}_{3-\delta}$ ($x = 0, 0.25, 0.50$). *Chem Mater* 2013, **25**(15): 3011-3019.
31. Muñoz-García AB, Bugaris DE, Pavone M, Hodges JP, Huq A, Chen F, *et al.* Unveiling Structure–Property Relationships in $\text{Sr}_2\text{Fe}_{1.5}\text{Mo}_{0.5}\text{O}_{6-\delta}$, an Electrode Material for Symmetric Solid Oxide Fuel Cells. *J Am Chem Soc* 2012, **134**(15): 6826-6833.
32. Malashevich A, Ismail-Beigi S. First-principles study of oxygen-deficient LaNiO_3 structures. *Physical Review B* 2015, **92**(14): 144102.
33. Hardin WG, Slanac DA, Wang X, Dai S, Johnston KP, Stevenson KJ. Highly Active, Nonprecious Metal Perovskite Electrocatalysts for Bifunctional Metal–Air Battery Electrodes. *J Phys Chem Lett* 2013, **4**(8): 1254-1259.
34. Menil F. Systematic trends of the ^{57}Fe Mössbauer isomer shifts in (FeO_n) and (FeF_n) polyhedra. Evidence of a new correlation between the isomer shift and the inductive effect of the competing bond $T\text{-X}$ ($\rightarrow \text{Fe}$) (where X is O or F and T any element with a formal positive charge). *Journal of Physics and Chemistry of Solids* 1985, **46**(7): 763-789.

35. Takeda Y, Imayoshi K, Imanishi N, Yamamoto O, Takano M. Preparation and characterization of $\text{Sr}_{2-x}\text{La}_x\text{FeO}_4$ ($0 \leq x \leq 1$). *Journal of Materials Chemistry* 1994, **4**(1): 19-22.
36. Hinatsu Y, Tezuka K, Inamura M, Masaki NM. Magnetic Susceptibilities and Mössbauer Spectra of $\text{Sr}_{2-x}\text{La}_x\text{FeO}_{4-\delta}$ ($0 \leq x \leq 0.5$). *Journal of Solid State Chemistry* 1999, **146**(1): 253-257.
37. Burriel M, Wilkins S, Hill JP, Muñoz-Márquez MA, Brongersma HH, Kilner JA, *et al.* Absence of Ni on the outer surface of Sr doped La_2NiO_4 single crystals. *Energy Environ Sci* 2013, **7**(1): 311-316.
38. Zhou W, Zhao M, Liang F, Smith SC, Zhu Z. High activity and durability of novel perovskite electrocatalysts for water oxidation. *Mater Horiz* 2015, **2**(5): 495-501.
39. Lee JG, Hwang J, Hwang HJ, Jeon OS, Jang J, Kwon O, *et al.* A New Family of Perovskite Catalysts for Oxygen-Evolution Reaction in Alkaline Media: BaNiO_3 and $\text{BaNi}_{0.83}\text{O}_{2.5}$. *J Am Chem Soc* 2016, **138**(10): 3541-3547.
40. Grimaud A, May KJ, Carlton CE, Lee Y-L, Risch M, Hong WT, *et al.* Double perovskites as a family of highly active catalysts for oxygen evolution in alkaline solution. *Nature Communications* 2013, **4**: 2439.
41. Yagi S, Yamada I, Tsukasaki H, Seno A, Murakami M, Fujii H, *et al.* Covalency-reinforced oxygen evolution reaction catalyst. *Nature Communications* 2015, **6**: 8249.
42. Ebrahimizadeh Abrishami M, Risch M, Scholz J, Roddatis V, Osterthun N, Jooss C. Oxygen Evolution at Manganite Perovskite Ruddlesden-Popper Type Particles: Trends of Activity on Structure, Valence and Covalence. *Materials* 2016, **9**(11).
43. Liu R, Liang F, Zhou W, Yang Y, Zhu Z. Calcium-doped lanthanum nickelate layered perovskite and nickel oxide nano-hybrid for highly efficient water oxidation. *Nano Energy* 2015, **12**: 115-122.

44. Jung J-I, Risch M, Park S, Kim MG, Nam G, Jeong H-Y, *et al.* Optimizing nanoparticle perovskite for bifunctional oxygen electrocatalysis. *Energy Environ Sci* 2016, **9**(1): 176-183.
45. Görlin M, Ferreira de Araújo J, Schmies H, Bernsmeier D, Dresp S, Gliech M, *et al.* Tracking Catalyst Redox States and Reaction Dynamics in Ni–Fe Oxyhydroxide Oxygen Evolution Reaction Electrocatalysts: The Role of Catalyst Support and Electrolyte pH. *J Am Chem Soc* 2017, **139**(5): 2070-2082.

Appendix E: Highly Active Perovskite and Ruddlesden-Popper Composite Electrocatalysts for Water Oxidation

E.1 EXTENDED EXPERIMENTAL INFORMATION

All chemical were used as-received. Isooctane (2,2,4-trimethylpentane, $\geq 99\%$), 1-butanol ($\geq 99\%$), cetrimonium bromide (CTAB, $\geq 99\%$), and 5 wt% Nafion solution in lower alcohols were purchased from Sigma-Aldrich. Lanthanum(III) nitrate hexahydrate (99.995%), strontium(II) nitrate hexahydrate (99%), nickel(II) nitrate hexahydrate (99%), iron(III) nitrate non-anhydrate (99.99%), cobalt(II) hexahydrate ($\geq 99\%$), tetramethylammonium hydroxide pentahydrate (TMAOH, 99%), and potassium hydroxide ($\geq 85\%$) were obtained from Fisher Scientific. Millipore high purity water (DI water, 18 M Ω) was used. Oxygen (research grade, 99.999% purity) and argon (research grade, 99.999% purity) were obtained from Praxair. Ethanol (Absolute 200 proof) was obtained from Aaper Alcohol. Vulcan XC72 carbon (VC) was purchased from Cabot Corporation and ball-milled prior to use.

E.1.1 Catalyst Synthesis

All samples were synthesized using reverse water-in-oil microemulsion methods adopted from Zhao et al.²⁴ Reverse microemulsions containing the hydrolysis agent and required cations were prepared (abbreviated HYD and CAT, respectively) in parallel, after which they were combined, the mixed-metal hydroxide particles collected and washed by centrifugation, nebulized into liquid N₂, followed by lyophilization and crystallization at elevated temperatures to form the desired phase. The HYD and CAT reverse microemulsions were each formed by adding 3 g of CTAB to a mixture of 15 mL of isooctane and 3 mL of 1-butanol. The solutions were stirred to break up aggregated

CTAB particles such that upon addition of water, all CTAB is easily solvated. A turbid, homogenous solution in which no bulk particles of CTAB are visible indicated that the CTAB was adequately dispersed. Bath sonication was used to accelerate this process. 4 mL of 1 M KOH (4 mmol) was added to the HYD solution, under stirring, after which the solution rapidly became clear which indicated successful formation of the water-in-oil microemulsion. It is important to be precise with the addition of the KOH, as little as ~50 μL excess will not form a microemulsion. Separately, 4 mL of a variable molarity (typical 0.327 M) alkali and metal nitrate solution is added to the CAT solution under stirring, transforming it from turbid to clear almost immediately.

The precise determination of the nitrate solution molarity requires consideration of the oxidation states of the alkali earth or transition metal nitrate salts. As Zhao et al.²⁴ served as the foundation for the modification of this synthesis, we decided to maintain the same ratio of hydroxide ions in the HYD solution ($[\text{OH}^-]$), to cations in the CAT solution ($[\text{M}]$), modified to account for the average oxidation state (z) of cations in the nitrate salts, $\text{M}(\text{NO}_3)_z$, such that $[\text{OH}^-]:z[\text{M}] = 11/9$. The synthesis of LaNiO_3 used 4 mL of 0.327 M nitrate salts, 0.356 M for LSNF and 0.348 M for SNF.

The HYD and CAT solutions were left stirring for an hour after becoming transparent, to ensure complete formation of the reverse microemulsion phase. After one hour, the CAT solution was added drop-wise, over the course of 1 - 2 minutes, to the vigorously stirring (~1200 rpm) HYD solution. 10 minutes after the CAT solution was completely transferred, the HYD solution stir-rate was reduced to 600 rpm to minimize micellar collision and potential nanoparticle aggregation or Ostwald ripening. Shortly after addition of the CAT solution, the reverse microemulsion becomes colored and turbid, indicating the onset of nanoparticle nucleation via hydrolysis, and likely transformation of the spherical water-in-oil micelles to a bicontinuous micellar

structure.^{19, 22} The reactant solution was left to stir for 6 hours, and then let statically age (no stirring) for 18 - 24 hours. Static ageing has been reported³⁰ to decrease hydroxide nanoparticle size and improve phase purity.

After aging, the reactant solution (~50 mL) is split between 3 centrifuge tubes and the resultant hydroxide particles are precipitated out by addition of excess EtOH and collected via centrifugation at 6000 rpm for 3 min. Following collection and using the same number of centrifugation tubes, the hydroxide particles are washed by centrifugation in the presence of EtOH 3x at 6000 rpm and 3 min each, with the supernatant discarded after every wash. After washing, the particles are suspended in DI water across 3 centrifuge tubes and probe sonicated (20 - 30% power, 0.3 s duty cycle) for 5 min per tube. The particles are then combined into a single centrifuge tube, and nebulized into a liquid N₂ in a crystallization dish. Nebulization was achieved using a PET spray bottle purchased from Fischer Scientific, with a variable spray-head. The degree of misting was tuned running pure DI water through it, and selecting the spray setting that produced the finest mist while remaining confined to the volume of the recrystallization dish.

The frozen nanoparticles were placed in a freezer at -20°C and the residual liquid N₂ was left to evaporate. Separately, a lyophilizer was chilled to -40°C. Once all residual liquid N₂ had evaporated and the lyophilizer reached -40°C, the sample was freeze dried at -10°C and ~50 mTorr for 24+ hours, followed by an 8 hour ramp to 20°C and a 12 hour hold to ensure complete drying. The lyophilization times are dependent on the volume of frozen water that needs to be removed, and the times listed above are for a single sample, corresponding to ~60 mL of ice.

Finally, the dried nanoparticle powder is placed in a sealed tube furnace, whereupon it is heated at a rate of 1°C until the desired crystallization temperature, and

held for a time. This entire process is under 200 mL of flowing dehumidified air or pure O₂, depending on the catalyst composition. For example, LaNiO₃ was crystallized at 650°C under pure O₂ with a hold of only 30 minutes, while La_{0.6}Sr_{0.4}Ni_{0.6}Fe_{0.4}O₃ was crystallized at 825°C and held there for 5 hours. All catalyst compositions are furnace-cooled to room temperature under their respective flowing gas.

E.1.2 Electrochemical Characterization

Catalyst inks were prepared by adding 2 mL of a NaOH neutralized 0.05 wt% Nafion solution to 2 mg of catalyst powder and bath sonicated for at least one hour. A volume of ink (10 µL) was drop cast onto a clean 5 mm (0.196 cm², Pine Instruments) glassy carbon electrode and dried under ambient conditions overnight. The glassy carbon electrodes were cleaned prior to drop casting by sonication in a 1:1 DI water:ethanol solution. The electrode was then polished using 50 nm alumina powder, sonicated in a fresh DI water:ethanol solution, and dried in ambient air. All electrochemical tests were performed on electrodes prepared by this method, obtaining a composite catalyst loading of 51 µg_{total} cm⁻²_{geo}, yielding 15.3 µg_{oxide} cm⁻²_{geo} for catalysis tests (30 wt% on carbon).

Electrochemical testing was performed on either a CH Instruments CHI832a or a Metrohm Autolab PGSTAT302N potentiostat, both equipped with high speed rotators from Pine Instruments. All testing was done at room temperature in 0.1 M KOH (measured pH ≈ 12.8). Current interrupt and positive feedback methods were used to determine electrolyte resistance (46 Ω) and all data was iR compensated after testing unless stated otherwise. Each test was performed in a standard 3 electrode cell using a CH Instruments Hg/HgO (1 M KOH) reference electrode, a Pt or Au wire counter electrode, and a film of catalyst ink on glassy carbon as the working electrode. All

potentials are reported versus the regular hydrogen electrode (RHE), which was determined experimentally to be +0.8976 V vs. Hg/HgO (1 M KOH).

Quantification of Oxygen Evolution Activities. All OER testing was performed on newly dropcast electrodes which had not undergone previous testing, drop-cast with 30 wt% catalyst on VC ($15.3 \mu\text{g}_{\text{oxide}} \text{cm}^{-2}_{\text{geo}}$). Cyclic voltammetry scans were performed from 1 to 2 V vs RHE at 10 mV/s with a rotation rate of 1600 rpm in O₂-saturated 0.1 M KOH. The anodic and cathodic scans were averaged and iR corrected, and the current at 1.63 V vs RHE-iR was selected from the polarization curves to compare OER activities. Scatter in the data at high current densities is due to oxygen bubble formation and desorption on the electrode surface. Data reported herein is the average taken from at least three tests on fresh electrodes.

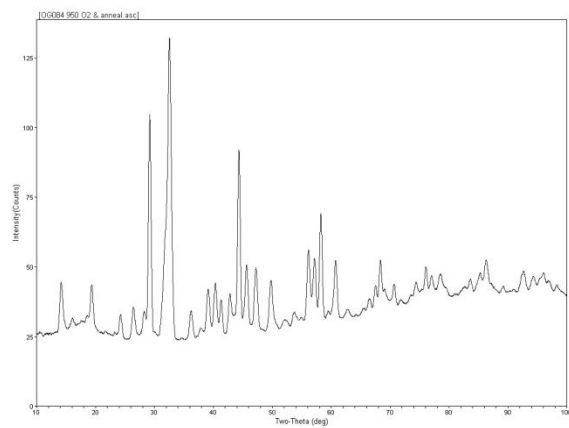


Figure E.1: X-ray diffraction pattern of SNF made by the polymerizable complex synthetic method

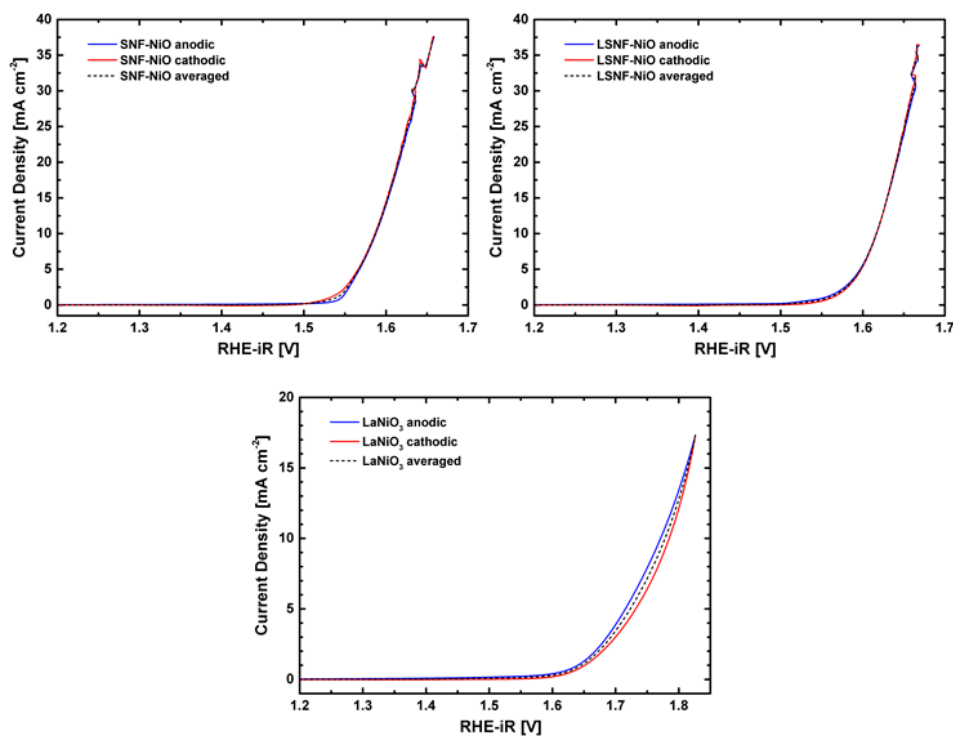


Figure E.2: Representative polarization curves for LNO, LSNF and SNF

Taken in O_2 saturated 0.1 M KOH at 1600 rpm and 10 mV s^{-1} . Catalysts were first swept positive (anodic), then negative (cathodic), and the curves averaged before iR correction. Electrolyte resistance was measured to be 46Ω . Total electrode loading is $51 \mu\text{g}_{\text{total}} \text{cm}_{\text{geo}}^{-2}$ with 30 wt% catalyst on XC72 Vulcan Carbon (VC), yielding $15.3 \mu\text{g}_{\text{ox}} \text{cm}_{\text{geo}}^{-2}$.

E.2 ALTERNATIVE OIL PHASE TESTS

Table E.1: Results of decane oil phase tests

	Hydrolysis Solutions		
Composition	7.5 mL decane 1.5 g CTAB 1.5 mL 1-butanol 1.5 mL 1 M KOH	7.5 mL decane 1.5 g CTAB 1.5 mL 1-butanol 1.5 mL 0.3M NH ₄ oxalate	7.5 mL decane 1.5 g CTAB 1.5 mL 1-butanol 1.5 mL 1 M TMAOH
Mixing Behavior	CTAB took a long time to dissolve. It was not fully dissolved after stirring, and the mixture was cloudy	Cloudy	Completely Clear
	Cationic Solutions		
Composition	7.5 mL decane 1.5 g CTAB 1.5 mL 1-butanol 1.5 mL 0.8175 M NaCl	7.5 mL decane 1.5 g CTAB 1.5 mL 1-butanol 1.5 mL 0.8175M NaCl	7.5 mL decane 1.5 g CTAB 1.5 mL 1-butanol 1.5 mL 0.8175M NaCl
Mixing Behavior	Clear	Clear	Clear
	Mixing Behavior After Solutions Combined		
	The mixture became clear. The undissolved CTAB dissolved after a few minutes	Clear. There was a very small amount of CTAB seen, but it dissolved very quickly when mixed	Clear

All with $W_0 = 0.75$. The ‘soft’ base TMAOH forms stable microemulsions, while KOH does not. Oxalate also forms a microemulsion after mixing.

Table E.2: Results of cyclohexane oil phase tests

	Hydrolysis Solutions		
Composition	7.5 mL cyclohexane 1.5 g CTAB 1.5 mL 1-butanol 1.5 mL 1 M KOH	7.5 mL cyclohexane 1.5 g CTAB 1.5 mL 1-butanol 1.5 mL 0.3M NH ₄ oxalate	7.5 mL cyclohexane 1.5 g CTAB 1.5 mL 1-butanol 1.5 mL 1 M TMAOH
Mixing Behavior	Cloudy- CTAB amount?	Cloudy- CTAB amount?	Completely Clear
	Cationic Solutions		
Composition	7.5 mL cyclohexane 1.5 g CTAB 1.5 mL 1-butanol 1.5 mL 0.8175 M NaCl	7.5 mL cyclohexane 1.5 g CTAB 1.5 mL 1-butanol 1.5 mL 0.8175M NaCl	7.5 mL cyclohexane 1.5 g CTAB 1.5 mL 1-butanol 1.5 mL 0.8175M NaCl
Mixing Behavior	Clear	Clear	Clear
	Mixing Behavior After Solutions Combined		
	The mixture stayed cloudy. No undissolved CTAB notice	Clear.	Clear

All with $W_0 = 0.75$. The ‘soft’ base TMAOH forms stable microemulsions, while KOH does not. Oxalate also forms a microemulsion after mixing.

E.3 REFERENCES

1. Hardin WG, Forslund RP, Abakumov AM, Rong X, Filimonov D, Alexander CT, *et al.* Exceptional Electrocatalytic Oxygen Evolution Via Tunable Charge Transfer Interactions in $\text{La}_{0.5}\text{Sr}_{1.5}\text{Ni}_{1-x}\text{Fe}_x\text{O}_{4+\delta}$ Ruddlesden-Popper Oxides. *Nat Mater* 2017.
2. Man IC, Su H-Y, Calle-Vallejo F, Hansen HA, Martínez JI, Inoglu NG, *et al.* Universality in Oxygen Evolution Electrocatalysis on Oxide Surfaces. *ChemCatChem* 2011, 3(7): 1159-1165.
3. Zhu H, Zhang P, Dai S. Recent Advances of Lanthanum-Based Perovskite Oxides for Catalysis. *ACS Catal* 2015, 5(11): 6370-6385.
4. Chen D, Chen C, Baiye ZM, Shao Z, Ciucci F. Nonstoichiometric Oxides as Low-Cost and Highly-Efficient Oxygen Reduction/Evolution Catalysts for Low-Temperature Electrochemical Devices. *Chem Rev* 2015, 115(18): 9869-9921.
5. Hunter BM, Gray HB, Müller AM. Earth-Abundant Heterogeneous Water Oxidation Catalysts. *Chem Rev* 2016, 116(22): 14120-14136.
6. Suntivich J, May KJ, Gasteiger HA, Goodenough JB, Shao-Horn Y. A Perovskite Oxide Optimized for Oxygen Evolution Catalysis from Molecular Orbital Principles. *Science* 2011, 334(6061): 1383-1385.
7. Seitz LC, Dickens CF, Nishio K, Hikita Y, Montoya J, Doyle A, *et al.* A highly active and stable $\text{IrO}_x/\text{SrIrO}_3$ catalyst for the oxygen evolution reaction. *Science* 2016, 353(6303): 1011-1014.
8. Mefford JT, Rong X, Abakumov AM, Hardin WG, Dai S, Kolpak AM, *et al.* Water electrolysis on $\text{La}_{1-x}\text{Sr}_x\text{CoO}_{3-\delta}$ perovskite electrocatalysts. *Nature Communications* 2016, 7: 11053.
9. Galasso FS. *Structure, Properties and Preparation of Perovskite-Type Compounds*, vol. 5. Pergamon Press, 1969.
10. Bockris JO, Otagawa T. Mechanism of oxygen evolution on perovskites. *J Phys Chem* 1983, 87(15): 2960-2971.
11. Hardin WG, Mefford JT, Slanac DA, Patel BB, Wang X, Dai S, *et al.* Tuning the Electrocatalytic Activity of Perovskites through Active Site Variation and Support Interactions. *Chem Mater* 2014, 26(11): 3368-3376.
12. Rong X, Parolin J, Kolpak AM. A Fundamental Relationship between Reaction Mechanism and Stability in Metal Oxide Catalysts for Oxygen Evolution. *ACS Catal* 2016, 6(2): 1153-1158.
13. Yagi S, Yamada I, Tsukasaki H, Seno A, Murakami M, Fujii H, *et al.* Covalency-reinforced oxygen evolution reaction catalyst. *Nature Communications* 2015, 6: 8249.

14. Takeda Y, Hashino T, Miyamoto H, Kanamaru F, Kume S, Koizumi M. Synthesis of SrNiO_3 and related compound, $\text{Sr}_2\text{Ni}_2\text{O}_5$. *Journal of Inorganic and Nuclear Chemistry* 1972, 34(5): 1599-1601.
15. Oliveira FS, Pimentel PM, Oliveira RMPB, Melo DMA, Melo MAF. Effect of lanthanum replacement by strontium in lanthanum nickelate crystals synthesized using gelatin as organic precursor. *Materials Letters* 2010, 64(24): 2700-2703.
16. Seki H, Saito T, Shimakawa Y. High Pressure Synthesis of $\text{SrFe}_{1-x}\text{Ni}_x\text{O}_3$. *Journal of the Japan Society of Powder and Powder Metallurgy* 2016, 63(7): 609-612.
17. Takeda Y, Kanno R, Sakano M, Yamamoto O, Takano M, Bando Y, *et al.* Crystal chemistry and physical properties of $\text{La}_{2-x}\text{Sr}_x\text{NiO}_4$ ($0 \leq x \leq 1.6$). *Materials Research Bulletin* 1990, 25(3): 293-306.
18. Gilev AR, Kiselev EA, Cherepanov VA. Homogeneity range, oxygen nonstoichiometry, thermal expansion and transport properties of $\text{La}_{2-x}\text{Sr}_x\text{Ni}_{1-y}\text{Fe}_y\text{O}_{4+\delta}$. *RSC Adv* 2016, 6(77): 72905-72917.
19. Pileni M-P. The role of soft colloidal templates in controlling the size and shape of inorganic nanocrystals. *Nat Mater* 2003, 2(3): 145-150.
20. Eastoe J, Hollamby MJ, Hudson L. Recent advances in nanoparticle synthesis with reversed micelles. *Advances in Colloid and Interface Science* 2006, 128-130: 5-15.
21. Ganguli AK, Ganguly A, Vaidya S. Microemulsion-based synthesis of nanocrystalline materials. *Chemical Society Reviews* 2010, 39(2): 474-485.
22. Giannakas AE, Ladavos AK, Pomonis PJ. Preparation, characterization and investigation of catalytic activity for NO+CO reaction of LaMnO_3 and LaFeO_3 perovskites prepared via microemulsion method. *Applied Catalysis B: Environmental* 2004, 49(3): 147-158.
23. Garg N, Basu M, Upadhyaya K, Shivaprasad SM, Ganguli AK. Controlling the aspect ratio and electrocatalytic properties of nickel cobaltite nanorods. *RSC Adv* 2013, 3(46): 24328-24336.
24. Zhao Y, Xu L, Mai L, Han C, An Q, Xu X, *et al.* Hierarchical mesoporous perovskite $\text{La}_{0.5}\text{Sr}_{0.5}\text{CoO}_{2.91}$ nanowires with ultrahigh capacity for Li-air batteries. *Proceedings of the National Academy of Sciences* 2012, 109(48): 19569-19574.
25. Ma X, Wang B, Xhafa E, Sun K, Nikolla E. Synthesis of shape-controlled $\text{La}_2\text{NiO}_{4+\delta}$ nanostructures and their anisotropic properties for oxygen diffusion. *Chem Commun* 2015, 51(1): 137-140.

26. Ma X, Carneiro JSA, Gu X-K, Qin H, Xin H, Sun K, *et al.* Engineering Complex, Layered Metal Oxides: High-Performance Nickelate Oxide Nanostructures for Oxygen Exchange and Reduction. *ACS Catal* 2015, 5(7): 4013-4019.
27. Zhang Z, Greenblatt M. Synthesis, Structure, and Properties of $\text{Ln}_4\text{Ni}_3\text{O}_{10-\delta}$ (Ln = La, Pr, and Nd). *Journal of Solid State Chemistry* 1995, 117(2): 236-246.
28. Conesa JC. Electronic Structure of the (Undoped and Fe-Doped) NiOOH O_2 Evolution Electrocatalyst. *J Phys Chem C* 2016, 120(34): 18999-19010.
29. Merkle R, Mastrikov YA, Kotomin EA, Kuklja MM, Maier J. First Principles Calculations of Oxygen Vacancy Formation and Migration in $\text{Ba}_{1-x}\text{Sr}_x\text{Co}_{1-y}\text{Fe}_y\text{O}_{3-\delta}$ Perovskites. *J Electrochem Soc* 2011, 159(2): B219-B226.
30. Soleymani M, Edrissi M. Preparation of manganese-based perovskite nanoparticles using a reverse microemulsion method: biomedical applications. *Bulletin of Materials Science* 2016, 39(2): 487-490.
31. Takeda Y, Imayoshi K, Imanishi N, Yamamoto O, Takano M. Preparation and characterization of $\text{Sr}_{2-x}\text{La}_x\text{FeO}_4$ ($0 \leq x \leq 1$). *Journal of Materials Chemistry* 1994, 4(1): 19-22.
32. Lee Y, Suntivich J, May KJ, Perry EE, Shao-Horn Y. Synthesis and Activities of Rutile IrO_2 and RuO_2 Nanoparticles for Oxygen Evolution in Acid and Alkaline Solutions. *J Phys Chem Lett* 2012, 3(3): 399-404.

Appendix F: Anion charge storage through oxygen intercalation in LaMnO_3 perovskite pseudocapacitor electrodes⁹

F.1 EXPERIMENTAL

Peroxide studies of LaNiO_3 : Electrodes were tested in a 0.1M KOH electrolyte that had been degassed with Ar for 15 min to purge the cell of oxygen. Then 150 μL of 10wt% H_2O_2 was added and immediately cyclic voltammetry was performed at a scan rate of 5 mV/s between the potentials 0.2 to -0.6V vs. Hg/HgO.

Oxygen reduction studies of LaNiO_3 : Oxygen reduction activity of the electrodes was performed using rotating disk cyclic voltammetry in 150 mL of 0.1M KOH saturated with O_2 at a scan rate of 5 mV/s and a rotation rate of 1600 rpm.

Electrochemical Cycling of Carbon-Free $\text{LaMnO}_{3\pm\delta}$ Electrodes: In order to ensure sufficient sample sizes for XPS and XRD analysis, films of 1 mg/cm^2 were prepared by dispersing either $\text{LaMnO}_{3.09}$ or r- $\text{LaMnO}_{2.91}$ without any carbon additive in EtOH containing 0.05 wt% Na-substituted Nafion in a ratio of 2.5 mg mL^{-1} and sonicated for 30 min. 78.4 μL of this solution was spuncast at 700 rpm onto a glassy carbon electrode (0.196 cm^2 , Pine Instruments). These electrodes were cycled in Ar saturated 1M KOH for 1, 25, 100, 250, and 500 cycles. After cycling, the electrodes were removed from the electrolyte and gently washed with DI water followed by drying under vacuum.

Surface Analysis of $\text{LaMnO}_{3\pm\delta}$: Due the semiconducting properties of $\text{LaMnO}_{3\pm\delta}$, charge neutralization must be employed during the collection of high resolution data. This minimizes, but does not eliminate, a global shift in the binding energies (BEs) for neat $\text{LaMnO}_{3\pm\delta}$ samples. To correct for these shifts, the Kratos AXIS Ultra DLD was first calibrated against the Ag 3d spectrum of freshly sputtered 99.99% pure Ag. Following

⁹Large parts of this chapter have been published as Mefford JT, Hardin WG, Dai S, Johnston KP, Stevenson KJ. Anion charge storage through oxygen intercalation in LaMnO_3 perovskite pseudocapacitor electrodes. *Nat Mater* 2014, **13**(7): 726-732.

spectrum calibration to Ag, the BE shifts due to $\text{LaMnO}_{3\pm\delta}$ charging were compensated by reconstruction of the La 3d 5/2 spectra, as outlined by Mickevicius *et al.*¹ This reconstruction procedure enabled us to shift the BE of the $\text{LaMnO}_{3\pm\delta}$ spectra relative to the deconvoluted La^{3+} 3d 5/2 peak with confidence, due to the electronic configuration of La^{3+} being that of xenon. Following these corrections, the O 1s spectra of both samples were deconvoluted utilizing Mickevicius *et al.* for H_2O and La-O peak assignments, De Asha *et al.* for La-OH assignment and Djurfors *et al.* for Mn-O and Mn-OH assignments.¹⁻⁴

XRD of Electrochemically Cycled $\text{LaMnO}_{3.09}$ and $r\text{-LaMnO}_{2.91}$ Electrodes: Structural information about cycled $\text{LaMnO}_{3\pm\delta}$ electrodes was obtained using wide-angle X-ray diffraction (Rigaku Spider, Cu $K\alpha$ radiation, $\lambda = 1.5418 \text{ \AA}$) and analyzed with JADE software (Molecular Diffraction Inc.). Carbon-free electrodes were electrochemically cycled at 20 mV/s as described above for 1, 25, 100, 250, and 500 cycles. The active material on the electrode was gently rinsed free of residual electrolyte with DI water and dried under vacuum. The active material was then removed for XRD analysis.

F.1.1 XPS of Electrochemically Cycled $\text{LaMnO}_{3.09}$ and $r\text{-LaMnO}_{2.91}$ Electrodes

XPS of Electrochemically Cycled $\text{LaMnO}_{3.09}$ and $r\text{-LaMnO}_{2.91}$ Electrodes. XPS data was acquired using a Kratos AXIS Ultra DLD spectrometer equipped with a monochromatic Al X-ray source (Al α , 1.4866 keV). Carbon-free electrodes of $\text{LaMnO}_{3.09}$ and $\text{LaMnO}_{2.91}$ were electrochemically cycled, as previously described, for 25, 100 and 500 cycles. The active material on the electrode was removed, washed with DI water and dried in a vacuum. To avoid signal convolution with the Nafion binder and provide a reference peak with which to calibrate the spectra, the Mn 2p 1/2 and La 4p 3/2

core regions were selected for analysis. The Mn 2p 1/2 region was used to avoid convolution with a copper LMM auger peak resulting from the copper tape on which each sample was mounted.⁵ Where convolution did occur, the auger was fitted and removed prior to analysis. High resolution elemental analysis was performed on each sample, using a 20 eV pass energy, 0.1 eV step size and a 4 second dwell time. All spectra are the average of four collections. Charge compensation was used for the collection of all data, due to the lack of conductive carbon. To correct for shifts in binding energy due to charge compensation, peak reconstruction of the La 4p 3/2 region was performed as previously reported and the Mn 2p 1/2 region was shifted relative to the La 4p 3/2 C_{4f^0} component.

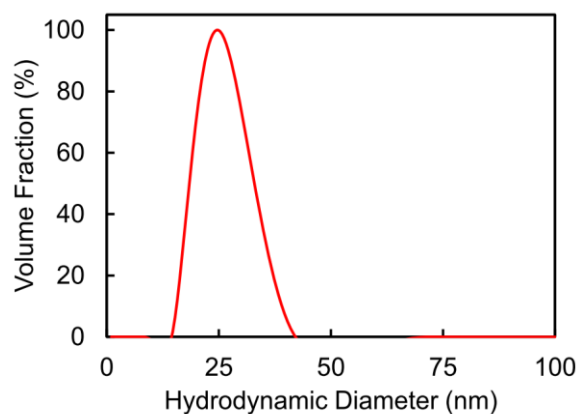


Figure F.1: Dynamic light scattering measurements of initial mixed metal hydroxides

During the reverse phase hydrolysis step of the synthesis, mixed metal hydroxides of La and Mn are formed. These mixed metal hydroxides may be individual particles or agglomerations with a hydrodynamic radius centered at 25 nm and a peak width of ± 7 nm. A small volume fraction of larger agglomerates is present as well with diameters between 75-100 nm.

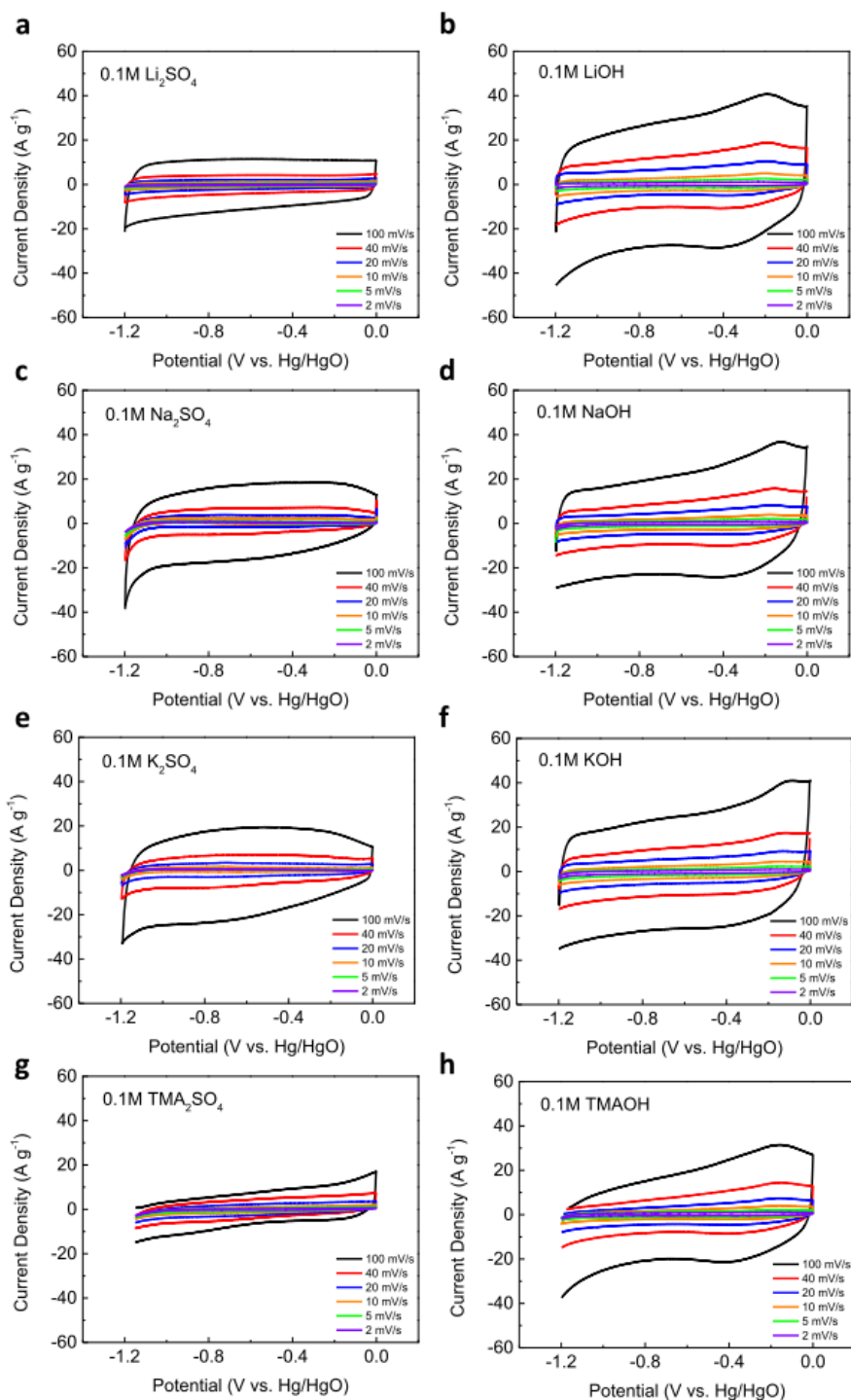


Figure F.2: Electrolyte studies of $\text{LaMnO}_{3+\delta}$

Cyclic voltammograms of $\text{LaMnO}_{3+\delta}$ in 0.1M sulfate based electrolytes in order of cationic radius Li^+ (a), Na^+ (c), K^+ (e), TMA^+ (g) compared to cyclic voltammograms of $\text{LaMnO}_{3+\delta}$ in 0.1M basic electrolytes in order of cationic radius Li^+ (b), Na^+ (d), K^+ (f), TMA^+ (h). In all of these CV's, the current contribution from the N-OMC carbon support has been subtracted. The presence of both oxidation and reduction peaks in the 0.1M basic electrolytes is demonstrative of the role of OH^- ions as intercalating species in $\text{LaMnO}_{3.09}$.

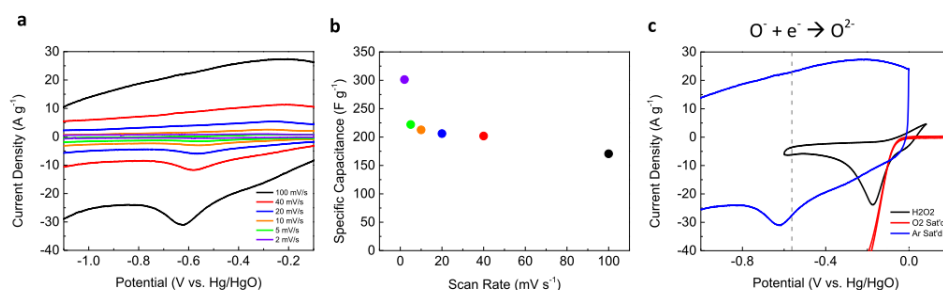


Figure F.3: Capacitive responses of LaNiO₃ and peroxide CV

(a) Cyclic voltammogram and (b) specific capacitance versus scan rate for LaNiO_{3-δ}. c, Overlay of hydrogen peroxide voltammogram at 5 mV/s, oxygen reduction at 5 mV/s and a rotation rate of 1600 rpm, and the pseudocapacitive CV curves at 100 mV/s for LaNiO₃. The large peak in the peroxide curve corresponds to reduction of O₂ from the chemical disproportionation of H₂O₂. The upturn at ~-0.6V corresponds to the reduction of the peroxide species (also indicated by the dashed line).

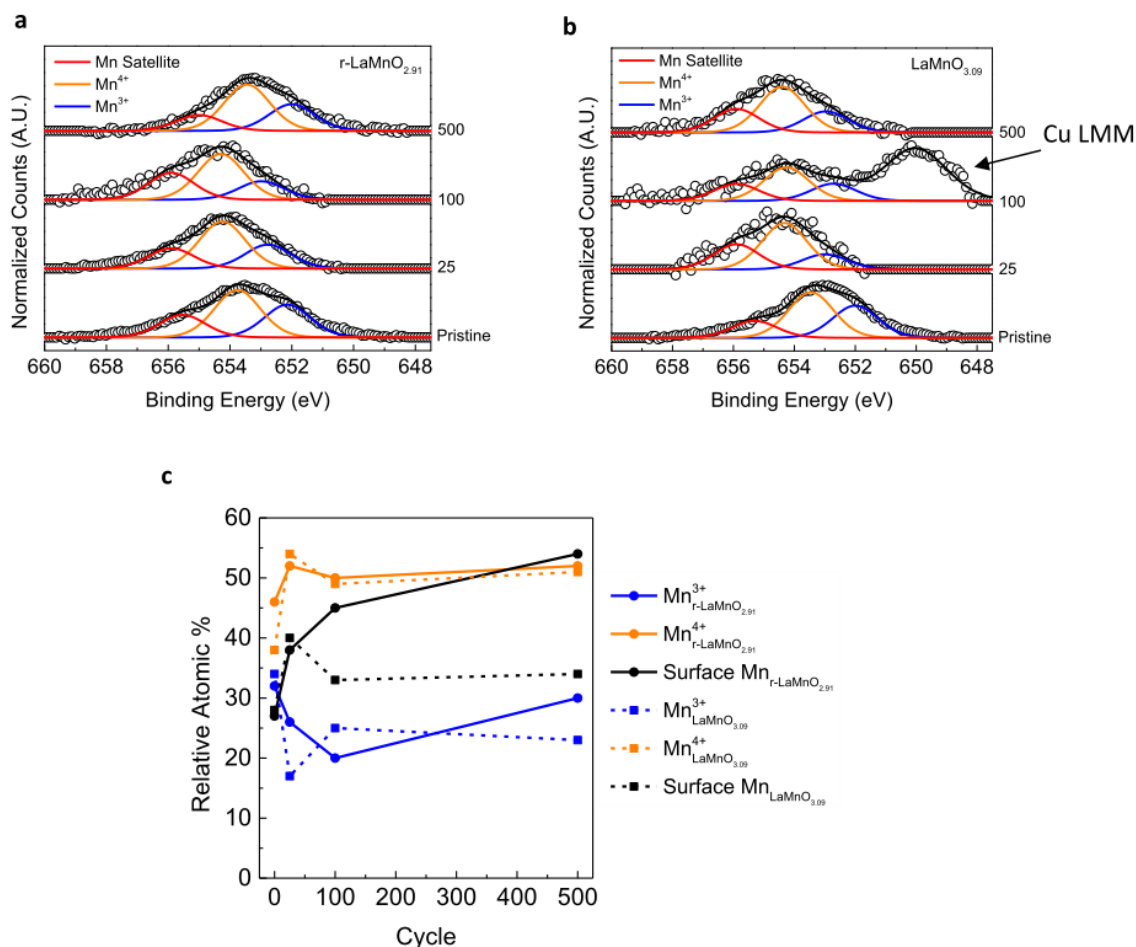


Figure F.4: Cycling *ex-situ* Mn 2p_{1/2} XPS Studies of LaMnO_{3±δ}

Carbon-free electrodes of r-LaMnO_{2.91} (a) and LaMnO_{3.09} (b) were cycled between 25-500 times and then characterized using XPS. c, Both electrodes were found to have an initial increase of surface manganese (compared to the relative atomic percent of lanthanum based on the La 4p 3/2 contribution) concomitant with an increase in the oxidation state to Mn⁴⁺ due to the addition of electrolyte oxygen ions. Because of this, it is likely that oxygen diffusion rates are greatly enhanced at the surface along grain boundaries leading to regions where oxygen intercalation is rapid and pseudocapacitive rather than purely faradaic.

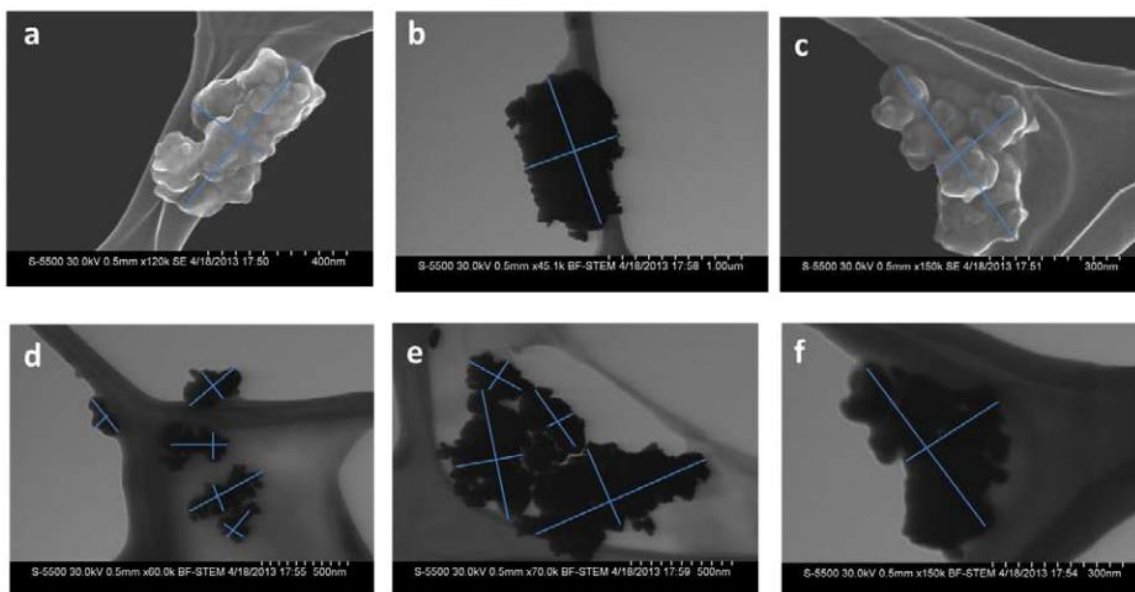


Figure F.5: | Particle thickness analysis for diffusion rate calculation

The thickness of the particles was approximated by taking the average of lateral dimension measurements of $\text{LaMnO}_{3.09}$ from SEM images. The average thickness corresponded to 380 ± 90 nm with an N value of 26.

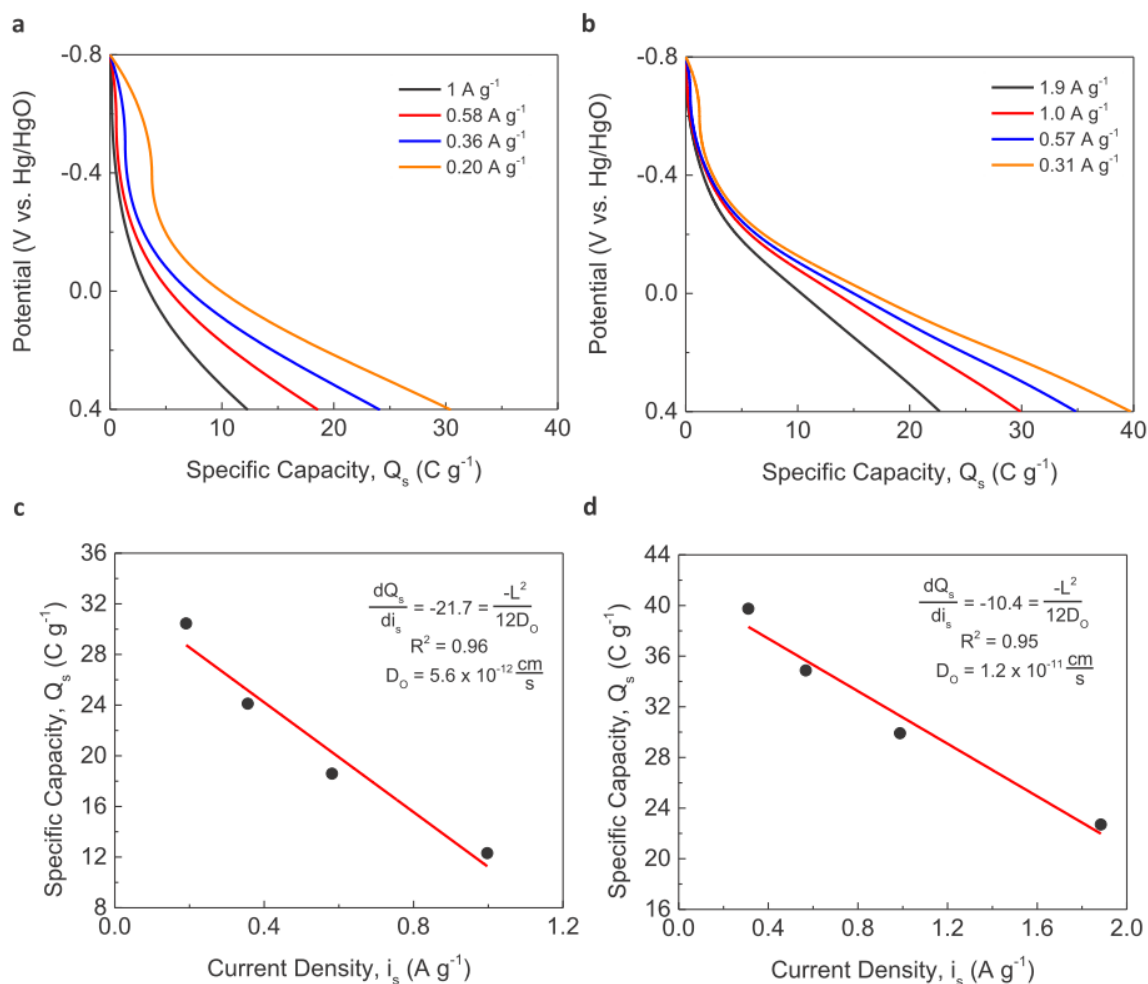


Figure F.6: Diffusion rate calculations on unsupported $\text{LaMnO}_{3\pm\delta}$

Calculation of the diffusion rates for a,c. $\text{LaMnO}_{3.09}$ and b,d. $\text{r-LaMnO}_{2.91}$. The potential versus capacity plots presented in a,b are calculated from integration of the oxidation current from the CV's presented in S4a and S4b. The sharp drop in potential at low capacity changes is indicative of the ohmic drop in both samples because carbon was not included as a conductive support in these samples. The thickness, L , was approximated from Figure F.5.

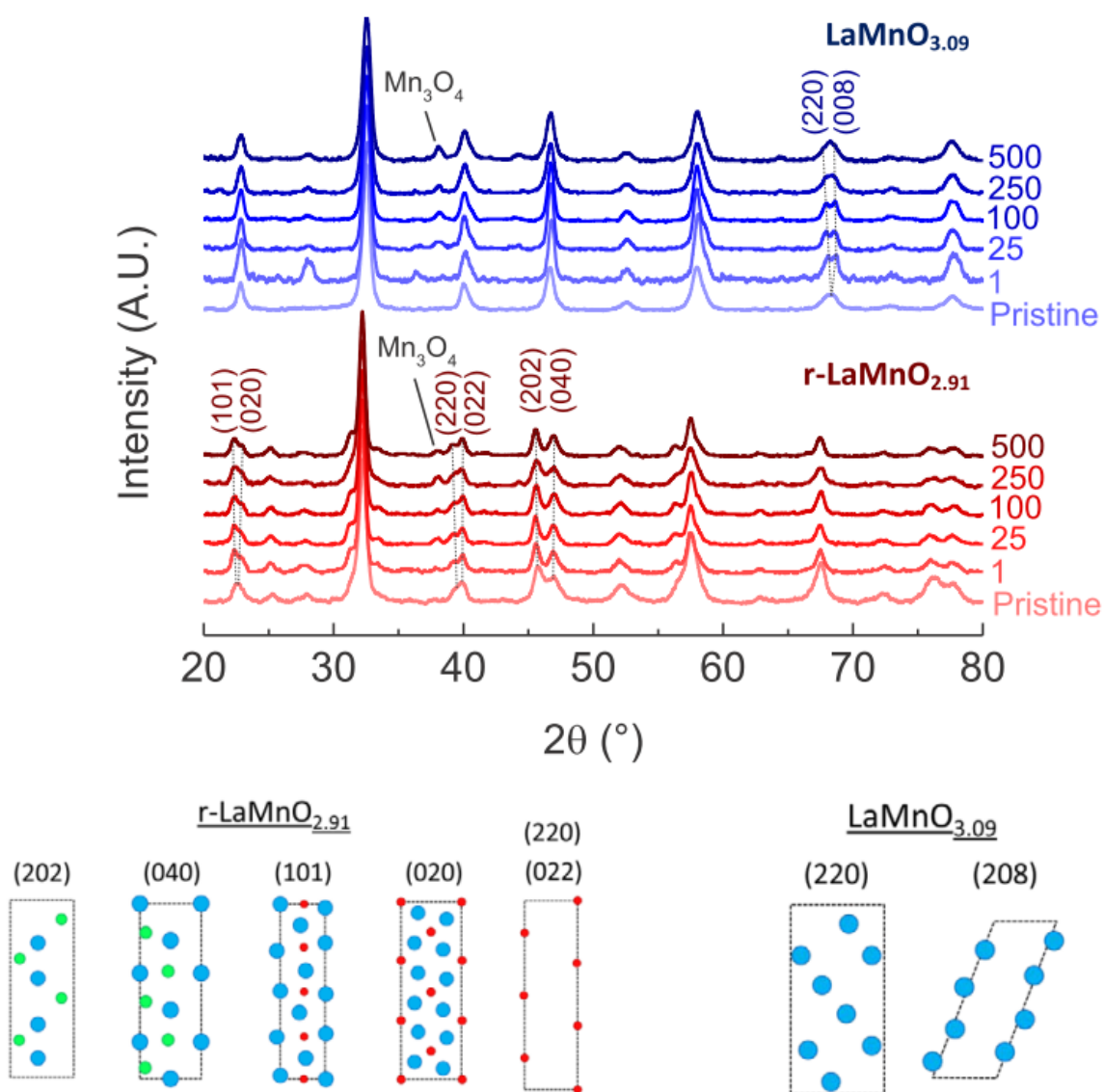


Figure F.7: Cycling *ex-situ* XRD Studies of $\text{LaMnO}_{3\pm\delta}$

The degree to which oxygen intercalation extended into the bulk was investigated through XRD on cycled electrode materials. However, over the course of cycling it was found that there were minimal changes in the bulk structure. The diffraction peaks that underwent the most drastic changes have been labeled in the figure and interestingly correspond to lattice planes that contain either only oxygen atoms, or direct pathways for oxygen diffusion.⁶⁻¹¹ In addition, a peak at 38° corresponding to Mn_3O_4 grew in over cycling in both samples, which is likely formed during the removal of surface oxygen which results in Mn^{2+} necessary to form the spinel phase. The lack of significant changes in the XRD spectrum is expected from previous work on $\text{LaMnO}_{3\pm\delta}$ materials, where vacancies are randomly distributed throughout the crystal structure but do not lead to significant distortions in atomic arrangements and lattice spacings.⁶⁻¹⁰ In combination with the XPS results, it is concluded that oxygen intercalation is dominated by the surface of the electrodes, but due to the high oxygen diffusion rates and high specific capacities found in this work, that the oxygen intercalation extends more deeply into the crystal than just the pure surface.

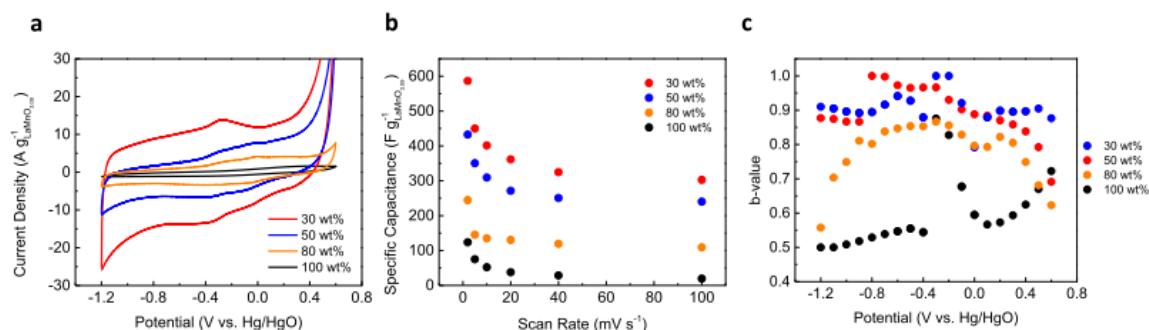


Figure F.8: Effect of weight loading on the capacitive contributions of $\text{LaMnO}_{3.09}$

a, Cyclic voltammograms at 100 mV s^{-1} for various weight loadings of $\text{LaMnO}_{3.09}$ on N-OMC. The contribution of the carbon support to the current and the capacitance have been subtracted. The sharp increase in current at $\sim 0.2 \text{ V}$ vs. Hg/HgO corresponds to the oxygen evolution reaction on $\text{LaMnO}_{3.09}$ in alkaline electrolytes. b, Specific capacitance versus scan rate for $\text{LaMnO}_{3.09}$ at various weight loadings. c, b-value analysis of $\text{LaMnO}_{3.09}$ at different mass loadings. The b-value peaks at approximately $E = -0.3 \text{ V}$ vs. Hg/HgO for all mass loadings which corresponds to the position of the redox peaks in the cyclic voltammograms. *In all of these figures, the current and capacitance contributions of the carbon support have been subtracted out to clearly demonstrate the electrochemical characteristics of $\text{LaMnO}_{3.09}$.

The effect of weight loading on carbon and the capacitive contribution to the current was investigated using a power-law dependence or b-value analysis method according to equation (F.1):¹²

$$i = av^b \quad (\text{F.1})$$

where i (A) is the current produced by $\text{LaMnO}_{3.09}$, a is a constant, v is the scan rate (V s^{-1}), and b is indicative of the capacitive contribution to the current obtained from a power fit of the current versus scan rate. Pure diffusion controlled reactions correspond to a b-value of 0.5 while a b-value of 1 is indicative of a purely capacitive current, including intercalation based pseudocapacitance. An extended potential window of -1.2 to 0.6 V vs.

Hg/HgO was used in order to encompass the redox peaks at all mass loadings, where resistive effects result in a substantial increase in the overpotential for oxygen intercalation in high weight loadings of $\text{LaMnO}_{3\pm\delta}$. As seen in Figure 6.4, the low electronic conductivity of LaMnO_3 requires the use of a substantial amount of carbon, ~70%, to achieve significant pseudocapacitive behavior. However, the b-value analysis peaks at the approximate potential of -0.3V vs. Hg/HgO for all samples, corresponding to the $E_{1/2}$ of the redox peaks present in the 30 wt% loading samples.

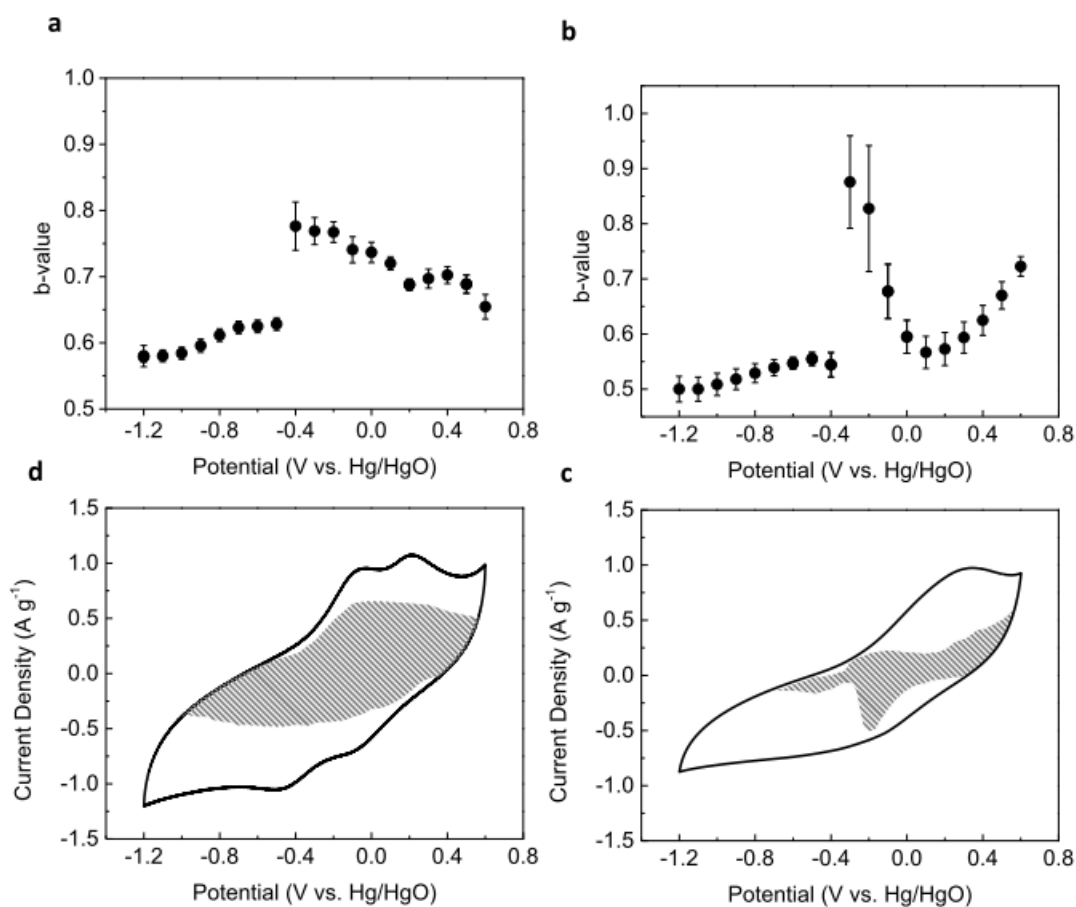


Figure F.9: b-value analysis of $\text{LaMnO}_{3\pm\delta}$

a,b. b-values for $\text{r-LaMnO}_{2.91}$ (a) and $\text{LaMnO}_{3.09}$ (b). c,d. CV's of $\text{r-LaMnO}_{2.91}$ (c) and $\text{LaMnO}_{3.09}$ (d). The shaded grey areas show the capacitive current envelope. The presence of a peak in the capacitance values at $E \sim -0.3\text{V}$ vs. Hg/HgO corresponds well with the $E_{1/2}$ of the reaction for oxygen intercalation.

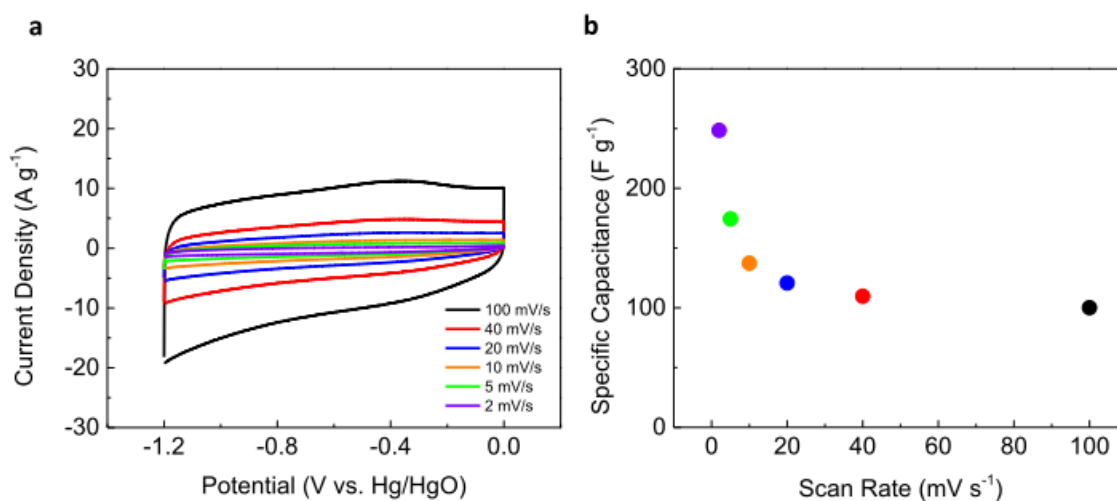


Figure F.10: Capacitive contributions of N-OMC Support

a, Cyclic voltammogram of nitrogen-doped ordered mesoporous carbon support (N-OMC) at various scan rates. b, Specific capacitance versus scan rate for N-OMC. Importantly there is an absence of redox peaks at $E_{1/2} \sim -0.3\text{V}$ vs. Hg/HgO which are present in the $\text{LaMnO}_{3\pm\delta}$ samples.

F.2 REFERENCES

1. Mickevicius, S. *et al.* Investigation of Epitaxial LaNiO_{3-x} Thin Films by High-Energy XPS. *J. Alloys Compd.* **423**, 107-111 (2006).
2. De Asha, A., Critchley, J. & Nix, R. Molecular Adsorption Characteristics of Lanthanum Oxide Surfaces: The Interaction of Water with Oxide Overlayers Grown on Cu (111). *Surf. Sci.* **405**, 201-214 (1998).
3. Djurfors, B., Broughton, J., Brett, M. & Ivey, D. Electrochemical Oxidation of Mn/MnO Films: Formation of an Electrochemical Capacitor. *Acta Mater.* **53**, 957-965 (2005).
4. Sunding, M. *et al.* XPS Characterisation of *in situ* Treated Lanthanum Oxide and Hydroxide Using Tailored Charge Referencing and Peak Fitting Procedures. *J. Electron Spectrosc.* **184**, 399-409 (2011).
5. Chen, J. *et al.* The Influence of Nonstoichiometry on LaMnO_3 Perovskite for Catalytic NO Oxidation. *Applied Catalysis B: Environmental* **134**, 251-257 (2013).
6. Mori, T., Inoue, K. & Kamegashira, N. Phase behavior in the system $\text{La}_x\text{Sr}_{1-x}\text{MnO}_{(5+x)/2}$ ($x=0.8-1.0$) with trivalent state of manganese ion. *J. Alloy Compd.* **308**, 87-93 (2003).
7. Ng-Lee, Y. *et al.* Low-temperature synthesis, structure and magnetoresistance of submicrometric $\text{La}_{1-x}\text{K}_x\text{MnO}_{3+\delta}$ perovskites. *J. Mater. Chem.* **7**, 1905-1909 (1997).
8. Barnabé, A. *et al.* Low temperature synthesis and structural characterization of over-stoichiometric $\text{LaMnO}_{3+\delta}$ perovskites. *Mat. Res. Bull.* **39**, 725-735 (2004).
9. Norby, P., Krogh Anderson, I. G. & Krogh Anderson, E. The Crystal Structure of Lanthanum Manganate(III), LaMnO_3 , at Room Temperature and at 1273K under N_2 . *J. Solid State Chem.* **119**, 191-196 (1995).
10. Sakai, N., Fjellvåg, H. & Lebech, B. Effect of Non-Stoichiometry on Properties of $\text{La}_{1-t}\text{MnO}_{3+\delta}$. Part II. Crystal Structure. *Acta Chem. Scand.* **51**, 904-909 (1997).
11. Momma, K. & Izumi, F. Vesta 3 for three-dimensional visualization of crystal, volumetric and morphology data. *J. Appl. Cryst.* **44**, 1272-1276 (2011).
12. Brezesinski, T., Wang, J., Tolbert, S. H. & Dunn, B. Ordered mesoporous $\alpha\text{-MoO}_3$ with iso-oriented nanocrystalline walls for thin-film pseudocapacitors. *Nature Mater.* **9**, 146-151 (2010).

Bibliography

- Abbate M, de Groot FMF, Fuggle JC, Fujimori A, Strebel O, Lopez F, et al. Controlled-valence properties of $\text{La}_{1-x}\text{Sr}_x\text{FeO}_3$ and $\text{La}_{1-x}\text{Sr}_x\text{MnO}_3$ studied by soft-x-ray absorption spectroscopy. *Physical Review B* 1992, 46(8): 4511-4519.
- Alonso Vante, N., Platinum and Non-Platinum Nanomaterials for the Molecular Oxygen Reduction Reaction. *ChemPhysChem*, 2010. 11(13): p. 2732-2744.
- Amow G, Davidson IJ, Skinner SJ. A comparative study of the Ruddlesden-Popper series, $\text{La}_{n+1}\text{Ni}_n\text{O}_{3n+1}$ ($n = 1, 2$ and 3), for solid-oxide fuel-cell cathode applications. *Solid State Ionics* 2006, 177(13–14): 1205-1210.
- Anisimov VI, Bukhvalov D, Rice TM. Electronic structure of possible nickelate analogs to the cuprates. *Physical Review B* 1999, 59(12): 7901-7906.
- Antolini, E., Carbon supports for low-temperature fuel cell catalysts. *Applied Catalysis B: Environmental*, 2009. 88(1): p. 1-24.
- Arico, A. S., Bruce, P., Scrosati, B., Tarascon, J. & Van Schalkwijk, W. Nanostructured materials for advanced energy conversion and storage devices. *Nature Mater.* 4, 366-377 (2005).
- Augustyn, V. et al. High-rate electrochemical energy storage through Li^+ intercalation pseudocapacitance. *Nature Mater.* 12, 518-522 (2013).
- Bajdich, M.; García-Mota, M.; Vojvodic, A.; Norskov, J. K.; Bell, A. T. *J Am Chem Soc* 2013.
- Bard AJ, Faulkner LR. *Kinetics of Electrode Reactions. Electrochemical Methods: Fundamentals and Applications*, 2nd edn. John Wiley & Sons, Inc.: New York, NY, 2001, pp 124-132.
- Bates MK, Jia Q, Doan H, Liang W, Mukerjee S. Charge-Transfer Effects in Ni–Fe and Ni–Fe–Co Mixed-Metal Oxides for the Alkaline Oxygen Evolution Reaction. *ACS Catal* 2016, 6(1): 155-161.
- Bell RJ, Millar GJ, Drennan J. Influence of synthesis route on the catalytic properties of $\text{La}_{1-x}\text{Sr}_x\text{MnO}_3$. *Solid State Ionics* 2000, 131(3–4): 211-220.
- Benloucif R, Nguyen N, Greneche JM, Raveau B. $\text{La}_{2-2x}\text{Sr}_{2x}\text{Ni}_{1-x}\text{Fe}_x\text{O}_{4-(x/2)+\delta}$: Magnetic and electron transport properties. *Journal of Physics and Chemistry of Solids* 1989, 50(4): 435-440.
- Bennett, T.; Poulidakos, D. Splat-Quench Solidification: Estimating the Maximum Spreading of a Droplet Impacting a Solid Surface. *J. Mater. Sci.* 1993, 28, 963-970.

- Bhalla, A.S., R.Y. Guo, and R. Roy, The perovskite structure - a review of its role in ceramic science and technology. *Materials Research Innovations*, 2000. 4(1): p. 3-26.
- Bhavaraju S, DiCarlo JF, Scarfe DP, Jacobson AJ, Buttrey DJ. Electrochemical oxygen intercalation in $\text{La}_2\text{NiO}_4 + \delta$ crystals. *Solid State Ionics* 1996, 86: 825-831.
- Bidault, F.; Brett, D. J. L.; Middleton, P. H.; Brandon, N. P. Review of Gas Diffusion Cathodes for Alkaline Fuel Cells. *J. Power Sources* 2009, 187, 39-48.
- Bielański, A., Oxygen in catalysis. Vol. 43. 1991: CRC Press.
- Blizanac, B., P. Ross, and N. Markovic, Oxygen Reduction on Silver Low-Index Single-Crystal Surfaces in Alkaline Solution: Rotating Ring Disk Ag(hkl) Studies. *The Journal of Physical Chemistry B*, 2006. 110(10): p. 4735-4741.
- Blöchl PE. Projector augmented-wave method. *Physical Review B* 1994, 50(24): 17953-17979.
- Bockris, J. O.; Otagawa, T. Mechanism of Oxygen Evolution on Perovskites. *J. Phys. Chem.* 1983, 87, 2960-2971.
- Boehm, H. P. Acidic and Basic Properties of Hydroxylated Metal Oxide Surfaces. *Discuss. Faraday Soc.* 1971, 52, 264-275.
- Bontempi, E., et al., Structural study of $\text{LaNi}_x\text{Fe}_{1-x}\text{O}_3$ prepared from precursor salts. *Journal of the European Ceramic Society*, 2003. 23(12): p. 2135-2142.
- Brezesinski, T., Wang, J., Tolbert, S. H. & Dunn, B. Ordered mesoporous $\alpha\text{-MoO}_3$ with iso-oriented nanocrystalline walls for thin-film pseudocapacitors. *Nature Mater.* 9, 146-151 (2010).
- Burke, L. D.; Murphy, O. J.; O'Neill, J. F.; Venkatesan, S. J. *Chem. Soc., Faraday Trans.* 1 1977, 73, 1659.
- Calle Vallejo, F., et al., Trends in stability of perovskite oxides. *Angewandte Chemie*, 2010. 122(42): p. 7865-7867.
- Calle-Vallejo, F.; Inoglu, N. G.; Su, H.-Y.; Martinez, J. I.; Man, I. C.; Koper, M. T. M.; Kitchin, J. R.; Rossmeisl, J. *Chemical Science* 2013, 4, 1245.
- Cao, L. and M. Kruk, Short synthesis of ordered silicas with very large mesopores. *RSC Advances*, 2014. 4(1): p. 331-339.
- Chen D, Chen C, Baiye ZM, Shao Z, Ciucci F. Nonstoichiometric Oxides as Low-Cost and Highly-Efficient Oxygen Reduction/Evolution Catalysts for Low-Temperature Electrochemical Devices. *Chem Rev* 2015, 115(18): 9869-9921.
- Chen G-Y, Ma C-L, Chen D, Zhu Y. Robust half-metallicity of hexagonal SrNiO_3 . *Journal of Solid State Chemistry* 2016, 233: 438-443.

- Chen JYC, Dang L, Liang H, Bi W, Gerken JB, Jin S, et al. Operando Analysis of NiFe and Fe Oxyhydroxide Electrocatalysts for Water Oxidation: Detection of Fe⁴⁺ by Mössbauer Spectroscopy. *J Am Chem Soc* 2015, 137(48): 15090-15093.
- Chen, Z., et al., Highly Active and Durable Core-Corona Structured Bifunctional Catalyst for Rechargeable Metal-Air Battery Application. *Nano Letters*, 2012. 12(4): p. 1946-1952.
- Cheng, F. Y.; Chen, J. Metal-Air Batteries: From Oxygen Reduction Electrochemistry to Cathode Catalysts. *Chem. Soc. Rev.* 2012, 41, 2172-2192.
- Cohen RE. Origin of ferroelectricity in perovskite oxides. *Nature* 1992, 358(6382): 136-138.
- Conesa JC. Electronic Structure of the (Undoped and Fe-Doped) NiOOH O₂ Evolution Electrocatalyst. *J Phys Chem C* 2016, 120(34): 18999-19010.
- Conway BE. *Electrochemical Supercapacitors*. Springer US: Boston, MA, 1999.
- Corrigan DA. The Catalysis of the Oxygen Evolution Reaction by Iron Impurities in Thin Film Nickel Oxide Electrodes. *J Electrochem Soc* 1987, 134(2): 377-384.
- Cortés-Gil, R. et al. Evolution of magnetic behavior in oxygen deficient LaMnO_{3-δ}. *J. Phys. Chem. Solids* 67, 579-582 (2006).
- Crumlin, E.J., et al., Oxygen Electrocatalysis on Epitaxial La_{0.6}Sr_{0.4}CoO_{3-δ} Perovskite Thin Films for Solid Oxide Fuel Cells. *Journal of The Electrochemical Society*, 2012. 159(7): p. F219-F225.
- Cushing, B.L., V.L. Kolesnichenko, and C.J. O'Connor, Recent advances in the liquid-phase syntheses of inorganic nanoparticles. *Chemical Reviews*, 2004. 104(9): p. 3893-3946.
- Das A, Xhafa E, Nikolla E. Electro- and thermal-catalysis by layered, first series Ruddlesden-Popper oxides. *Catalysis Today* 2016, 277, Part 2: 214-226.
- Dau, H.; Limberg, C.; Reier, T.; Risch, M.; Roggan, S.; Strasser, P. The Mechanism of Water Oxidation: From Electrolysis via Homogeneous to Biological Catalysis. *ChemCatChem* 2010, 2, 724-761.
- Dionigi F, Strasser P. NiFe-Based (Oxy)hydroxide Catalysts for Oxygen Evolution Reaction in Non-Acidic Electrolytes. *Advanced Energy Materials* 2016, 6(23): 1600621-n/a.
- Eastoe J, Hollamby MJ, Hudson L. Recent advances in nanoparticle synthesis with reversed micelles. *Advances in Colloid and Interface Science* 2006, 128–130: 5-15.
- Engstrom, J. D.; Lai, E. S.; Ludher, B. S.; Chen, B.; Milner, T. E.; Williams, R. O.; Kitto, G. B.; Johnston, K. P. Formation of Stable Submicron Protein Particles by Thin Film Freezing. *Pharm. Res.* 2008, 25, 1334-1346.

- Erat S, Braun A, Piamonteze C, Liu Z, Ovalle A, Schindler H, et al. Entanglement of charge transfer, hole doping, exchange interaction, and octahedron tilting angle and their influence on the conductivity of $\text{La}_{1-x}\text{Sr}_x\text{Fe}_{0.75}\text{Ni}_{0.25}\text{O}_{3-\delta}$: A combination of x-ray spectroscopy and diffraction. *Journal of Applied Physics* 2010, 108(12): 124906.
- Falcón H, Carbonio RE, Fierro JLG. Correlation of Oxidation States in $\text{LaFe}_x\text{Ni}_{1-x}\text{O}_{3+\delta}$ Oxides with Catalytic Activity for H_2O_2 Decomposition. *Journal of Catalysis* 2001, 203(2): 264-272.
- Falcón, H., et al., Crystal Structure Refinement and Stability of $\text{LaFe}_x\text{Ni}_{1-x}\text{O}_3$ Solid Solutions. *Journal of Solid State Chemistry*, 1997. 133(2): p. 379-385.
- Fierro, S.; Nagel, T.; Baltruschat, H.; Comninellis, C. Investigation of the Oxygen Evolution Reaction on Ti/IrO₂ Electrodes Using Isotope Labelling and on-Line Mass Spectrometry. *Electrochem. Commun.* 2007, 9, 1969-1974.
- Forslund RP, Mefford JT, Hardin WG, Alexander CT, Johnston KP, Stevenson KJ. Nanostructured LaNiO_3 Perovskite Electrocatalyst for Enhanced Urea Oxidation. *ACS Catal* 2016, 6(8): 5044-5051.
- Galal, A., N.F. Atta, and S.M. Ali, Investigation of the catalytic activity of LaBO_3 (B=Ni, Co, Fe or Mn) prepared by the microwave-assisted method for hydrogen evolution in acidic medium. *Electrochimica Acta*, 2011. 56(16): p. 5722-5730.
- Galasso FS. Structure, Properties and Preparation of Perovskite-Type Compounds, vol. 5. Pergamon Press, 1969.
- Ganguli AK, Ganguly A, Vaidya S. Microemulsion-based synthesis of nanocrystalline materials. *Chemical Society Reviews* 2010, 39(2): 474-485.
- Garg N, Basu M, Upadhyaya K, Shivaprasad SM, Ganguli AK. Controlling the aspect ratio and electrocatalytic properties of nickel cobaltite nanorods. *RSC Adv* 2013, 3(46): 24328-24336.
- Garsany, Y., Singer, I. L. & Swider-Lyons, K. E. Impact of film drying procedures on RDE characterization of Pt/VC electrocatalysis. *J. Electroanal. Chem.* 662, 396-406 (2011).
- Gasteiger, H.A., et al., Activity benchmarks and requirements for Pt, Pt-alloy, and non-Pt oxygen reduction catalysts for PEMFCs. *Applied Catalysis B: Environmental*, 2005. 56(1): p. 9-35.
- Giannakas AE, Ladavos AK, Pomonis PJ. Preparation, characterization and investigation of catalytic activity for NO+CO reaction of LaMnO_3 and LaFeO_3 perovskites prepared via microemulsion method. *Applied Catalysis B: Environmental* 2004, 49(3): 147-158.

- Gilev AR, Kiselev EA, Cherepanov VA. Homogeneity range, oxygen nonstoichiometry, thermal expansion and transport properties of $\text{La}_{2-x}\text{Sr}_x\text{Ni}_{1-y}\text{Fe}_y\text{O}_{4+\delta}$. RSC Adv 2016, 6(77): 72905-72917.
- Goodenough JB, Ramasesha S. Further evidence for the coexistence of localized and itinerant 3d electrons in La_2NiO_4 . Materials Research Bulletin 1982, 17(3): 383-390.
- Görlin M, Ferreira de Araújo J, Schmies H, Bernsmeier D, Dresch S, Gliech M, et al. Tracking Catalyst Redox States and Reaction Dynamics in Ni–Fe Oxyhydroxide Oxygen Evolution Reaction Electrocatalysts: The Role of Catalyst Support and Electrolyte pH. J Am Chem Soc 2017, 139(5): 2070-2082.
- Gorlin, Y.; Jaramillo, T. F. A Bifunctional Nonprecious Metal Catalyst for Oxygen Reduction and Water Oxidation. J. Am. Chem. Soc. 2010, 132, 13612-13614.
- Gou G, Grinberg I, Rappe AM, Rondinelli JM. Lattice normal modes and electronic properties of the correlated metal LaNiO_3 . Physical Review B 2011, 84(14): 144101.
- Grenier, J. C., Pouchard, M. & Wattiaux, A. Electrochemical synthesis: oxygen intercalation. Curr. Opin. Solid State Mater. Sci. 1, 233-240 (1996).
- Guidelli, R. & Schmickler, W. Electrosorption Valency and Partial Charge Transfer. In Modern Aspects of Electrochemistry 38, 303-371 (Springer, 2005).
- Hahn, B. P., Long, J. W. & Rolison, D. R. Something from Nothing: Enhancing Electrochemical Charge Storage with Cation Vacancies. Acc. Chem. Res. 46, 1181-1191 (2013).
- Haider, M. A.; Capizzi, A. J.; Murayama, M.; McIntosh, S. Reverse Micelle Synthesis of Perovskite Oxide Nanoparticles. Solid State Ionics 2011, 196, 65-72.
- Karlsson, G. Reduction of Oxygen on LaNiO_3 in Alkaline-Solution. J. Power Sources 1983, 10, 319-331.
- Karlsson, G., PEROVSKITE CATALYSTS FOR AIR ELECTRODES. Electrochimica Acta, 1985. 30(11): p. 1555-1561.
- Karvonen, L. et al. O-K and Co-L XANES Study on Oxygen Intercalation in Perovskite $\text{SrCoO}_{3-\delta}$ Chem. Mater. 22, 70-76 (2010).
- Kobussen AGC, van Buren FR, Broers GHJ. The influence of the particle size distribution on the measurement of oxygen ion diffusion coefficients in $\text{La}_{0.50}\text{Sr}_{0.50}\text{CoO}_{3-y}$. Journal of Electroanalytical Chemistry and Interfacial Electrochemistry 1978, 91(2): 211-217.
- Koc, R. and H. Anderson, Electrical conductivity and Seebeck coefficient of $(\text{La}, \text{Ca})(\text{Cr}, \text{Co})\text{O}_3$. Journal of materials science, 1992. 27(20): p. 5477-5482.

- Konysheva, E.; Irvine, J. T. S. Thermochemical and Structural Stability of A- and B-Site-Substituted Perovskites in Hydrogen-Containing Atmosphere. *Chem. Mater.* 2009, 21, 1514-1523.
- Koza, J. A.; He, Z.; Miller, A. S.; Switzer, J. A. *Chem Mater* 2012, 24, 3567.
- Koza, J.A., et al., Deposition of β -Co (OH) 2 films by electrochemical reduction of tris (ethylenediamine) cobalt (III) in alkaline solution. *Chemistry of Materials*, 2013. 25(9): p. 1922-1926.
- Kresse G, Furthmüller J. Efficient iterative schemes for ab initio total-energy calculations using a plane-wave basis set. *Physical Review B* 1996, 54(16): 11169-11186.
- Kudo, T., Obayashi, H. & Gejo, T. Electrochemical Behavior of the Perovskite-Type $\text{Nd}_{1-x}\text{Sr}_x\text{CoO}_3$ in an Aqueous Alkaline Solution. *J. Electrochem. Soc.* 122, 159-163 (1975).
- Laiho, R. et al. Low-field magnetic properties of $\text{LaMnO}_3+\delta$ with $0.065 \leq \delta \leq 0.154$. *J. Phys. Chem. Solids* 64, 2313-2319 (2003).
- Lee Y, Suntivich J, May KJ, Perry EE, Shao-Horn Y. Synthesis and Activities of Rutile IrO_2 and RuO_2 Nanoparticles for Oxygen Evolution in Acid and Alkaline Solutions. *J Phys Chem Lett* 2012, 3(3): 399-404.
- Lee Y-L, Lee D, Wang XR, Lee HN, Morgan D, Shao-Horn Y. Kinetics of Oxygen Surface Exchange on Epitaxial Ruddlesden–Popper Phases and Correlations to First-Principles Descriptors. *J Phys Chem Lett* 2016, 7(2): 244-249.
- Lee, C.; Riga, A.; Yeager, E. In *Mass Transport Phenomena in Ceramics*; Gordon, R. S., Cooper, A. R., Heuer, A. H., Eds.; Plenum Press: New York, 1975, p 489.
- Lee, J. S.; Kim, S. T.; Cao, R.; Choi, N. S.; Liu, M.; Lee, K. T.; Cho, J. *Adv Energy Mater* 2011, 1, 34.
- Lee, Y. N.; Lago, R. M.; Fierro, J. L. G.; González, J. *Applied Catalysis A: General* 2001, 215, 245.
- Lee, Y.-L.; Kleis, J.; Rossmeisl, J.; Morgan, D. *Physical Review B* 2009, 80, 224101.
- Lee, Y.-L.; Kleis, J.; Rossmeisl, J.; Shao-Horn, Y.; Morgan, D. *Energy Environ. Sci.* 2011, 4, 3966.
- Liang, Y. Y.; Li, Y. G.; Wang, H. L.; Zhou, J. G.; Wang, J.; Regier, T.; Dai, H. J. Co_3O_4 Nanocrystals on Graphene as a Synergistic Catalyst for Oxygen Reduction Reaction. *Nat. Mater.* 2011, 10, 780-786.
- Lin, M. Y.; Lindsay, H. M.; Weitz, D. A.; Ball, R. C.; Klein, R.; Meakin, P. Universality in Colloid Aggregation. *Nature* 1989, 339, 360-362.
- Liu, J.J., Advanced electron microscopy of metal–support interactions in supported metal catalysts. *ChemCatChem*, 2011. 3(6): p. 934-948.

- Louie MW, Bell AT. An Investigation of Thin-Film Ni–Fe Oxide Catalysts for the Electrochemical Evolution of Oxygen. *J Am Chem Soc* 2013, 135(33): 12329-12337.
- Ma X, Carneiro JSA, Gu X-K, Qin H, Xin H, Sun K, et al. Engineering Complex, Layered Metal Oxides: High-Performance Nickelate Oxide Nanostructures for Oxygen Exchange and Reduction. *ACS Catal* 2015, 5(7): 4013-4019.
- Ma X, Wang B, Xhafa E, Sun K, Nikolla E. Synthesis of shape-controlled $\text{La}_2\text{NiO}_{4+\delta}$ nanostructures and their anisotropic properties for oxygen diffusion. *Chem Commun* 2015, 51(1): 137-140.
- Macounová, K.; Jirkovský, J.; Makarova, M. V.; Franc, J.; Krtíl, P. *J Solid State Electrochem* 2009, 13, 959.
- Mahesh, R., Kannan, K. R. & Rao, C. N. R. Electrochemical Synthesis of Ferromagnetic LaMnO_3 and Metallic NdNiO_3 . *J. Solid State Chem.* 114, 294-296 (1995).
- Maldonado, S., S. Morin, and K.J. Stevenson, Structure, composition, and chemical reactivity of carbon nanotubes by selective nitrogen doping. *Carbon*, 2006. 44(8): p. 1429-1437.
- Maldonado, S.; Stevenson, K. J. Influence of Nitrogen Doping on Oxygen Reduction Electrocatalysis at Carbon Nanofiber Electrodes. *J. Phys. Chem. B* 2005, 109, 4707-4716.
- Man IC, Su H-Y, Calle-Vallejo F, Hansen HA, Martínez JI, Inoglu NG, et al. Universality in Oxygen Evolution Electrocatalysis on Oxide Surfaces. *ChemCatChem* 2011, 3(7): 1159-1165.
- Manthiram, A., Kuo, J. F. & Goodenough, J. B. Characterization of Oxygen Deficient Perovskites as Oxide Ion Electrolytes. *Solid State Ionics* 52, 225-234 (1993).
- Markovic, N.; Gasteiger, H.; Ross, P. N. *J Electrochem Soc* 1997, 144, 1591.
- Masato K, Masahiro Y. Synthesis and Characteristics of Complex Multicomponent Oxides Prepared by Polymer Complex Method. *Bulletin of the Chemical Society of Japan* 1999, 72(7): 1427-1443.
- Mefford JT, Hardin WG, Dai S, Johnston KP, Stevenson KJ. Anion charge storage through oxygen intercalation in LaMnO_3 perovskite pseudocapacitor electrodes. *Nat Mater* 2014, 13(7): 726-732.
- Mefford JT, Rong X, Abakumov AM, Hardin WG, Dai S, Kolpak AM, et al. Water electrolysis on $\text{La}_{1-x}\text{Sr}_x\text{CoO}_{3-\delta}$ perovskite electrocatalysts. *Nature Communications* 2016, 7: 11053.
- Merkle R, Mastrikov YA, Kotomin EA, Kuklja MM, Maier J. First Principles Calculations of Oxygen Vacancy Formation and Migration in

- Ba_{1-x}Sr_xCo_{1-y}Fe_yO_{3-δ} Perovskites. *J Electrochem Soc* 2011, 159(2): B219-B226.
- Mickevicius, S.; Grebinskij, S.; Bondarenka, V.; Vengalis, B.; Sliuziene, K.; Orłowski, B. A.; Osinniy, V.; Drube, W. Investigation of Epitaxial LaNiO_{3-x} Thin Films by High-Energy XPS. *J. Alloys Compd.* 2006, 423, 107-111.
- Mogni L, Prado F, Ascolani H, Abbate M, Moreno MS, Manthiram A, et al. Synthesis, crystal chemistry and physical properties of the Ruddlesden–Popper phases Sr₃Fe_{2-x}Ni_xO_{7-δ} (0<x<1.0). *Journal of Solid State Chemistry* 2005, 178(5): 1559-1568.
- Neburchilov, V.; Wang, H.; Martin, J. J.; Qu, W. A Review on Air Cathodes for Zinc-Air Fuel Cells. *J. Power Sources* 2010, 195, 1271-1291.
- Nemudry, A., Goldberg, E. L., Aguirre, M. & Alario-Franco, M. Á. Electrochemical Topotactic Oxidation of Nonstoichiometric Perovskites at Ambient Temperature. *Solid State Sci.* 4, 677-690 (2002).
- Nørskov JK, Abild-Pedersen F, Studt F, Bligaard T. Density functional theory in surface chemistry and catalysis. *Proceedings of the National Academy of Sciences* 2011, 108(3): 937-943.
- Nørskov, J.K., et al., Origin of the overpotential for oxygen reduction at a fuel-cell cathode. *The Journal of Physical Chemistry B*, 2004. 108(46): p. 17886-17892.
- Oliveira FS, Pimentel PM, Oliveira RMPB, Melo DMA, Melo MAF. Effect of lanthanum replacement by strontium in lanthanum nickelate crystals synthesized using gelatin as organic precursor. *Materials Letters* 2010, 64(24): 2700-2703.
- Ovenstone, J., K.C. Chan, and C.B. Ponton, Hydrothermal processing and characterisation of doped lanthanum chromite for use in SOFCs. *Journal of Materials Science*, 2002. 37(15): p. 3315-3322.
- Ovenstone, J.; Chan, K. C.; Ponton, C. B. Hydrothermal Processing and Characterisation of Doped Lanthanum Chromite for Use in Sofcs. *J. Mater. Sci.* 2002, 37, 3315-3322.
- Overhoff, K. A.; Engstrom, J. D.; Chen, B.; Scherzer, B. D.; Milner, T. E.; Johnston, K. P.; Williams Iii, R. O. Novel Ultra-Rapid Freezing Particle Engineering Process for Enhancement of Dissolution Rates of Poorly Water-Soluble Drugs. *Eur. J. Pharm. Biopharm.* 2007, 65, 57-67.
- Patel, M. N. et al. High pseudocapacitance of MnO₂ nanoparticles in graphitic disordered mesoporous carbon at high scan rates. *J. Mater. Chem.* 22, 3160-3169 (2012).
- Patzke, G. R.; Zhou, Y.; Kontic, R.; Conrad, F. Oxide Nanomaterials: Synthetic Developments, Mechanistic Studies, and Technological Innovations. *Angew. Chem.-Int. Edit.* 2011, 50, 826-859.

- Perdew JP, Burke K, Ernzerhof M. Generalized Gradient Approximation Made Simple. *Physical Review Letters* 1996, 77(18): 3865-3868.
- Petříček V, Dušek M, Palatinus L. Crystallographic Computing System JANA2006: General features. *Zeitschrift für Kristallographie*; 2014. p. 345.
- Pileni M-P. The role of soft colloidal templates in controlling the size and shape of inorganic nanocrystals. *Nat Mater* 2003, 2(3): 145-150.
- Piovano, A. et al. Time Resolved in Situ XAFS Study of the Electrochemical Oxygen Intercalation in SrFeO_{2.5} Brownmillerite Structure: Comparison with the Homologous SrCoO_{2.5} System. *J. Phys. Chem. C* 115, 1311-1322 (2011).
- Pletcher, D. and X. Li, Prospects for alkaline zero gap water electrolyzers for hydrogen production. *International Journal of Hydrogen Energy*, 2011. 36(23): p. 15089-15104.
- Pourbaix, M., *Atlas of Electrochemical Equilibria in Aqueous Solutions* 1974: NACE International.
- Poux, T.; Napolskiy, F.; Dintzer, T.; Kéranguéven, G.; Istomin, S. Y.; Tsirlina, G.; Antipov, E.; Savinova, E. *Catal Today* 2012, 189, 83.
- Rao CNR, Ganguly P, Singh KK, Ram RAM. A comparative study of the magnetic and electrical properties of perovskite oxides and the corresponding two-dimensional oxides of K₂NiF₄ structure. *Journal of Solid State Chemistry* 1988, 72(1): 14-23.
- Read, M. S.; Islam, M. S.; Watson, G. W.; King, F.; Hancock, F. E. *J Mater Chem* 2000, 10, 2298.
- Ritzmann AM, Muñoz-García AB, Pavone M, Keith JA, Carter EA. Ab Initio DFT+U Analysis of Oxygen Vacancy Formation and Migration in La_{1-x}Sr_xFeO_{3-δ} (x = 0, 0.25, 0.50). *Chem Mater* 2013, 25(15): 3011-3019.
- Rong X, Parolin J, Kolpak AM. A Fundamental Relationship between Reaction Mechanism and Stability in Metal Oxide Catalysts for Oxygen Evolution. *ACS Catal* 2016, 6(2): 1153-1158.
- Rossmesl, J.; Qu, Z. W.; Zhu, H.; Kroes, G. J.; Norskov, J. K. Electrolysis of Water on Oxide Surfaces. *J. Electroanal. Chem.* 2007, 607, 83-89.
- Rozenberg GK, Milner AP, Pasternak MP, Hearne GR, Taylor RD. Experimental confirmation of a p–p intraband gap in Sr₂FeO₄. *Physical Review B* 1998, 58(16): 10283-10287.
- Ruiz-González, L., Cortés-Gil, R., Alonso, J. M., González-Calbet, J. M. & Vallet-Regí, M. Revisiting the Role of Vacancies in Manganese Related Perovskites. *The Open Inorganic Chemistry Journal* 1, 37-46 (2007).

- Saitoh T, Bocquet AE, Mizokawa T, Namatame H, Fujimori A, Abbate M, et al. Electronic structure of $\text{La}_{1-x}\text{Sr}_x\text{MnO}_3$ studied by photoemission and x-ray-absorption spectroscopy. *Physical Review B* 1995, 51(20): 13942-13951.
- Schaak, R.E. and T.E. Mallouk, Prying apart ruddlesden-popper phases: exfoliation into sheets and nanotubes for assembly of perovskite thin films. *Chemistry of Materials*, 2000. 12(11): p. 3427-3434.
- Schmidt, T. J. et al. Characterization of High-Surface-Area Electrocatalysts Using a Rotating Disk Electrode Configuration. *J. Electrochem. Soc.* 145, 2354-2358 (1998).
- Seitz LC, Dickens CF, Nishio K, Hikita Y, Montoya J, Doyle A, et al. A highly active and stable $\text{IrO}_x/\text{SrIrO}_3$ catalyst for the oxygen evolution reaction. *Science* 2016, 353(6303): 1011-1014.
- Seki H, Saito T, Shimakawa Y. High Pressure Synthesis of $\text{SrFe}_{1-x}\text{Ni}_x\text{O}_3$. *Journal of the Japan Society of Powder and Powder Metallurgy* 2016, 63(7): 609-612.
- Sepa, D.; Vojnovic, M.; Damjanovic, A. *Electrochim Acta* 1981, 26, 781.
- Shao, Z. P.; Zhou, W.; Zhu, Z. H. Advanced Synthesis of Materials for Intermediate-Temperature Solid Oxide Fuel Cells. *Prog. Mater. Sci.* 2012, 57, 804-874.
- Sharma IB, Singh D. Solid state chemistry of Ruddlesden-Popper type complex oxides. *Bulletin of Materials Science* 1998, 21(5): 363-374.
- Shein IR, Shein KI, Kozhevnikov VL, Ivanovskii AL. Band structure and the magnetic and elastic properties of SrFeO_3 and LaFeO_3 perovskites. *Physics of the Solid State* 2005, 47(11): 2082-2088.
- Slanac, D. A.; Hardin, W. G.; Johnston, K. P.; Stevenson, K. J. Atomic Ensemble and Electronic Effects in Ag-Rich AgPd Nanoalloy Catalysts for Oxygen Reduction in Alkaline Media. *J. Am. Chem. Soc.* 2012, 134, 9812-9819.
- Slanac, D. A.; Lie, A.; Paulson, J. A.; Stevenson, K. J.; Johnston, K. P. Bifunctional Catalysts for Alkaline Oxygen Reduction Reaction Via Promotion of Ligand and Ensemble Effects at Ag/MnO_x Nanodomains. *J. Phys. Chem. C* 2012, 116, 11032-11039.
- Slanac, D.A., et al., Atomic resolution structural insights into PdPt nanoparticle-carbon interactions for the design of highly active and stable electrocatalysts. *Electrochimica Acta*, 2012. 64: p. 35-45.
- Soleymani M, Edrissi M. Preparation of manganese-based perovskite nanoparticles using a reverse microemulsion method: biomedical applications. *Bulletin of Materials Science* 2016, 39(2): 487-490.
- Souza Filho, A., et al., Raman spectroscopy for probing chemically/physically induced phenomena in carbon nanotubes. *Nanotechnology*, 2003. 14(10): p. 1130.

- Spendelow, J. S.; Wieckowski, A. Electrocatalysis of Oxygen Reduction and Small Alcohol Oxidation in Alkaline Media. *Phys. Chem. Chem. Phys.* 2007, 9, 2654-2675.
- Sreedhar K, Honig JM. Low-Temperature Electron Transport Properties of $\text{La}_{2-x}\text{Sr}_x\text{NiO}_4$ with $0.5 \leq x \leq 1.3$. *Journal of Solid State Chemistry* 1994, 111(1): 147-150.
- Stoneham, A., Systematics of metal-insulator interfacial energies: A new rule for wetting and strong catalyst-support interactions. *Applications of Surface Science*, 1983. 14(3): p. 249-259.
- Subbaraman, R.; Tripkovic, D.; Chang, K.-C.; Strmcnik, D.; Paulikas, A. P.; Hirunsit, P.; Chan, M.; Greeley, J.; Stamenkovic, V.; Markovic, N. M. Trends in Activity for the Water Electrolyser Reactions on 3d $\text{M}(\text{Ni}, \text{Co}, \text{Fe}, \text{Mn})$ Hydr(Oxy)Oxide Catalysts. *Nat. Mater.* 2012, 11, 550-557.
- Sunarso, J., et al., Oxygen Reduction Reaction Activity of La-Based Perovskite Oxides in Alkaline Medium: A Thin-Film Rotating Ring-Disk Electrode Study. *Journal of Physical Chemistry C*, 2012. 116(9): p. 5827-5834.
- Sunarso, J.; Torriero, A. A. J.; Zhou, W.; Howlett, P. C.; Forsyth, M. *J Phys Chem C* 2012, 116, 5827.
- Sunarso, J.; Torriero, A. A. J.; Zhou, W.; Howlett, P. C.; Forsyth, M. Oxygen Reduction Reaction Activity of La-Based Perovskite Oxides in Alkaline Medium: A Thin-Film Rotating Ring-Disk Electrode Study. *J. Phys. Chem. C* 2012, 116, 5827-5834.
- Suntivich J, Gasteiger HA, Yabuuchi N, Shao-Horn Y. Electrocatalytic Measurement Methodology of Oxide Catalysts Using a Thin-Film Rotating Disk Electrode. *J Electrochem Soc* 2010, 157(8): B1263-B1268.
- Suntivich J, May KJ, Gasteiger HA, Goodenough JB, Shao-Horn Y. A Perovskite Oxide Optimized for Oxygen Evolution Catalysis from Molecular Orbital Principles. *Science* 2011, 334(6061): 1383-1385.
- Suntivich, J.; Gasteiger, H. A.; Yabuuchi, N.; Nakanishi, H.; Goodenough, J. B.; Shao-Horn, Y. Design Principles for Oxygen-Reduction Activity on Perovskite Oxide Catalysts for Fuel Cells and Metal-Air Batteries. *Nat. Chem.* 2011, 3, 546-550.
- Suntivich, J.; Gasteiger, H. A.; Yabuuchi, N.; Nakanishi, H.; Goodenough, J. B.; Shao-Horn, Y. *Nat Chem* 2011, 3, 546.
- Takeda Y, Hashino T, Miyamoto H, Kanamaru F, Kume S, Koizumi M. Synthesis of SrNiO_3 and related compound, $\text{Sr}_2\text{Ni}_2\text{O}_5$. *Journal of Inorganic and Nuclear Chemistry* 1972, 34(5): 1599-1601.

- Takeda Y, Imayoshi K, Imanishi N, Yamamoto O, Takano M. Preparation and characterization of $\text{Sr}_{2-x}\text{La}_x\text{FeO}_4$ ($0 < x < 1$). *Journal of Materials Chemistry* 1994, 4(1): 19-22.
- Takeda Y, Kanno R, Sakano M, Yamamoto O, Takano M, Bando Y, et al. Crystal chemistry and physical properties of $\text{La}_{2-x}\text{Sr}_x\text{NiO}_4$ ($0 \leq x \leq 1.6$). *Materials Research Bulletin* 1990, 25(3): 293-306.
- Teraoka, Y.; Nanri, S.; Moriguchi, I.; Kagawa, S.; Shimanoe, K.; Yamazoe, N. Synthesis of Manganite Perovskites by Reverse Homogeneous Precipitation Method in the Presence of Alkylammonium Cations. *Chem. Lett.* 2000, 1202-1203.
- Thomas, M. G. S. R., Bruce, P. G. & Goodenough, J. B. Lithium Mobility in the Layered Lithium Cobalt Oxide ($\text{Li}_{1-x}\text{CoO}_2$). *Solid State Ionics* 17, 13-19 (1985).
- Torrance JB, Lacorre P, Nazzari AI, Ansaldo EJ, Niedermayer C. Systematic study of insulator-metal transitions in perovskites RNiO_3 ($\text{R}=\text{Pr}, \text{Nd}, \text{Sm}, \text{Eu}$) due to closing of charge-transfer gap. *Physical Review B* 1992, 45(14): 8209-8212.
- Trasatti, S. Electrocatalysis by Oxides - Attempt at a Unifying Approach. *J. Electroanal. Chem.* 1980, 111, 125-131.
- Trotochaud L, Young SL, Ranney JK, Boettcher SW. Nickel-Iron Oxyhydroxide Oxygen-Evolution Electrocatalysts: The Role of Intentional and Incidental Iron Incorporation. *J Am Chem Soc* 2014, 136(18): 6744-6753.
- Trotochaud, L.; Ranney, J. K.; Williams, K. N.; Boettcher, S. W. Solution-Cast Metal Oxide Thin Film Electrocatalysts for Oxygen Evolution. *J. Am. Chem. Soc.* 2012, 134, 17253-17261.
- Twu, J.; Gallagher, P. K. In *Properties and Applications of Perovskite-Type Oxides*; L.G. Tejuca, J. L. G. F., Ed.; Marcel Dekker, Inc.: New York, 1993.
- Van Buren FR, Broers GHJ, Bouman AJ, Boesveld C. An electrochemical method for the determination of oxygen ion diffusion coefficients in $\text{La}_{1-x}\text{Sr}_x\text{CoO}_{3-y}$ compounds. *Journal of Electroanalytical Chemistry and Interfacial Electrochemistry* 1978, 87(3): 389-394.
- Vojvodic, A.; Calle-Vallejo, F.; Guo, W.; Wang, S.; Toftelund, A.; Studt, F.; Martinez, J. I.; Shen, J.; Man, I. C.; Rossmeisl, J. *The Journal of chemical physics* 2011, 134, 244509.
- Wagner, F.T., et al., Catalyst development needs and pathways for automotive PEM fuel cells. *ECS Transactions*, 2006. 3(1): p. 19-29.
- Wang, H.; Sanchez Casalongue, H.; Liang, Y. & Dai, H. $\text{Ni}(\text{OH})_2$ Nanoplates Grown on Graphene as Advanced Electrochemical Pseudocapacitor Materials *J. Am. Chem. Soc.* 132, 7472-7477(2010).

- Wang, J., Polleux, J., Lim, J., & Dunn, B. Pseudocapacitive contributions to electrochemical energy storage in TiO₂ (anatase) nanoparticles. *J. Phys. Chem. C* 111, 14925-14931 (2007).
- Wang, N., et al., A comparison study on methane dry reforming with carbon dioxide over LaNiO₃ perovskite catalysts supported on mesoporous SBA-15, MCM-41 and silica carrier. *Catalysis Today*, 2013. 212(0): p. 98-107.
- Wang, X. Q.; Lee, J. S.; Zhu, Q.; Liu, J.; Wang, Y.; Dai, S. Ammonia-Treated Ordered Mesoporous Carbons as Catalytic Materials for Oxygen Reduction Reaction. *Chem. Mater.* 2010, 22, 2178-2180.
- Wattiaux, A. et al. A Novel Preparation Method of the SrFeO₃ Cubic Perovskite by Electrochemical Means. *Solid State Comm.* 77, 489-493 (1991).
- Wiberg, G. K. H., Mayrhofer, K. J. J. & Arenz, M. Investigation of the Oxygen Reduction Activity on Silver – A Rotating Disc Electrode Study. *Fuel Cells* 10, 575-581 (2010).
- Wiberg, G. K. H.; Mayrhofer, K. J. J.; Arenz, M. *Fuel Cells* 2010, 10, 575.
- Wiggins-Camacho, J. D.; Stevenson, K. J. Mechanistic Discussion of the Oxygen Reduction Reaction at Nitrogen-Doped Carbon Nanotubes. *J. Phys. Chem. C* 2011, 115, 20002-20010.
- Wilde, P. M., Guther, T. J., Oesten, R. & Garche, J. Strontium ruthenate perovskite as the active material for supercapacitors. *J. Electroanal. Chem.* 461, 154-160 (1999).
- Wohlfahrt-Mehrens, M. et al. New materials for supercapacitors. *J. Power Sources* 105, 182-188 (2002).
- Wohlfahrt-Mehrens, M.; Heitbaum, J. Oxygen Evolution on Ru and RuO₂ Electrodes Studied Using Isotope Labelling and on-Line Mass Spectrometry. *Journal of Electroanalytical Chemistry and Interfacial Electrochemistry* 1987, 237, 251-260.
- Yagi S, Yamada I, Tsukasaki H, Seno A, Murakami M, Fujii H, et al. Covalency-reinforced oxygen evolution reaction catalyst. *Nature Communications* 2015, 6: 8249.
- Yi, N., et al., Nanocrystalline LaCoO₃ perovskite particles confined in SBA-15 silica as a new efficient catalyst for hydrocarbon oxidation. *Journal of Catalysis*, 2005. 230(1): p. 249-253.
- Yuasa, M., et al., Preparation of nano-LaNiO₃ support electrode for rechargeable metal-air batteries. *Electrochemistry Communications*, 2012. 24(0): p. 50-52.
- Yuasa, M.; Nishida, M.; Kida, T.; Yamazoe, N.; Shimano, K. Bi-Functional Oxygen Electrodes Using LaMnO₃/LaNiO₃ for Rechargeable Metal-Air Batteries. *J. Electrochem. Soc.* 2011, 158, A605-A610.

- Yuasa, M.; Sakai, G.; Shimanoe, K.; Teraoka, Y.; Yamazoe, N. Exploration of Reverse Micelle Synthesis of Carbon-Supported LaMnO₃. *J. Electrochem. Soc.* 2004, 151, A1477-A1482.
- Yuasa, M.; Shimanoe, K.; Teraoka, Y.; Yamazoe, N. High-Performance Oxygen Reduction Catalyst Using Carbon-Supported La-Mn-Based Perovskite-Type Oxide. *Electrochem. Solid St.* 2011, 14, A67-A69.
- Zhang D, Song Y, Du Z, Wang L, Li Y, Goodenough JB. Active LaNi_{1-x}Fe_xO₃ bifunctional catalysts for air cathodes in alkaline media. *J Mater Chem A* 2015, 3(18): 9421-9426.
- Zhang Z, Greenblatt M. Synthesis, Structure, and Properties of Ln₄Ni₃O_{10-δ} (Ln = La, Pr, and Nd). *Journal of Solid State Chemistry* 1995, 117(2): 236-246.
- Zhao Y, Xu L, Mai L, Han C, An Q, Xu X, et al. Hierarchical mesoporous perovskite La_{0.5}Sr_{0.5}CoO_{2.91} nanowires with ultrahigh capacity for Li-air batteries. *Proceedings of the National Academy of Sciences* 2012, 109(48): 19569-19574.
- Zheng, J. P. & Jow, T. R. A New Charge Storage Mechanism for Electrochemical Capacitors. *J. Electrochem. Soc.* 142, 6-8 (1995).
- Zhou JS, Goodenough JB, Dabrowski B. Transition from Curie-Weiss to enhanced Pauli paramagnetism in RNiO₃ (R = La, Pr,...Gd). *Physical Review B* 2003, 67(2): 020404.
- Zhou W, Zhao M, Liang F, Smith SC, Zhu Z. High activity and durability of novel perovskite electrocatalysts for water oxidation. *Mater Horiz* 2015, 2(5): 495-501.
- Zhu H, Zhang P, Dai S. Recent Advances of Lanthanum-Based Perovskite Oxides for Catalysis. *ACS Catal* 2015, 5(11): 6370-6385.
- Zhu, Y.; Murali, S.; Stoller, M. D.; Ganesh, K. J.; Cai, W.; Ferreira, P. J.; Pirkle, A.; Wallace, R. M.; Cychosz, K. A.; Thommes, M.; Su, D.; Stach, E. A.; Ruoff, R. S. *Science* 2011, 332, 1537.
- Zhuang, S. X.; Huang, C. H.; Huang, K. L.; Hu, X.; Tu, F. Y.; Huang, H. X. Preparation of Homogeneous Nanoporous La_{0.6}Ca_{0.4}CoO₃ for Bi-Functional Catalysis in an Alkaline Electrolyte. *Electrochem. Commun.* 2011, 13, 321-324.